

**A freeze-drying-based hydration stop
technique used for the time-variant
analysis of the early hydration
products of cementitious
suspensions**

VON DER NATURWISSENSCHAFTLICHEN FAKULTÄT DER
GOTTFRIED WILHELM LEIBNIZ UNIVERSITÄT HANNOVER

ZUR ERLANGUNG DES GRADES
DOKTOR DER NATURWISSENSCHAFTEN (DR. RER. NAT.)

GENEHMIGTE DISSERTATION
VON
PATRICK ANDRÉ KIBLING, M.Sc.

2023

Referentin: Prof. Dr. rer. nat. Nadja-Carola Bigall

Korreferent: Prof. Dr. rer. nat. Jürgen Caro

weiterer Korreferent: Prof. Dr. rer. nat. Georg Garnweitner

weiterer Korreferent: Prof. Dr.-Ing. Ludger Lohaus

Tag der Promotion: 20.11.2023

‘WHEN WE ARE NO LONGER ABLE TO CHANGE A SITUATION, WE ARE
CHALLENGED TO CHANGE OURSELVES’
– VIKTOR E. FRANKL, MAN’S SEARCH FOR MEANING

‘Αν θέλεις να εξελιχθείς, πρέπει να είσαι πρόθυμος να σε θεωρούν
ανόητο και τρελό’ {‘IF YOU WANT TO GROW, YOU HAVE TO BE
WILLING TO BE SEEN AS STUPID AND CRAZY’}
– ΕΠΙΚΤΕΤ, Εγχειριδιον {Encheiridion}

KURZZUSAMMENFASSUNG

Die vorliegende Dissertation widmet sich der Entwicklung einer auf Gefriertrocknung basierenden Hydratationsabbruchtechnik, welche die Reaktion einer zementösen Suspension mit Wasser möglichst instantan, vollständig sowie non-invasiv unterbindet, um eine vollständige Charakterisierung des frühen Hydratationszustandes zu ermöglichen. Hierbei ist ein besonderes Augenmerk auf die Veränderungen der chemischen Zusammensetzung und Morphologie der Probe und insbesondere des frühen Hydratationsprodukts Ettringit gelegt worden, welches durch die Beeinflussung der rheologischen Eigenschaften von technischer Bedeutung ist. Des Weiteren wird basierend auf der entwickelten Abbruchtechnik der Einfluss von Ettringit auf die Rheologie einer auf Quarzmehl beruhenden Modellsuspension quantifiziert. Zuletzt werden die durch die Zugabe von hartmagnetischen Eisenoxidnanopartikeln induzierten Änderungen an erhärteten Zementsuspensionen untersucht.

Es ist essentiell, den Hydratationsprozess zu jedem Zeitpunkt instantan vollständig beenden zu können, denn die Eigenschaften von erhärtetem Beton können bereits von den rheologischen Eigenschaften der Zementleimsuspension abgeleitet werden. Dies war jedoch mit einem Isopropanol-Wasser-Austausch (dem Stand der Technik) nicht realisierbar. Daher musste eine gefriertrocknungsbasierte Hydratationsabbruchtechnik entwickelt werden. Hierzu wurden in einer ersten Untersuchung drei verschiedene Abbruchtechniken, die Lyophilisierung, der Stand der Technik sowie die Kombination beider voran genannten Techniken an Zementsuspensionen verglichen, deren Hydratation zu jeweils vier Zeitpunkten gestoppt wurde. Die nicht eindeutigen Ergebnisse des Probenvergleichs führten dazu, dass im nächsten Schritt der Einfluss der Stärke sowie der Dauer der Unterdruckbehandlung auf reines synthetisches Ettringit untersucht worden ist. Hieraus ergab sich, dass ein Druck von 400 Pa die Morphologie sowie die chemische Zusammensetzung von Ettringit für mindestens 72 h nicht verändert. Diese Erkenntnisse wurden in einem zweiten Artikel veröffentlicht. Darauf basierend wurde die Gefriertrocknungstechnik so weit optimiert, dass nach diesem Hydratationsabbruch verglichen mit dem Stand der Technik und der kombinierten Methode, sowohl der Gehalt an Ettringit am höchsten ist als auch die Proben die höchste Reproduzierbarkeit aufweisen.

Im weiteren Verlauf konnte durch die Charakterisierung von auf Quarzmehl beruhenden Modellsuspensionen mit verschiedenen zuvor festgelegten Mengen an *in situ* gebildetem Ettringit dessen Einfluss auf die Rheologie quantifiziert werden. Die erhaltenen Ergebnisse könnten dabei helfen, zwischen den verschiedenen Einflussfaktoren (zum Beispiel konkurrierende Hydratationsprozesse) in zementösen Suspensionen zu differenzieren.

Zur Verallgemeinerung der Anwendbarkeit der entwickelten Methode wurden der Zementsuspension hartmagnetische Eisenoxidnanopartikel zugegeben, um wiederum deren Einfluss auf physikalische Eigenschaften im erhärteten Zustand zu untersuchen. Hierbei wurde gezeigt, dass die Zugabe magnetischer Nanopartikel einen deutlichen Einfluss auf die mechanischen sowie magnetischen Eigenschaften (wie Magnetisierung) von erhärtetem Zementleim hat, wobei die Ausprägung dieser Effekte von der zugegebenen Menge abhängt.

Dieser Doktorarbeit liegen fünf Veröffentlichungen zugrunde, bei denen ich federführend war. Diese wurden in international renommierten Fachzeitschriften veröffentlicht und in logisch-chronologischer Reihenfolge dargestellt.

Schlagnworte: Hydratationsabbruch; Zeitaufgelöste Analyse; Zementöse Suspensionen; Ettringit; Quarzmehl als Modellsystem; Rheologie; Nanopartikuläre Additive.

ABSTRACT

The present dissertation is dedicated to the development of a lyophilisation-based hydration stop technique, which works as instantaneously, completely, and non-invasively as possible in order to enable a complete characterisation of the early hydration stage with a particular focus on changes to chemical composition and morphology of the sample and in particular of the early hydration product ettringite that is of technical importance due to its influence on rheological properties. Furthermore, based on the developed lyophilisation technique, the impact of ettringite on the rheological properties of a model system containing quartz sand is quantified. Lastly, changes to hardened cement paste induced by the addition of hard magnetic iron oxide nanoparticles are investigated.

It is essential to stop the hydration process instantaneously and entirely at any given time since the properties of hardened concrete can already be derived from the rheological properties of the cement paste suspension. However, it was not feasible with the state-of-the-art isopropanol-water exchange. Thus, a freeze-drying-based hydration stop technique had to be developed. In a first study, cementitious suspensions that were stopped at four different hydration times by lyophilisation, the state-of-the-art, as well as the combination of both techniques mentioned above, were compared. The ambiguous results of the samples' comparison led, in the next step, to the examination of the influence of the levels and duration of treatment with low-pressure on pure synthetic ettringite. It was shown that a low-pressure of 400 Pa does not change the chemical composition nor the morphology of ettringite for at least 72 h. These results were published in a second article. Based on these, the freeze-drying technique was optimised to the extent that the ettringite content is highest after this hydration stop. The samples show the highest reproducibility compared to the state-of-the-art and the combined technique, leading to the third published article.

Further, the influence of ettringite on the rheological properties was quantified by characterising a model system based on quartz sand with different pre-set amounts of *in situ* formed ettringite. Derived data sets could allow for a differentiation between various influencing factors (*exempli gratia* simultaneous competitive hydration processes) being present in a cementitious suspension.

In order to generalise the applicability of the developed method, hard magnetic iron oxide nanoparticles were added to cementitious suspensions, in turn, to investigate their influence on physical properties in the hardened state. It was shown that adding magnetic nanoparticles significantly influences the mechanical and magnetic properties (as magnetisation) of hardened cement paste, with the extent of these effects depending on the amount added.

Five publications, which I was responsible for as the first author, form the basis of this dissertation. These have been published in internationally renowned journals and are presented in logically chronological order.

Keywords: Hydration stop; Time-variant analysis; Cementitious suspension; Ettringite; Quartz sand as a model system; Rheology; Nanoparticulate additives.

PREFACE

The present thesis condenses the elaborated, deduced, and published results during my time supervised by Prof. Dr. rer. nat. Nadja-Carola Bigall at the Institute of Physical Chemistry and Electrochemistry of the Leibniz Universität Hannover since 2018. Financially, this work was supported by the German Research Foundation project BI 1708/5-1 in the course of the 1st funding period of the priority programme SPP2005 – “Opus Fluidum Futurum – Rheology of reactive, multiscale, multiphase construction materials”. The research in this thesis has been published in five peer-reviewed research articles, of which I am the first author. Further, 12 peer-reviewed articles have been published, of which I am a co-author, which are not included in this thesis but listed in the appendix (*Publications and Conferences*).

The contributions of each author to the contained publications are listed in the following paragraphs.

For the first article, “Comparison of Water-Isopropanol Replacement and Lyophilisation for Hydration Stop of Cementitious Suspensions” (**section 3.2**), I conducted the preparation of the samples, all analytics, all the data interpretation as well as wrote the research article. Further, I thank D. Cotardo, T. von Bronk, Prof. Dr.-Ing. L. Lohaus as well as Prof. Dr. rer. nat. N.-C. Bigall for support and valuable discussions during the writing of the manuscript, as well as Prof. Dr. rer. nat. A. Feldhoff and Prof. Dr. rer. nat. J. Caro for access to the scanning electron microscope, as well as A. Schlosser and Dr. rer. nat. M. Jahns for help with nitrogen physisorption measurements.

Individual author contributions based on the Contributor Roles Taxonomy (CRediT):

- P. A. Kießling:** Conceptualization, Methodology, Validation, Formal Analysis, Investigation, Data Curation, Writing – Original Draft, Writing – Review & Editing, Visualization, Project Administration.
- D. Cotardo:** Writing – Review & Editing.
- T. von Bronk:** Writing – Review & Editing.
- L. Lohaus:** Resources, Supervision, Writing – Review & Editing.
- N.-C. Bigall:** Conceptualization, Resources, Writing – Review & Editing, Supervision, Funding Acquisition.

For the second article, “Influence of Low-Pressure Treatment on the Morphological and Compositional Stability of Microscopic Ettringite”, I conducted the synthesis of ettringite, X-ray diffraction measurements, Pawley-Fit, Raman spectroscopy, thermogravimetric analysis,

most of the data interpretation, as well as writing most of the article. I thank Prof. Dr. rer. nat. A. Feldhoff for recording single area electron diffraction, scanning transmission electron microscopy, energy dispersive X-ray spectroscopy, support, valuable discussions, and Prof. Dr.-Ing. M. Haist, Prof. Dr.-Ing. L. Lohaus, and Prof. Dr. rer. nat. N.-C. Bigall for support and valuable discussions. Further, I thank Prof. Dr. rer. nat. J. Caro for access to the X-ray diffractometer and transmission electron microscopy, F. Steinbach for scanning transmission electron microscope, transmission electron microscope, and scanning transmission electron microscope coupled with energy dispersive X-ray spectroscopy measurements, Dr. rer. nat. C. Rozanski for help with the interpretation of thermogravimetric analysis spectra, A. Krabbenhöft for environmental scanning electron microscope measurements, Prof. Dr. rer. nat. C. Rüscher for access to the Raman spectrometer and Dr. rer. nat. I. Strauß for help during the measurements.

Individual author contributions based on the Contributor Roles Taxonomy (CRediT):

- P. A. Kießling:** Conceptualization, Validation, Formal Analysis, Investigation, Data Curation, Writing – Original Draft, Writing – Review & Editing, Visualization.
- F Lübke****mann:** Validation, Writing – Review & Editing.
- T. von Bronk:** Writing – Review & Editing.
- D. Cotardo:** Writing – Review & Editing.
- L. Lei:** Writing – Review & Editing.
- A. Feldhoff** Writing – Review & Editing.
- L. Lohaus:** Resources, Writing – Review & Editing.
- M. Haist:** Writing – Review & Editing.
- N.-C. Bigall:** Conceptualization, Validation, Resources, Writing – Review & Editing, Supervision, Funding Acquisition.

For the third article, “Is freeze-drying an alternative to solvent exchange for the hydration stop of cementitious suspensions?”, I conducted all preparatory work, all analytics besides the recording of environmental scanning electron microscope micrographs, all the data interpretation, and wrote the article. I thank Dr. rer. nat. F. Lübke**mann-Warwas**, Dr. rer. nat. A. Mundstock, Prof. Dr.-Ing. L. Lohaus, Prof. Dr.-Ing. M. Haist, Prof. Dr. rer. nat. J. Caro, and Prof. Dr. rer. nat. N.-C. Bigall for support and valuable discussions. Further, I thank Prof. Dr. rer. nat. A. Feldhoff for access to the X-ray diffractometer as well as A. Krabbenhöft for environmental scanning electron microscope measurements.

Individual author contributions based on the Contributor Roles Taxonomy (CRediT):

- P. A. Kießling:** Conceptualization, Validation, Formal Analysis, Investigation, Data Curation, Writing – Original Draft, Writing – Review & Editing, Visualization.
- F Lübke**mann: Writing – Review & Editing.
- A. Mundstock:** Writing – Review & Editing.
- L. Lohaus:** Resources, Writing – Review & Editing.
- M. Haist:** Writing – Review & Editing.
- J. Caro:** Writing – Review & Editing.
- N.-C. Bigall:** Conceptualization, Validation, Resources, Writing – Review & Editing, Supervision, Funding Acquisition.

For the fourth article, “Influence of *in situ* ettringite formation on the rheological properties of quartz suspensions”, I wrote most of the article, conducted all preparatory work, all analytics besides the measurements of scanning electron microscopy of quartz powder and part of the nitrogen physisorption, as well as made most of the data interpretation. I thank J. Link for the execution and interpretation of the rheological measurements, M. Heinemann, Dr. rer. nat. F. Lübkemann-Warwas, Dr. rer. nat. F. Rieck genannt Best, Dr.-Ing. T. Sowoidnich, Dr. rer. nat. A. Mundstock, Prof. Dr.-Ing. H.-M. Ludwig, Prof. Dr.-Ing. M. Haist, and Prof. rer. nat. N.-C. Bigall for support and valuable discussions. Further, I thank Prof. Dr. rer. nat. J. Caro for access to the infrared spectrometer, C. Matthes for scanning electron microscope measurements, A. Schulz for nitrogen physisorption as well as laser diffraction measurements, and G. Bohne for inductively coupled plasma optical emission spectrometer measurements.

Individual author contributions based on the Contributor Roles Taxonomy (CRediT):

- P. A. Kießling:** Conceptualization, Methodology, Validation, Formal Analysis, Investigation, Data Curation, Writing – Original Draft, Writing – Review & Editing, Visualization.
- J. Link:** Conceptualization, Methodology, Investigation, Writing – Original Draft, Writing – Review & Editing.
- M. Heinemann:** Writing – Review & Editing.
- F Lübke**mann-Warwas: Writing – Review & Editing.
- F. Rieck genannt Best** Writing – Review & Editing.
- T. Sowoidnich:** Writing – Review & Editing.
- A. Mundstock:** Writing – Review & Editing, Visualization.

- H.-M. Ludwig:** Writing – Review & Editing.
- M. Haist:** Conceptualization, Resources, Writing – Review & Editing, Supervision, Funding Acquisition.
- N.-C. Bigall:** Conceptualization, Resources, Writing – Review & Editing, Supervision, Funding Acquisition.

For the fifth article, “Impact of Hard Magnetic Nanocrystals on the Properties of Hardened Cement Paste”, I wrote most of the article, conducted all preparatory work, most analytics, as well as most data interpretation. I thank M. Mahlbacher for mercury intrusion, compressive strength test, micro and nano indentation, C. Wesemann for MÖSSBAUER spectroscopy, superconducting quantum interference device measurements, and transmission electron microscopy, Dr. rer. nat. S. Klimke for MÖSSBAUER spectroscopy, as well as Dr. rer. nat. A. Mundstock, Dr. rer. nat. F. Lübkeemann-Warwas, Prof. Dr. rer. nat. F. Renz, Prof. Dr.-Ing. L. Lohaus, Prof. Dr.-Ing. M. Haist, and Prof. Dr. rer. nat. N.-C. Bigall for support and valuable discussions. Further, I thank Prof. Dr. rer. nat. A. Feldhoff for access to the X-ray diffractometer and scanning electron microscopy.

Individual author contributions based on the Contributor Roles Taxonomy (CRediT):

- P. A. Kießling:** Conceptualization, Methodology, Validation, Formal Analysis, Investigation, Data Curation, Writing – Original Draft, Writing – Review & Editing, Visualization, Project Administration.
- M. Mahlbacher:** Conceptualization, Software, Formal Analysis, Investigation, Data Curation, Writing – Original Draft, Writing – Review & Editing, Visualization.
- C. Wesemann:** Conceptualization, Validation, Formal Analysis, Investigation, Data Curation, Writing – Original Draft, Writing – Review & Editing, Visualization.
- A. Mundstock:** Writing – Review & Editing, Visualization.
- F Lübkeemann-Warwas:** Writing – Review & Editing.
- S. Klimke:** Writing – Review & Editing.
- F. Renz:** Writing – Review & Editing.
- L. Lohaus:** Writing – Review & Editing.
- M. Haist:** Resources, Writing – Review & Editing, Supervision, Funding Acquisition.
- N.-C. Bigall:** Conceptualization, Resources, Writing – Review & Editing, Supervision, Funding Acquisition.

NOTE OF THANKS

Prof. Nadja-Carola Bigall möchte ich für die Vergabe dieses spannenden Forschungsthemas, die vertrauensvolle Betreuung und ihre motivierenden Worte in so manchem Gespräch danken. Ohne ihre konstruktiven Vorschläge, die kreativen Impulse, die ich fruchtbar aufnehmen konnte und die enge Abstimmung wäre diese Arbeit nicht entstanden.

Zudem möchte ich Prof. Caro, Prof. Lohaus und Prof. Garnweitner ein Dankeschön aussprechen, meine Arbeit begutachtet zu haben.

Mein Dank gilt Apl. Prof. Feldhoff für die Übernahme des Vorsitzes der Disputationsprüfung. Dem gesamten Arbeitskreis Bigall danke ich für die Hilfsbereitschaft, die kooperative Zusammenarbeit und die zeitnahe Unterstützung, die mir auf dem Weg zur Erstellung meiner wissenschaftlichen Abhandlungen und dieser Arbeit zuteil geworden sind.

Dank gilt auch Prof. Haist und Julian Link für ihre rheologische Fachexpertise, die einen wichtigen Baustein im Gesamtkontext darstellt.

Gewinnen kann man nur im Team, deswegen geht ebenfalls ein herzlicher Dank an die Sekretariate für die stets guten organisatorischen Rahmenbedingungen, die chemisch-technischen Assistenten sowie die Mitarbeiter der hauseigenen Werkstatt, ohne die so mancher Laboraufbau nicht möglich gewesen wäre und auch an die Kollegen der anverwandten Arbeitsgruppen für lange, anregende Diskussionen in beeindruckender Fachtiefe und Leidenschaft.

TABLE OF CONTENTS

<i>KURZZUSAMMENFASSUNG</i>	III
<i>ABSTRACT</i>	V
<i>PREFACE</i>	VII
<i>NOTE OF THANKS</i>	XI
<i>TABLE OF CONTENTS</i>	XIII
1 SETTING THE SCENE	- 1 -
1.1 THE HISTORY OF CEMENT	- 1 -
1.2 MOTIVATION	- 4 -
1.3 OBJECTIVE	- 5 -
2 INTRODUCTION AND THEORETICAL BACKGROUND	- 7 -
2.1 MICROSTRUCTURE.....	- 8 -
2.2 RHEOLOGY	- 11 -
2.3 HYDRATION PRODUCTS	- 13 -
2.3.1 SILICATE REACTION (C_3S AND C_2S)	- 13 -
2.3.2 ALUMINATE REACTION (C_3A)	- 16 -
2.4 HYDRATION STOP TECHNIQUES.....	- 18 -
2.4.1 SOLVENT-BASED	- 18 -
2.4.2 TEMPERATURE- AND PRESSURE-BASED.....	- 20 -
2.5 ADDITIVES IN CEMENT	- 24 -
2.5.1 LARGE-SCALE / GENERAL.....	- 24 -
2.5.2 LAB-SCALE / NANOPARTICLES	- 25 -
3 DEVELOPMENT OF A FREEZE-DRYING-BASED HYDRATION STOP TECHNIQUE	- 27 -
3.1 SUMMARY	- 27 -
3.2 COMPARISON OF WATER-ISOPROPRANOL REPLACEMENT AND LYOPHILISATION FOR HYDRATION STOP OF CEMENTITIOUS SUSPENSIONS	- 29 -
3.3 INFLUENCE OF LOW-PRESSURE TREATMENT ON THE MORPHOLOGICAL AND COMPOSITIONAL STABILITY OF MICROSCOPIC ETTRINGITE.....	- 39 -
3.4 IS FREEZE-DRYING AN ALTERNATIVE TO SOLVENT EXCHANGE FOR THE HYDRATION STOP OF CEMENTITIOUS SUSPENSIONS?.....	- 69 -

4 APPLICATION OF THE FREEZE-DRYING-BASED HYDRATION STOP TECHNIQUE	- 95 -
4.1 SUMMARY	- 95 -
4.2 INFLUENCE OF <i>IN SITU</i> FORMED ETTRINGITE ON THE RHEOLOGICAL PROPERTIES OF QUARTZ SUSPENSIONS.....	- 97 -
4.3 IMPACT OF HARD MAGNETIC IRON OXIDE NANOCRYSTALS ON THE PROPERTIES OF HARDENED CEMENT PASTE	- 123 -
5 SUMMARY OF THE WHOLE WORK	- 147 -
6 CRITICAL DISCUSSION AND OUTLOOK	- 149 -
<i>APPENDIX</i>	XV
<i>GREEK LETTERS</i>	XV
<i>SYMBOLS</i>	XV
<i>ABBREVIATIONS</i>	XVI
<i>FIGURES</i>	XVIII
<i>TABLES</i>	XIX
<i>EQUATIONS</i>	XIX
<i>CURRICULUM VITAE</i>	XX
<i>PUBLICATIONS AND CONFERENCES</i>	XXI

1 SETTING THE SCENE

1.1 THE HISTORY OF CONCRETE

Since the Neolithic period, people have been using materials nowadays known as concrete^{1} (derived from the Latin *concretus* = grown together; being the past participle passive of *concrecere*). But how did the ancient material change into modern concrete?

This development can be partitioned into five periods, (1) Neolithic (10000 BC – 4500 BC)^{2}, (2) ancient times (3000 BC – 476)^{3}, (3) Middle Ages (476 – 1492)^{3}, (4) Industrial Era, and (5) modern age (since 1789)^{3}. The first to use concrete-like materials were the Nabataea traders or Bedouins living in southern Syria and northern Jordan around 6500 BC. Their knowledge about the importance of water and when to add it, enabled them to construct rubble masonry houses, concrete floors, and underground waterproof cisterns by incorporating hydraulic lime.^{4} Around 3000 BC Egyptians started to use straw mixed with mud to bind dried bricks and gypsum or lime mortars for pyramids. Meanwhile, the Chinese added glutinous, sticky rice to the mortar applied on *exempli gratia* the Great Wall.^{5} Although Romans were not the inventor of concrete, as often stated, they were the first to study building materials on a large scale^{6-11} resulting in the development of *opus caementicium* and its implementation for the construction of various types of buildings^{12,13}, *exempli gratia* the Colosseum, Curia Iulia, and the Pantheon, which are still standing today after roughly 2000 years. The reason for this long-term durability was recently found by the investigation of hardened mortar mixed following the ancient recipe of Vitruvius^{10,11}, whereby Romans used a mixture of volcanic ash, lime and seawater, which in turn led to the formation of stratlingite

¹ S. L., Marusin, 'Ancient Concrete Structures', *Concrete International*, 18(1), **1996**.

² J. Lubbock, Pre-historic times, Williams and Norgate, **1865**.

³ C. Cellarius, *Historia universalis*, Bielck, **1702**.

⁴ Gromicko, N. and Shepard, K. 'The History of Concrete', *International Association of Certified Home Inspectors, Inc.*, **2016**.

⁵ P. Jähren, T. Sui, *History of Concrete*, **2018**. <https://doi.org/10.1142/10172>.

⁶ Marcus Porcius Cato 'De agri cultura', *circa 150 BC* in: Cato M.P., Keil H., Goetz G. 'De agri cultura liber', aedibus B.G. Teubneri, **1922**.

⁷ Marcus Porcius Cato 'De agri cultura', *circa 150 BC* in: Cato M.P., Thielscher, P. 'De agricultura', Thomas de Blacis, de Alexandria, Berlin, **1963**.

⁸ Marcus Terrentius Varro 'De re rustica', **37 BC** in: Varro M.T. 'De re rustica', Fritsch, **1730**.

⁹ Marcus Vitruvius Pollio 'De architectura', **22 BC** in: Vitruvius 'M. Vitruvius De architectura', sumptu Ioannis de Tridino, alias Tacuion, Venetiis, **1730**. <https://doi.org/https://doi.org/10.11588/diglit.1712>.

¹⁰ Marcus Vitruvius Pollio 'De architectura', **22 BC** in: Vitruvius M.P., Rose V., Müller-Strübing H. 'Vitruvii de architectura libri decem', aedibus B.G. Teubneri, **1867**.

¹¹ Gaius Plinius Secundus Maior 'Naturalis historia', *circa 75* in: Pliny the Elder 'Caius Plinius Marco suo salute ...', Thomas de Blavis, de Alexandria, Venice, **1491**. <https://doi.org/10.5962/bhl.title.141852>.

¹² Lancaster, L.C. 'Concrete Vaulted Construction in Imperial Rome', Cambridge University Press, **2015**. <https://doi.org/10.1017/CBO9780511610516>.

¹³ D.S. Robertson, *Greek and Roman Architecture*, 2nd edition, Cambridge University Press, **1969**.

(2 CaO · Al₂O₃ · SiO₂ · 8 H₂O)^{14}. Further, due to volcanic ash being dissolved by seawater, a scarce hydrothermal mineral called aluminium tobermorite and a porous mineral called phillipsite formed over time^{15}, strengthening concrete over centuries and thus making it more fracture-resistant, enabling the safe use in seismically active regions^{16}. Besides the compressive strength of Roman concrete being similar to modern-day concrete based on standard cement^{17}, its tensile strength is lower, as resistance to tension solely depends on the concrete's bonding strength, and their consistency deviates. Modern concrete is a plastic, flowing material that normally fills moulds, but Roman concrete had a high viscosity and was mainly used to hand-fill spaces between stones.^{18} Due to the enormous migration period after the fall of the Western Roman Empire in the year 476^{19,20}, a large part of knowledge regarding Roman concrete or the use of building materials and how to prepare them was lost. Thus, the use of pozzolanic-based (siliceous or siliceous and aluminous material)^{21} mortar declined until in the early 16th century, the ten-volume work *De architectura* by VITRUVIUS^{10,11}, summarising the Roman knowledge, was found in a Swiss monastery library^{5}, wherein it is hypothesised by G. M. IDORN^{22} that the use of concrete was a secret shared by monasteries and the church until the end of 18th century. Since then, a widespread interest in reproducing Roman cement led to several improvements^{23-28} in Western Europe^{5,22}, resulting in the invention and patenting of Portland Cement by J. ASPDIN^{29} in 1824, which combined

¹⁴ S. Kwan S., J. LaRosa J., M.W. Grutzeck M.W., *J. Am. Ceram. Soc.* 78, **1995**.

<https://doi.org/10.1111/j.1151-2916.1995.tb08910.x>.

¹⁵ M.D. Jackson, S.R. Mulcahy, H. Chen, Y. Li, Q. Li, P. Cappelletti, H.R. Wenk, *Am. Mineral.* 102, **2017**, 1435-1450. <https://doi.org/10.2138/am-2017-5993CCBY>.

¹⁶ M.D. Jackson, E.N. Landis, P.F. Brune, M. Vitti, H. Chen, Q. Li, M. Kunz, H.R. Wenk, P.J.M. Monteiro, A.R. Ingraffea, *Proc. Natl. Acad. Sci. U. S. A.* 111, **2014**, 18484–18489. <https://doi.org/10.1073/pnas.1417456111>.

¹⁷ H.J. Cowan, *The Master-builders: A History of Structural and Environmental Design from Ancient Egypt to the Nineteenth Century*, John Wiley & Sons, Inc., **1978**.

¹⁸ R. Mark, P. Hutchinson, *Art Bull.* 68, **1986**, 24–34. <https://doi.org/10.1080/00043079.1986.10788309>.

¹⁹ E. Nack, W. Wagner, *Rom: Land und Volk der alten Romer*, ungekurzte Lizenzausgabe, RM-Buch-und-Medien-Vertrieb, Rheda-Wiedenbruck, Gutersloh, **2004**.

²⁰ F. Bedurftig, *Das Romische Imperium: [100 Bilder, 100 Fakten]*, NGV, Koln, **2008**.

²¹ ASTM C618-19, Standard Specification for Coal Fly Ash and Raw or Calcined Natural Pozzolan for Use in Concrete, *Annu. B. ASTM Stand.* 04.02, **2019**, 5. <https://doi.org/10.1520/C0618-19>.

²² G.M. Idorn, *Concrete progress from antiquity to third millenium*, Thomas Telford Publishing, **1997**. <https://doi.org/10.1680/cpftattm.26315>.

²³ B. Higgins [B. Harrison, H.C.H. Matthew, *Oxford Dictionary of National Biography - Volume 27: Hickeringill-Hooper*, Oxford University Press, New York, **2004**].

²⁴ J. Parker, *A certain Cement or terras to be used in Aquatic and other Buildings and Stucco Work*, BP 2120, **1796**.

²⁵ E. Dobbs [patent **1810**; E. Dobbs, *Composition for making watertproof cement, mortar, and stucco; applicable as a colouring wash*, BP 3367, 1810. and B. Harrison, H.C.H. Matthew, *Oxford Dictionary of National Biography - Volume 16: Dewes-Dryland*, Oxford University Press, New York, **2004**].

²⁶ L.J. Vicat [<https://www.vicat.com/about-us/vision/history-of-louis-vicat>], March 11, **2022**.

²⁷ F. Cointeraux [H. Guillaud, *Les carnets de l'architecture de terre*, **1997**].

²⁸ M. Lebrun and F. Coignet [F. Werner, *Der lange Weg zum neuen Bauen / Ferdinand Werner; Band 1: Beton: 43 Manner erfinden die Zukunft*, Wernersche Verlagsgesellschaft, Worms, **2016**].

²⁹ J. Aspdin, *An Improvement in the Modes of Producing an Artificial Stone*, BP 5022, **1824**.

with the clinker found by JOHNSON^{30} in 1845, marked the beginning of the modern concrete age. Over the subsequent decades, the annual amount of produced Portland cement reached 10 million tons, made possible by implementing rotating kilns and early ball mills since the 20th century. Due to the increased use and further development of kilns^{5,22}, annual production keeps growing, *exempli gratia* it reached 2.77 billion tons in 2007. Further developments concerning the low tensile strength of Roman concrete, especially problematic in the fields of application as *exempli gratia* harbour construction, coastal protection, or infrastructure, were and are still linked, as in the ancient times, with social needs (multi-storage buildings due to overpopulated cities) and prevalent economy (trade routes). To address these requirements, additives such as steel, sand, or superplasticisers were introduced to the cement mix and the quality, manufacturing, and handling were summarised and standardised by the inter-European materials research association (RILEM, France, found 1947)^{31,32}, National Bureau of Standards (US, found 1901)^{33}, the international federation for structural concrete (*fib*, Switzerland, formed by the merger of the Euro-International Committee for Concrete (CEB; found 1953) and the International Federation for Pressing (FIP, found 1952))^{34}, as well as the research institute of German cement industry (VDZ, Germany, found again 1948)^{35}.

³⁰ A.J. Francis, The Cement Industry 1796-1914: A History, David & Charles, **1977**.

³¹ RILEM, 50 years of experience in the service of building materials and structures, RILEM, **1997**.

³² RILEM, History, <https://www.rilem.net/history>, March 14, **2022**.

³³ NIST, History, <https://www.nist.gov/history>, March 14, **2022**.

³⁴ *fib*, History, <https://www.fib-international.org/federation/history.html>, August 04, **2022**.

³⁵ Verein Deutscher Zementwerke e.V., Historisches. <https://www.vdz-online.de/historisches>, March 14, **2022**.

1.2 MOTIVATION

Why has cement or concrete been of such importance since ancient times, has become even more critical since the last century, and is seen as one of the most essential building blocks in our current millennium^{36,37}? After constant development, did mankind not yet reach the most profound understanding of cement or concrete?

On the one hand, it took humankind only around four centuries to invent and develop fully functional electric cars, starting with *exempli gratia* the work of W. GILBERT^{38} in 1600 about the difference between electrical and magnetic attractive forces as well as the successful visualisation of electric charge by O. VON GUERICKE in 1672^{39}. On the other hand, eight millennia seem insufficient time to reach a profound understanding of cement and concrete, which would enable a quick custom-made development response to all requirements due to world affairs or scarcity!?

For a very trivial reason: One knows how building with concrete works, but still, not yet how it comes, for what reason, and why it works. This knowledge is today necessary, since right now, we need accommodations for more than eight billion people, but unfortunately, the concrete required for this cannot be manufactured taking advantage of the raw materials provided by the world's silting up/ desertification which due to its smooth fine grain still cannot be used as an additive in concrete building.

In an ideal-typical world, it would be possible to adjust the properties of the hardened state of cement or concrete as desired, which can directly be derived from the microscale and rheology of the suspension. What is needed to achieve this? The knowledge about the time-variant profile is essential. As this material class is rigid, non-fluent, and opaque, it is impossible to instantly see through all the little details without taking on a herculean task. Luckily, concrete is not as unknown as alchemists' dream, *id est* the expertise foundation exists.

For gaining profound knowledge, it is necessary to understand what happens when water is added to cement or concrete. Cement suspensions are subjected to hydration processes, causing precipitation of hydration products and dissolution of cement clinker. Thus, an understanding of the influencing factors during this hydration process, such as the underlying kinetics and

³⁶ E.D. Hondros, E. Bullock, *Angew. Chemie Int. Ed. English*. 28, **1989**, 1088–1097.
<https://doi.org/10.1002/anie.198910881>.

³⁷ J. Rieger, M. Kellermeier, L. Nicoleau, *Angew. Chemie Int. Ed.* 53, **2014**, 12380–12396.
<https://doi.org/10.1002/anie.201402890>.

³⁸ W. Gilbert, *De magnete, magnetisque corporibus, et de magno magnete tellure: physiologia nova, plurimis et argumentis, et experimentis demonstrata*, Excudebat Petrus Short, Londinium, **1600**.

³⁹ O. von Guericke, *Experimenta nova (ut vocantur) magdeburgica de vacuo spatio*, J. Jansson à Waesberge, Amsterdam, **1672**. <https://doi.org/10.5962/bhl.title.20217>.

mechanisms at the initial colloidal scale, has to be obtained. These mechanisms occur in parallel and impact cement suspensions' workability (mainly rheology).

The composition has to be analysed to correlate the colloidal state of the cementitious suspensions with their rheology. Since a colloidal suspension's depiction, considering the hydration process itself, requires a time-dependent analysis, the hydration must be stopped at definite times. For this, it is paramount to identify a method to stop the hydration process at any given time, as fast, complete, non-invasive, and reproducible as possible.

Achieving this method is not the end of the road since it has to be checked to what extent the results regarding the nano scale can be transferred to paste, mortar, and concrete, which involves several orders of magnitudes on the size scale ranging from nanometres to metres.

1.3 OBJECTIVE

Overall, the present dissertation focuses on identifying and applying a suitable and reliable method for stopping the hydration process in cementitious suspensions with as little disturbance as possible to the cement matrix, including the formed hydration products, at any given time. Due to the fact that it would exceed the scope of this thesis, the abovementioned cross-scale transfer is left out.

The main objective is the development and evaluation of a reliable, fast, complete, non-invasive, and reproducible freeze-drying-based hydration stop technique for the analysis of the suspensions of the less complex binder cement (compared to concrete, which also includes aggregates) (see **section 3**). The secondary objective's content is applying the developed hydration stop method to assess the influence of the first hydration product, ettringite, on rheological properties (see **section 4.2**). Further, to generalise the applicability of the developed method, hard magnetic iron oxide nanoparticles were added to cementitious suspensions, in turn, to investigate their influence on physical properties in the hardened state, creating the basis that enables the increase in knowledge up to the profound level (see **section 4.3**).

2 INTRODUCTION AND THEORETICAL BACKGROUND

Modern concrete is mainly based on Portland cement, which is defined by the European Standard EN 197-1^{40} as Portland cement clinker being a hydraulic material that must consist of at least two-thirds calcium silicates ($3 \text{ CaO} \cdot \text{SiO}_2$ and $2 \text{ CaO} \cdot \text{SiO}_2$) by mass. The remainder consists of clinker phases containing aluminium, iron, and other compounds. Its mass ratio of $\text{CaO}:\text{SiO}_2$ (C/S) has to be at least 2.0, in addition, the mass fraction of magnesium oxide (MgO) must not exceed 5.0 wt%. These clinker phases, in turn, are made by sintering (up to $1450 \text{ }^\circ\text{C}$) primary as well as secondary supplier rocks containing mainly calcium oxide (CaO), silica or silicon oxide (SiO_2), a lesser amount of aluminium oxide (Al_2O_3), and iron oxide (Fe_2O_3) as *exempli gratia* natural limestone or chalk (CaCO_3), clay or shale, as well as secondary^{41}, lime sludge, foundry sand, and fly ash.^{42} This sintering can, as described in the literature^{42}, be divided into several steps: (1) Dehydration at temperatures $T \leq 750 \text{ }^\circ\text{C}$, wherein adsorbed water ($T \leq 200 \text{ }^\circ\text{C}$), physically bound water ($100 \text{ }^\circ\text{C} \leq T \leq 400 \text{ }^\circ\text{C}$), and chemically bound water are evaporated; (2) Decomposition of CaCO_3 into CaO and CO_2 below $T = 550 \text{ }^\circ\text{C}$; (3) Formation of dicalcium silicate (Ca_2SiO_4 , belite^{43}) as well as intermediary compounds containing Al_2O_3 and Fe_2O_3 ; (4) Formation of tricalcium silicate (Ca_3SiO_6 , alite^{44}) out of CaO and Ca_2SiO_4 at $T = 1450 \text{ }^\circ\text{C}$ in the presence of a melt containing mainly Al_2O_3 and Fe_2O_3 adding up to 20 wt% to 30 wt%; and (5) Crystallization of tricalcium aluminate ($\text{Ca}_3\text{Al}_2\text{O}_6$) and tetra calcium aluminoferrite ($\text{Ca}_4\text{Al}_2\text{Fe}_2\text{O}_{10}$, brownmillerite^{45}) during the rapid cooling of the melt. For the sake of simplicity, when it comes to the complex mineralogical compounds in non-hydrated and hydrated cement, the so-called Cement Chemistry Notation (CCN) was developed^{46} and extended^{47-50}, wherein $\text{C} \equiv \text{CaO}$, $\text{A} \equiv \text{Al}_2\text{O}_3$, $\text{S} \equiv \text{SiO}_2$, $\text{H} \equiv \text{H}_2\text{O}$, $\text{F} \equiv \text{Fe}_2\text{O}_3$, $\text{N} \equiv \text{Na}_2\text{O}$, $\text{K} \equiv \text{K}_2\text{O}$, $\text{M} \equiv \text{MgO}$, $\text{L} \equiv \text{Li}_2\text{O}$, $\text{T} \equiv \text{TiO}_2$, $\bar{\text{S}} \equiv \text{SO}_3$, and $\bar{\text{C}} \equiv \text{CO}_2$. Depending on the area of use

⁴⁰ DIN German Institute for Standardization, DIN EN 197-1:2011-11, Cement – Part 1: Composition, specifications and conformity criteria for common cements; German version EN 197-1:2011, Beuth Verlag GmbH, Berlin, Germany, **2011**.

⁴¹ S. Sprung, Umweltentlastung durch Verwertung von Sekundärrohstoffen, *Zement, Kalk, Gips* **45**, **1992**, 213–221.

⁴² Zement-Taschenbuch, Verein Deutscher Zementwerke e.V., Düsseldorf, **2002**.

⁴³ A.E. Törnebohm, Die Petrographie des Portlanzements, *Tonindustrie-Zeitung Und Keramische Rundschau*. **21**, **1897**, 1157–1159.

⁴⁴ A.E. Törnebohm, Die Petrographie des Portlanzements, *Tonindustrie-Zeitung Und Keramische Rundschau*. **21**, **1897**, 1148–1151.

⁴⁵ A.A. Colville, S. Geller, *Acta Crystallogr. Sect. B Struct. Crystallogr. Cryst. Chem.* **27**, **1971**, 2311–2315. <https://doi.org/10.1107/s056774087100579x>.

⁴⁶ G.A. Rankin, *Am. J. Sci.* **XXXIX**, **1915**, 1–79. <https://doi.org/10.2475/ajs.s4-39.229.1>.

⁴⁷ R.H. Bogue, *Ind. Eng. Chem. Anal. Ed.*, **1929**, 192–197. <https://doi.org/10.1021/ac50068a006>.

⁴⁸ L.T. Brownmiller, R.H. Bogue, *Bur. Stand. J. Res.* **8**, **1932**, 289. <https://doi.org/10.6028/jres.008.021>.

⁴⁹ L.T. Brownmiller, *Am. J. Sci.* **s5-29**, **1935**, 260–277. <https://doi.org/10.2475/ajs.s5-29.171.260>.

⁵⁰ R.H. Bogue, *The chemistry of Portland cement*, Reinhold Publishing Corp., New York, **1947**.

or application, five main types of Portland cement (CEM I: Portland cement^{40} or ordinary^{51}; CEM II: Portland composite cement^{40} or modified^{51}; CEM III: blast furnace cement^{40} or high-early-strength^{51}; CEM IV: pozzolan cement^{40} or low-heat^{51}; CEM V: composite cement^{40} or sulphate-resistant^{51}) and several modified types are used, whose composition is shown in “*Zement-Taschenbuch*” by VEREIN DEUTSCHER ZEMENTWERKE E.V.^{42} or **Table 1**.

Table 1: Composition of the five main types of cement and their modifications according to DIN EN 197-1^{40}.

type	phase content / wt%										
	K	S	D	P	Q	V	W	T	L	LL	minor
CEM I	95 - 100	-	-	-	-	-	-	-	-	-	≤ 5
CEM II/A-S	80 - 94	6 - 20	-	-	-	-	-	-	-	-	≤ 5
CEM II/B-S	65 - 79	21 - 35	-	-	-	-	-	-	-	-	≤ 5
CEM II/A-D	90 - 94	-	6 - 10	-	-	-	-	-	-	-	≤ 5
CEM II/A-P	80 - 94	-	-	6 - 20	-	-	-	-	-	-	≤ 5
CEM II/B-P	65 - 79	-	-	21 - 35	-	-	-	-	-	-	≤ 5
CEM II/A-Q	80 - 94	-	-	-	6 - 20	-	-	-	-	-	≤ 5
CEM II/B-Q	65 - 79	-	-	-	21 - 35	-	-	-	-	-	≤ 5
CEM II/A-V	80 - 94	-	-	-	-	6 - 20	-	-	-	-	≤ 5
CEM II/B-V	65 - 79	-	-	-	-	21 - 35	-	-	-	-	≤ 5
CEM II/A-W	80 - 94	-	-	-	-	-	6 - 20	-	-	-	≤ 5
CEM II/B-W	65 - 79	-	-	-	-	-	21 - 35	-	-	-	≤ 5
CEM II/A-T	80 - 94	-	-	-	-	-	-	6 - 20	-	-	≤ 5
CEM II/B-T	65 - 79	-	-	-	-	-	-	21 - 35	-	-	≤ 5
CEM II/A-L	80 - 94	-	-	-	-	-	-	-	6 - 20	-	≤ 5
CEM II/B-L	65 - 79	-	-	-	-	-	-	-	21 - 35	-	≤ 5
CEM II/A-LL	80 - 94	-	-	-	-	-	-	-	-	6 - 20	≤ 5
CEM II/B-LL	65 - 79	-	-	-	-	-	-	-	-	21 - 35	≤ 5
CEM II/A-M	80 - 94									6 - 20	≤ 5
CEM II/B-M	65 - 79									21 - 35	≤ 5
CEM III/A	35 - 64	36 - 65	-	-	-	-	-	-	-	-	≤ 5
CEM III/B	20 - 34	66 - 80	-	-	-	-	-	-	-	-	≤ 5
CEM III/C	5 - 19	81 - 95	-	-	-	-	-	-	-	-	≤ 5
CEM IV/A	65 - 89	-	11 - 35				-	-	-	-	≤ 5
CEM IV/B	45 - 64	-	36 - 55				-	-	-	-	≤ 5
CEM V/A	40 - 64	18 - 30	-	18 - 30			-	-	-	-	≤ 5
CEM V/B	20 - 38	31 - 50	-	31 - 50			-	-	-	-	≤ 5

K ≡ Portland cement clinker; **S** ≡ blast furnace slag; **D** ≡ silica fume, maximum 10 wt%; **P** ≡ natural pozzolan; **Q** ≡ tempered pozzolan; **V** ≡ siliceous fly ash; **W** ≡ calcareous fly ash; **T** ≡ burnt slate; **L** ≡ limestone with an organics' content TOC ≤ 0.50 wt%; **LL** ≡ limestone with TOC ≤ 0.20 wt%, and **minor** ≡ unbound MgO and CaO.

2.1 MICROSTRUCTURE

As already known in ancient times, the amount of water or, more precisely, the mass ratio of water to cement (w/c) and how it is mixed with pristine cement is essential knowledge.^{9,10}

⁵¹ ASTM Standard C150, **2021**, Standard Specification for Portland Cement, ASTM International, West Conshohocken, PA, 1956, https://doi.org/10.1520/C0150_C0150M-21, www.astm.org.

As soon as the pristine material is wetted, a hydration process starts, which can be subdivided into five periods^{52-55}, (1) Pre-induction ($t_{hyd} \leq 0.5$ h), (2) Induction or dormant ($0.5 \text{ h} \leq t_{hyd} \leq 2$ h), (3 + 4) Acceleration and retardation ($2 \text{ h} \leq t_{hyd} \leq 24$ h), as well as (5) Final ($t_{hyd} \geq 24$ h). Of the contained components, alite (C_3S) and tricalcium aluminate (C_3A) exhibit the highest reaction speed and brownmillerite (C_4AF), as well as belite (C_2S), are less fast. The strength ($1 \text{ d} \leq t_{hyd} \leq 360 \text{ d}$) of a cementitious suspension comes mainly from the formation of calcium silicate hydrate ($C-S-H$; $m \text{ CaO} \cdot \text{SiO}_2 \cdot n \text{ H}_2\text{O}$; $1.2 \leq m \leq 2.3$ ^{56}) phases out of C_3S . At later hydration stages ($t_{hyd} \geq 360 \text{ d}$), the reaction of C_2S replaces alite as the main contributor to the strength of hardened cement paste (**Figure 1**).^{57}

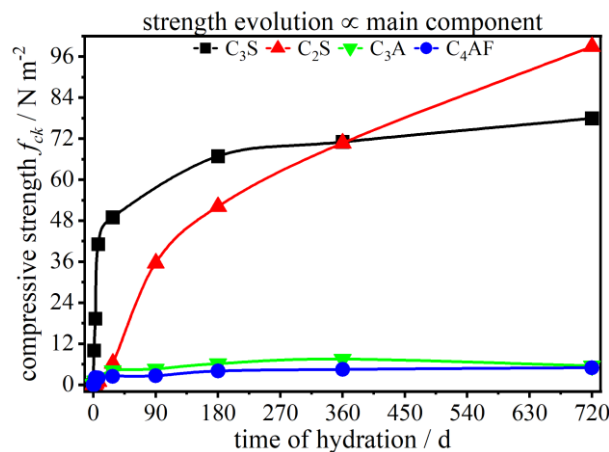


Figure 1: Evolution of compressive strength f_{ck} of cement's main components (C_3S , C_2S , C_3A , and C_4AF) in a cementitious suspension with $w/c = 0.5$; derived from BOGUE ET AL.^{57}.

Depending on the available amount of sulphate ions (SO_4^{2-}) in the cementitious suspension, two reactions of C_3A and C_4AF are induced. In the latter case, no or meagre amounts lead to the formation of metastable tetra calcium aluminate ferrite hydrate ($\text{Ca}_4\text{Al}_{2-x}\text{Fe}_x\text{O}_7 \cdot 19 \text{ H}_2\text{O}$, $C_4(A,F)H_{19}$) and di calcium aluminate ferrite hydrate ($\text{Ca}_2\text{Al}_{2-x}\text{Fe}_x\text{O}_5 \cdot 8 \text{ H}_2\text{O}$, $C_2(A,F)H_8$), reacting to tri calcium aluminate ferrite hydrate ($\text{Ca}_3\text{Al}_{2-x}\text{Fe}_x\text{O}_6 \cdot 6 \text{ H}_2\text{O}$, $C_3(A,F)H_6$). Due to the addition of sulphate carriers like calcium sulphates (mainly $\text{CaSO}_4 \cdot 2 \text{ H}_2\text{O}$, gypsum, $C\bar{S}H_2$) the formation of calcium trisulfoaluminate ferrite hydrate ($\text{Ca}_6\text{Al}_{2-x}\text{Fe}_x(\text{SO}_4)_3(\text{OH})_{12} \cdot 26 \text{ H}_2\text{O}$, iron ettringite, $C_6(A,F)\bar{S}_3H_{32}$) is here further enabled on the surface of C_4AF grains.^{58}

⁵² H.F.W. Taylor, Cement chemistry, Thomas Telford Publishing, **1997**. <https://doi.org/10.1680/cc.25929>.

⁵³ F.W. Locher, W. Richartz, S. Sprung, Erstarren von Zement - Teil 1. Reaktion und Gefügeentwicklung, *ZKG Int.* **29**, **1976**, 435–442.

⁵⁴ F.W. Locher, Zement - Grundlagen der Herstellung und Verwendung, Bau + Technik, Düsseldorf, **2000**.

⁵⁵ O. Henning, D. Knöfel, Baustoffchemie - Eine Einführung für Bauingenieure und Architekten, 5. Auflage, Verlag für Bauwesen; Bauverlag GmbH, Berlin, Wiesbaden, **1997**. <https://doi.org/10.1007/978-3-322-80183-8>.

⁵⁶ I. Odler, Hydration, Setting and Hardening of Portland Cement, in: P.C. Hewlett (Ed.), Lea's Chem. Cem. Concr., Elsevier, **1998**: pp. 241–297. <https://doi.org/10.1016/B978-075066256-7/50018-7>.

⁵⁷ R. H. Bogue, W. Lerch, *Ind. Eng. Chem.* **26**, **1934**, 837–847. <https://doi.org/10.1021/ie50296a007>.

⁵⁸ P.W. Brown, *J. Am. Ceram. Soc.* **70**, **1987**, 493–496. <https://doi.org/10.1111/j.1151-2916.1987.tb05682.x>.

In the case of C_3A , a similar reaction course is known with the notable variation that no iron oxide is present, *id est* that no or meagre amounts of sulphate lead to the formation of metastable tetra ($Ca_4Al_2O_7 \cdot 19 H_2O$, C_4AH_{19}) and di calcium aluminate hydrate ($Ca_2Al_2O_5 \cdot 8 H_2O$, C_2AH_8), reacting to tri calcium aluminate hydrate ($Ca_3Al_2O_6 \cdot 6 H_2O$, cubic hydrogarnet, C_3AH_6).^{52} Analogously, sulphate carriers enable the formation of calcium trisulfoaluminate hydrate ($Ca_6Al_2(SO_4)_3(OH)_{12} \cdot 26 H_2O$, ettringite, $C_6A\bar{S}_3H_{32}$) on the surface of C_3A grains slowing down the diffusion of dissolving ions, whereby preventing the flash-set or rapid hardening of cement, which, in turn, is of major interest, as with the setting of the cement workability becomes very difficult due to high viscosity. To subdue this flash-set, mainly superplasticisers^{59,60} are implemented, wherein different ways of retardation by deflocculation are possible due to the diverse chemical nature of these polymer-based additives adsorbing on hydrating cement particles (**Figure 2**).^{59-62}

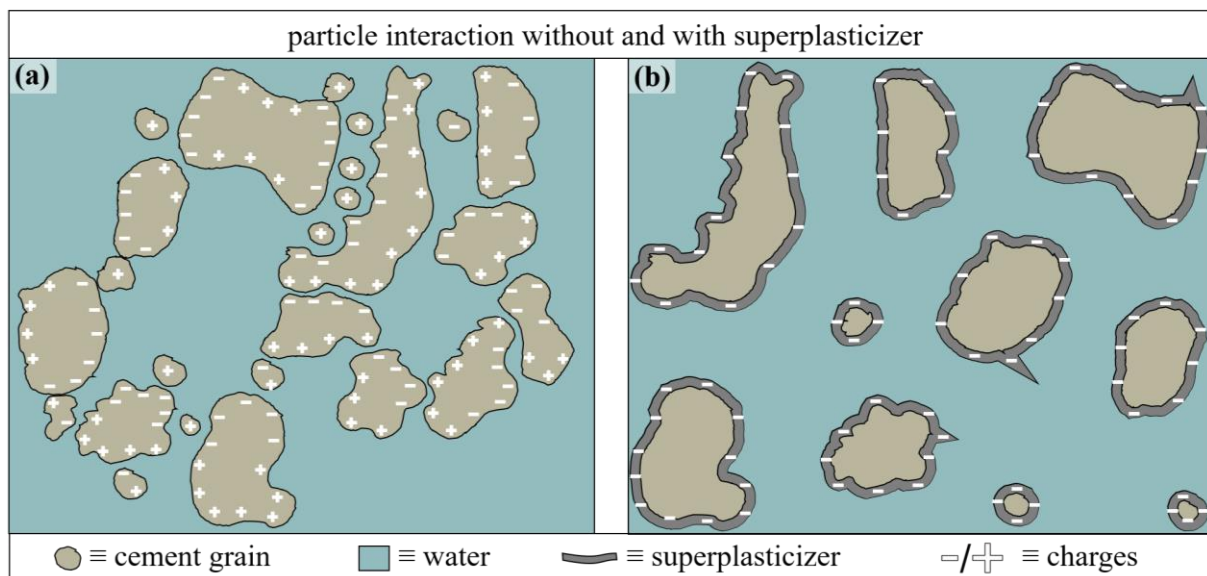


Figure 2: Scheme of particle interaction (a) without, resulting in coagulation/agglomeration, and (b) with superplasticiser, resulting in dispersion due to COULOMB^{63,64} forces.

Accumulation of ionic superplasticisers, as *exempli gratia* lignosulphonate-based, sulfonated melamine formaldehyde condensate, and naphthalene formaldehyde condensate, induce a negative surface charge resulting in a repulsion rooted in the COULOMB^{63,64} force between

⁵⁹ H. Uchikawa, D. Sawaki, S. Hanehara, *Cem. Concr. Res.* 25, **1995**, 353–364.

[https://doi.org/10.1016/0008-8846\(95\)00021-6](https://doi.org/10.1016/0008-8846(95)00021-6).

⁶⁰ J. Björnström, S. Chandra, *Mater. Struct.* 36, **2003**, 685–692. <https://doi.org/10.1617/13912>.

⁶¹ G. Spanka, H. Grube, G. Thielen, Wirkungsmechanismen verflüssigender Betonzusatzmittel, *Bet. Die Fachzeitschrift Für Bau + Tech.* 45, **1995**, 802–810.

⁶² G. Spanka, H. Grube, G. Thielen, Wirkungsmechanismen verflüssigender Betonzusatzmittel, *Bet. Die Fachzeitschrift Für Bau + Tech.* 45, **1995**, 876–881.

⁶³ C.-A. Coulomb, Premier mémoire sur l'électricité et le magnétisme, in: *Hist. l'Académie R. Des Sci.*, **1785**: pp. 569–577.

⁶⁴ C.-A. Coulomb, Second mémoire sur l'électricité et le magnétisme, in: *Hist. l'Académie R. Des Sci.*, **1785**: pp. 578–611.

identical charges. Mixing in steric superplasticisers, mainly polycarboxylether-based (PCE), leads to local separation via the non-ionic pendant chains and thus, the dispersion of cement particles is induced.^{65} By these means, rheological properties are adjustable.

2.2 RHEOLOGY

Via the evaluation of the shear rate $\dot{\gamma}$ dependent rheological parameters, yield stress τ_0 , plastic viscosity μ , and dynamic viscosity η , of fresh cement paste ($t_{hyd} \leq 90$ min), it is possible to infer the properties of the hardened state.^{66,67} Cementitious suspensions show a viscoelastic flow behaviour^{68-70}, which can be distinguished into structural viscous, if the dynamic viscosity η sinks with higher shear rate $\dot{\gamma}$, and dilatant, if $\eta \propto \dot{\gamma}$ (**Figure 3**), thus making non-linearly coupled differential equations necessary.^{71-75}

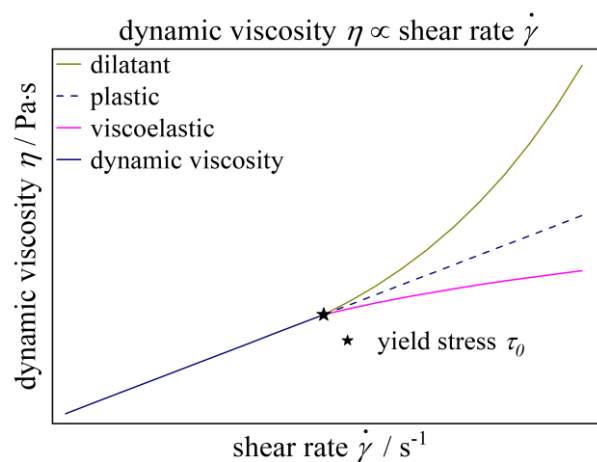


Figure 3: Dynamic viscosity η dependent on applied shear rate $\dot{\gamma}$, of a cementitious suspension exhibiting a viscoelastic (magenta), plastic (navy), or dilatant (dark yellow) flow behaviour.

⁶⁵ K. Yamada, T. Takahashi, S. Hanehara, M. Matsuhisa, *Cem. Concr. Res.* 30, **2000**, 197–207.
[https://doi.org/10.1016/S0008-8846\(99\)00230-6](https://doi.org/10.1016/S0008-8846(99)00230-6).

⁶⁶ H.-W. Reinhardt, *Beton*, in: *Beton-Kalender 2005*, Ernst & Sohn Verlag, **2005**: pp. 3–141.

⁶⁷ S.E. Chidiac, O. Maadani, A.G. Razaqpur, N.P. Mailvaganam, *J. Mater. Civ. Eng.* 15, **2003**, 391–399.
[https://doi.org/10.1061/\(ASCE\)0899-1561\(2003\)15:4\(391\)](https://doi.org/10.1061/(ASCE)0899-1561(2003)15:4(391)).

⁶⁸ M. Reiner, *Rheology*, in: S. Flügge (Ed.), *Elast. Plast. / Elastizität Und Plast. Handb. Der Phys. / Encycl. Physics*, Vol 3 / 6., Springer Berlin Heidelberg, Berlin, Heidelberg, **1958**: pp. 434–550.
https://doi.org/10.1007/978-3-642-45887-3_4.

⁶⁹ M. Reiner, *Rheologie in elementarer Darstellung*, Hanser, München, **1968**.

⁷⁰ H.A. Barnes, J.F. Hutton, K. Walters, *An introduction to rheology*, Elsevier Science, Amsterdam, **1989**.

⁷¹ M. Reiner, *The Rheology of Concrete*, in: F. Eirich (Ed.), *Rheology*, Academic Press, **1960**: pp. 341–364.
<https://doi.org/10.1016/B978-0-12-395696-5.50014-9>.

⁷² W. Vom Berg, *Zum Fließverhalten von Zementsuspensionen*, RWTH Aachen, **1982**.
<https://publications.rwth-aachen.de/record/68322>.

⁷³ G.H. Tattersall, P.F.G. Banfill, *The Rheology of fresh concrete*, Pitman, Boston, **1983**.

⁷⁴ K. Hattori, K. Izumi, *A new viscosity equation for non-Newtonian suspensions and its application*, in: P.F.G. Banfill (Ed.), *Rheol. Fresh Cem. Concr.*, CRC Press, Liverpool, **1990**: pp. 83–92.

⁷⁵ O. Blask, *Zur Rheologie von polymermodifizierten Bindemittelleimen und Mörtelsystemen*, Universität-Gesamthochschule Siegen, **2002**.

Generally, two models are used to describe cementitious suspensions' viscoelasticity: the continuum or the particle approach. In the latter case^{74,78-80}, each grain and inter- as well as intraparticulate force, no matter if attractive (coagulation) or repulsive (dispersion), have to be taken into account over the whole shear history, which is very complex and can only be attained computer-aided. Instead, the continuum model^{72,81-85} neglects the aforementioned physical processes during shearing, the idle state, as well as the elastic part of the total deformation. It describes the suspension as being homogenous and is based on the presence of a yield stress τ_0 , but enables a less complex evaluation at shear rates $\dot{\gamma} > 10 \text{ s}^{-1}$. Both models address changes to flow behaviour dependent on torsion, shear, but not time. This missing contribution was examined by KECK^{77} and, in turn, can be expressed by three independent exponential functions representing coagulation, hydration, and dispersion, whereby only the latter lowers the suspension's shear resistance. Derived from the different approaches to describe the rheological properties of cementitious suspensions in use, it can be concluded that these are a function of the suspended particles' characteristics^{86}. First, topologic or morphologic changes due to the formation of hydration products might result in steric forces, intra- and interparticulate interaction, as VAN DER WAALS^{87} as well as COULOMB^{63,64} forces lead to coagulation or dispersion^{80,88-90}. Second, the medium's type and amount may engender a higher hydrodynamic flow force as described by BERNOULLI^{91,92}, because particles become more dispersed in the suspension with a higher water-to-cement mass ratio (w/c).

⁷⁸ A. Zubov, J.F. Wilson, M. Kroupa, M. Šoóš, J. Kosek, *Langmuir* 35, **2019**, 12754–12764. <https://doi.org/10.1021/acs.langmuir.9b01107>.

⁷⁹ U. Costa, F. Massazza, Structure and Properties of Cement Suspensions, in: Proc. 8th Int. Congr. Chem. Cem., Rio de Janeiro, **1986**: pp. 248–259.

⁸⁰ J.E. Walleveick, Rheology of particle suspension: fresh concrete, mortar and cement paste with various types of lignosulfates, The Norwegian University of Science and Technology (NTNU), **2003**.

⁸¹ E.C. Bingham, An Investigation of the Laws of Plastic Flow, *Bull. Bur. Stand.* 13, **1916**, 309–353.

⁸² W.H. Herschel, R. Bulkley, *Kolloid-Zeitschrift* 39, **1926**, 291–300. <https://doi.org/10.1007/BF01432034>.

⁸³ T. Mezger, Das Rheologie Handbuch: für Anwender von Rotations- und Oszillations-Rheometern, 5., vollst., Vincentz Network GmbH & Co. KG; Hannover, **2016**.

⁸⁴ E.J. Windhab, Allgemeine Rheologische Messprinzipie, Geräte und Methoden, in: D. Weipert, H.-D. Tscheuschner, E.J. Windhab (Eds.), *Rheol. Der Leb.*, Behr's Verlag, Hamburg, **1993**: pp. 173–218.

⁸⁵ E.J. Windhab, Ausgewählte Beispiele Der Ingenieurtechnischen Anwendung Der Rheologie, in: D. Weipert, H.-D. Tscheuschner, E.J. Windhab (Eds.), *Rheol. Der Leb.*, Behr's Verlag, Hamburg, **1993**: pp. 219–256.

⁸⁶ G. Barthelmes, Theoretische Untersuchungen zum Einfluß der Agglomeration auf die Rheologie konzentrierter Suspensionen, Shaker, **2000**.

⁸⁷ J.D. van der Waals, Over de Continuïteit van den Gas-en Vloeïstoftoestand, A.W. Sijthoff, Leyden, **1873**. <https://doi.org/10.14463/KXP:1681851091>.

⁸⁸ O. Stern, *Zeitschrift Für Elektrochemie Und Angew. Phys. Chemie* 30, **1924**, 508–516. <https://doi.org/10.1002/bbpc.192400182>.

⁸⁹ F. London, *Trans. Faraday Soc.* 33, **1937**, 8b–26. <https://doi.org/10.1039/TF937330008B>.

⁹⁰ H.C. Hamaker, *Physica* 4, **1937**, 1058–1072. [https://doi.org/10.1016/S0031-8914\(37\)80203-7](https://doi.org/10.1016/S0031-8914(37)80203-7).

⁹¹ D. Bernoulli, *Hydrodynamica, sive de viribus et motibus fluidorum commentarii.*, Johannis Reinholdi Dulseckeri, Argentorati, **1738**.

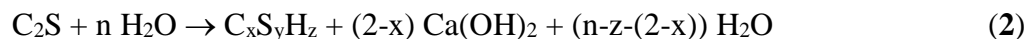
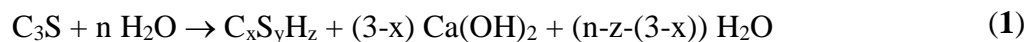
⁹² J. Bernoulli, *Hydraulica nunc primum detecta ac demonstrata divete ex fundamentis pure mechanicis* (1732), *Opera Omnia.* 4, **1742**, 387–493.

2.3 HYDRATION PRODUCTS

Adding water to cement initiates the hydration process leading to several hydration products, with calcium silicate hydrate, portlandite, and ettringite being the main and most important ones. In the following, the silicate (**section 2.3.1**) and aluminate reaction (**section 2.3.2**) will be examined more closely regarding their crystal structure and formation.

2.3.1 SILICATE REACTION (C₃S AND C₂S)

The hydration process of the main component of Portland cement, calcium silicate (C₃S and C₂S), is not fully understood in detail yet. Still, several studies^{93-101} showed that the reaction with water, displayed in equations (Eqs.) (1+2)^{102,103}, can be divided into three stages, (1) Early ($t_{hyd} < 4h$), (2) Middle ($4 h \leq t_{hyd} \leq 24 h$), and (3) Late ($t_{hyd} > 24 h$), resulting in different modifications and stoichiometries of calcium silicate hydrate (C-S-H), wherein the belite's reaction can be neglected in the first two days due to a significantly lower reaction rate^{104-108}.



-
- ⁹³ R. Kondo, S. Ueda, Kinetics and Mechanisms of the Hydration of Cements, in: Proc. 5th Int. Congr. Chem. Cem., Tokyo, **1968**; pp. 203–255.
- ⁹⁴ R.B. Williamson, *Science* 164, **1969**, 549–551. <https://doi.org/10.1126/science.164.3879.549>.
- ⁹⁵ R.B. Williamson, *Prog. Mater. Sci.* 15, **1972**, 189–286. [https://doi.org/10.1016/0079-6425\(72\)90001-1](https://doi.org/10.1016/0079-6425(72)90001-1).
- ⁹⁶ K. Fujii, W. Kondo, *J. Am. Ceram. Soc.* 57, **1974**, 492–497. <https://doi.org/10.1111/j.1151-2916.1974.tb11400.x>.
- ⁹⁷ M. Daimon, S. Ueda, R. Kondo, *Cem. Concr. Res.* 1, **1971**, 391–401. [https://doi.org/10.1016/0008-8846\(71\)90032-9](https://doi.org/10.1016/0008-8846(71)90032-9).
- ⁹⁸ D. Ménétrier, I. Jawed, T.S. Sun, J. Skalny, *Cem. Concr. Res.* 9, **1979**, 473–482. [https://doi.org/10.1016/0008-8846\(79\)90044-9](https://doi.org/10.1016/0008-8846(79)90044-9).
- ⁹⁹ J.A. Card, K. Mohan, H.F.W. Taylor, G. Cliff, *J. Am. Ceram. Soc.* 63, **1980**, 336–337. <https://doi.org/10.1111/j.1151-2916.1980.tb10733.x>.
- ¹⁰⁰ H.F.W. Taylor, P. Barret, P.W. Brown, D.D. Double, G. Frohnsdorff, V. Johansen, D. Ménétrier-Sorrentino, I. Odler, L.J. Parrott, J.M. Pommersheim, M. Regourd, J.F. Young, *Mater. Struct.* 17, **1984**, 457–468. <https://doi.org/10.1007/BF02473986>.
- ¹⁰¹ H.M. Jennings, B.J. Dalgeish, P.L. Pratt, *J. Am. Ceram. Soc.* 64, **1981**, 567–572. <https://doi.org/10.1111/j.1151-2916.1981.tb10219.x>.
- ¹⁰² T. Gutberlet, Hydratation von Tricalciumsilikat – Die ersten 30 Stunden, Technische Universität München, **2016**.
- ¹⁰³ F.M. Lea, Lea's Chemistry of Cement and Concrete, 3. ed. Elsevier, London, **1998**. <https://doi.org/10.1016/B978-0-7506-6256-7.X5007-3>.
- ¹⁰⁴ J.N. Maycock, J. Skalny, R. Kalyoncu, *Cem. Concr. Res.* 4, **1974**, 835–847. [https://doi.org/10.1016/0008-8846\(74\)90054-4](https://doi.org/10.1016/0008-8846(74)90054-4).
- ¹⁰⁵ I. Odler, J. Schüppstuhl, *Cem. Concr. Res.* 12, **1982**, 13–20. [https://doi.org/10.1016/0008-8846\(82\)90093-X](https://doi.org/10.1016/0008-8846(82)90093-X).
- ¹⁰⁶ H.S. Tong, J.F. Young, *J. Am. Ceram. Soc.* 60, **1977**, 321–323. <https://doi.org/10.1111/j.1151-2916.1977.tb15551.x>.
- ¹⁰⁷ K. Fujii, W. Kondo, *J. Am. Ceram. Soc.* 62, **1979**, 161–167. <https://doi.org/10.1111/j.1151-2916.1979.tb19045.x>.
- ¹⁰⁸ P. Fierens, J. Tirlocq, *Cem. Concr. Res.* 13, **1983**, 41–48. [https://doi.org/10.1016/0008-8846\(83\)90126-6](https://doi.org/10.1016/0008-8846(83)90126-6).

Although calcium silicate structures are well-known and discussed manifoldly^{109}, the standard technique X-ray diffraction (XRD) cannot be used in this case, since C-S-H formed during cement's hydration is X-ray amorphous due to a lack of long-range order or being nanocrystalline.^{102,110} Nevertheless, naturally crystalline, highly-ordered calcium silicate hydrate phases can be used to model C-S-H formed in cementitious suspensions, with the tobermorite and jennite groups being the most important.^{110,111} Both mineral groups are based on a layered silicate structure consisting of so-called “three chain” as building blocks (**Figure 4a**), which were introduced by BERNAL ET AL.^{112} in this context first. The C/S ratio allows for distinction between different C-S-H phases, wherein studies indicate $1.2 \leq C/S \leq 2.3$ with $\overline{C/S} \cong 1.7$ for hydration times around one year.^{102,110,111,113-116} Additionally, considering nuclear magnetic resonance data^{117-119}, jennite^{120} and tobermorite 14Å^{121} (**Figure 4b**), which exhibits the same structure as the 11Å polymorph depicted in **Figure 4a** but with an elongated c-axis, are best suited^{102} for modelling C-S-H in cementitious suspensions. This elongation and, in turn, bigger pore sizes enable a higher loading of H₂O molecules, which coordinate Ca²⁺ ions in the interlayer (**Figure 4b**). With the chemical formula Ca₅Si₆O₁₆(OH)₂ · 7 H₂O (C₅S₆H₈), tobermorite 14Å has a C/S $\cong 0.83$, which lies below the C-S-H phases found in longer hydrated samples, indicating that this phase may correspond to the early state of silicate reaction ($t_{hyd} < 4h$), wherein C-S-H is said to be a gel with low density ρ , often described as outer C-S-H. These outer hydration products exhibit fibre-like, below an expansion of 2 μ m, or honeycomb-like structures forming a reticular framework^{101}, which

¹⁰⁹ I.G. Richardson, *Cem. Concr. Res.* 38, **2008**, 137–158. <https://doi.org/10.1016/j.cemconres.2007.11.005>.

¹¹⁰ S. Tränkle, *Synthese und Modifikation von Calciumsilicathydrat-Phasen*, Universität Augsburg, **2014**.

¹¹¹ I. Richardson, *Cem. Concr. Res.* 29, **1999**, 1131–1147. [https://doi.org/10.1016/S0008-8846\(99\)00168-4](https://doi.org/10.1016/S0008-8846(99)00168-4).

¹¹² J.D. Bernal, J.W. Jeffery, H.F.W. Taylor, *Mag. Concr. Res.* 4, **1952**, 49–54. <https://doi.org/10.1680/mac.1952.4.11.49>.

¹¹³ R.J.M. Pellenq, A. Kushima, R. Shahsavari, K.J. Van Vliet, M.J. Buehler, S. Yip, F.-J. Ulm, *Proc. Natl. Acad. Sci.* 106, **2009**, 16102–16107. <https://doi.org/10.1073/pnas.0902180106>.

¹¹⁴ L.S. Dent Glasser, E.E. Lachowski, K. Mohan, H.F.W. Taylor, *Cem. Concr. Res.* 8, **1978**, 733–739. [https://doi.org/10.1016/0008-8846\(78\)90082-0](https://doi.org/10.1016/0008-8846(78)90082-0).

¹¹⁵ R. Kondo, M. Daimon, *J. Am. Ceram. Soc.* 52, **1969**, 503–508. <https://doi.org/10.1111/j.1151-2916.1969.tb09203.x>.

¹¹⁶ D.L. Kantro, S. Brunauer, C.H. Weise, *J. Phys. Chem.* 66, **1962**, 1804–1809. <https://doi.org/10.1021/j100816a007>.

¹¹⁷ J. Hirljac, Z.-Q. Wu, J.F. Young, *Cem. Concr. Res.* 13, **1983**, 877–886. [https://doi.org/10.1016/0008-8846\(83\)90089-3](https://doi.org/10.1016/0008-8846(83)90089-3).

¹¹⁸ X. Cong, R.J. Kirkpatrick, *Adv. Cem. Based Mater.* 3, **1996**, 144–156. [https://doi.org/10.1016/s1065-7355\(96\)90046-2](https://doi.org/10.1016/s1065-7355(96)90046-2).

¹¹⁹ I. Klur, B. Pollet, J. Virlet, A. Nonat, *Nucl. Magn. Reson. Spectrosc. Cem. Mater.*, **1998**, 119–141. https://doi.org/10.1007/978-3-642-80432-8_8.

¹²⁰ E. Bonaccorsi, S. Merlino, H.F.W. Taylor, *Cem. Concr. Res.* 34, **2004**, 1481–1488. <https://doi.org/10.1016/j.cemconres.2003.12.033>.

¹²¹ E. Bonaccorsi, S. Merlino, A.R. Kampf, *J. Am. Ceram. Soc.* 88, **2005**, 505–512. <https://doi.org/10.1111/j.1551-2916.2005.00116.x>.

contains a high amount of interlayer water. Due to further hydration of inner C_3S or C_2S ($4\text{ h} \leq t \leq 24\text{ h}$), desorption of interlayer water occurs, resulting in drying and, in turn, leads to the formation of hollow cigar-shaped, slightly tapered needles, and fibres, which in the late stage ($t > 24\text{ h}$) become compacted to dense gelatinous inner products^[101].

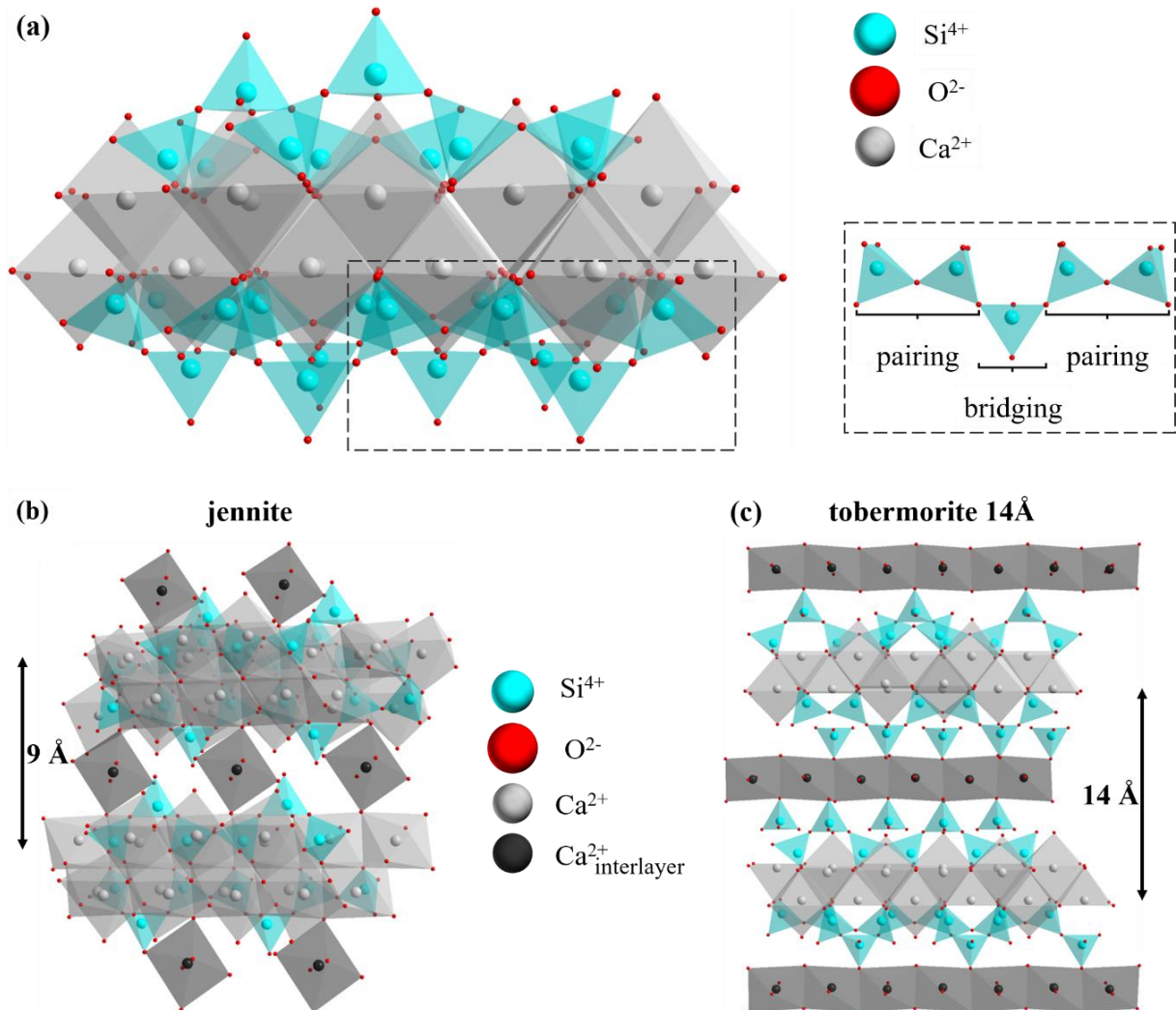


Figure 4: (a) Theoretical crystal structure of the so-called “three chain” building blocks in calcium silicate hydrate (C-S-H) on the example of tobermorite 11Å (ICSD-92941)^[122] in the $[10\bar{1}0]$ projection with edge-sharing octahedrally coordinated Ca^{2+} , and either bridging or pairing corner-sharing tetrahedrally Si^{4+} ; crystal structure of (b) jennite (ICSD-151413)^[120] in the $[\bar{5}141]$ projection with edge-sharing octahedrally coordinated Ca^{2+} , and (c) tobermorite 14Å (ICSD-152489)^[121] in the $[10\bar{1}0]$ projection with alternating edge-sharing Ca-O trigonal prisms and capped trigonal prisms; projection given in BRAVAIS-MILLER indices^[123].

This hydration product could be described by the jennite ($Ca_9Si_6O_{18}(OH)_6 \cdot 8 H_2O$, $C_9S_6H_{11}$) structure (**Figure 4b**)^[120], with $C/S = 1.5$ being in the range of C-S-H found in hydrated cement. The structure of the mineral jennite, which was finally elucidated by BONACCORSI ET

¹²² S. Merlino, E. Bonaccorsi, T. Armbruster, *Eur. J. Mineral.* 13, **2001**, 577–590.
<https://doi.org/10.1127/0935-1221/2001/0013-0577>.

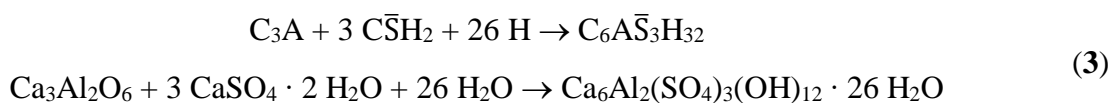
¹²³ W.H. Miller, *A Treatise on Crystallography*, J. & J. J. Deighton; John W. Parker, Cambridge, London, **1839**.

AL.^{120}, consists of edge-sharing Ca-O octaeders (coordination number C.N. = 6), alternating paired and bridged corner-sharing Si-O tetraeders (C.N. = 4), building the so-called “three-chain” building block, and Ca-O octaeders in the interlayer with a width of 9 Å (**Figure 4b**). Jennite forms triclinic crystals in the space group 2 (*P* -1) with the following cell parameters: $a = 10.576(2)$ Å, $b = 7.265(2)$ Å, $c = 10.931(3)$ Å, $\alpha = 101.30(1)^\circ$, $\beta = 96.98(1)^\circ$, and $\gamma = 109.65(1)^\circ$.^{120}

The second type of natural calcium silicate hydrate, namely tobermorite, also elucidated by BONACCORSI ET AL.^{121}, consists of alternating edge-sharing Ca-O trigonal prisms (C.N. = 6) and Ca-O capped trigonal prisms (C.N. = 7), alternating paired and bridged corner-sharing Si-O tetraeders (C.N. = 4), building the so-called “three-chain” building block, and edge-sharing Ca-O octaeders in the interlayer with a width of 14 Å (**Figure 4b**). Tobermorite 14Å forms monoclinic crystals in the space group 9 (*B* 1 1 b) with the following cell parameters: $a = 6.735(2)$ Å, $b = 7.425(2)$ Å, $c = 27.987(5)$ Å, $\alpha = \beta = 90.^\circ$, and $\gamma = 123.25(1)^\circ$.^{121}

2.3.2 ALUMINATE REACTION (C₃A)

Besides the hydration process of the silicate phases (C₃S and C₂S), which make up around 70 % of Portland cement, the aluminate reaction of mainly C₃A is of utmost importance especially at the early state of hydration. Ettringite, which is very important for the early stiffening of cementitious suspensions, is formed by the reaction of tricalcium aluminate (C₃A), gypsum (C \bar{S} H₂), and water (Eq. (3)). A prerequisite is a ratio of sulphate to C₃A of at least 3:1.



Previous works proved that the crystal structure of ettringite consists of dodecahedrally (C.N. = 12) coordinated calcium ions, octahedrally (C.N. = 6) coordinated aluminium ions forming face-linked hexagonal prisms, columns along the c-axis [0001], as well as two channels with sulphate as guest molecules orthogonal to the a-b-plane^{124-127}. The corresponding structure is depicted in **Figure 5** in two different projections, wherein BRAVAIS-MILLER indices^{123} according to a trigonal symmetry in a hexagonal cell are used.

¹²⁴ A. Moore, H.F.W. Taylor, *Nature* 218, **1968**, 1048–1049. <https://doi.org/10.1038/2181048a0>.

¹²⁵ A.E. Moore, H.F.W. Taylor, *Acta Crystallogr. Sect. B Struct. Crystallogr. Cryst. Chem.* 26, **1970**, 386–393. <https://doi.org/10.1107/S0567740870002443>.

¹²⁶ H.F.W. Taylor, *Mineral. Mag.* 39, **1973**, 377–389. <https://doi.org/10.1180/minmag.1973.039.304.01>.

¹²⁷ A. Bezjak, I. Jelenić, Crystal Structure Investigation of Calcium Aluminium Sulphate Hydrate- Ettringite, *Croat. Chem. Acta.* 38, **1966**, 239–242. <https://hrcak.srce.hr/208166>.

Ettringite forms needle-like hexagonal crystals in the space group 159 ($P 3 1 c$) with the following cell parameters: $a = b = 11.229(1) \text{ \AA}$, $c = 21.478(3) \text{ \AA}$, $\alpha = \beta = 90.^\circ$, and $\gamma = 120.^\circ$.

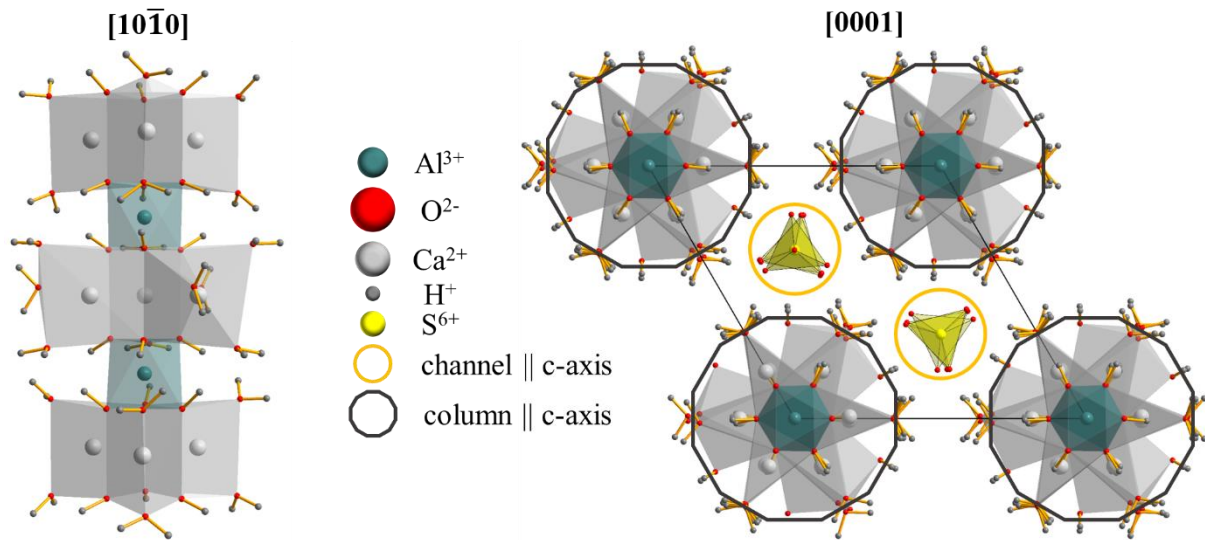
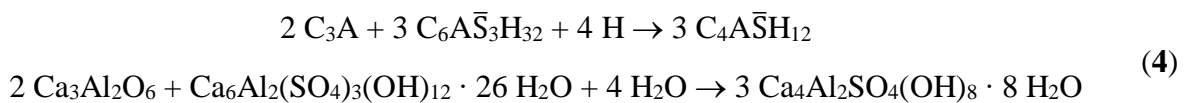


Figure 5: Crystal structure of ettringite following HARTMAN ET AL.^{128}; **(left)** part of a single column in the $[10\bar{1}0]$ projection and **(right)** build-up in the $[0001]$ projection showing columns and channels parallel to c -axis; BRAVAIS-MILLER indices^{123} according to a trigonal symmetry in a hexagonal cell.

Due to ettringite's distinct crystal morphology, its influence on the properties of cementitious suspensions is especially pronounced for rheology. (see **section 4.2**)

After $24 \text{ h} \leq t \leq 48 \text{ h}$, ettringite reacts further with C_3A and water to form calcium aluminate hydrates (AFm, $[\text{Ca}_2(\text{Al,Fe})(\text{OH})_6]_2 \cdot X \cdot n \text{ H}_2\text{O}$, where mainly $X \equiv \text{OH}^-$, SO_4^{2-} , or CO_3^{2-}), *exempli gratia* shown in Eq. (4).^{52}



¹²⁸ M.R. Hartman, R. Berliner, *Cem. Concr. Res.* 36, **2006**, 364–370.
<https://doi.org/10.1016/j.cemconres.2005.08.004>.

2.4 HYDRATION STOP TECHNIQUES

For evaluating rheological properties and developing new building materials, a profound understanding of the structural build-up or break-down, *id est* the hydration processes in cementitious suspension is fundamental. However, previous works^{59,61,62,129-140} did not draw a complete picture yet. An overview of different methods or models and their suitability for the determination of rheological factors is given by HAIST^{141}, wherein various approaches are shown. In order to further develop numerical (particle-based) models, knowledge about particles' morphology, aggregation, amount, and type, as well as the morphology of hydration products, whether in solution or on the cement grains' surface, has to be acquired. This, in turn, led to the development of different types of hydration stop techniques, either based on solvent exchange (**section 2.4.1**) or changing the external parameters temperature T and pressure p (**section 2.4.2**), which shall briefly be introduced in the following.

2.4.1 SOLVENT-BASED

In principle, the solvent exchange-based hydration stop technique uses diffusion to replace the aqueous pore solution with an organic solvent, which has a lower vapour pressure and does not form hydration products, and the solvent's subsequent removal by convective heating^{142} or drying^{143} by vacuum or evacuation combined with heating^{144}. Used so far in literature are

-
- ¹²⁹ H. Uchikawa, S. Uchida, S. Hanehara, Flocculation Structure of Fresh Cement Paste Determined by Sample Freezing – Back Scattered Electron Image Method, *Cim.* 84, **1987**, 3–22.
- ¹³⁰ L. Holzer, F. Winnefeld, B. Lothenbach, D. Zampini, The Early Cement Hydration: A Multi-Method Approach, in: G. Grieve, G. Owens (Eds.), *Proc. 11th Int. Congr. Chem. Cem.*, Durban, South Africa, **2003**: pp. 236–248.
- ¹³¹ F. Winnefeld, L. Holzer, Monitoring Early Cement Hydration, in: G. Grieve, G. Owens (Eds.), *Proc. 11th Int. Congr. Chem. Cem.*, Durban, South Africa, **2003**: pp. 330–339.
- ¹³² J. Stark, B. Möser, A. Eckart, Neue Ansätze zur Zementhydratation, Teil 1, *Zement, Kalk, Gips Int.* 54, **2001**, 52–60.
- ¹³³ J. Stark, B. Möser, A. Eckart, Neue Ansätze zur Zementhydratation, Teil 2, *Zement, Kalk, Gips Int.* 54, **2001**, 114–119.
- ¹³⁴ T.C. Powers, *The Properties of Fresh Concrete*, John Wiley & Sons, **1968**.
- ¹³⁵ C. Legrand, *Cem. Concr. Res.* 2, **1972**, 17–31. [https://doi.org/10.1016/0008-8846\(72\)90020-8](https://doi.org/10.1016/0008-8846(72)90020-8).
- ¹³⁶ W.G. Lei, L.J. Struble, *J. Am. Ceram. Soc.* 80, **1997**, 2021–2028. <https://doi.org/10.1111/j.1151-2916.1997.tb03086.x>.
- ¹³⁷ A.H.M. Andreasen, *Kolloid-Zeitschrift.* 50, **1930**, 217–228. <https://doi.org/10.1007/BF01422986>.
- ¹³⁸ R.A. Helmuth, Structure and rheology of fresh cement paste, in: *Proc. 7th Int. Congr. Chem. Cem.*, Paris, **1980**: pp. VI-0/16-VI-0/30.
- ¹³⁹ M. Hunger, H.J.H. Brouwers, *Cem. Concr. Compos.* 31, **2009**, 39–59. <https://doi.org/10.1016/j.cemconcomp.2008.09.010>.
- ¹⁴⁰ C. Legrand, *Matériaux Constr.* 5, **1972**, 379–393. <https://doi.org/10.1007/BF02476286>.
- ¹⁴¹ M. Haist, *Zur Rheologie und den physikalischen Wechselwirkungen bei Zementsuspensionen*, Fridericiana zu Karlsruhe (TH), **2009**.
- ¹⁴² L.D. Mitchell, J.C. Margeson, *J. Therm. Anal. Calorim.* 86, **2006**, 591–594. <https://doi.org/10.1007/s10973-006-7712-1>.
- ¹⁴³ L.J. Parrott, *Cem. Concr. Res.* 13, **1983**, 18–22. [https://doi.org/10.1016/0008-8846\(83\)90123-0](https://doi.org/10.1016/0008-8846(83)90123-0).
- ¹⁴⁴ R.F. Feldman, J.J. Beaudoin, *Cem. Concr. Res.* 21, **1991**, 297–308. [https://doi.org/10.1016/0008-8846\(91\)90011-6](https://doi.org/10.1016/0008-8846(91)90011-6).

acetone^{145,146}, benzene^{147}, dimethyl sulfoxide^{146}, ethanol^{148,149}, methanol^{146-149}, tetrahydrofuran^{150} and, last but not least, propan-2-ol (iPrOH)^{146-149,151-15419} being state-of-the-art (for more details about the used solvents see the review by ZHANG ET AL.^{115}). The time of exposure to reach the diffusion equilibrium time t_E is dependent on the sample's volume or cross-section, referred to as characteristic length x and the material's specific diffusivity D , as shown in Eq. (5)^{155-157}, *id est* the bigger the sample, the slower the hydration stop. Further, a sufficient amount of solvent is needed for a complete exchange. Different volumetric ratios of solvent:sample (100:1^{158}, 500:1^{159}, and 10⁵:3^{146}) have been reported, ensuring a complete replacement under continuous stirring without renewing the exchange media for 14 d.

$$t_E \cong x^2 \cdot (2D)^{-1} \quad (5)$$

This type of hydration stop technique is the best to preserve the pore structure^{160-163}, since during the drying of the exchanged sample, less capillary pressure occurs compared to a process involving water's drying. Disadvantageous is that the organic solvent reacts with the cement matrix^{145,146,148,164}, resulting in the morphing of the hydrated cement's surface either by the formation of carbonate-like phases, already after several minutes^{142,165,166}, or by dehydration

¹⁴⁵ H.F.W. Taylor, A.B. Turner, *Cem. Concr. Res.* 17, **1987**, 613–623.
[https://doi.org/10.1016/0008-8846\(87\)90134-7](https://doi.org/10.1016/0008-8846(87)90134-7).

¹⁴⁶ J.J. Beaudoin, B. Tamtsia, J. Marchand, H.R. Myers, *Cem. Concr. Res.* 30, **2000**, 359–370.
[https://doi.org/10.1016/S0008-8846\(99\)00260-4](https://doi.org/10.1016/S0008-8846(99)00260-4).

¹⁴⁷ J.J. Beaudoin, P. Gu, J. Marchand, B. Tamtsia, R.E. Myers, Z. Liu, *Adv. Cem. Based Mater.* 8, **1998**, 56–65.
[https://doi.org/10.1016/S1065-7355\(98\)00008-X](https://doi.org/10.1016/S1065-7355(98)00008-X).

¹⁴⁸ J.J. Beaudoin, Interaction of aliphatic alcohols with cement systems, *Cem.* 83, **1986**, 199–210.

¹⁴⁹ M.D.A. Thomas, *Adv. Cem. Res.* 2, **1989**, 29–34. <https://doi.org/10.1680/adcr.1989.2.5.29>.

¹⁵⁰ J. Zhang, G.W. Scherer, *Cem. Concr. Res.* 41, **2011**, 1024–1036.
<https://doi.org/10.1016/j.cemconres.2011.06.003>.

¹⁵¹ J.J. Beaudoin, B.T. Tamtsia, *J. Adv. Concr. Technol.* 2, **2004**, 113–120. <https://doi.org/10.3151/jact.2.113>.

¹⁵² D.C. Hughes, *Cem. Concr. Res.* 18, **1988**, 321–324. [https://doi.org/10.1016/0008-8846\(88\)90016-6](https://doi.org/10.1016/0008-8846(88)90016-6).

¹⁵³ L. Konecny, S.J. Naqvi, *Cem. Concr. Res.* 23, **1993**, 1223–1228. [https://doi.org/10.1016/0008-8846\(93\)90183-A](https://doi.org/10.1016/0008-8846(93)90183-A).

¹⁵⁴ R.F. Feldman, *Cem. Concr. Res.* 17, **1987**, 602–612. [https://doi.org/10.1016/0008-8846\(87\)90133-5](https://doi.org/10.1016/0008-8846(87)90133-5).

¹⁵⁵ A. Einstein, *Ann. Phys.* 322, **1905**, 549–560. <https://doi.org/10.1002/andp.19053220806>.

¹⁵⁶ J. Crank, *The Mathematics of Diffusion*, 2nd edition, Clarendon Press, Oxford, **1975**.

¹⁵⁷ J. Dunkel, P. Hänggi, *Phys. Rep.* 471, **2009**, 1–73. <https://doi.org/10.1016/j.physrep.2008.12.001>.

¹⁵⁸ K.K. Aligizaki, *Pore Structure of Cement-Based Materials*, CRC Press, **2005**.
<https://doi.org/10.1201/9781482271959>.

¹⁵⁹ R.L. Day, B.K. Marsh, *Cem. Concr. Res.* 18, **1988**, 63–73. [https://doi.org/10.1016/0008-8846\(88\)90122-6](https://doi.org/10.1016/0008-8846(88)90122-6).

¹⁶⁰ G.G. Litvan, *Cem. Concr. Res.* 6, **1976**, 139–143. [https://doi.org/10.1016/0008-8846\(76\)90058-2](https://doi.org/10.1016/0008-8846(76)90058-2).

¹⁶¹ V. Kocaba, *Development and Evaluation of Methods to Follow Microstructural Development of Cementitious Systems Including Slags*, École Polytechnique Fédérale de Lausanne, **2009**.

¹⁶² S. Mantellato, M. Palacios, R.J. Flatt, *Cem. Concr. Res.* 67, **2015**, 286–291.
<https://doi.org/10.1016/j.cemconres.2014.10.009>.

¹⁶³ S. Mantellato, M. Palacios, R.J. Flatt, *Cem. Concr. Res.* 86, **2016**, 20–28.
<https://doi.org/10.1016/j.cemconres.2016.04.005>.

¹⁶⁴ D.H. Bager, E.J. Sellevold, *Cem. Concr. Res.* 9, **1979**, 653–654. [https://doi.org/10.1016/0008-8846\(79\)90151-0](https://doi.org/10.1016/0008-8846(79)90151-0).

¹⁶⁵ K. Scrivener, R. Snellings, B. Lothenbach, *A Practical Guide to Microstructural Analysis of Cementitious Materials*, CRC PR INC (22. Dezember 2015), **2015**.

¹⁶⁶ Z. Zhang, G.W. Scherer, *Cem. Concr. Res.* 145, **2021**, 106461.
<https://doi.org/10.1016/j.cemconres.2021.106461>.

of the hydration products^{161-163,165,167-169}. In addition, the continuous mechanical mixing and the resulting perturbation of the cement matrix could damage hydration products or weaker interconnections. An alternative method to dry the sample after solvent exchange while preserving the microstructure ideally, might be based on supercritical drying^{170}. Thereby, the organic solvent is exchanged with liquid carbon dioxide (CO₂) before the sample is heated at a pressure $p \cong 5$ MPa, resulting in its supercritical state (no phase boundary), enabling drying without capillary pressure. The biggest issue in this case is CO₂ itself, as carbonation of cement paste densifies the material^{171,172}. Therefore, an inert solvent miscible with water and a low critical point has to be found before supercritical drying can be regarded as an alternative hydration stop technique.

2.4.2 TEMPERATURE- AND PRESSURE-BASED

Alternatively, techniques based on either pressure p or temperature T can be used to stop the hydration process or are used subsequently after an exchange of the aqueous media within the cementitious suspension with an organic solvent to dry the sample before analysis.

Temperature-based

In the case of the temperature-based method, the sample is either heated in a ventilated oven (up to 105 °C) at atmospheric pressure ($p = \text{atm} \cong 100$ kPa) for up to 24 h or in a microwave (900 W, 15 min, 1 kg sample, 100 kPa)^{173,174}. Both techniques excel in the speed of removing evaporable water completely, though, at $T = 105$ °C, damage to cement's pore structure^{153,175} and microstructure^{158,176,177} occur, and due to the presence of CO₂^{178} during drying, higher amounts of CaCO₃ are found. At a lower drying temperature of $T = 35$ °C, no decomposition

¹⁶⁷ J.M. Makar, T. Sato, *Mater. Struct. Constr.* 46, **2013**, 1–12. <https://doi.org/10.1617/s11527-012-9878-2>.

¹⁶⁸ A. Mezhev, D. Kulisch, A. Goncharov, S. Zhutovsky, Effect of Soaking Time in a Solvent on Hydration Stoppage of Cement, in: K. Kovler, S. Zhutovsky, S. Spatari, O.M. Jensen (Eds.), Springer International Publishing, Cham, **2020**: pp. 23–27. https://doi.org/10.1007/978-3-030-43332-1_5.

¹⁶⁹ V. Kocaba, E. Gallucci, K.L. Scrivener, *Cem. Concr. Res.* 42, **2012**, 511–525. <https://doi.org/10.1016/j.cemconres.2011.11.010>.

¹⁷⁰ S.S. Kistler, *J. Phys. Chem.* 36, **1932**, 52–64. <https://doi.org/10.1021/j150331a003>.

¹⁷¹ J.B. Rubin, J. Carey, C.M. V Taylor, Enhancement of cemented waste forms by supercritical CO₂ carbonation of standard portland cements, in: Am. Nucl. Soc. 1st Top. Meet. "Decommissioning, Decontam. Reutil. Commer. Government Facil., Los Alamos National Laboratory, New Mexico, **1997**.

¹⁷² C.A. García-González, N. el Grouh, A. Hidalgo, J. Fraile, A.M. López-Periago, C. Andrade, C. Domingo, *J. Supercrit. Fluids.* 43, **2008**, 500–509. <https://doi.org/10.1016/j.supflu.2007.07.018>.

¹⁷³ M. Nagi, D. Whiting, *Cem. Concr. Aggregates.* 16, **1994**, 125. <https://doi.org/10.1520/CCA10290J>.

¹⁷⁴ T.R. Naik, B.W. Ramme, *Cem. Concr. Res.* 17, **1987**, 927–938. [https://doi.org/10.1016/0008-8846\(87\)90081-0](https://doi.org/10.1016/0008-8846(87)90081-0).

¹⁷⁵ M.C. Garci Juenger, H.M. Jennings, *Cem. Concr. Res.* 31, **2001**, 883–892. [https://doi.org/10.1016/S0008-8846\(01\)00493-8](https://doi.org/10.1016/S0008-8846(01)00493-8).

¹⁷⁶ A. Korpa, R. Trettin, *Cem. Concr. Res.* 36, **2006**, 634–649. <https://doi.org/10.1016/j.cemconres.2005.11.021>.

¹⁷⁷ C. Gallé, *Cem. Concr. Res.* 31, **2001**, 1467–1477. [https://doi.org/10.1016/S0008-8846\(01\)00594-4](https://doi.org/10.1016/S0008-8846(01)00594-4).

¹⁷⁸ N.C.C. Collier, J.H.H. Sharp, N.B.B. Milestone, J. Hill, I.H.H. Godfrey, *Cem. Concr. Res.* 38, **2008**, 737–744. <https://doi.org/10.1016/j.cemconres.2008.02.012>.

of the hydration products, ettringite and C-S-H, or micro-cracking is found^{179}. Still, at this temperature, the hydration process is accelerated, thus changing the microstructure and altering the hydration stage^{176}. During microwave drying, microwave radiation is electromagnetically absorbed by loosely bound water, resulting in vibrations and, in turn, heat^{180} with an inverse temperature gradient^{181}, leading to a fast thermal expansion in the sample. This procedure could damage the sample^{182} or possibly accelerate the hydration process^{183,184}. However, microwave drying is a very practical method to determine the water content^{173,174,185,186} of a cementitious suspension or mixture on site as quality control^{173,174}.

Pressure-based

The second type of external hydration stop or subsequent drying techniques is based on lowering the pressure p to $70 \text{ mPa} \leq p \leq 4 \text{ Pa}$, wherein four types have to be distinguished (**Figure 6**): (1) Vacuum drying via a pump, (2) Dry ice drying or D-drying, (3) Perchlorate drying or P-drying, and (4) Freeze-drying or lyophilisation. Apart from the latter case, the other three techniques lower the pressure to facilitate the evaporation of water and are slow drying techniques, wherein drying time is dependent on low-pressure levels, samples' size and mass, making these methods unsuitable for a time-variant analysis^{176}. Further, vacuum drying dehydrates the hydration products^{187} (ettringite, mono sulphate, as well as C-S-H), induces micro cracks^{177}, and alters the pore structure leading to a higher specific volume^{187}.

D-drying and P-drying have a similar setup^{188,189} including a desiccator, a trap containing either dry ice in alcohol or magnesium perchlorate di or tetra hydrate ($\text{Mg}(\text{ClO}_4) \cdot 2$ or $4 \text{ H}_2\text{O}$), and induce similar changes to the sample during drying. P-drying does not drain all residual

¹⁷⁹ R.J. Detwiler, L.J. Powers, U.H. Jakobsen, W.U. Ahmed, K.L. Scrivener, K.O. Kjellsen, Preparing Specimens for Microscopy Improper techniques can make examination results less reliable, *Concr. Int.* 23, **2001**, 50–58.

¹⁸⁰ K. Šuhajda, M. Novotný, J. Škrámlík, Monitoring of effectivity of microwave desiccation by means of rod plug-in antenna, *E-Journal Nondestruct. Test.*, **2008**. <https://www.ndt.net/article/v13n06/skramlík.pdf>.

¹⁸¹ C.K. Wei, H.T. Davis, E.A. Davis, J. Gordon, *AIChE J.* 31, **1985** 842–848. <https://doi.org/10.1002/aic.690310521>.

¹⁸² H. Ai, J.F. Young, G.W. Scherer, *J. Am. Ceram. Soc.* 84, **2004**, 385–91. <https://doi.org/10.1111/j.1151-2916.2001.tb00666.x>.

¹⁸³ W. Xuequan, D. Jianbo, T. Mingshu, *Cem. Concr. Res.* 17, **1987**, 205–210. [https://doi.org/10.1016/0008-8846\(87\)90103-7](https://doi.org/10.1016/0008-8846(87)90103-7).

¹⁸⁴ P. Rattanadecho, N. Suwannapum, B. Chatveera, D. Atong, N. Makul, *Mater. Sci. Eng. A.* 472, **2008**, 299–307. <https://doi.org/10.1016/j.msea.2007.03.035>.

¹⁸⁵ R.T. Peterson, D. Leftwich, Determination of Water Content of Plastic Concrete Using a Microwave Oven, North Dakota State Highway Dept., Bismarck. Materials and Research Div; **1978**.

¹⁸⁶ E.C. Roshore, Use of Microwave Oven to Determine Water Content of Fresh Concrete, Army Engineer Waterways Experiment Station Vicksburg Miss; **1973**.

¹⁸⁷ L. Zhang, F.P. Glasser, *Adv. Cem. Res.* 12, **2000**, 79–88. <https://doi.org/10.1680/adcr.2000.12.2.79>.

¹⁸⁸ L.E. Copeland, J.C. Hayes, Determination of non-evaporable water in hardened Portland-cement paste, American Society for Testing Materials (ASTM), **1953**.

¹⁸⁹ L.E. Copeland, J.C. Hayes, Determination of non-evaporable water in hardened Portland-cement paste, Engineering Index Backfile, **1953**.

water in the pores. Though D-drying removes not only residual but also some bound water^{190}, it is commonly identified as the best standard drying technique^{176,187} as it is assumed that all unbound water becomes depleted and the microstructure is preserved best. The last pressure-based technique, freeze-drying^{177,178,191}, uses liquid nitrogen (LN₂) to freeze the free water in the pores to stop the hydration process and subsequent drying at $p \leq 6$ Pa to sublimate unbound water without capillary pressure. A further development of the known freeze-drying method regarding sample's freezing, drying pressure, and drying time is shown in **section 3**.

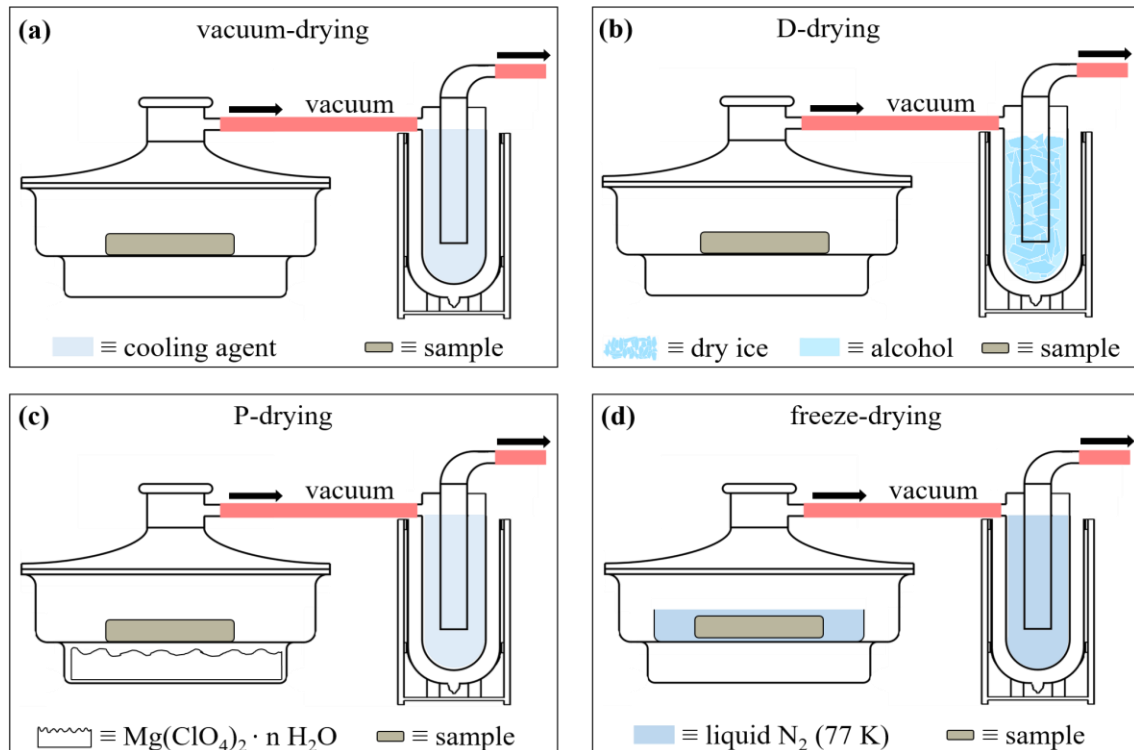


Figure 6: Scheme for pressure-based hydration stop techniques; (a) vacuum-drying, (b) D-drying, (c) P-drying, and (d) freeze-drying or lyophilisation.

Although hydration is stopped fast, the freezing process with liquid nitrogen (LN₂) does not exhibit the formation of amorphous ice, as due to the LEIDENFROST effect^{192,193} the needed cooling of at least $10^6 \text{ K}\cdot\text{s}^{-1}$ ^{194} could not be achieved. This, in turn, could potentially induce damaging stresses^{195-197} due to volume expansion during freezing or formation of ice crystals.

¹⁹⁰ J.J. Thomas, H.M. Jennings, A.J. Allen, *Adv. Cem. Based Mater.* 7, **1998**, 119–122.

[https://doi.org/10.1016/S1065-7355\(97\)00086-2](https://doi.org/10.1016/S1065-7355(97)00086-2).

¹⁹¹ S. Chandra, B. Hedberg, L. Berntsson, *Cem. Concr. Res.* 10, **1980**, 467–469.

[https://doi.org/10.1016/0008-8846\(80\)90124-6](https://doi.org/10.1016/0008-8846(80)90124-6).

¹⁹² J.G. Leidenfrost, *De aquae communis nonnullis qualitatibus tractatus*, Duisburgi ad Rhenum, **1756**.

¹⁹³ J.E. Gillot, Importance of Specimen Preparation in Microscopy, in: *Soil Specim. Prep. Lab. Test.*, American Society for Testing Materials (ASTM), Canada, **1976**: pp. 289-307. <https://doi.org/10.1520/STP39089S>.

¹⁹⁴ P.G. Debenedetti, *Metastable Liquids: Concepts and Principles*, Princeton University Press, Princeton, **1997**.

¹⁹⁵ G.W. Scherer, J. Valenza II, Mechanisms of frost damage, in: *Mater. Sci. Concr. Vol VII*, **2005**: pp. 209–246.

¹⁹⁶ J. Marchand, R. Pleau, R. Gagné, Deterioration of concrete due to freezing and thawing, in: *Mater. Sci. Concr. Vol. IV*, **1995**: pp. 283–354.

¹⁹⁷ G.W. Scherer, *J. Non. Cryst. Solids.* 155, **1993**, 1–25. [https://doi.org/10.1016/0022-3093\(93\)90467-C](https://doi.org/10.1016/0022-3093(93)90467-C).

Table 2: Overview of the previously described hydration stop and drying techniques, including a short introduction, their respective advantages, as well as disadvantages.

name	short abstract	advantage(s)	disadvantage(s)
solvent exchange	diffusion-controlled exchange of pore water to organic solvent in excess (renewal needed regularly) subsequent drying with oven or desiccator needed	+ preserves pore structure	- morphing of surface - hydration products dehydrate - introduces carbonation quickly - diffusion controlled (slow) - not removable without affecting the microstructure
supercritical drying	exchange of pore water to organic solvent to supercritical CO ₂ and its subsequent evaporation	+ no capillary pressure + best microstructural preservation	- CO ₂ carbonates and densifies cement - complex process - water-miscible solvent needed
oven drying	heating wet sample at atmospheric pressure p and enhanced temperature T (35 °C – 105 °C); mainly 60 °C or 105 °C	+ simple	- micro cracking - hydration products decompose - hydration process not stopped - 35 °C might accelerate the hydration process
microwave drying	microwave radiation electromagnetically absorbed by loosely bound water results in vibration and inverse heat gradient	+ very fast (1 kg, 900 W, 15 min) + practical for on-site assessment of water content	- damage to microstructure - might accelerate the hydration process
vacuum drying	wet or exchanged wet sample continuously treated with low-pressure $p < 4$ Pa	+ no carbonation	- slow, unsuitable for time-variant analysis - hydration products dehydrate - damage to pore structure
D-drying	wet or exchanged wet sample stored in a desiccator under vacuum ($p \leq 4$ Pa) connected to trap with dry ice-alcohol mixture	+ assessment of non-evaporable water	- slow, unsuitable for time-variant analysis - removal of some bound water
P-drying	wet or exchanged sample stored in a desiccator over Mg(ClO ₄) ₂ · n H ₂ O [n = 2 or 4] inducing partial pressure $p = 1.1$ Pa; connected to trap	+ no external vacuum needed + gentle drying	- slow, unsuitable for time-variant analysis - residual pore water
freeze-drying or lyophilisation	wet sample frozen in liquid nitrogen (LN ₂) for at least 15 min, drying under vacuum ($p \leq 4$ Pa)	+ nearly instant hydration stop + no capillary pressure	- damage to microstructure due to ice crystals - dehydration of hydration products

2.5 ADDITIVES IN CEMENT

Different types of additives are in use to further modify, improve, and influence the properties of cementitious suspensions or hardened cement paste as well as concrete. These can be divided into well-trying large-scale materials (**section 2.5.1**) and new types on a lab-scale (**section 2.5.2**), which are envisioned to beneficially alter the properties of cement-based materials^{198}.

2.5.1 LARGE-SCALE / GENERAL

On a large-scale^{199}, mainly at building sites, additives can have two impacts: (1) Reduction of the water demand, *id est* less water is bound to cement grains, as their surface is already occupied by additives, which, in turn, enables controlled hydration at low or high outside temperatures T for cementitious suspensions. (2) Protection of the hardened cement paste against external parameters. Lignosulphonate-based liquefiers as well as superplasticisers reduce the water demand, resulting in enhanced processability, *exempli gratia* pumpability, durability, strength, and increased early strength. Superplasticisers based on polycarboxylether as well as retarder based on phosphate and sucrose, enable a controlled hydration at elevated ambient temperature or the production of larger components or monoliths. In contrast, hardening or setting accelerators based on either mineralogical salts or a mixture of organic and inorganic complex agents, respectively, are needed at low ambient temperatures. In order to protect the hardened components against frost damage, road salt, and or capillary water, root-resin-based air entraining agents, modified melamine resin sulfonate-based stabilisers, and or sealants based on organosilicon compounds are added, whereby the bleeding (segregation of water and cement particles) of the suspensions is reduced additionally (summarised in **Table 3**).

¹⁹⁸ F. Sanchez, K. Sobolev, *Constr. Build. Mater.* 24, **2010**, 2060–2071.
<https://doi.org/10.1016/j.conbuildmat.2010.03.014>.

¹⁹⁹ D. Küchlin, O. Hersel, *Betontechnische Daten*, HeidelbergCement AG, Leimen, **2017**.

Table 3: Large-scale additives in cementitious suspensions and their respective impact.^{199}

type	based on	impact
liquefier	lignosulphonate	enhanced processability at the same w/c ratio
superplasticiser	lignosulphonate	enhanced durability, strength, and early strength
	polycarboxylether	retarded hydration, enabling bigger components and working at elevated ambient temperature
retarder	phosphate and sucrose	
hardening accelerator	mineralogical salts	enhanced hardening, enabling working at low ambient temperature
setting accelerator	mixture of organic and inorganic complex agents	enhanced setting, enabling working at low ambient temperature
air entraining agent	root resin	enhanced resistance against damage due to frost and thawing or road salt, as well as reduced bleeding
stabiliser	modified melamine resin sulphonate	reduced bleeding and segregation
sealant	organosilicon	prevented capillary water absorption

2.5.2 LAB-SCALE / NANOPARTICLES

In the last decades, a growing number of works dealt with the influence of nanoscopic materials, nanoparticles, or ultrafine particles with a size below 100 nm^{200-202} as additives to cementitious suspensions and concrete on the respective hardened material. In around 8 out of 10 studies, the implemented particles are mainly quasi-spherical (aspect ratio $AR \cong 1$) metal oxides with diameters of $d \leq 100$ nm.^{203} These examined materials are amorphous silicon SiO_2 ^{204-207}, α - or γ - Al_2O_3 ^{203-205,207}, anatase- or rutile- TiO_2 ^{203-205}, α - or γ - Fe_2O_3 ^{203,204,207}, $CaCO_3$ ^{206,208}, MgO ^{209}, CaO ^{209}, ZnO_2 ^{204}, ZrO_2 ^{208}, Cu_2O_3 ^{208}, and CuO ^{208}. Independent of the used type of oxide material, all nanoparticles reduce the amount of free water due to their high specific surface area (SSA)^{210}, and, in turn, workability and fluidity of cementitious

²⁰⁰ U.S. Environmental Protection Agency (EPA), BCES: Module 3 - Characteristics of Particles, **2010**. <https://web.archive.org/web/20110415150714/http://www.epa.gov/apti/bces/module3/category/category.htm>, April 27, **2022**.

²⁰¹ National Science and Technology Council, The National Nanotechnology Initiative, **2007**.

²⁰² M. Vert, Y. Doi, K.-H. Hellwich, M. Hess, P. Hodge, P. Kubisa, M. Rinaudo, F. Schué, *Pure Appl. Chem.* 84, **2012**, 377–410. <https://doi.org/10.1351/PAC-REC-10-12-04>.

²⁰³ Y. Reches, *Constr. Build. Mater.* 175, **2018**, 483–495. <https://doi.org/10.1016/j.conbuildmat.2018.04.214>.

²⁰⁴ Y. Reches, K. Thomson, M. Helbing, D.S. Kosson, F. Sanchez, *Constr. Build. Mater.* 167, **2018**, 860–873. <https://doi.org/10.1016/j.conbuildmat.2018.02.032>.

²⁰⁵ X. He, X. Shi, *Transp. Res. Rec.*, **2008**, 13–21. <https://doi.org/10.3141/2070-03>.

²⁰⁶ S. Kawashima, P. Hou, D.J. Corr, S.P. Shah, *Cem. Concr. Compos.* 36, **2013**, 8–15. <https://doi.org/10.1016/j.cemconcomp.2012.06.012>.

²⁰⁷ M. Oltulu, R. Şahin, *Energy Build.* 58, **2013**, 292–301. <https://doi.org/10.1016/j.enbuild.2012.12.014>.

²⁰⁸ A.M. Rashad, *Constr. Build. Mater.* 48, **2013**, 1120–1133. <https://doi.org/10.1016/j.conbuildmat.2013.06.083>.

²⁰⁹ R. Polat, R. Demirboğa, W.H. Khushefati, *Constr. Build. Mater.* 81, **2015**, 268–275. <https://doi.org/10.1016/j.conbuildmat.2015.02.032>.

²¹⁰ J. Chen, S.C. Kou, C.S. Poon, *Cem. Concr. Compos.* 34, **2012**, 642–649. <https://doi.org/10.1016/j.cemconcomp.2012.02.009>.

suspensions^{211,212}. In addition, this material class can introduce a higher amount of entrained air^{213}, which has an ambiguous effect, as workability and resistance against frost damage and thawing are enhanced while strength is reduced.^{214} Further, the addition of nanoscopic material shortens the initial setting^{203}, which is obstructive for transport but increases early-strength. This, in turn, is beneficial for faster construction schedules, possibly enabling more environmentally-friendly admixtures to be used on building sites. However, these are partially restricted due to low reactivity^{215}. Besides enhanced mechanical properties, such as early strength, compressive strength f_{ck} , and tensile or flexural strength, durability against extrinsic parameters (mainly weathering and elevated temperature) gets enhanced using nanoscopic additives.^{203} For more details about the distinct influences of different amounts and species of nanoparticles, please read the reviews provided by RECHES^{203}, AGGARWAL ET AL.^{211}, MENDES ET AL.^{216}, SANCHEZ ET AL.^{198}, and OLAFUSI ET AL.^{217}.

Despite this extensive amount of studies, until now, no study has tried to enhance or control the electromagnetic wave absorption rate of hardened cement paste. This possibility was approached in a recent study (**section 4.3**) using unmodified gallium-substituted hard-magnetic ϵ -Fe₂O₃ nanocrystals, which were synthesised via a sol-gel method and demonstrated their capability to absorb millimetre waves^{218}. The partial substitution of iron with gallium is needed to stabilise the normally metastable ϵ -phase of Fe₂O₃.^{218} Implementing these properties should enable constructions to protect sensitive machinery negatively influenced by radio waves, like magnetic resonance tomography in the medical field, to ensure greater lifetime and efficiency. At the same time, sensitive data can be protected by blocking external access from third parties, *id est* enhanced tap-proofness.

²¹¹ P. Aggarwal, R.P. Singh, Y. Aggarwal, *Cogent Eng.* 2, **2015**.
<https://doi.org/10.1080/23311916.2015.1078018>.

²¹² L.E. Zapata, G. Portela, O.M. Suárez, O. Carrasquillo, *Constr. Build. Mater.* 41, **2013**, 708–716.
<https://doi.org/10.1016/j.conbuildmat.2012.12.025>.

²¹³ N.-M. Barkoula, C. Ioannou, D.G. Aggelis, T.E. Matikas, *Constr. Build. Mater.* 125, **2016**, 546–552.
<https://doi.org/10.1016/j.conbuildmat.2016.08.055>.

²¹⁴ American Concrete Institute Committee 211, Standard Practice for Selecting Proportions for Normal, Heavyweight, and Mass Concrete (ACI 211.1-91), American Concrete Institute, Detroit, **1997**.

²¹⁵ M.H. Zhang, J. Islam, *Constr. Build. Mater.* 29, **2012**, 573–580.
<https://doi.org/10.1016/j.conbuildmat.2011.11.013>.

²¹⁶ T.M. Mendes, D. Hotza, W.L. Repette, Nanoparticles in cement based materials: A review, *Rev. Adv. Mater. Sci.* 40, **2015**, 89–96.

²¹⁷ O.S. Olafusi, E.R. Sadiku, J. Snyman, J.M. Ndambuki, W.K. Kupolati, *SN Appl. Sci.* 1, **2019**.
<https://doi.org/10.1007/s42452-019-0600-7>.

²¹⁸ S. Ohkoshi, S. Kuroki, S. Sakurai, K. Matsumoto, K. Sato, S. Sasaki, *Angew. Chemie Int. Ed.* 46, **2007**, 44, 8392–8395. <https://doi.org/10.1002/anie.200703010>.

3 DEVELOPMENT OF A FREEZE-DRYING-BASED HYDRATION STOP TECHNIQUE

3.1 SUMMARY

One of the main issues encountered in modern cement-based works is the lack of knowledge about the rheological properties of cement-based suspensions during processing. That is why rheology is a crucial tool for the characterisation of fresh cement-based suspensions. Many factors influence these physically defined parameters-based properties and predominantly affect paste levels. In order to obtain an understanding of influencing factors, such as the underlying kinetics and mechanisms at the initial colloidal scale, a time variant analysis of cementitious suspensions is needed. Amongst the manifold examined suspensions with different w/c ratios, stopped at various times by miscellaneous techniques, it was ascertained that each technique has advantages and disadvantages and that, hitherto, the best method to stop the hydration of cementitious suspensions is a solvent-water-exchange with iPrOH. The identification and development of a suitable technique to stop the hydration process nearly instantly without disturbing the cement matrix, damaging or morphing the surface of hydrated cement, as well as without changes to the chemical composition *exempli gratia* the formation of carbonate-like phases, which the state-of-the-art technique is not capable of, is demonstrated by the following three publications.

The first research article^{219} (**section 3.1**) shows the comparison of samples whose hydration was stopped by three techniques, namely the state-of-the-art iPrOH-H₂O exchange (**I**), lyophilisation in combination with iPrOH-H₂O exchange (**IL**), and lyophilisation (**L**) also known as freeze-drying. The overall results do not crayon a distinct picture of which technique is the most suitable, as both standalone methods, lyophilisation and solvent exchange, exhibited ambiguity, wherein the first ever tried combination of both turned out to be a jack of all traits but master of none. By employing **I**, water remains in the system even after the drying procedure, which leads to an incompletely quenched hydration, making this method unsuitable for the intended time-variant analysis of cementitious suspensions. Although this issue is less or not pronounced by using **IL** or **L**, it is unclear, whether lyophilisation results in a de-agglomeration of already agglomerated particles or whether the addition of iPrOH causes the observation of microscale particle agglomerates. If the latter case applies, **IL** would be the

²¹⁹ P.A. Kißling, D. Cotardo, T. von Bronk, L. Lohaus, N.C. Bigall, Springer, Cham, **2020**, pp. 610–618.
https://doi.org/10.1007/978-3-030-22566-7_71.

preferable route, as it would not change the morphology and particle size distribution while possibly ensuring a nearly instant hydration stop.

For further optimizing the hydration stop technique by incorporating lyophilisation or freeze-drying, the author took a step back and looked into the influence of low-pressure treatment on the first hydration product, ettringite, resulting in the second research article^{220} (**section 3.2**). Here, three different levels of low-pressure ($p = 400 \text{ Pa}$, 6 Pa , and $90 \text{ }\mu\text{Pa}$ or 3.53 mPa) and various durations of treatment under this low-pressure ($t_{l-p} \leq 72 \text{ h}$) were applied on pure synthetic ettringite. It was shown that low-pressure of $p = 400 \text{ Pa}$ does not change the chemical composition nor the morphology of ettringite for at least $t_{l-p} \leq 72 \text{ h}$.

Based on the aforementioned results, the previously used hydration stop techniques based on lyophilisation (**L**), iPrOH-H₂O exchange (**I**), and the combination of solvent exchange and lyophilisation (**IL**) were optimised (**Table 4**). The development of the lyophilisation-based method (**L**) resulted in the pioneered freeze-drying-based hydration stop method (**FD**). It was optimised to such an extent that after its, use the ettringite content is highest, and samples show the highest reproducibility compared to the state-of-the-art (**Iso**) as well as the combined technique (**IFD**). The third research article^{221} (**section 3.3**) summarises all used methods and can be seen partly as an evolution of the first part of this section.

Table 4: Changes to the previously used hydration stop techniques^{219}.

technique	previous	optimised	reason (if applicable)
(Iso)	iPrOH RT	iPrOH pre-cooled to 5 °C	lowering of hydration's kinetic
↑	mixing mechanically for 10 min at 50 rpm	shaking for 5 min at 1487 rpm	mixing without mechanical stress to prevent mechanical-based destruction of hydration products
(I)	iPrOH RT	iPrOH pre-cooled to 5 °C	lowering of hydration's kinetic
(IFD) and (FD)	transfer into a pre-cooled flask in LN ₂	transfer into a flask, then slow rotation to get a homogenous thin layer, and freezing at once in LN ₂	increased surface facilitates faster and more homogenous freezing
↑ and ↑ (IL) (L)	freeze-dried for 36 h at 15 μbar	freeze-dried for 3 h at 4 mbar	results of section 3.2 showed that 4 mbar is the best pressure to preserve ettringite

²²⁰ P.A. Kißling, F. Lübkeemann, T. von Bronk, D. Cotardo, L. Lei, A. Feldhoff, L. Lohaus, M. Haist, N.C. Bigall, *Materials* (Basel). 14, **2021**, 2720. <https://doi.org/https://doi.org/10.3390/ma14112720>.

²²¹ P.A. Kißling, F. Lübkeemann, A. Mundstock, L. Lohaus, M. Haist, J. Caro, N.C. Bigall, *Cem. Concr. Res.* 159, **2022**, 106841. <https://doi.org/10.1016/j.cemconres.2022.106841>.

3.2 COMPARISON OF WATER-ISOPROPANOL REPLACEMENT AND LYOPHILISATION FOR HYDRATION STOP OF CEMENTITIOUS SUSPENSIONS

P. A. Kießling, D. Cotardo, T.von Bronk, L. Lohaus, N. C. Bigall

V. Mechtcherine, K. Khayat, E. Secrieru (Eds.) *Rheol. Process. Constr. Mater.* RheoCon 2019, SCC2019, Springer, Cham, **2020**: pp. 610–618.

https://doi.org/10.1007/978-3-030-22566-7_71.



Comparison of Water-Isopropanol Replacement and Lyophilisation for Hydration Stop of Cementitious Suspensions

Patrick A. Kießling¹(✉), Dario Cotardo³, Tabea von Bronk³,
Ludger Lohaus³, and Nadja C. Bigall^{1,2}(✉)

¹ Institute of Physical Chemistry and Electrochemistry,
Leibniz Universität Hannover, Hannover, Germany
{patrick.kissling,nadja.bigall}@pci.uni-hannover.de

² Laboratory of Nano and Quantum Engineering,
Leibniz Universität Hannover, Hannover, Germany

³ Institute of Building Materials Science,
Leibniz Universität Hannover, Hannover, Germany

Abstract. For modern concrete technology, rheology is crucial for characterizing the properties of fresh concrete on the basis of physically defined parameters. These properties can be influenced by many factors, but have an effect on paste level predominantly. To obtain an understanding of influencing factors such as the underlying kinetics and mechanisms at the initial colloidal scale a time variant analysis of cementitious suspensions is needed. In this article, a method to stop the hydration process of cementitious suspensions at any time by gradual water-isopropanol replacement and lyophilisation is demonstrated. Therefore, three different methods for hydration stop are investigated, namely water-isopropanol exchange, lyophilisation as well as a combination of both, and compared to pristine (non-reacted) cement particles. Analysis of dried samples leads to the observation that direct lyophilisation leads to particles of similar size as the pristine cement particles. Water-isopropanol replacement as well as water-isopropanol exchange with subsequent lyophilisation, instead, leads to a very broad particle size distribution with larger particles, which might be attributed to secondary agglomerations of particles. We further investigate the three different hydration stop methods by evaluating the pore size distribution by means of nitrogen physisorption. Additionally, scanning electron microscopy (SEM) as an imaging method is used.

Keywords: Rheology · Hydration stop · Time variant analysis · Cementitious suspension · Freeze drying/lyophilisation

1 Introduction

For understanding the fundamental processes in modern concrete technology, characterizing the properties of fresh concrete on the basis of physically defined parameters is of utmost importance. For example, rheological properties can be influenced by various factors. Many of them having an effect on paste level predominantly.

© RILEM 2020

V. Mechtcherine et al. (Eds.): RheoCon 2019/SCC 2019, RILEM Bookseries 23, pp. 610–618, 2020.

https://doi.org/10.1007/978-3-030-22566-7_71

Thus, parameter studies are preferably carried out on paste level. Also for reasons of practicability, with particular focus on limiting the test duration and the handling in general, more extensive concrete variations are often performed on paste level and not on concrete level. Nevertheless, concrete remains the real object of reflection of concrete technology. In general, it is the aim to obtain an understanding of influencing factors such as the underlying kinetics and mechanisms at the initial colloidal scale, and later on to transfer these influences to paste, mortar and concrete level. The cross-scale transfer from colloidal suspension to paste, mortar, and concrete is a challenge for concrete technology since it involves several orders of magnitudes on the size scale ranging from nanometres to metres. In order to characterize a colloidal suspension taking into account the hydration process, a time dependent (kinetic) analysis is needed. This scrutiny can be achieved by hydration stop at defined times after adding water to the mixture. The state of the art for such a hydration stop is based on water exchange with organic solvents, mostly isopropanol [1]. However, kinetic aspects of the mixing of isopropanol with the reaction of water should be considered. Alternatively, to get rid of liquid water as quickly as possible freezing at a high rate can be considered. Due to quick freezing in liquid nitrogen $N_2(l)$, vitreous water is formed. Previous works concentrating on biological samples have shown that such vitreous water does not change the sample's morphology [2, 3] and can easily be evaporated by subsequent lyophilisation [3]. The motive for this procedure was, that after this freeze-type quenching the structural analysis of the dried system can be performed with relatively slow analytic methods, such as N_2 -physisorption and X-ray diffraction (XRD). In addition, imaging methods such as scanning electron microscopy (SEM) and transmission electron microscopy (TEM) can be employed. The present article focuses on the question, whether the properties of dried suspensions after water-isopropanol replacement are comparable to the properties of freeze-dried suspensions. The second focus lies on finding the most sensitive method for hydration stop of cementitious suspensions.

2 Experimental

2.1 Chemicals

CEM I 42.5 R from HeidelbergCement AG was stored at ambient temperature ($20\text{ °C} \pm 2\text{ °C}$) and humidity (18%–45%). Anhydrous isopropanol ($\geq 99.95\%$) and anhydrous copper sulphate ($\geq 98\%$) from Carl Roth, Millipore water ($18.2\text{ M}\Omega\cdot\text{cm}$) cleaned by Arium 611DI from Sartorius and liquid nitrogen ($\geq 99.999\%$) from Linde were used.

2.2 Cementitious Suspensions and Mixing Program

Following the mixing program shown in Table 1, 610 g CEM I 42.5 R and 305 g Millipore water – precooled to 10 °C – was mixed with a balloon whisk using a Kenwood KitchenAid KM336 S Chef Classic to simulate concrete mixing as usually performed at larger scales. During the first ten minutes, the mixture's temperature rose

612 P. A. Kießling et al.

to 20 °C. The last step of slow stirring at level 2 (approx. 72 rpm) was performed for different times (6, 26, 56, and 86 min) in order to investigate the reaction kinetic. All dried samples were stored at 19.2 °C ± 0.4 °C in a dry nitrogen atmosphere for 0 to 2 days before any characterization method.

2.3 Procedure for Freeze-Dried Samples

After a total reaction duration of 10 min, 30 min, 60 min, and 90 min after adding water (related to slow stirring at level 2 for 6 min, 26 min, 56 min, and 86 min, respectively), 10 mL of the cementitious suspension were taken with an Eppendorf pipette and instantly dropped into N₂(l) (approx. 100 mL in a precooled flask for approx. 20 min). Each sample was freeze-dried using an Alpha 1-2 LDplus from Christ for 36 h at 1.5·10⁻² mbar.

2.4 Procedure for Water-Isopropanol Replaced Samples

10, 30, 60 and 90 min after adding water to the mixture, 10 mL of the cementitious suspension were taken with an Eppendorf pipette, instantly dropped into 50 mL anhydrous isopropanol and stirred for 10 min at 50 rpm with a magnetic stirrer. Afterwards using a Buchner funnel the water-isopropanol suspension was filtrated (mesh size 4 µm to 12 µm). The sample was washed three times by adding 10 mL isopropanol. Approximately half of each (humid) sample was taken and dropped into N₂(l) (approx. 100 mL in a precooled flask for approx. 20 min). Each sample was freeze-dried using an Alpha 1-2 LDplus from Christ for 36 h at 1.5·10⁻² mbar. The other half was stored under ambient conditions (19.2 °C ± 0.4 °C) for 36 h. To exclude an impact of the big mesh size on the particle size distribution, the experiment was repeated using a smaller filter (mesh size 0.1 µm); no changes to the size distribution were observed. Secondly, in all cases the filtrate was not turbid. Therefore, particles smaller than 1 µm can be excluded.

Table 1. Mixing program for cementitious suspensions.

Type	Duration	Mode (Kenwood KitchenAid) [rpm]
Dry mixing of CEM I	60 s	Level 2 [approx. 72]
Adding water	30 s	Level 2 [approx. 72]
Pre-homogenisation	15 s	Level 2 [approx. 72]
Homogenisation	15 s	Level maximum [approx. 220]
Stop and sting manually	60 s	Off
Homogenisation II	120 s	Level maximum [approx. 220]
Slow stirring	Until stopped	Level 2 [approx. 72]

2.5 Characterization

Nitrogen (N_2)-physisorption was performed at a NOVA 3000 from Quantachrome operating at 77 K. Prior to physisorption measurements, the samples were degassed under vacuum at 298 K for 24 h. Specific surface areas and volumes were estimated by applying the Brunauer-Emmett-Teller (BET) [4] equation, pore volumina at $p/p_0 = 0.95345$ respectively by applying Density Functional Theory (DFT) [5, 6] as well as pore size distributions by applying Barrett-Joyner-Halenda (BJH) [7].

The morphologies of the dried samples were investigated by scanning electron microscopy (SEM) using a JOEL JSM 6700F, equipped with a cold field emission gun electron source. The acceleration voltage was 2 kV for each measurement. The powder was dropped on a sticky carbon patty. Excess of powder was blown away by a compressed air gun and a conductive carbon layer was sputtered.

By evaluation of eight SEM pictures at a magnification of 1000 times with ImageJ 1.52a, for each sample, a particle size distribution was determined.

The anhydrousness of the samples was tested by adding anhydrous copper sulphate to small amounts of the samples (colour change to blue for humid samples).

3 Results and Discussion

Following the mixing program shown in Table 1, cementitious suspensions were mixed with a water to cement mass ratio of $w/c = 0.5$ and the hydration process was stopped at four defined times. The hydration stop was induced either by lyophilisation after freezing in $N_2(l)$ (**L**), or by a water-isopropanol exchange (**I**), or last by a gradual water-isopropanol replacement combined with freezing in $N_2(l)$ and lyophilisation (**II**). This allows analysing the suspension with N_2 -physisorption and SEM in order to evaluate the influence of the hydration process and the used hydration stop method on changes to morphology, porosity and crystal phases.

In order to rate the possibility of further hydration processes after drying, a copper sulphate test was conducted. This test showed, that in case of isopropanol exchange (**I**), residual water was present, while methods involving lyophilisation (**L** and **II**) yielded totally dry samples. Consequently, in the latter two cases further growth (after employing the hydration stop method) can be excluded, while in case of **I** hydration reactions might still occur.

Therefore, to get a quick overview about the expected changes of porosity due to hydration, the nitrogen ad- and desorption behavior was examined. The evaluation of the isotherms shows a small hysteresis, which varies at its width for the three different methods (Fig. 1a) used. The broadest hysteresis appears by using the gradual **II** method. This effect is especially pronounced after a reaction time of 60 min (Fig. 1b).

614 P. A. Kießling et al.

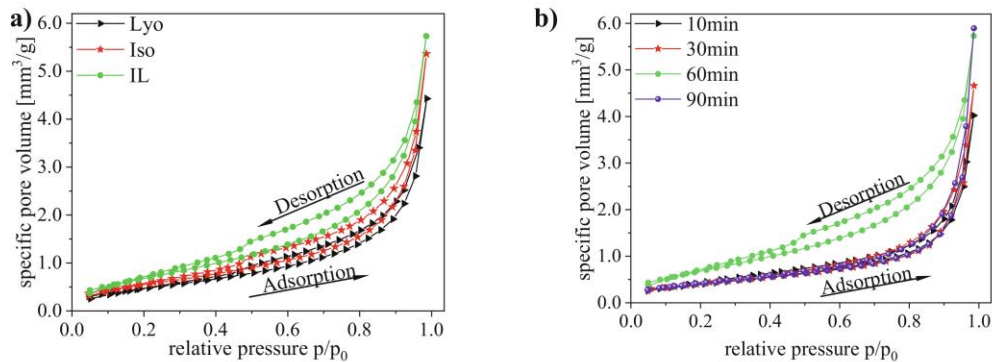


Fig. 1. N₂-physorption measurement for comparison of isotherms of (a) hydrated CEM I stopped at 60 min and (b) time dependent comparison of method IL.

The N₂-physorption measurements show also that independent of the used hydration stop method during the reaction the specific surface area (SSA) as well as the specific volume (SV) of the cement paste rises and drops after a maximum at 60 min (Fig. 2). These findings can be explained by looking at the reaction's course. During hydration, early hydration products were formed on the surface of the cement particles, which leads to an increase of the SSA. It can be assumed that this process is more dominant than the agglomeration of the cement particles, which occurs simultaneously during the reaction. A possible reason for this effect could be the reduced hydration kinetics at the dormant stage, which has been reported to be between 30 and 90 min [8]. A possible reason for the decay of the SSA and SV, hypothetically, is that the early hydration products on the surface had no more open surface to grow on, which resulted in a growing together into a layer, leading to a decreased specific surface area.

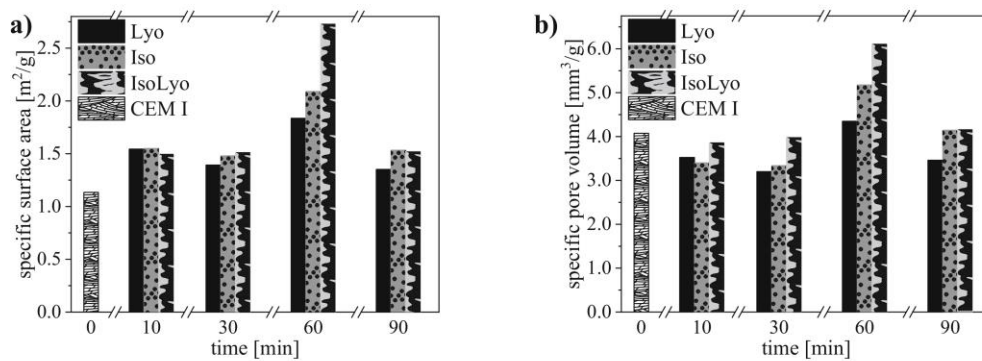


Fig. 2. N₂-physorption; (a) specific surface area and (b) specific volume of raw and hydrated CEM I; hydration stopped at four times by three methods (L, I & IL).

The pore size distribution (PSD) after 60 min reaction time, derived from N₂-physorption measurements is shown in Fig. 3. Compared to the starting material CEM I, with a mean pore size $d_{50} = 4.89 \text{ nm} \pm 0.12 \text{ nm}$, the PSD after hydration becomes broader with a shift of the mean pore size to $d_{50} = 5.77 \text{ nm} \pm 0.12 \text{ nm}$.

The broadening can be explained by the presence of various hydration products leading to a larger surface roughness and hence to both a larger **SSA** and a larger amount of small pores. This find derives from the agglomeration of cement particles during the dormant phase of the hydration process. In this period the surface is passivated [8] leading to usage of inner material for incorporating water into the crystal structure and respectively to bigger pore sizes.

For the sake of clarity, we note that the shown **PSD** cannot directly be transferred to mortar, as it is most likely that the drying leads to different pore sizes compared to mortar. The reason is that during the first hours no robust structure building occurs, which in turn conserves the pore structure during treating the sample.

Despite the slight differences discussed in the previous paragraphs, it can be derived that (as after 60 min) the change of pores in the nanometre range along with the change of surface area is of the same order of magnitude for all three hydration stop techniques. This is an indication that all three methods indeed lead to a reaction stop. This result is supported by SEM images. Here, at higher magnifications (see Fig. 4 bottom), grains or particles of similar morphology on the sub-micron range can be found on the larger particles in all three cases. The presence of these grains, which is likely to result in a nanoscopic **PSD** (Fig. 3), is much less pronounced for the pristine sample (**CEM I**).

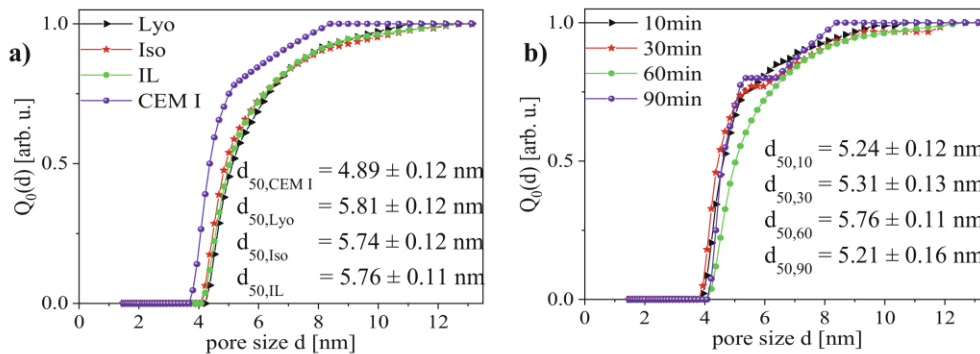


Fig. 3. N_2 -physisorption; pore size distribution of (a) hydrated CEM I stopped at 60 min compared to non-hydrated CEM I and (b) time dependent comparison of method **II**.

At lower magnification (Fig. 4 top), however, SEM analysis reveals significant differences in the sizes of larger particles. The results are quantitatively analysed by particle size distribution from these samples, see Fig. 5. The size distributions of the pristine sample (**CEM I**) and the lyophilised sample (**L**) are similar. Instead, samples treated with isopropanol (**I** and **II**) have larger particle sizes. Since the larger particles are likely to be agglomerations of smaller particles, there are two possible ways to interpret the strong difference in results upon adding or not adding isopropanol:

616 P. A. Kießling et al.

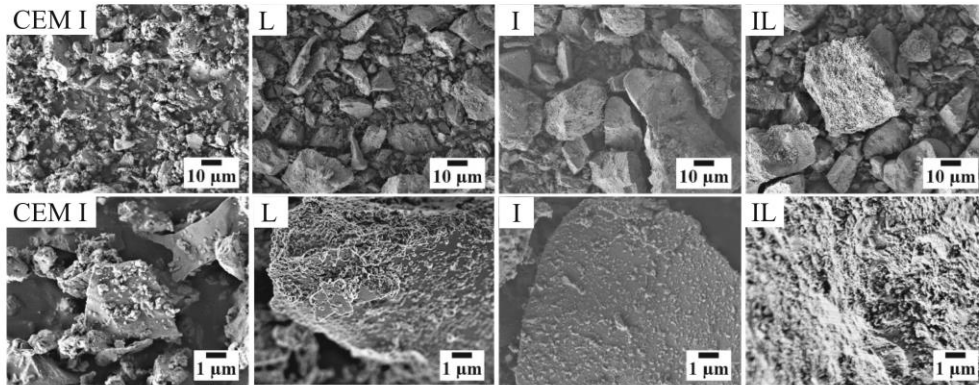


Fig. 4. SEM pictures of raw (CEM I) and hydrated cement; hydration stopped at 60 min by three different methods (L, I & IL); top row shows 1.000 times magnification and bottom row 10.000 times.

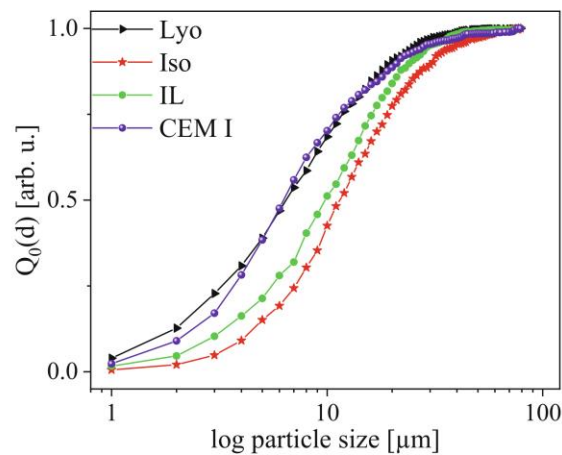


Fig. 5. Particle size distribution of hydrated CEM I stopped at 60 min using **Iso**, **Lyo** and **IL** compared to non-hydrated CEM I at low magnification.

- (1) In the lyophilisation method, likely during the freezing of the sample, particles (especially the larger, agglomerated ones) are prone to shear forces, which leads to destroying of the agglomerates. If vitreous ice is indeed formed, however, this effect is unlikely to occur, since in this case no ice crystallites would be formed and the particles should be homogenously distributed in the ice without further movement (and, therefore, the shear forces would be considered to be low). This would mean that if this reason applies, no vitreous ice but ice crystallites have been formed, which would mean that for an improved hydration quenching procedure even faster freezing conditions would have to be employed. An argument against this explanation is that, since the size distribution of the lyophilised (L) and the pristine sample (CEM I) overlap, it would mean that all agglomerates

would have been completely destroyed again using the freezing/lyophilisation method. *Id est*, both effects of agglomeration during reaction and grinding using this method would be of equal magnitude and exactly compensating each other, which we consider not very likely.

- (2) Upon adding isopropanol to the colloidal suspension, agglomeration of particles takes place. This would mean, larger particles found in Fig. 4 top might not be present prior to adding isopropanol. This would, however, point towards the direction, that the hydration stop induced via adding isopropanol can be misleading when it comes to the interpretation of certain processes during cementitious growth. An argument for reason 2 would be, that isopropanol may not dilute the cementitious dispersion and by this quenches the reaction but also may lead to reduced repulsion (likewise by change of polarity and viscosity of the liquid phase) of the dispersed particles and therefore the formation of such larger agglomerated particles.

Under the given parameter set, it is not possible to judge, which of these two explanations is the correct one. Further works, *exempli gratia* in combination with *in situ* analysis, will reveal more insight into this question.

4 Conclusion

In summary, the used hydration stop methods, namely lyophilisation of samples frozen in liquid nitrogen (**L**), isopropanol-water exchange (**I**), as well as the combination of both routes (**IL**), has a slight impact on the specific surface area, the specific volume, and the pore size distribution. By employing isopropanol (**I**), water remains in the system even after the drying procedure, which leads to an incompletely quenched hydration. For the intended time variant (kinetic) investigations of cementitious growth, this route is thus less suitable than quenching by fast freezing and lyophilisation (**IL**) or lyophilisation (**L**). Regarding the observation of microscale particle agglomerates, it still needs to be clarified whether adding isopropanol causes their presence or whether stop by lyophilisation leads to a de-agglomeration of already agglomerated particles. If the latter case would apply, the **IL** route (combination of both methods) would be the preferable route, since it would enable to nearly instantly stop the hydration process without a change in morphology and particle size distribution. If the first case would apply, it would mean that employing isopropanol could be disadvantageous for investigating the cementitious growth behaviour on the micrometre scale.

Acknowledgments. Financial support from the German Research Foundation (DFG) within the framework of SPP 2005 (BI 1708/5-1 and LO 751/26-1), as well as from the project BI 1708/4-1.

The authors thank A. Feldhoff and J. Caro for access to SEM and A. Schlosser and M. Jahns for help with nitrogen physisorption measurements.

618 P. A. Kießling et al.

References

1. Scrivener K, Bazzoni A, Mota B, Rossen JE (2015) A practical guide to microstructural analysis of cementitious materials. CRC PR INC, Boca Raton, pp 359–362
2. Dowell LG, Rinfret AP (1960) Low-temperature forms of ice as studied by x-ray diffraction. *Nature* 188:1144–1148
3. Rey L (1975) Freezing and freeze-drying. *Proc R Soc Lond B* 191:9–19
4. Brunauer S, Emmett PH, Teller E (1938) Adsorption of gases in multimolecular layers. *J Am Chem Soc* 60:309–319
5. Dreizler RM, Gross EKV (1990) Density functional theory: an approach to the quantum many-body problem. Springer, Heidelberg
6. Gelb LD, Gubbins KE, Radhakrishnan R, Sliwiska-Bartkowiak M (1999) Phase separation in confined systems. *Rep Prog Phys* 62:1573–1659
7. Barrett EP, Joyner LG, Halenda PP (1951) The determination of pore volume and area distributions in porous substances. I. Computations from nitrogen isotherms. *J Am Chem Soc* 73(1):373–380
8. Locher FW (2000) Zement - Grundlagen der Herstellung und Verwendung, Bau + Technik

3.3 INFLUENCE OF LOW-PRESSURE TREATMENT ON THE MORPHOLOGICAL AND COMPOSITIONAL STABILITY OF MICROSCOPIC ETTRINGITE

P. A. Kißling, F. Lübke, T. von Bronk, D. Cotardo, L. Lei, A. Feldhoff, L. Lohaus, M. Haist, N. C. Bigall, *Materials* (Basel). 14, **2021**, 2720.
<https://doi.org/https://doi.org/10.3390/ma14112720>.



Article

Influence of Low-Pressure Treatment on the Morphological and Compositional Stability of Microscopic Ettringite

Patrick A. Kißling ¹, Franziska Lübkeermann ¹, Tabea von Bronk ², Dario Cotardo ², Lei Lei ³, Armin Feldhoff ¹, Ludger Lohaus ², Michael Haist ² and Nadja C. Bigall ^{1,*}

- ¹ Institute of Physical Chemistry and Electrochemistry, Leibniz Universität Hannover, 30167 Hanover, Germany; patrick.kissling@pci.uni-hannover.de (P.A.K.); franziska.luebkeermann@pci.uni-hannover.de (F.L.); armin.feldhoff@pci.uni-hannover.de (A.F.)
- ² Institute of Building Materials Science, Leibniz Universität Hannover, 30167 Hanover, Germany; t.von-bronk@baustoff.uni-hannover.de (T.v.B.); d.cotardo@baustoff.uni-hannover.de (D.C.); lohaus@baustoff.uni-hannover.de (L.L.); haist@baustoff.uni-hannover.de (M.H.)
- ³ Chair for Construction Chemistry, Technische Universität München, 85747 Munich, Germany; lei.lei@bauchemie.ch.tum.de
- * Correspondence: nadja.bigall@pci.uni-hannover.de; Tel.: +49-511-762-14439



Citation: Kißling, P.A.; Lübkeermann, F.; von Bronk, T.; Cotardo, D.; Lei, L.; Feldhoff, A.; Lohaus, L.; Haist, M.; Bigall, N.C. Influence of Low-Pressure Treatment on the Morphological and Compositional Stability of Microscopic Ettringite. *Materials* **2021**, *14*, 2720. <https://doi.org/10.3390/ma14112720>

Academic Editors: Jose Antonio Alonso and Daniela Kovacheva

Received: 24 March 2021

Accepted: 17 May 2021

Published: 21 May 2021

Publisher's Note: MDPI stays neutral with regard to jurisdictional claims in published maps and institutional affiliations.



Copyright: © 2021 by the authors. Licensee MDPI, Basel, Switzerland. This article is an open access article distributed under the terms and conditions of the Creative Commons Attribution (CC BY) license (<https://creativecommons.org/licenses/by/4.0/>).

Abstract: The impact of low-pressure treatment on the crystal structure, morphology, and chemical composition of ettringite, due to their major importance with respect to processability (i.e., drying conditions) and to the analysis of ettringite-containing samples, is examined utilizing X-ray diffraction, thermogravimetric analysis, Raman spectroscopy, and environmental scanning electron microscopy. Synthetic ettringite was treated for various durations (5 min up to 72 h) and at two different levels of low-pressure (4.0 mbar and 60 µbar). Evaluation showed a correlation between the procedural parameters (time and pressure), the chemical composition, and the morphology of ettringite. The experiments reveal that, when exposed to 4 mbar pressure, nearly no changes occur in the ettringite's morphology, whereas the crystals undergo swelling and slight deformations at very low pressures (60 µbar and 35.3 nbar), which is attributed to the loss of bound water and the partial transformation from ettringite to quicklime, anhydrite, and calcium aluminate. Furthermore, the strongly dehydrated ettringite shows the same morphology.

Keywords: morphology; chemical composition; ettringite; low-pressure; Pawley fit

1. Introduction

Ettringite ($\text{Ca}_6\text{Al}_2(\text{SO}_4)_3(\text{OH})_{12}\cdot 26\text{H}_2\text{O}$) is formed as small needle-shaped crystals on the surface of cement particles during the early stages of hydration [1–6] and thus is of significant technical importance, as it influences the rheological properties of fresh cement suspensions. Furthermore, ettringite is used as white pigment in paper production [7,8] or for high-coverage emulsion wall paints [1]. Previous works proved that the crystal structure of ettringite consists of dodecahedrally coordinated calcium ions and octahedrally coordinated aluminium ions forming face-linked hexagonal prisms along the c-axis [1,9–11] (Figure S1). The pioneering works of Skoblinskaya et al. revealed prominent changes in the crystal structure: a shrinkage in the cell parameters at different hydration stages using isobar treatment at 8.0 µbar in a range of 25 °C to 325 °C was observed [5,6]. Within their study, four different types of water (adsorption sites) were identified in the ettringite structure [5,6]. Additionally, characterizations of the changes in ettringite's crystal structure were performed after the treatment at ambient pressure in a range of 25 °C to 200 °C for up to 7 h [12]. The above-mentioned works have already demonstrated that the bound crystal water of ettringite can be effectively removed by low-pressure or elevated temperatures. Nevertheless, a set of parameters where the original crystal structure of ettringite can be preserved upon the removal of adsorbed water is still sought after. To the best of our

knowledge, no systematic study has investigated the impact of different levels (4 mbar, 60 μ bar, and 35.3 nbar) of low-pressure yet. Due to widely used characterization techniques and processing conditions, as well as the investigation of growth kinetics, the stability of the crystal structure and morphology under low-pressure treatment is of paramount importance. In particular, high performance imaging techniques, such as transmission electron microscopy (TEM) or scanning electron microscopy (SEM), require high-vacuum treatment (0.9 nbar or 35.3 nbar). This, in turn, raises the question of which techniques are suitable for the noninvasive and nondestructive analysis of ettringite's crystallinity, chemical composition, and morphology, which are relevant, e.g., for the properties of cementitious suspensions [3,13–18].

This article documents a study of the chemical composition, crystallinity, and morphology of synthetic ettringite depending on the level (4 mbar, 60 μ bar, and 35.3 nbar) and the duration (up to 72 h) of low-pressure treatment to which the sample was exposed. X-ray diffraction analysis (XRD) was used to gain insight into the stability of the crystals under the various pressure conditions, while the cell parameters were investigated by employing the Pawley fit method [19]. The bound water content was evaluated by thermogravimetric analysis (TGA) as well as Raman spectroscopy (Raman) to distinguish between hydroxide groups and bound water while giving insight into the chemical composition. Scanning transmission electron microscopy coupled with energy-dispersive X-ray spectroscopy (STEM-EDXS) was used to clarify the chemical composition of the fully dehydrated sample. To identify the degree of crystallinity of the strongly dehydrated ettringite, selected area electron diffraction (SAED) was employed. The morphology of ettringite was investigated by environmental scanning electron microscopy (ESEM). Through time-dependent measurements with the characterization techniques mentioned above, the chemical, crystallographic, and morphological stability of ettringite at various levels of low-pressure was examined.

2. Materials and Methods

2.1. Materials

The main materials for this study were CASUL[®] H1i from Remondis, aluminium sulphate octadecahydrate ($\geq 98\%$) from Carl Roth, calcium hydroxide ($\geq 95\%$) from Sigma-Aldrich, Millipore water (18.2 M Ω -cm) cleaned by an Arium 611DI from Sartorius GmbH & Co. KG, Goettingen, Germany (in the following referred to as water), and liquid nitrogen ($\geq 99.999\%$) from Linde. As an internal standard for XRD measurements, silicon (97.5%) from Riedel-de Haën was used. The synthetic ettringite was stored at inert conditions (25 °C, 1.015 bar, Ar atmosphere) for the whole study.

2.2. Methods

2.2.1. Synthesis of Ettringite

Following Struble et al. [20], a solution of aluminium sulphate octadecahydrate [$\text{Al}_2(\text{SO}_4)_3 \cdot 18\text{H}_2\text{O}$, 38.3 mM, 1 Veq.] and a saturated solution of calcium hydroxide [$\text{Ca}(\text{OH})_2$, 10 Veq.] in water were prepared. The alkaline solution was filtrated using a Buchner funnel with a glass fibre filter (retention 0.4 μm , $d = 125$ mm; MN-GF 5 by Macherey-Nagel GmbH, Co. KG, Dueren, Germany). Both solutions were mixed quickly (30 s) under vigorous stirring (500 rpm, Hei-Torque Precision 400 by Heidolph Instruments GmbH, Co. KG; anchor AR 19 PTFE, $d_{\text{shaft}} = 8$ mm). Instantaneous precipitation of ettringite was evident from the solution turning turbid. After centrifugation (60 min, 10,000 G, Sigma 3-18KS, 20 °C), the precipitate was decanted. To remove the adsorbed water, or rather remaining reaction medium, with neither phase transition (25 °C, 1.015 bar) nor the formation of lime [CaCO_3] (Ar atmosphere), the precipitate was dried in a vacuum furnace (Vakuumschrank VO29 by Memmert GmbH + Co. KG, Büchenbach, Germany) for 24 h at the aforementioned ambient and inert conditions.

2.2.2. Influence of Low Pressure

To assess the influence of low-pressure on the morphology and chemical composition of ettringite, various durations (5 min up to 72 h) and levels of pressure (4.0 mbar, 60 μ bar, and 2.8 nbar) were applied. These levels of pressure were chosen as 4.0 mbar, which is near the triple point of water (6.1 mbar) [21,22], 60 μ bar, the standard pressure of freeze-drying devices, and 2.8 nbar, a common pressure during scanning electron microscopy. For achieving different pressure values (4 mbar and 60 mbar), a freeze-dryer (Alpha 1-2 LDplus by Martin Christ Gefriertrocknungsanlagen GmbH) coupled with a two-stage rotary vane pump (RV 3F by Edwards Vacuum) was used. A high vacuum (2.8 nbar) was realized in the antechamber of the scanning electron microscope Zeiss Supra VP 55. Each treatment was performed on a different sample taken out of the same batch.

2.2.3. X-ray Diffraction and Pawley fit

The crystallinity was investigated by X-ray diffraction (XRD) using a Bruker D8 Advance in reflection mode. It was operated at 20 °C, 40 kV, and 40 mA using Cu-K α radiation. Each measurement was done 30 min after the low-pressure treatment in a 2 θ range from 5° to 70° with a step size of 0.006571365° and 4 s per step, resulting in a total measurement time of 7.25 h. The powder of each sample was transferred into an X-ray amorphous PVC powder carrier and smoothed to ensure no sample displacement. To guarantee that the shift of the reflections in the XRD was not caused by a sample displacement error in the preparation, 2.2 wt% (11 mg) silicon was added as an internal standard. The diffraction patterns were evaluated by the database of the Powder Diffraction File (PDF-2) 2020 of the International Centre for Diffraction Data (ICDD).

Furthermore, the cell parameters were analysed with a Pawley fit [19] using the data provided by Hartman et al. [23], the measured XRD data of this work, and the software TOPASv6 by Bruker.

2.2.4. Thermogravimetric Analysis

To evaluate the content of bound water, which accounts for 46% of the molar mass of ettringite and is responsible for the stability of its crystal structure, any synthesized or dried sample was investigated by thermogravimetric analysis (TGA) using a TGA/DSC 3+ from Mettler-Toledo GmbH. The samples were transferred into aluminium oxide crucibles (70 μ L) before measurement. It was operated in a temperature range from 20 °C to 1100 °C under a nitrogen flow of 25 mL/min and a heating ramp of 5 °C/min, followed by holding the temperature at 1100 °C for 15 min. The data was normalized by mass (mg), derived once by time (s), multiplied by 3600 (for plotting in h), and plotted against temperature (°C).

2.2.5. Quick Assessment of Mass Loss

For an assessment of mass loss of ettringite after the treatment for various durations (5 min up to 72 h) and different levels of pressure (4.0 mbar and 60 μ bar), a balance Praxium224-1S from Sartorius GmbH & Co. KG was used before and after treatment (Figures S2 and S3, Tables S1 and S2).

2.2.6. Environmental Scanning Electron Microscopy

To reassess the results about the morphology of ettringite derived from the Pawley fit, environmental scanning electron microscopy (ESEM) using a Zeiss Supra VP 55 equipped with a cold field emission gun and a 4-quadrant backscatter electron detector (QBSD) was implemented as an imaging method. The acceleration voltage was 10 kV, the current 6 nA, and variable pressure 1.0 mbar and 60 μ bar for each measurement. The powder was transferred onto an adhesive carbon disk and was cleaned of excess sample with a compressed air gun. Each sample was degassed in the antechamber for 2.5 min for safety reasons. At a pressure of 375 nbar in the antechamber, the “variable pressure” mode was started. For the investigation of the influence of the electron beam during the micrograph

acquisition on the morphology, the treatment at 0.5 mbar and 10,000 times magnification was recorded for 2.2 min (Section 3.2.3).

2.2.7. Scanning Electron Microscopy

For the scanning electron microscopy (SEM) (Carl Zeiss AG, Oberkochen, Baden-Württemberg, Germany), a Zeiss Supra VP 55 equipped with a cold field emission gun and a 4-quadrant backscatter electron detector (QBSD) was used as an imaging method. The acceleration voltage was 10 kV, the current 6 nA, and the pressure 375 nbar for each measurement. The powder was transferred on an adhesive carbon disk and was cleaned of excess sample with a compressed air gun. Each sample was degassed in the antechamber for 2.5 min for safety reasons.

2.2.8. Raman Spectroscopy

To distinguish the bound water and hydroxide in the crystal structure of ettringite, further structural analysis was performed by Raman spectroscopy (Bruker Corporation, Billerica, MA, USA) using a Bruker Senterra Raman spectrometer equipped with an Olympus LMPlanFl N 50x lens with the FlexFocus™ system for confocal depth profiling and an ANDOR DU420-OE with a thermoelectric cooling system as a charge-coupled device (CCD). The green laser ($\lambda = 532$ nm) was operated with a total power of 20 mW and a spectral resolution of 3 cm^{-1} to 5 cm^{-1} . Each spectra was collected with an acquisition time of 5 s per scan, merging five consecutive scans in a range of 50 cm^{-1} to 1555 cm^{-1} , 1522 cm^{-1} to 2739 cm^{-1} , and 2705 cm^{-1} to 3705 cm^{-1} . The grating calibration was controlled by checking the position of the Raman line of a Si standard at 519.9 cm^{-1} [24]. The samples were transferred as powder on a glass slide.

2.2.9. Transmission Electron Microscopy and Energy-Dispersive X-ray Spectroscopy

The local distribution of elements before and after the treatment of ettringite at $60\text{ }\mu\text{bar}$ for 48 h was investigated by scanning transmission electron microscopy (JEOL Ltd., Tokyo, Japan) coupled with energy-dispersive X-ray spectroscopy (STEM-EDXS) using a JEOL JEM-2100F-UHR ($C_s = 0.5$ mm and $C_C = 0.5$ mm) equipped with a field-emission gun. The acceleration voltage was 200 kV and the pressure 0.9 nbar for each measurement. Prior to EDXS, micrographs were taken in high angle annular dark-field (HAADF) scanning transmission electron (STEM) mode. The powder was transferred on a carbon coated copper TEM grid.

2.2.10. Selected Area Electron Diffraction

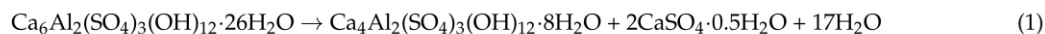
The zone axis pattern before and after the treatment of ettringite at $60\text{ }\mu\text{bar}$ for 48 h was investigated by selected area electron diffraction (SAED) (JEOL Ltd., Tokyo, Japan) using a JEOL JEM-2100F-UHR ($C_s = 0.5$ mm and $C_C = 0.5$ mm) equipped with a field-emission gun. The acceleration voltage was 200 kV and pressure 0.9 nbar for each measurement, and all samples were transferred as powder on a carbon coated copper TEM grid.

3. Results and Discussion

3.1. Synthetic Ettringite

The synthetic colourless powder was analysed using XRD and TGA and thus was proven to be ettringite $[\text{Ca}_6\text{Al}_2(\text{SO}_4)_3(\text{OH})_{12}\cdot 26\text{H}_2\text{O}]$. Figure 1a shows the diffractogram comparing the measured 2θ data with its most prominent reflections ($I_{\text{reflection}} > 0.1 I_{\text{max}}$) in the angle range of $7.5^\circ \leq 2\theta \leq 51^\circ$ [23], which align with the data by Hartman et al. [23]. Both discrepancies in the intensity of the reflections at $2\theta = 32.03^\circ$ and $2\theta = 34.84^\circ$ compared with the literature are most likely induced by the faceting of the crystals. This is especially prominent for the reflection at $2\theta = 34.84^\circ$, due to two different underlying crystal planes ($(10\bar{1}8)$ and $(30\bar{3}5)$) [23], which are given by their Bravais–Miller indices according to a trigonal symmetry in a hexagonal cell. In the TGA measurement depicted in Figure 1b, a large mass loss of 34.62% can be seen between 50°C and 210°C . This is at-

tributed to the decomposition of ettringite to calcium aluminate monosulphate [AFm-14H; $\text{Ca}_4\text{Al}_2(\text{SO}_4)_3(\text{OH})_{12}\cdot 8\text{H}_2\text{O}$] and basanite [$\text{CaSO}_4\cdot 0.5\text{H}_2\text{O}$], as described by Hall et al. [25], see Equation (1):



Further dehydration of basanite at $225\text{ }^\circ\text{C} \pm 25\text{ }^\circ\text{C}$ and dehydration of AFm-14H at $775\text{ }^\circ\text{C} \pm 125\text{ }^\circ\text{C}$ are visible. At $900\text{ }^\circ\text{C}$ ettringite is fully decomposed to quicklime [CaO], anhydrite [CaSO_4], and calcium aluminate [$(\text{CaO})_x(\text{Al}_2\text{O}_3)_y$] [26–28]. The total mass loss of 46.41% matches with the bound water content of ettringite.

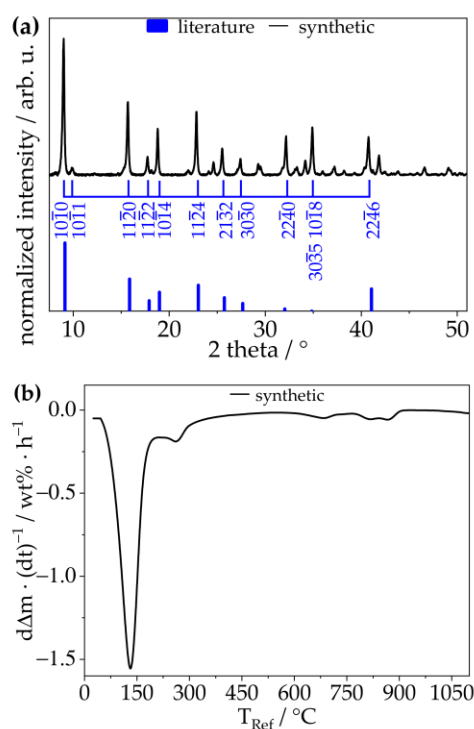


Figure 1. (a) Powder X-ray diffraction pattern of synthetic ettringite (black) and its literature data reflections (blue) [9,23] indexed using Bravais–Miller indices according to a trigonal symmetry in a hexagonal cell and (b) TGA data plotted as mass normalized time derived weight loss ($d\Delta m \cdot (dt)^{-1}$) per hour against the reference temperature of synthetic ettringite with a heating rate of $5\text{ }^\circ\text{C}/\text{min}$.

In addition, STEM-EDXS measurements were recorded from different sites to analyse the chemical composition of the pristine ettringite. The STEM micrographs showed a needle-like shape of the as-synthesized ettringite (Figure 2a) and residues of the unreacted precursor [$\text{Al}_2(\text{SO}_4)_3\cdot 18\text{H}_2\text{O}$ and $\text{Ca}(\text{OH})_2$] (Figure 2b). The corresponding STEM-EDXS analysis showed an elemental distribution and elemental stoichiometric ratio indicating ettringite and residues of unreacted precursor (Figure 2).

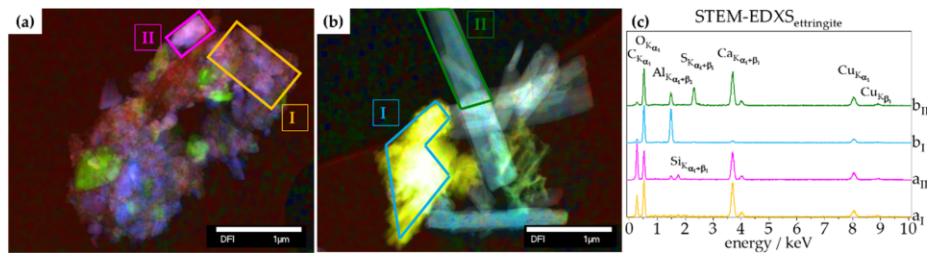


Figure 2. STEM micrographs of pristine ettringite (a,b) sites of EDXS and (c) corresponding STEM-EDXS spectra of different sites.

3.2. Treatment of Ettringite with Low-Pressure

The synthetic ettringite was exposed to different low-pressure values, as described in Section 2.2. To analyse the influence of low pressure on the crystal structure, morphology, and chemical composition of ettringite, three different aspects are considered. First, the chemical composition of ettringite after different durations and levels of exposure to low-pressure is characterized by TGA, XRD, Raman, and STEM-EDXS (Section 3.2.1). Second, changes of cell parameters are assessed by SAED and the Pawley fit of the measured XRD data (Section 3.2.2). Third, the ettringite's crystal morphology is analysed by SEM and ESEM (Section 3.2.3).

3.2.1. Chemical Composition—TGA, XRD, Raman, STEM-EDXS

The depletion of the bound water induced by different pressure treatments was investigated by TGA measurements (Figure 3). The change of chemical composition by depletion of water is shown by the decrease of the first peak at $130\text{ °C} \pm 80\text{ °C}$, which correlates to the main decomposition of ettringite (Equation (1)). At 4 mbar, the main decomposition peak shrinks almost linear over 72 h by an amount of 9.4%. At 60 μbar , the same degree of alteration is already reached after 30 min (Figures S4 and S5, and Table S3). At both stages the theoretical ettringite composition should have changed from $\text{Ca}_6\text{Al}_2(\text{SO}_4)_3(\text{OH})_{12} \cdot 26\text{H}_2\text{O}$ to $\text{Ca}_6\text{Al}_2(\text{SO}_4)_3(\text{OH})_{10.8} \cdot 23.4\text{H}_2\text{O}$. Following from this, lower pressure seems to destroy ettringite more quickly. It is also remarkable that the range of the complete dehydration of AFm-14H at $775\text{ °C} \pm 125\text{ °C}$ becomes a single peak at $730\text{ °C} \pm 60\text{ °C}$, and both ranges have the same integral. This change appears after 72 h at 4 mbar and already after 6 h at 60 μbar . Furthermore, at 60 μbar , the decrease of ettringite's main decomposition peak is not linear but rather follows an exponential decay until 36 h (Figure S5 and Table S3). In the last 12 h of the treatment with low pressure, the remaining 20% of ettringite is destroyed, since the main decomposition peak at $130\text{ °C} \pm 80\text{ °C}$ disappears.

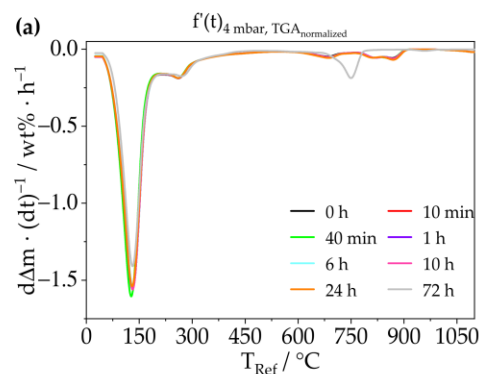


Figure 3. Cont.

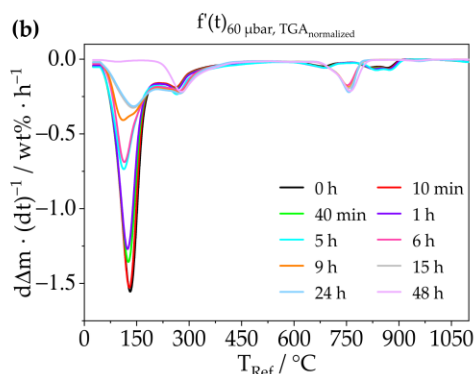


Figure 3. TGA data plotted as mass normalized time derived weight loss ($d\Delta m \cdot (dt)^{-1}$) per hour against the reference temperature of synthetic ettringite with a heating rate of $5\text{ }^{\circ}\text{C}/\text{min}$ after treatment at two different levels of low pressure (a) 4 mbar and (b) $60\text{ }\mu\text{bar}$ for various durations (up to 72 h); full time frame depicted in Figure S4.

Many temperature studies suggested that the dehydration of ettringite leads to a change of its crystal structure [5,6,29–31]. Treatment with different levels of low-pressure for various durations changes the chemical compositions as well as the characteristic XRD pattern of ettringite. The XRD patterns of low-pressure treated samples are shown in Figure 4. At 4 mbar, the reflection $10\bar{1}0$, originating mainly from bound water, especially begins to broaden [5,6,12,29–31]. This behaviour can be caused either by shrinking crystallite sizes or by defects in the crystal structure and, in our case, is most probably attributable to dehydration. At the lower pressure of $60\text{ }\mu\text{bar}$, the broadened reflections lose intensity over time until after 9 h, the intensity of reflection $10\bar{1}0$ is equal to reflection $10\bar{1}2$, with an intensity of 2.5% relative to pristine ettringite. After 12 h, reflection $10\bar{1}0$ is ultimately eliminated. Over the following 36 h, nearly all reflections are diminished, as either the structure of ettringite is destroyed or the remaining ettringite becomes X-ray amorphous [5,6,12].

When comparing TGA and XRD results, there seems to be an interdependency between the aforementioned decomposition peak in the TGA at $730\text{ }^{\circ}\text{C} \pm 60\text{ }^{\circ}\text{C}$ and the reflection in the XRD at 29° after 6 h at $60\text{ }\mu\text{bar}$ (Figure 4). The corresponding phase is indexed as CaCO_3 , which forms over time due to carbon dioxide in the air [12,32,33], see Equation (2):



To identify whether the removal of water delineated by TGA and XRD was induced by the removal of hydroxide groups or bound water, Raman was used as a complementary structural method. This technique shows that the stretching vibrations of the hydroxide groups ($3644.0\text{ cm}^{-1} \pm 42.0\text{ cm}^{-1}$) are preserved in both cases, but the stretching bands of the bound water ($3444.8\text{ cm}^{-1} \pm 102.8\text{ cm}^{-1}$) [24,34] disappear after 48 h at $60\text{ }\mu\text{bar}$ (Figure 5). Hence, it is clear that the bound water of ettringite was fully extracted after 48 h at $60\text{ }\mu\text{bar}$. The full assignment of the characteristic bands of vibrations of pristine ettringite and of the treated samples is shown in Table S4.

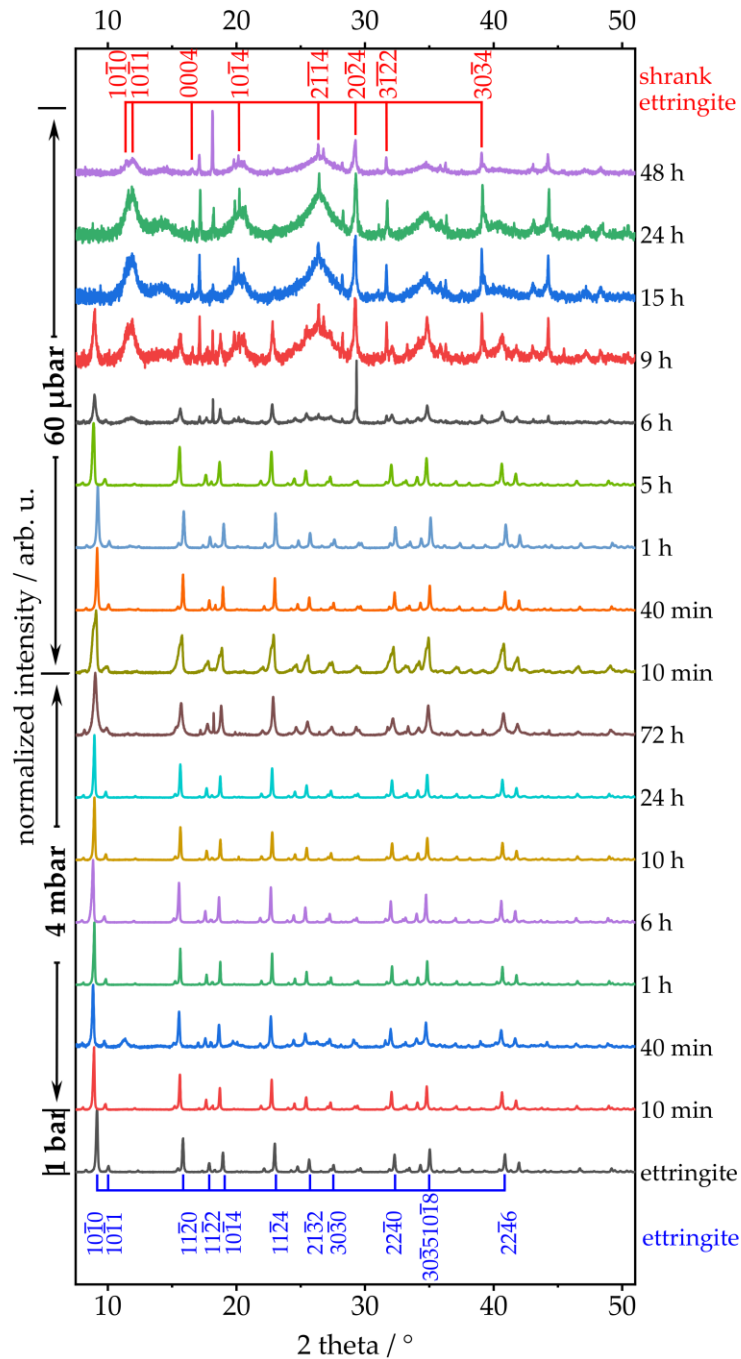


Figure 4. Identification of ettringite reflections (blue) and shrank ettringite (red) in the diffraction pattern of synthetic ettringite; after treatment at two different levels of low pressure (4 mbar and 60 μbar) for various durations (up to 72 h), each treatment was performed on a different sample from the same batch. Bravais–Miller indices are given according to a trigonal symmetry in a hexagonal cell; full time frame depicted in Figure S6.

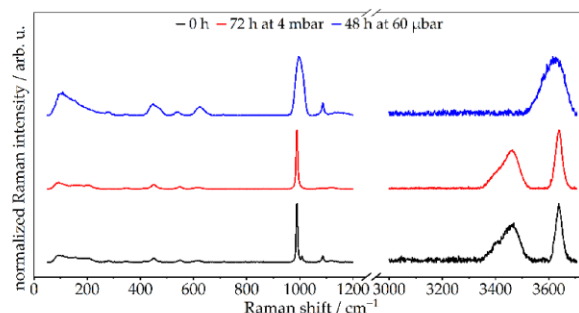


Figure 5. Raman spectra of pristine synthetic ettringite and treated ettringite after treatment at two different levels of low pressure (4 mbar for 72 h and 60 μ bar for 48 h).

To link the XRD of fully dehydrated ettringite (after treatment at 60 μ bar for 48 h) with the results of TGA and Raman, scanning transmission electron microscopy coupled with energy-dispersive X-ray spectroscopy (STEM-EDXS) was employed. This performed high-vacuum treatment (0.9 nbar) had no effect on the morphology, as the sample was already fully dehydrated. Combining these results with the elemental distribution and elemental stoichiometric ratio derived from STEM-EDXS, the following compounds could be indicated as the most probable dehydration products of ettringite: CaCO_3 , Al_2O_3 , CaSO_4 , CaO , $(\text{CaO})_x(\text{Al}_2\text{O}_3)_y$. Apart from Al_2O_3 , all of these phases are found in the XRD of retrogressed ettringite (Figure 6f). The unidentified reflections did not match with reflections from the PDF-2 2020 database of ICDD. Based on the needle-like shape (Figure 6b) and an elemental distribution similar to pristine ettringite (Figure 2), as well as the fact that after dehydration, the zone axes were found to be exactly half compared to pristine ettringite, it is assumed that the unidentified reflections in XRD belong to ettringite with different cell parameters (Figure 7).

In summary, TGA showed the expected decomposition of ettringite (Equation (1)) as well as a correlation between bound water content and vacuum treatment conditions. Furthermore, Raman spectroscopy showed that the bound water of ettringite is extracted first. By applying 4 mbar, ettringite loses linearly up to 6.6 wt% of bound water after 72 h of treatment. By a lower pressure of 60 μ bar, this extraction is faster, as after 20 min, 5.8 wt% of bound water is extracted, and follows an exponential decay. XRD analysis also shows a retrogression of ettringite's diffraction pattern, wherein the process for 4 mbar is barely visible compared to 60 μ bar being distinctive. STEM-EDXS analysis confirmed ettringite's chemical composition and needle-like shape (Figure 2). It was respectively shown that, as indicated by TGA and XRD, CaCO_3 is formed over time during the treatment of ettringite with low-pressure (Figure 2a). Furthermore, this technique indicates that, aligning with the known phases after a complete decomposition of ettringite [26–28], CaCO_3 , Al_2O_3 , CaSO_4 , CaO , and $(\text{CaO})_x(\text{Al}_2\text{O}_3)_y$ are the most probable retrogressed phases of ettringite.

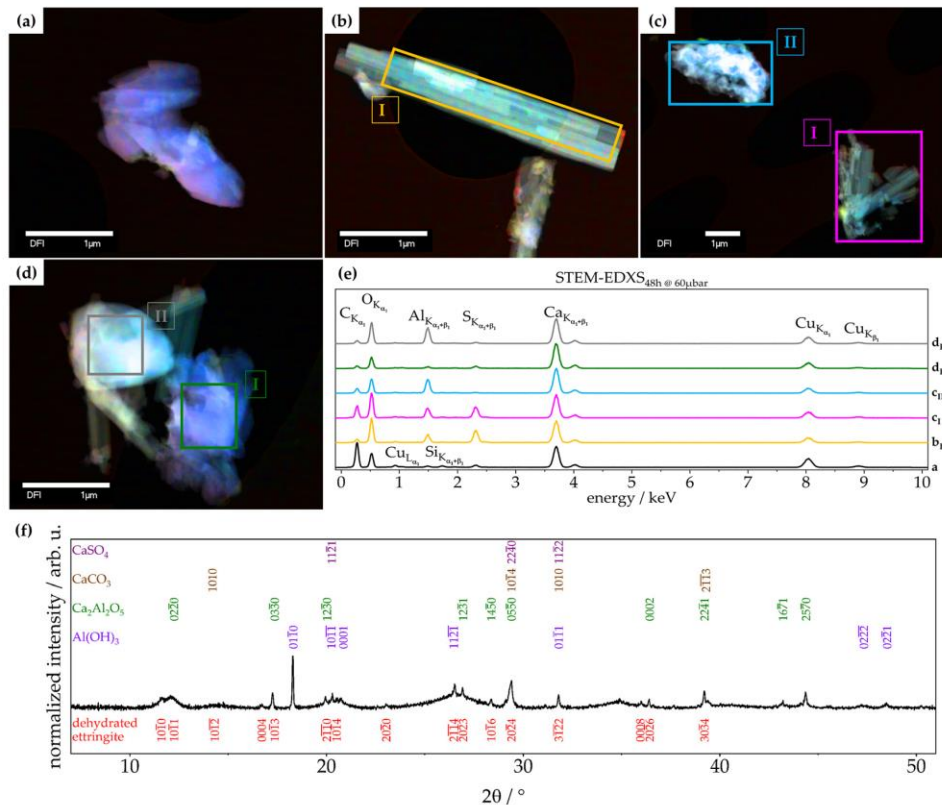
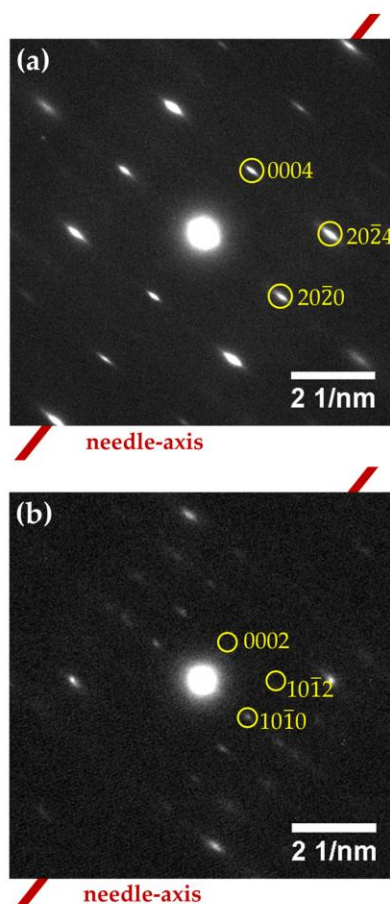


Figure 6. STEM micrograph of ettringite treated at 60 μ bar for 48 h; (a–d) sites of EDXS and (e) STEM-EDXS spectra of different sites; (f) X-ray diffractogram showing identified phases of retrogressed ettringite after treatment at 60 μ bar for 48 h; CaCO_3 [35], $\text{Ca}_2\text{Al}_2\text{O}_5$ [36], $\text{Al}(\text{OH})_3$ [37], and CaSO_4 [38].

3.2.2. Crystallographic Assessment—SAED, Pawley fit

TEM-based selected area electron diffraction (SAED) of pristine ettringite and retrogressed ettringite after a treatment of 48 h at 60 μ bar was employed. This technique proves the crystallinity in both cases but reveals differences in the $[10\bar{1}0]$ zone axis pattern (Figure 7). In the TEM vacuum (0.9 nbar), pristine ettringite has become elongated by about 0.7% along the c-axis ($1.007 c_0$) but shrinks at about 14.7% in directions perpendicular to the c-axis ($0.853 a_0$). This elongation of the reflection spots is perpendicular to the c-axis—in this case, also the needle-axis—which hints at disorder in this direction, due to partial dehydration under these harsh conditions (Figure 7a). The strongly dehydrated ettringite (Figure 7b) shrank by about 6.2% along the c-axis ($0.938 c_0$) and by about 25.5% in directions perpendicular to the c-axis ($0.745 a_0$), relative to the results shown by Hartman et al. [23]. This pronounced shrinkage seems reasonable and has been reported by Skoblinkaya et al. [5,6].

The fact that after dehydration the needle-like shape of ettringite is retained (Figure 6b), as well as the zone axes found to be exactly half compared to pristine ettringite, leads to the assumption that the unidentified reflections in XRD belong to ettringite with different cell parameters (Figure 7).



(c)	Literature [23] / Å	Ettringite 0 h / Å	48 h at 60 μbar / Å
c	21.35	21.496 = 4 × 5.374	20.1 = 2 × 10.05
a = b	11.16	9.723 = 2 d ₂₀₂₀ / cos (30°)	8.313 = 2 d ₁₀₁₀ / cos (30°)
d ₂₀₂₀	4.833	4.21	---
d ₁₀₁₀	9.665	---	7.2

Figure 7. SAED micrographs of ettringite; 200 kV, 50,000 times magnification; (a) 550 nm selected circular area on pristine ettringite; (b) 250 nm selected circular area on dehydrated ettringite after a treatment of 48 h at 60 μbar; [10 $\bar{1}$ 0] zone axis; Bravais–Miller indices of both patterns are indexed according to a hexagonal unit cell; and (c) cell parameters derived from TEM-based SAED of pristine ettringite and ettringite treated at 60 μbar for 48 h compared to data by Hartman et al. [23].

The changes to crystal structure as described in the section above are further investigated by applying the Pawley fit [19] on the diffraction patterns of ettringite after treatment at two different levels of low pressure (4 mbar and 60 μbar) for various durations (up to 72 h). The Pawley fit was chosen to assess changes to ettringite's cell parameters, as there is no model to describe the occupation of lattice sites of the bound water molecules at the different stages of the dehydration process of ettringite, which is essential for Rietveld refinement. For pristine ettringite, the cell parameters $a_0 = 11.24$ Å, $c_0 = 21.48$ Å and volume $V_0 = 2351$ Å³ are in perfect accordance with the literature [5,6,9,23]. At 4 mbar, cell parameter a remains at 11.24 Å \pm 0.004 Å ($0.9998 a_0 \pm 0.0003 a_0$), and cell parameter c remains at 21.46 Å \pm 0.007 Å ($0.9993 c_0 \pm 0.0003 c_0$) over the whole treatment period

of 72 h (Figure 8 and Table S5). Although the reported shrinkage of cell parameter c is different, the calculated data show a good accordance to Shimada et al. [12].

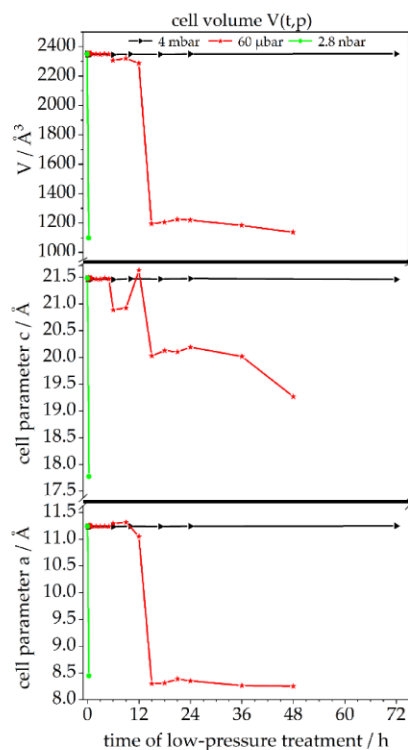


Figure 8. Cell parameters a and c and cell volume V derived from Pawley fits of powder XRD data; retrogression of the cell of synthetic ettringite after treatment at three different levels of low pressure (4 mbar: black; 60 μ bar: red; 2.8 nbar: green) for various durations (up to 72 h).

The treatment of ettringite at 60 μ bar exposes different stages. For the first 5 h, cell parameter a remains at $11.24 \text{ \AA} \pm 0.004 \text{ \AA}$ ($1.0001 a_0 \pm 0.0004 a_0$), and cell parameter c remains at $21.47 \text{ \AA} \pm 0.01 \text{ \AA}$ ($0.9998 c_0 \pm 0.0004 c_0$). Additional treatment for 4 h (total 9 h at 60 μ bar) leads to an expansion of cell parameter a to $11.30 \text{ \AA} \pm 0.01 \text{ \AA}$ ($1.006 a_0 \pm 0.0015 a_0$) and a shrinkage of cell parameter c to $20.91 \text{ \AA} \pm 0.03 \text{ \AA}$ ($0.9734 c_0 \pm 0.0012 c_0$). After 12 h of treatment, both cell parameters show shrinkage to cell parameter $a = 11.05 \text{ \AA}$ ($0.983 a_0$) and cell parameter $c = 20.63 \text{ \AA}$ ($0.96 c_0$). The last dehydration step seems to occur between 12 h and 15 h. Afterwards, cell parameter $a = 8.31 \text{ \AA} \pm 0.05 \text{ \AA}$ ($0.74 a_0 \pm 0.01 a_0$) and cell parameter $c_0 = 19.96 \text{ \AA} \pm 0.34 \text{ \AA}$ ($0.93 c_0 \pm 0.02 c_0$) remain stable for at least 33 h (total 48 h at 60 μ bar). A correlation between the maximum retrogressed cell parameters of ettringite's crystal structure, TGA, and Raman spectroscopy is depicted in Figure S7. The sensitivity of ettringite to very low-pressure conditions is investigated via scanning electron microscopy (SEM) operating at a pressure of 2.8 nbar, which, according to previous investigation, should lead to a very strong dehydration and fast transformation. A treatment of 20 min in the antechamber is, according to the Pawley fit, sufficient to deform the original crystal structure of ettringite, which can be derived from Figure 8 and Table S6. The deformation of the needle-like shape particles within the SEM measurement is shown in Figure S8. Hence, a condition for the imaging analysis of the morphology of ettringite is a working pressure as high as possible. Therefore, environmental SEM (ESEM) is an adequate imaging method, as the working pressure is 1.0 mbar. Micrographs obtained by ESEM at 1.0 mbar are not as high resolution as normal SEM micrographs achieved in a

high vacuum but can depict the morphology of ettringite without changing the chemical composition due to low pressure.

3.2.3. Morphology—SEM, ESEM

After treatment at two different levels of low pressure (4 mbar and 60 μ bar) for various duration (72 h and 48 h), the ettringite needle-shaped particles were investigated via environmental scanning electron microscopy (ESEM) (Figure 9a–c). Pristine ettringite crystals have a mean length of $l_{50} = 1.59 \mu\text{m} \pm 0.67 \mu\text{m}$, a mean width of $w_{50} = 0.36 \mu\text{m} \pm 0.17 \mu\text{m}$, and an aspect ratio of $AR = 6.6 \pm 4.9$. These values shift to a more homogenous distribution after 72 h at 4 mbar with $l_{50} = 1.38 \mu\text{m} \pm 0.49 \mu\text{m}$, $w_{50} = 0.30 \mu\text{m} \pm 0.14 \mu\text{m}$, and $AR = 7.0 \pm 5.0$. By changing the parameters to 48 h at 60 μ bar, the crystals shrunk to $l_{50} = 1.13 \mu\text{m} \pm 0.38 \mu\text{m}$, $w_{50} = 0.27 \mu\text{m} \pm 0.11 \mu\text{m}$, and $AR = 5.6 \pm 3.6$ (Figure 9d,e).

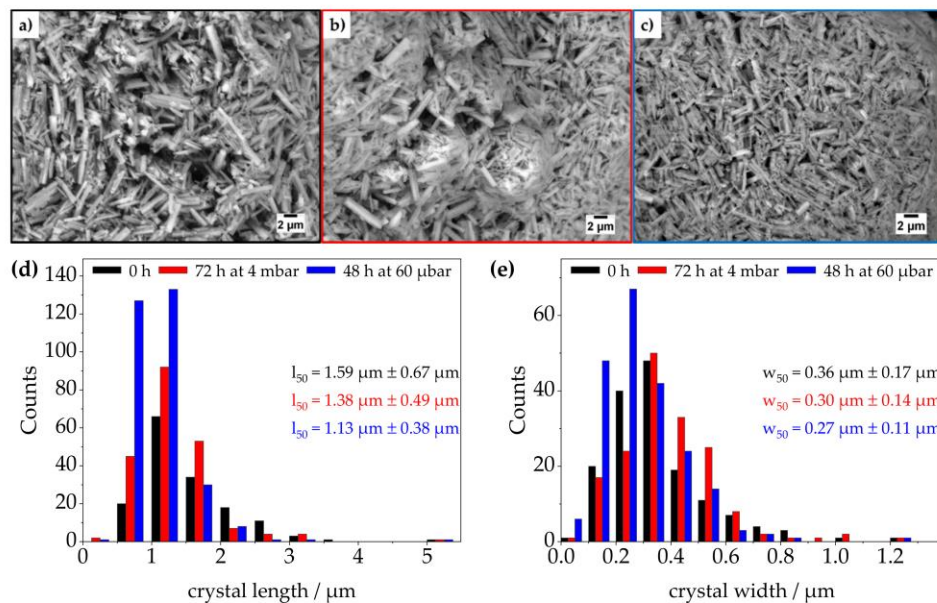


Figure 9. ESEM micrographs of (a) pristine synthetic ettringite and treated ettringite after treatment at three different levels of low pressure, (b) 4 mbar for 72 h, (c) 60 μ bar for 48 h, (d) respective length, and (e) width of ettringite's crystals derived from ESEM micrographs.

To exclude the influence of the electron beam of the ESEM during the micrograph's acquisition on the morphology, treatment at 0.5 mbar and 10,000 times magnification was recorded (Figure 10). It is clearly visible that the ettringite crystals swell after 12 scans (equivalent to 48 s in the electron beam). After 17 scans (equivalent to 76 s in the electron beam), the first cavities are formed by the explosive evaporation of the bound water of ettringite. After a total of 33 scans (equivalent to 136 s in the electron beam), no new cavities can be observed. Furthermore, the crystals' length shrinks only slightly, while their width increases considerably, which must be taken into account for future morphological investigations implementing imaging methods as ESEM, TEM, and SEM.

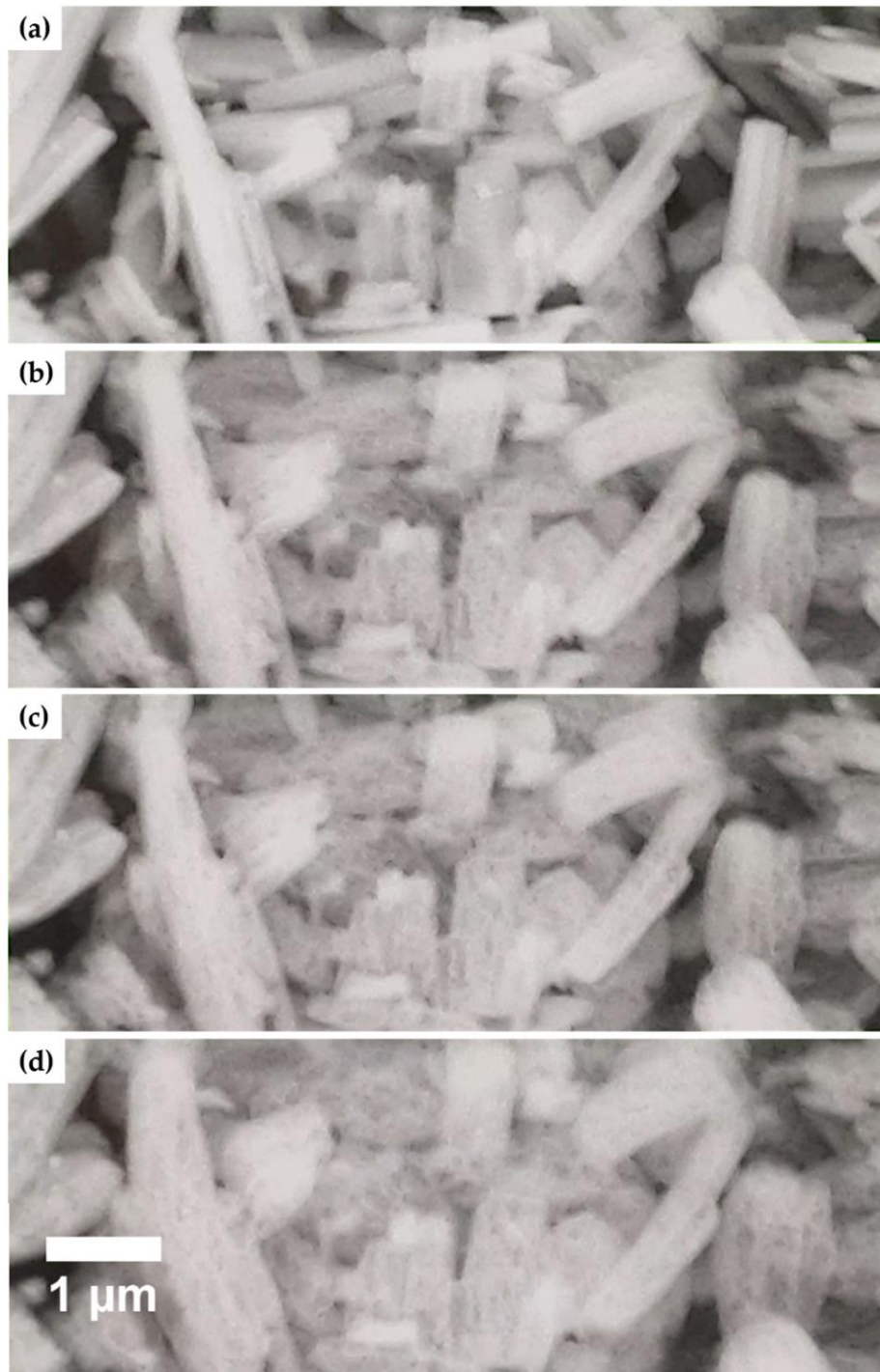


Figure 10. ESEM micrographs of the recorded decomposition of pristine ettringite's crystals by the electron beam over time; 1 mbar, 10 kV, 6 nA, 10,000 times magnification, 4 s per scan; (a) 1 scan, (b) 12 scans, (c) 23 scans, and (d) 33 scans.

4. Conclusions

Synthetic ettringite was chosen as model system to investigate the impact of different levels of low-pressure treatment (4 mbar, 60 μ bar, 2.8 nbar) on its chemical composition, crystal structure, and morphology during characterization measurements and the drying process. It was shown that the level as well as the duration of exposure to low pressure is of importance, as a lower pressure dehydrates ettringite faster. The bound water content in treated ettringite, derived from thermogravimetric analysis (TGA), shows at 4 mbar, a linear decrease of 14% over 72 h and at 60 μ bar, a dehydration of 67% within 48 h, following an exponential decrements. These findings are supported by the retrogression of the characteristic X-ray diffraction (XRD) pattern of ettringite and by the change of the cell parameters of ettringite, derived by selected area electron diffraction (SAED) as well as Pawley fits of the XRD data. SAED additionally revealed that despite phase conversion of ettringite due to dehydration, no change to the underlying crystal symmetry occurs. Raman measurements confirm that water loss comes mostly from bound water and not from adsorbed water. Our findings suggest that morphological investigation on a microscopic scale should only be conducted (if possible) using noninvasive characterization techniques requiring a low vacuum, such as environmental scanning electron microscopy (ESEM) or liquid cell transmission electron microscopy (LCTEM) [39]. The results of this manuscript might help future work, for example, in evaluating the crystal growth of early hydration products in cementitious suspensions.

Supplementary Materials: The following are available online at <https://www.mdpi.com/article/10.3390/ma14112720/s1>, Figure S1. Crystal structure of ettringite following Hartman et al. [1]; (a) part of a single column in $[10\bar{1}0]$ projection and (b) schematic build-up in the $[0001]$ projection. Figure S2. Water content of synthetic ettringite derived from (a) balance and (b) TGA after treatment at various level of low pressure (4 mbar: black; 60 μ bar: green) for different durations (up to 72 h) calculated on the assumption that during heat treatment, water is the sole decomposition product; (c) mass increase of treated ettringite (24 h at 60 μ bar) over time due to relative humidity in ambient air. Figure S3. Mass loss of synthetic ettringite measured (a) by balance and (b) through TGA after treatment at two different levels of low pressure (4 mbar: black; 60 μ bar: green) for different durations (up to 72 h); (c) combined assessment of mass loss of synthetic ettringite by balance and TGA after treatment at two different levels of low pressure (4 mbar: black; 60 μ bar: green) for various durations (up to 72 h). Figure S4. TGA data plotted as mass normalized weight loss ($d\Delta m \cdot (dt)^{-1}$) per hour against the temperature of synthetic ettringite with a heating rate of 5 $^{\circ}\text{C}/\text{min}$ after treatment at two different levels of low pressure (a) 4 mbar and (b) 60 μ bar for various durations (up to 72 h); full time frame. Figure S5. TGA data plotted as mass normalized weight loss ($d\Delta m \cdot (dt)^{-1}$) per hour against the temperature of synthetic ettringite with a heating rate of 5 $^{\circ}\text{C}/\text{min}$ after treatment at three different levels of low pressure; (a) steepness of first peak; (b) comparison of 4 mbar, 60 μ bar, and 2.8 nbar. Figure S6. Retrogression of the characteristic diffraction pattern of synthetic ettringite after treatment at two different levels of pressures (4 mbar and 60 μ bar) for various durations (up to 72 h); Bravais–Miller indices are given accordingly to a trigonal symmetry in a hexagonal cell; full time frame. Figure S7. Correlation between the retrogression derived by Pawley fit of ettringite's (a) cell parameter a , (b) cell parameter c , (c) cell volume V after treatment at three different levels of low pressure (4 mbar: black; 60 μ bar: red; 2.8 nbar: green) for various durations (up to 72 h), (d) Raman spectroscopy, and (e) TGA of pristine synthetic ettringite and treated ettringite after treatment at two different levels of low pressure (4 mbar for 72 h and 60 μ bar for 48 h); TGA data plotted as mass normalized time derived weight loss ($d\Delta m \cdot (dt)^{-1}$) per hour against the reference temperature of synthetic ettringite with a heating rate of 5 $^{\circ}\text{C}/\text{min}$. Figure S8. ESEM; ESEM micrographs of synthetic ettringite after treatment at two different levels of pressure (a) 1 mbar for 2 min and (b) 35.3 nbar for 2 min. Table S1. Mass loss of synthetic ettringite measured by balance after treatment at different levels of reduced pressure for various durations; $m_0(t) = 5.00$ g; $m_{0,\text{H}_2\text{O}}(t) = 2.30$ g; device specific deviation: ± 0.1 mg. Table S2. Mass loss of synthetic ettringite calculated after TGA after treatment at different levels of low pressure for various durations; $m_0(t) = 51.10$ mg ± 2.39 mg; $m_{0,\text{H}_2\text{O}}(t) = 23.47$ mg ± 1.10 mg; device specific deviation: $\pm 0.005\%$ (min. 1 μ g). Table S3. Equations of the decay of the first decomposition peak during TGA measurements after treatment at different levels of low pressure (4 mbar and 60 μ bar). Table S4. Vibration bands of pristine ettringite, of ettringite treated

for 72 h at 4 mbar, of ettringite treated for 48 h at 60 μ bar, and of ettringite exposed to the reduced pressure in the antechamber of the SEM decreasing to 2.8 nbar within 20 min. Table S5. Data for Figure 8; retrogression of the cell of synthetic ettringite after treatment at two different levels of low pressure (4.0 mbar and 60 μ bar) for various durations (up to 72 h); R_{wp} , R_{exp} and GOF derived by Pawley fit [4,5] [19,40]. Table S6. Data for Figure 8; retrogression of the cell of synthetic ettringite; sample exposed to the reduced pressure in the antechamber of the SEM decreasing to 2.8 nbar within 20 min; R_{wp} , R_{exp} and GOF derived by Pawley fit [4,5].

Author Contributions: Conceptualization, P.A.K. and N.C.B.; XRD, P.A.K. and A.F.; SAED, A.F.; Raman spectroscopy, P.A.K.; TEM, A.F.; TGA, P.A.K.; formal analysis, P.A.K.; validation, P.A.K., F.L., and N.C.B.; investigation, P.A.K.; resources, N.C.B. and L.L. (Ludger Lohaus); data curation, P.A.K.; writing—original draft preparation, P.A.K.; writing—review and editing, P.A.K., F.L., A.F., T.v.B., D.C., L.L. (Ludger Lohaus), M.H., L.L. (Lei Lei), and N.C.B.; visualization, P.A.K.; supervision, N.C.B.; funding acquisition, N.C.B. All authors have read and agreed to the published version of the manuscript.

Funding: Funded by the Deutsche Forschungsgemeinschaft (DFG, German Research Foundation, projects BI 1708/5-1 and LO 751/26-1 in the framework of SPP 2005 priority program ‘Opus Fluidum Futurum—Rheology of reactive, multiscale, multiphase construction materials’ [41], as well as by the project BI 1708/4-1. In addition, the project leading to these results has received funding in part from the European Research Council (ERC) under the European Union’s Horizon 2020 research and innovation program (grant agreement No. 714429).

Institutional Review Board Statement: Not applicable.

Informed Consent Statement: Not applicable.

Data Availability Statement: Data supporting reported results can be acquired per request to the corresponding author.

Acknowledgments: The authors thank J. Caro for access to XRD and TEM. The authors thank F. Steinbach for STEM, TEM, and STEM-EDXS measurements. The authors thank C. Rozanski for help with the interpretation of TGA spectra. The authors thank A. Krabbenhöft (IW) for ESEM measurements. The authors thank C. Rüscher for access to the Raman spectrometer and I. Strauß for help during the measurements. The authors thank T. von Bronk for exciting discussions. The authors thank Heidelberger Cement AG for providing the cement during the DFG SPP 2005 priority program. The authors thank the Laboratory for Nano- and Quantum Engineering (LNQE) for its support.

Conflicts of Interest: The authors declare no conflict of interest. The funders had no role in the design of the study; in the collection, analyses, or interpretation of data; in the writing of the manuscript; or in the decision to publish the results.

References

1. Moore, A.; Taylor, H.F.W. Crystal Structure of Ettringite. *Nature* **1968**, *218*, 1048–1049. [[CrossRef](#)]
2. Barger, G.S.; Bayles, J.; Blair, B.; Brown, D.; Chen, H.; Conway, T.; Hawkins, P. *Ettringite Formation and the Performance of Concrete*; Portland Cement Association: Skokie, IL, USA, 2001; pp. 1–16.
3. Jakob, C.; Jansen, D.; Ukrainczyk, N.; Koenders, E.; Pott, U.; Stephan, D.; Neubauer, J. Relating Ettringite Formation and Rheological Changes during the Initial Cement Hydration: A Comparative Study Applying XRD Analysis, Rheological Measurements and Modeling. *Materials* **2019**, *12*, 2957. [[CrossRef](#)] [[PubMed](#)]
4. Merlini, M.; Artioli, G.; Cerulli, T.; Cella, F.; Bravo, A. Tricalcium aluminate hydration in additivated systems. A crystallographic study by SR-XRPD. *Cem. Concr. Res.* **2008**, *38*, 477–486. [[CrossRef](#)]
5. Skoblinkaya, N.N.; Krasilnikov, K.G. Changes in crystal structure of ettringite on dehydration. 1. *Cem. Concr. Res.* **1975**, *5*, 381–394. [[CrossRef](#)]
6. Skoblinkaya, N.N.; Krasilnikov, K.G.; Nikitina, L.V.; Varlamov, V.P. Changes in crystal structure of ettringite on dehydration. 2. *Cem. Concr. Res.* **1975**, *5*, 419–431. [[CrossRef](#)]
7. Stroh, J.; Ali, N.Z.; Maierhofer, C.; Emmerling, F. Ettringite via Mechanochemistry: A Green and Rapid Approach for Industrial Application. *ACS Omega* **2019**, *4*, 7734–7737. [[CrossRef](#)] [[PubMed](#)]
8. Lehmkuhl, J.; Fendel, A.D.; Bings, H. Mineralischer Füllstoff und Baustoff-Additiv auf Basis von Calciumaluminiumsulfat und deren Herstellung und Verwendung. German Patent DE19611454, 25 September 1997.
9. Moore, A.; Taylor, H.F.W. Crystal Structure of Ettringite. *Acta Crystallogr. Sect. B Struct. Crystallogr. Cryst. Chem.* **1970**, *26*, 386–393. [[CrossRef](#)]
10. Taylor, H.F.W. Crystal structures of some double hydroxide minerals. *Mineral. Mag.* **1973**, *39*, 377–389. [[CrossRef](#)]

11. Bezjak, A.; Jelenić, I. Crystal Structure Investigation of Calcium Aluminium Sulphate Hydrate—Ettringite. *Croat. Chem. Acta* **1966**, *38*, 239–242.
12. Shimada, Y.; Young, J.F. Structural changes during thermal dehydration of ettringite. *Adv. Cem. Res.* **2001**, *13*, 77–81. [[CrossRef](#)]
13. Winnefeld, F.; Zingg, A.; Holzer, L.; Pakusch, J.; Becker, S. The Ettringite-superplasticizer interaction and its impact on ettringite distribution in cement suspensions. In Proceedings of the 9th ACI International Conference on Superplasticizers and Other Chemical Admixtures in Concrete, Sevilla, Spain, 12–14 October 2009; pp. 420.1–420.17.
14. Tattersall, G.H. *Workability and Quality Control of Concrete*, 1st ed.; CRC Press: London, UK, 2014; ISBN 9781482267006.
15. Gołaszewski, J. Influence of cement properties on rheology of fresh cement mortars without and with superplasticizer. *Archit. Civ. Eng. Environ.* **2008**, *4*, 49–66.
16. Struble, L.J.; Lei, W.-G. Rheological changes associated with setting of cement paste. *Adv. Cem. Based Mater.* **1995**, *2*, 224–230. [[CrossRef](#)]
17. Uchikawa, H.; Ogawa, K.; Uchida, S. Influence of character of clinker on the early hydration process and rheological property of cement paste. *Cem. Concr. Res.* **1985**, *15*, 561–572. [[CrossRef](#)]
18. Pott, U.; Ehm, C.; Jakob, C.; Stephan, D. Investigation of the Early Cement Hydration with a New Penetration Test, Rheometry and In-Situ XRD. In *Rheology and Processing of Construction Materials*; Springer: Cham, Switzerland, 2020; pp. 246–255.
19. Pawley, G.S. Unit-cell refinement from powder diffraction scans. *J. Appl. Crystallogr.* **1981**, *14*, 357–361. [[CrossRef](#)]
20. Struble, L.J. Synthesis and characterization of ettringite and related phases. In *8th International Congress on the Chemistry of Cement*; Abta Grafica e Editora: Rio de Janeiro, Brazil, 1986; pp. 582–588.
21. Guildner, L.; Johnson, D.; Jones, F.E. Vapor pressure of water at its triple point. *J. Res. Natl. Bur. Stand. Sect. A Phys. Chem.* **1976**, *80A*, 505. [[CrossRef](#)] [[PubMed](#)]
22. The International Association for the Properties of Water and Steam. *IAPWS G5-01, Guideline on the Use of Fundamental Physical Constants and Basic Constants of Water*. Available online: <http://www.iapws.org/relguide/fundam.pdf> (accessed on 20 March 2021).
23. Hartman, M.R.; Berliner, R. Investigation of the structure of ettringite by time-of-flight neutron powder diffraction techniques. *Cem. Concr. Res.* **2006**, *36*, 364–370. [[CrossRef](#)]
24. Renaudin, G.; Filinchuk, Y.; Neubauer, J.; Goetz-Neunhoeffer, F. A comparative structural study of wet and dried ettringite. *Cem. Concr. Res.* **2010**, *40*, 370–375. [[CrossRef](#)]
25. Hall, C.; Barnes, P.; Billimore, A.D.; Jue, A.C.; Turrillas, X. Thermal decomposition of ettringite $\text{Ca}_6[\text{Al}(\text{OH})_6]_2(\text{SO}_4)_3 \cdot 26\text{H}_2\text{O}$. *J. Chem. Soc. Faraday Trans.* **1996**, *92*, 2125–2129. [[CrossRef](#)]
26. European Commission; Joint Research Centre; Institute for Health and Consumer Protection; European Chemicals Bureau. *IUCLID-CD-ROM*, 2000th ed.; European Commission: Ispra, Italy, 2000.
27. Roth, L.; Weller, U. *Gefährliche Chemische Reaktionen: Stoffinformationen, Reaktionstabellen, Unfallberichte/Roth; Weller; 1*; Ecomed-Storck GmbH: Landsberg am Lech, Germany, 1982; ISBN 360964530X.
28. Taylor, H.F.W. *Cement Chemistry*; Thomas Telford Publishing: London, UK, 1997; ISBN 0-7277-3945-X.
29. Lea, F.M. *Lea's Chemistry of Cement and Concrete*, 3rd ed.; Elsevier: London, UK, 1998; ISBN 9780750662567.
30. Ghorab, H.Y.; Kishar, E.A. Studies on the stability of the calcium sulfoaluminate hydrates. Part 1: Effect of temperature on the stability of ettringite in pure water. *Cem. Concr. Res.* **1985**, *15*, 93–99. [[CrossRef](#)]
31. Grounds, T.; Midgley, H.G.; Nowell, D. The use of thermal methods to estimate the state of hydration of calciumtrisulphoaluminate hydrate $3\text{CaO} \cdot \text{Al}_2\text{O}_3 \cdot 3\text{CaSO}_4 \cdot n\text{H}_2\text{O}$. *Thermochim. Acta* **1985**, *85*, 215–218. [[CrossRef](#)]
32. Stepkowska, E.T.; Blanes, J.M.; Real, C.; Perez-Rodriguez, J.L. Hydration products in two aged cement pastes. *J. Therm. Anal. Calorim.* **2005**, *82*, 731–739. [[CrossRef](#)]
33. Villain, G.; Thiery, M.; Platret, G. Measurement methods of carbonation profiles in concrete: Thermogravimetry, chemical analysis and gammadensimetry. *Cem. Concr. Res.* **2007**, *37*, 1182–1192. [[CrossRef](#)]
34. Renaudin, G.; Segni, R.; Mentel, D.; Nedelec, J.M.; Leroux, F.; Taviot-Gueho, C. A Raman study of the sulfated cement hydrates: Ettringite and monosulfoaluminate. *J. Adv. Concr. Technol.* **2007**, *5*, 299–312. [[CrossRef](#)]
35. Effenberger, H.; Mereiter, K.; Zemann, J. Crystal structure refinements of magnesite, calcite, rhodochrosite, siderite, smithonite, and dolomite, with discussion of some aspects of the stereochemistry of calcite type carbonates. *Z. Krist. Cryst. Mater.* **1981**, *156*, 233–243. [[CrossRef](#)]
36. Aggarwal, P.; Gard, J.; Glasser, F.; Biggar, G. Synthesis and properties of dicalcium aluminate, $2\text{CaO} \cdot \text{Al}_2\text{O}_3$. *Cem. Concr. Res.* **1972**, *2*, 291–297. [[CrossRef](#)]
37. Clark, G.R.; Rodgers, K.A.; Henderson, G.S. The crystal chemistry of doyleite, $\text{Al}(\text{OH})_3$. *Z. Krist. Cryst. Mater.* **1998**, *213*, 96–100. [[CrossRef](#)]
38. Bezou, C.; Nonat, A.; Mutin, J.-C.; Christensen, A.N.; Lehmann, M.S. Investigation of the Crystal Structure of $\gamma\text{-CaSO}_4$, $\text{CaSO}_4 \cdot 0.5\text{H}_2\text{O}$, and $\text{CaSO}_4 \cdot 0.6\text{H}_2\text{O}$ by Powder Diffraction Methods. *J. Solid State Chem.* **1995**, *117*, 165–176. [[CrossRef](#)]
39. Ross, F.M. (Ed.) *Liquid Cell Electron Microscopy*; Cambridge University Press: Cambridge, UK, 2016; ISBN 9781316337455. [[CrossRef](#)]
40. Toby, B.H. R factors in Rietveld analysis: How good is good enough? *Powder Diffr.* **2006**, *21*, 67–70. [[CrossRef](#)]
41. DFG SPP 2005—Priority Programm Opus Fluidum Futurum—Rheology of Reactive, Multiscale, Multiphase Construction Materials. Available online: <https://www.spp2005.de> (accessed on 29 October 2019).



Supporting Information

Influence of Low-Pressure Treatment on the Morphological and Compositional Stability of Microscopic Ettringite

Patrick A. Kißling ¹, Franziska Lübke mann ¹, Tabea von Bronk ², Dario Cotardo ², Lei Lei ³, Armin Feldhoff ¹, Ludger Lohaus ², Michael Haist ² and Nadja C. Bigall ^{1,*}

- ¹ Institute of Physical Chemistry and Electrochemistry, Leibniz Universität Hannover, 30167 Hanover, Germany; patrick.kissling@pci.uni-hannover.de (P.A.K.); franziska.luebke mann@pci.uni-hannover.de (F.L.); armin.feldhoff@pci.uni-hannover.de (A.F.)
- ² Institute of Building Materials Science, Leibniz Universität Hannover, 30167 Hanover, Germany; t.von-bronk@baustoff.uni-hannover.de (T.v.B.); d.cotardo@baustoff.uni-hannover.de (D.C.); lohause@baustoff.uni-hannover.de (L.L.); haist@baustoff.uni-hannover.de (M.H.)
- ³ Chair for Construction Chemistry, Technische Universität München, 85747 Munich, Germany; lei.lei@bauchemie.ch.tum.de
- * Correspondence: nadja.bigall@pci.uni-hannover.de; Tel.; +49-511-762-14439

Citation: Kißling, P.A.; Lübke mann, F.; von Bronk, T.; Cotardo, D.; Lei, L.; Feldhoff, A.; Lohaus, L.; Haist, M.; Bigall, N.C. Influence of Low-Pressure Treatment on the Morphological and Compositional Stability of Microscopic Ettringite. *Materials* **2021**, *14*, 2720. <https://doi.org/10.3390/ma14112720>

Academic Editors: Jose Antonio Alonso and Daniela Kovacheva

Received: 24 March 2021
Accepted: 17 May 2021
Published: 21 May 2021

Publisher's Note: MDPI stays neutral with regard to jurisdictional claims in published maps and institutional affiliations.



Copyright: © 2021 by the authors. Licensee MDPI, Basel, Switzerland. This article is an open access article distributed under the terms and conditions of the Creative Commons Attribution (CC BY) license (<http://creativecommons.org/licenses/by/4.0/>).

Abstract: The impact of low-pressure treatment on the crystal structure, morphology, and chemical composition of ettringite, due to their major importance with respect to processability (i.e., drying conditions) and to the analysis of ettringite-containing samples, is examined utilizing X-ray diffraction, thermogravimetric analysis, Raman spectroscopy, and environmental scanning electron microscopy. Synthetic ettringite was treated for various durations (5 min up to 72 h) and at two different levels of low-pressure (4.0 mbar and 60 µbar). Evaluation showed a correlation between the procedural parameters (time and pressure), the chemical composition, and the morphology of ettringite. The experiments reveal that, when exposed to 4 mbar pressure, nearly no changes occur in the ettringite's morphology, whereas the crystals undergo swelling and slight deformations at very low pressures (60 µbar and 35.3 nbar), which is attributed to the loss of bound water and the partial transformation from ettringite to quicklime, anhydrite, and calcium aluminate. Furthermore, the strongly dehydrated ettringite shows the same morphology.

Keywords: morphology; chemical composition; ettringite; low-pressure; Pawley fit

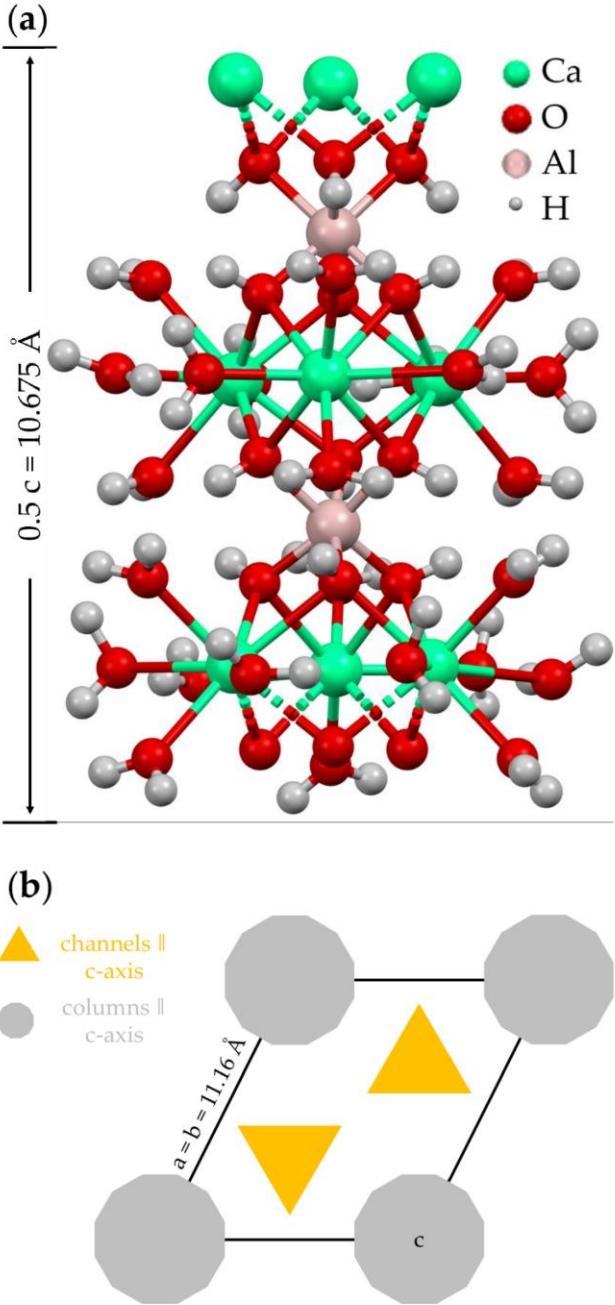


Figure S1. Crystal structure of ettringite following Hartman et al. [1]; (a) part of a single column in the $[10\bar{1}0]$ projection and (b) schematic buildup in the $[0001]$ projection.

By simple mass measurements using a balance, the loss of water was investigated gravimetrically after treatment with low pressure for different durations (see **Figure S2a,b** and **Tables S1** and **S2**). A slightly reduced pressure of 4.0 mbar manages to extract only 6.4 wt% of bound water after 72 h. A similar degree of extraction (6.7 wt % of bound water) is reached after 2 h at a pressure of 60 μ bar. After 24 h the low-pressure treatment at 60 μ bar leads to a mass loss of 30.2 wt% of bound water, which then stays nearly constant for at least 24 h.

A similar curve can be derived from the maximal difference in mass over the whole decomposition range of TGA measurements (see **Figures S2** and **S3** and **Table S2**). The obtained maximum discrepancy in mass loss of 10% between balance and TGA measurements is most probably induced by the loss of small grains during vacuum application: less loss with less vacuum, after 24 h at 60 μ bar around 1 %. The main factor is the time needed to transfer the sample from the freeze dryer to the TGA device to complete the weigh-in and to start the measurement, as the relative humidity in the air leads to rehydration of the activated ettringite over time (see **Figure S2c**). Measuring the mass loss by balance gives a good first impression of the extracted bound water.

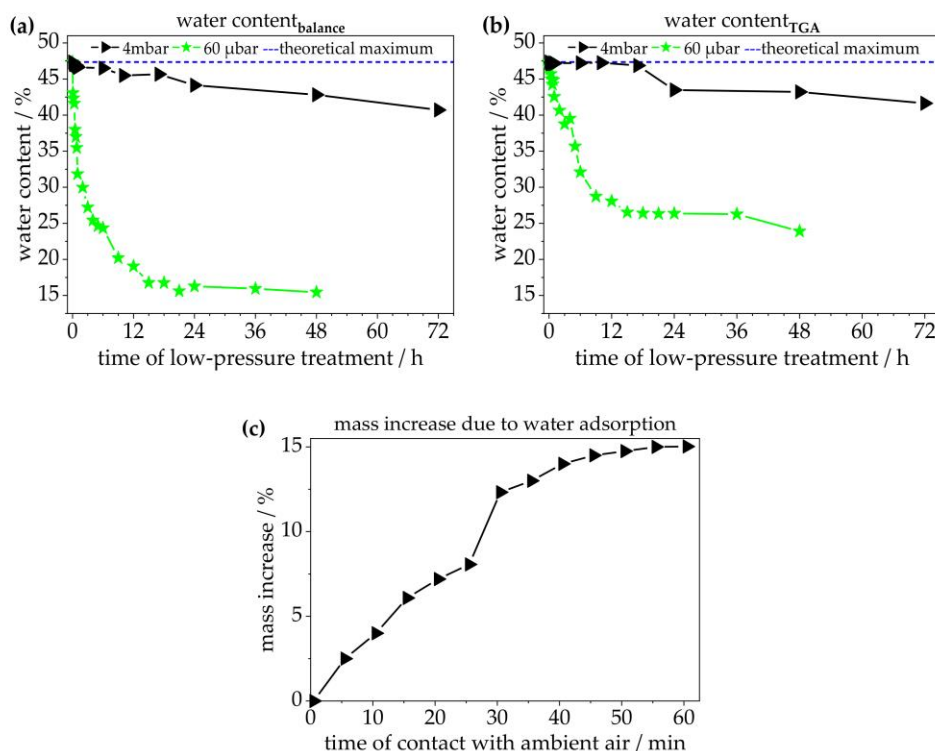


Figure S2. Water content of synthetic ettringite derived from (a) balance and (b) TGA after treatment at various level of low pressure (4 mbar: black; 60 μ bar: green) for different durations (up to 72 h); calculated on the assumption that during heat treatment, water is the sole decomposition product; (c) mass increase of treated ettringite (24 h at 60 μ bar) over time due to relative humidity in ambient air.

The extent of mass loss decreases according to the higher extraction of bound water induced by a higher level and longer time of exposure to low pressure, so less water is still inside the crystal structure. The higher the extraction rate of bound water, the lower the mass loss induced by decomposition within TGA. Therefore, the course of the mass loss must be inversely proportional to that measured by the balance, which is depicted in

Figure S3. At a slightly reduced pressure of 4 mbar, the mass loss (Δm) stays around $100.34\% \pm 0.49\%$ within the first 17 h. Afterwards, the mass loss is underestimated at $94.94\% \pm 0.49\%$, so in total, there is a slight underestimation in the range of device error of $99.10\% \pm 2.33\%$ (see **Figure S3**). This statement is not valid for the exposure to lower pressure ($60\ \mu\text{bar}$). In the first 4 h, the desorbed amount is exaggerated by $3.53\% \pm 1.40\%$, and for the remaining 44 h, the underestimation is at $85.12\% \pm 8.61\%$, so in total, there is an underestimation of $5.67\% \pm 11.08\%$.

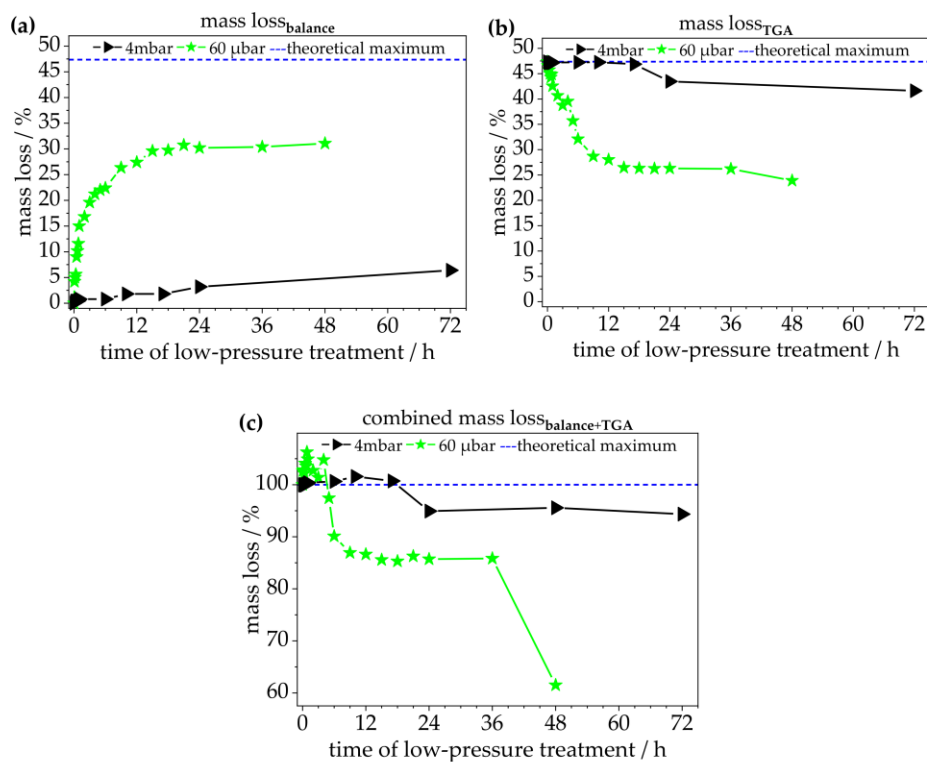


Figure S3. Mass loss of synthetic ettringite measured (a) by balance and (b) through TGA after treatment at two different levels of low pressure (4 mbar: black; $60\ \mu\text{bar}$: green) for different durations (up to 72 h); (c) combined assessment of mass loss of synthetic ettringite by balance and TGA after treatment at two different levels of low pressure (4 mbar: black; $60\ \mu\text{bar}$: green) for various durations (up to 72 h).

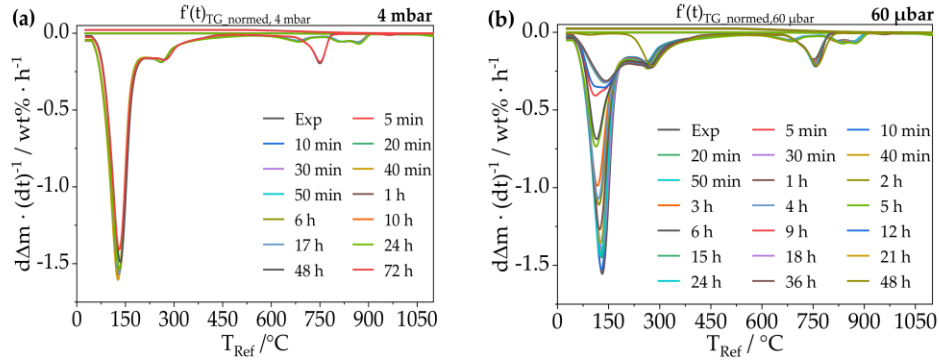


Figure S4. TGA data plotted as mass normalized time derived weight loss ($d\Delta m \cdot (dt)^{-1}$) per hour against the reference temperature of synthetic ettringite with a heating rate of $5\text{ }^{\circ}\text{C}/\text{min}$ after treatment at two different levels of low pressure, (a) 4 mbar and (b) $60\text{ }\mu\text{bar}$, for various durations (up to 72 h); full-time frame.

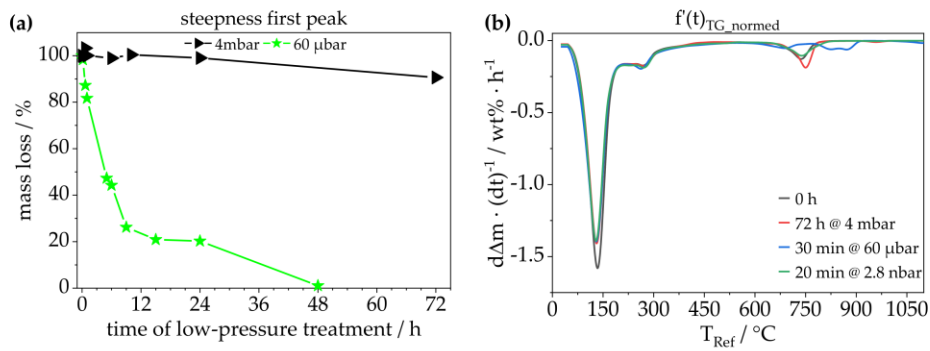


Figure S5. TGA data plotted as mass normalized time derived weight loss ($d\Delta m \cdot (dt)^{-1}$) per hour against the reference temperature of synthetic ettringite with a heating rate of $5\text{ }^{\circ}\text{C}/\text{min}$ after treatment at different levels of low pressure; (a) steepness of the first peak; (b) comparison of 4 mbar, $60\text{ }\mu\text{bar}$, and 2.8 nbar.

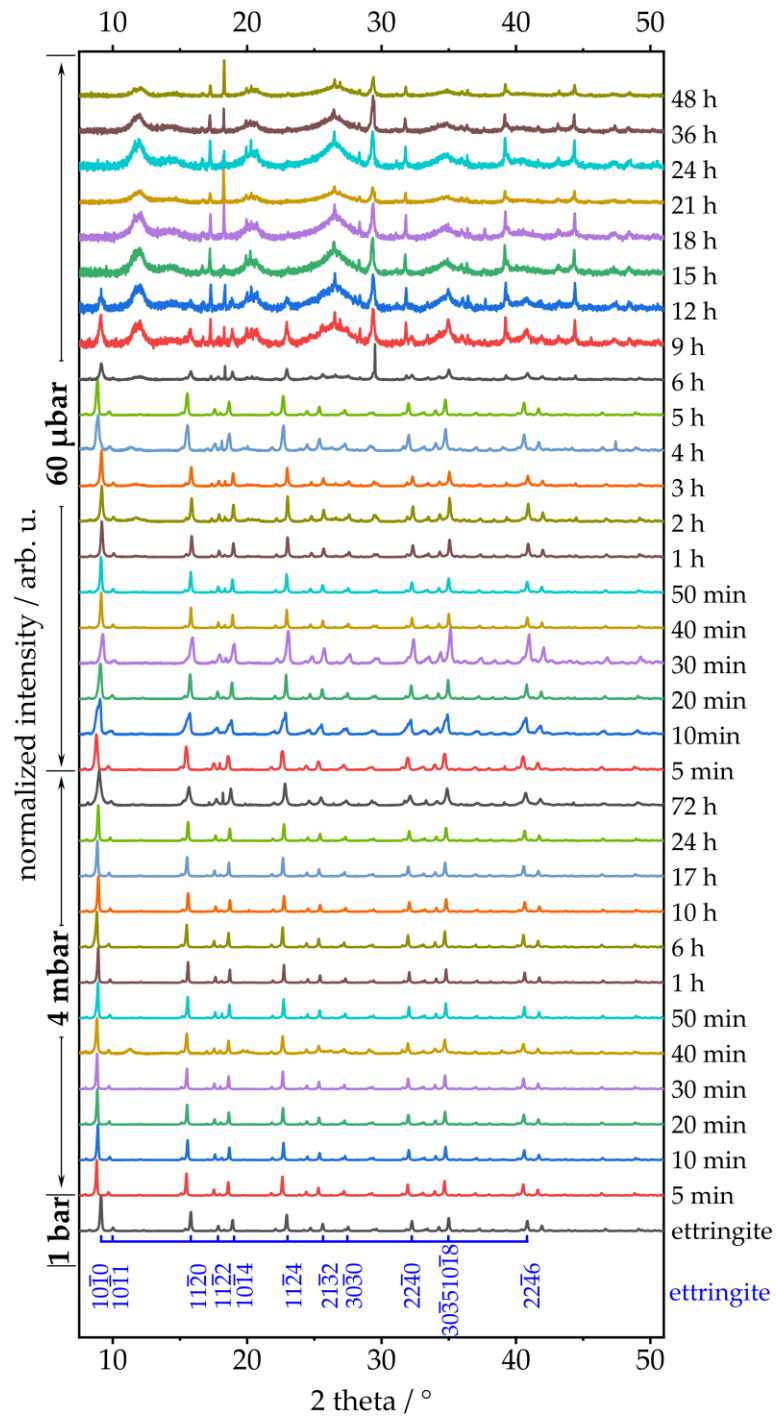


Figure S6. Retrogression of the characteristic diffraction pattern of synthetic ettringite after treatment at two different levels of pressures (4 mbar and 60 μ bar) for various durations (up to 72 h); Bravais–Miller indices are given according to a trigonal symmetry in a hexagonal cell; full-time frame.

The comparison of retrogression derived from Pawley fit of XRD data with the results of Raman spectroscopy and TGA of samples treated for 72 h at 4 mbar and 48 h at 60 μ bar shows correlation, (see **Figure S7**). Raman and TGA depict that at 60 μ bar, the bound water content is at its minimum. At this point, the cell parameters are also at their lowest values. In case of the sample treated at 4 mbar for 72 h, nearly no change in the cell parameters was detected, which is in good correlation with the TGA and Raman measurements. In both cases, no significant change to the bound water content (Raman at 3500 cm^{-1} and TGA at 150 $^{\circ}\text{C}$) was found.

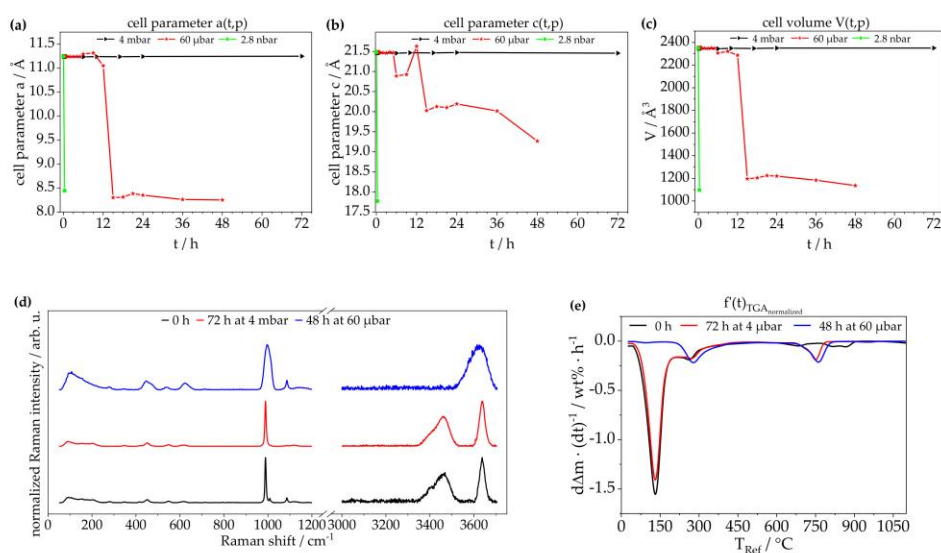


Figure S7. Correlation between the retrogression derived by Pawley fit of ettringite's (a) cell parameter a , (b) cell parameter c , and (c) cell volume V after treatment at three different levels of low pressure (4 mbar: black; 60 μ bar: red; 2.8 nbar: green) for various durations (up to 72 h), (d) Raman spectroscopy, and (e) TGA of pristine synthetic ettringite and treated ettringite; both (d+e) after treatment at two different levels of low pressure (4 mbar for 72 h and 60 μ bar for 48 h); TGA data plotted as mass normalized time derived weight loss ($d\Delta m \cdot (dt)^{-1}$) per hour against the reference temperature of synthetic ettringite with a heating rate of 5 $^{\circ}\text{C}/\text{min}$.

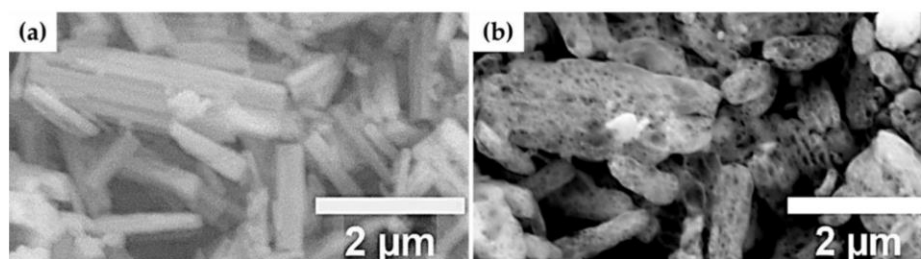


Figure S8. ESEM; ESEM micrographs of synthetic ettringite after treatment at two different levels of pressure, (a) 1 mbar for 2 min and (b) 35.3 nbar for 2 min.

Table S1. Mass loss of synthetic ettringite measured by balance after treatment at different levels of reduced pressure for various durations; $m_0(t) = 5.00$ g; $m_{0, H_2O}(t) = 2.30$ g; device-specific deviation: ± 0.1 mg.

4.0 mbar					t / h	60 μ bar				
m(t) / g	$\Delta m(t)$ / g	$\Delta m(t)$ / %	$\Delta m_{H_2O}(t)$ / %	$\Delta n_{H_2O}(t)$ / mmol		m(t) / g	$\Delta m(t)$ / g	$\Delta m(t)$ / %	$\Delta m_{H_2O}(t)$ / %	$\Delta n_{H_2O}(t)$ / mmol
5.00	0.00	0.00	0.00	0.00	0	5.00	0.00	0.00	0.00	0.00
5.00	0.01	0.20	0.43	0.00	0.083	4.79	0.21	4.20	9.14	0.36
4.99	0.02	0.40	0.87	0.03	0.17	4.76	0.25	4.99	10.86	0.43
4.99	0.02	0.40	0.87	0.03	0.33	4.72	0.28	5.60	12.19	0.49
4.98	0.02	0.40	0.87	0.03	0.50	4.55	0.45	9.00	19.59	0.78
4.98	0.02	0.40	0.87	0.03	0.67	4.50	0.51	10.18	22.16	0.88
4.97	0.03	0.60	1.31	0.05	0.83	4.42	0.58	11.60	25.25	1.01
4.97	0.04	0.80	1.74	0.07	1	4.25	0.75	15.00	32.66	1.30
					2	4.16	0.84	16.80	36.58	1.46
					3	4.02	0.98	19.60	42.67	1.70
					4	3.94	1.06	21.20	46.16	1.84
					5	3.90	1.10	22.00	47.90	1.91
4.96	0.04	0.80	1.74	0.07	6	3.88	1.12	22.40	48.77	1.94
					9	3.69	1.32	26.35	57.36	2.29
4.91	0.09	1.80	3.92	0.16	10					
					12	3.63	1.37	27.40	59.65	2.38
					15	3.52	1.48	29.60	64.44	2.57
4.92	0.09	1.80	3.91	0.16	17					
					18	3.52	1.49	29.74	64.75	2.58
					21	3.47	1.54	30.74	66.92	2.67
4.85	0.16	3.19	6.95	0.28	24	3.49	1.51	30.20	65.75	2.62
					36	3.48	1.52	30.40	66.19	2.64
					48	3.44	1.55	31.06	67.63	2.69
4.68	0.32	6.40	13.93	0.56	72					

Table S2. Mass loss of synthetic ettringite calculated after TGA after treatment at different levels of low pressure for various durations; $m_0(t) = 51.10 \text{ mg} \pm 2.39 \text{ mg}$; $m_{0, \text{H}_2\text{O}}(t) = 23.47 \text{ mg} \pm 1.10 \text{ mg}$; device-specific deviation: $\pm 0.005 \%$ (min. 1 μg).

4.0 mbar					t / h	60 μbar				
m(t) / mg	$\Delta m(t)$ / mg	$\Delta m(t)$ / %	$\Delta m_{\text{H}_2\text{O}}(t)$ / %	$\Delta n_{\text{H}_2\text{O}}(t)$ / μmol		m(t) / mg	$\Delta m(t)$ / mg	$\Delta m(t)$ / %	$\Delta m_{\text{H}_2\text{O}}(t)$ / %	$\Delta n_{\text{H}_2\text{O}}(t)$ / μmol
28.72	25.84	47.35	103.09	44.81	0	28.72	25.84	47.35	103.09	44.81
26.48	23.65	47.18	102.73	41.03	0.083	27.31	23.85	46.63	101.51	41.38
26.48	23.65	47.18	102.73	41.03	0.17	26.56	22.97	46.38	100.97	39.85
28.53	25.42	47.12	102.59	44.10	0.33	28.14	23.70	45.71	99.52	41.10
28.32	25.30	47.18	102.72	43.89	0.50	29.67	24.27	44.99	97.94	42.09
24.59	21.96	47.17	102.70	38.09	0.67	28.27	22.45	44.26	96.35	38.94
29.31	26.14	47.14	102.64	45.34	0.83	26.53	21.58	44.86	97.66	37.43
27.97	24.99	47.19	102.73	43.36	1	27.67	20.49	42.55	92.63	35.54
					2	30.96	21.20	40.65	88.49	36.78
					3	28.42	17.98	38.75	84.37	31.20
					4	30.46	19.91	39.53	86.06	34.54
					5	32.51	18.04	35.69	77.70	31.29
27.73	24.82	47.23	102.83	43.05	6	32.44	15.33	32.09	69.87	26.59
					9	36.34	14.61	28.68	62.44	25.35
26.86	24.05	47.25	102.86	41.73	10					
					12	37.92	14.76	28.01	60.99	25.60
					15	35.59	12.80	26.46	57.60	22.21
26.08	23.01	46.87	102.05	39.91	17					
					18	37.59	13.43	26.33	57.31	23.30
					21	37.57	13.38	26.26	57.17	23.20
30.28	23.29	43.47	94.65	40.40	24	37.15	13.26	26.30	57.27	23.00
					36	39.58	14.06	26.21	57.06	24.39
					48	40.06	12.58	23.90	52.03	21.82
30.13	21.48	41.62	90.61	37.26	72					

Table S3. Equations of the decay of the first decomposition peak during TGA measurements after treatment at different levels of low pressure (4 mbar and 60 μbar).

pressure	function	value		
4 mbar	$y = a + b \cdot x$	$a = 100.66228 \pm 0.4453$	$b = -0.11878 \pm 0.01808$	
60 μbar	$y = a - b \cdot c^x$	$a = 18.59904 \pm 1.19564$	$b = -81.34841 \pm 1.421$	$c = 0.80861 \pm 0.00983$

Table S4. Vibration bands of pristine ettringite, of ettringite treated for 72 h at 4 mbar, of ettringite treated for 48 h at 60 μ bar, and of ettringite exposed to the reduced pressure in the antechamber of the SEM (decreasing to 2.8 nbar within 20 min).

		Literature [2,3] / cm^{-1}	Ettringite 0 h / cm^{-1}	72 h at 4 mbar / cm^{-1}	48 h at 60 μ bar / cm^{-1}	20 min at 2.8 nbar / cm^{-1}
100 cm^{-1} to 12000 cm^{-1}	ν_2 [SO ₄]	452.1 \pm 15.8	451.5 \pm 28.5	452.5 \pm 36.5	455.8 \pm 49.8	454.3 \pm 29.8
	'[Al(OH) ₆ ']	548.7 \pm 10.2	536.5 \pm 11.5	548.8 \pm 25.8	543.8 \pm 31.3	548.0 \pm 20.5
	ν_4 [SO ₄]	610.2 \pm 22.2	612.0 \pm 26.0	618.0 \pm 29.5	625.3 \pm 47.3	620.0 \pm 20.0
	ν_7 [SO ₄]	988.5 \pm 4.7	988.5 \pm 30.5	990.3 \pm 32.3	996.8 \pm 45.8	986.8 \pm 20.8
	ν_3 [SO ₄]	1120.0 \pm 25.6	1086.0 \pm 20.0	1088.5 \pm 29.5	1086.5 \pm 28.0	-----
3000 cm^{-1} to 3700 cm^{-1}	[H ₂ O] stretching	3289.2 \pm 199.4	3444.8 \pm 102.8	3434.8 \pm 96.8	-----	3440.8 \pm 90.3
	[H ₂ O] stretching	3404.7 \pm 75.6				
	[H ₂ O] stretching	3464.2 \pm 107.8				
	[H ₂ O] stretching	3517.4 \pm 107.8				
	[OH] stretching	3638.0 \pm 18.5	3644.0 \pm 42.0	3640.0 \pm 46.0	3606.3 \pm 98.8	3644.4 \pm 42.4

Table S5. Data for Figure 8; retrogression of the cell parameter of synthetic ettringite after treatment at two different levels of low pressure (4.0 mbar and 60 μ bar) for various durations (up to 72 h); R_{wp} , R_{exp} and GOF derived by Pawley fit [4,5].

		4.0 mbar				t / h	60 μ bar					
a(t) / \AA	c(t) / \AA	V(t) / \AA^3	R_{wp}	R_{exp}	GOF		a(t) / \AA	c(t) / \AA	V(t) / \AA^3	R_{wp}	R_{exp}	GOF
11.24	21.48	2351	2.32	8.06	3.48	0	11.24	21.48	2351	2.32	8.06	3.48
11.23	21.46	2345	1.53	15.5	10.1	0.083	11.24	21.46	2346	1.74	16.4	9.43
11.24	21.47	2348	1.54	16.5	10.7	0.17	11.25	21.49	2355	1.79	13.8	7.71
11.24	21.47	2349	1.57	15.4	9.83	0.33	11.25	21.48	2352	1.58	15.5	9.76
11.24	21.46	2347	1.54	15.9	10.3	0.50	11.24	21.48	2352	1.83	14.3	7.83
11.24	21.46	2348	1.59	11.1	6.96	0.67	11.25	21.48	2353	1.65	13.2	7.97
11.24	21.46	2347	1.51	17.3	11.4	0.83	11.25	21.48	2353	1.67	10.0	5.99
11.24	21.46	2348	1.55	17.4	11.3	1	11.24	21.48	2351	1.75	8.05	4.61
						2	11.24	21.47	2349	1.75	11.4	6.49
						3	11.24	21.46	2348	1.74	9.01	5.19
						4	11.24	21.48	2351	1.53	7.99	5.22
						5	11.24	21.47	2348	1.48	16.8	11.4
11.23	21.45	2345	1.63	19.5	11.9	6	11.29	20.89	2307	1.57	2.98	1.90
						9	11.32	20.93	2321	1.56	2.95	1.88
11.24	21.47	2349	1.57	17.1	10.9	10						
						12	11.05	21.63	2287	1.58	3.89	2.47
						15	8.30	20.03	1195	1.58	2.05	1.30
11.24	21.46	2347	1.55	14.8	9.58	17						
						18	8.31	20.13	1205	1.57	4.15	2.64
						21	8.39	20.10	1224	1.63	2.63	1.62
11.24	21.47	2350	1.56	16.3	10.4	24	8.35	20.19	1220	1.57	2.41	1.53
						36	8.26	20.02	1183	1.59	2.42	1.52
						48	8.25	19.27	1136	1.22	1.88	1.54
11.25	21.46	2351	1.63	9.47	5.83	72						

Table S6. Data for **Figure 8**; retrogression of the cell of synthetic ettringite; sample exposed to the reduced pressure in the antechamber of the SEM decreasing to 2.8 nbar within 20 min; R_{wp} , R_{exp} and GOF derived by Pawley fit [4,5].

$a(t) / \text{\AA}$	$c(t) / \text{\AA}$	2.8 nbar				t / h
		$V(t) / \text{\AA}^3$	R_{wp}	R_{exp}	GOF	
11.24	21.48	2351	2.32	7.85	3.54	0
8.45	17.77	1098	0.73	3.99	5.48	0.33

References

- Hartman, M.R.; Berliner, R. Investigation of the structure of ettringite by time-of-flight neutron powder diffraction techniques. *Cem. Concr. Res.* **2006**, *36*, 364–370, doi:10.1016/j.cemconres.2005.08.004.
- Renaudin, G.; Filinchuk, Y.; Neubauer, J.; Goetz-Neunhoeffer, F. A comparative structural study of wet and dried ettringite. *Cem. Concr. Res.* **2010**, *40*, 370–375, doi:10.1016/j.cemconres.2009.11.002.
- Renaudin, G.; Segni, R.; Mentel, D.; Nedelec, J.M.; Leroux, F.; Taviot-Gueho, C. A Raman study of the sulfated cement hydrates: Ettringite and monosulfoaluminate. *J. Adv. Concr. Technol.* **2007**, *5*, 299–312, doi:10.3151/jact.5.299.
- Pawley, G.S. Unit-cell refinement from powder diffraction scans. *J. Appl. Crystallogr.* **1981**, *14*, 357–361, doi:10.1107/S0021889881009618.
- Toby, B.H. R factors in Rietveld analysis: How good is good enough? *Powder Diffr.* **2006**, *21*, 67–70, doi:10.1154/1.2179804.

3.4 IS FREEZE-DRYING AN ALTERNATIVE TO SOLVENT EXCHANGE FOR THE HYDRATION STOP OF CEMENTITIOUS SUSPENSIONS?

P. A. Kißling, F. Lübkemann, A. Mundstock, L. Lohaus, M. Haist, J. Caro, N. C. Bigall

Cem. Concr. Res. 159, **2022**, 106841.

<https://doi.org/10.1016/j.cemconres.2022.106841>.



Contents lists available at ScienceDirect

Cement and Concrete Research

journal homepage: www.elsevier.com/locate/cemconres

Is freeze-drying an alternative to solvent exchange for the hydration stop of cementitious suspensions?

Patrick A. Kießling^a, Franziska Lübke^a, Alexander Mundstock^a, Ludger Lohaus^b, Michael Haist^b, Jürgen Caro^a, Nadja C. Bigall^{a,*}^a Institute of Physical Chemistry and Electrochemistry, Leibniz Universität Hannover, Germany^b Institute of Building Materials Science, Leibniz Universität Hannover, Germany

ARTICLE INFO

Keywords:

Hydration stop
Time-variant analysis
Cementitious suspension
Freeze-drying

ABSTRACT

In order to understand the rheological properties of cementitious suspensions at early stages, among other phases, the formation of ettringite and its time-dependent influence, whether by amount or morphology, has to be examined in detail using a suitable method to stop the hydration process. It is state-of-the-art to exchange water with isopropanol, however, the water initially remains in the system possibly leading to reduced time resolution. Our group raised the question if freeze-drying or the combination of the water-isopropanol exchange with subsequent freeze-drying might be a suitable technique to achieve an almost complete hydration stop at any time. Recently, it was shown under which circumstances low-pressure characterization techniques can be employed without destroying the samples due to loss of crystal bound water. Here, by implementing these recent results, we show under which circumstances freeze-drying indeed can be employed as fast hydration stop method.

1. Introduction

In the early stages of the hydration of Portland cement, small needle-shaped crystals of ettringite are formed on the surface of cement particles, which have a noticeably impact on the suspension's rheological properties [1–7]. For a time-variant quantitative assessment of the influence of ettringite on the rheological properties, it is essential to gain knowledge about the amount of ettringite and its morphology at specific points of time during the early stage of hydration. This in turn requires a suitable method to stop the hydration process of cementitious suspensions at any possible time. In previous works by Wyrzykowski et al. [8] and Flatt et al. [9] it was stated that the reduction of relative humidity to 80% is sufficient to stop the hydration process. Here, Wyrzykowski et al. [8] showed that the hydration stop occurs under normal conditions and below a relative humidity of 80%, which takes several days (up to 10 days). The work of Flatt et al. [9] demonstrates a theoretical study of the kinetics of heat release by C₃S (alite) hydration and the evolution of ionic concentration in solution. In it, hydration stop under 80% relative humidity after a period of 90 days are shown. Here, below 80% relative

humidity, the hydration stops due to negative pressure within the capillary system of the porous structure. Since our work focuses on a different time scale (up to 90 min) and the early stages of hydration, where no porous system is formed, the distinct decrease of the water content seemed to be the most reproducible way to stop the hydration. To achieve a hydration stop, it is state-of-the-art to exchange the water matrix with an organic solvent, mostly isopropanol (iPrOH) [10,11]. In some studies it was shown that it is difficult to extract the iPrOH completely from the hydration stopped sample after the solvent exchange [12–16]. Alternatively, a suitable technique might be based on freezing with liquid nitrogen (LN₂) with subsequent freeze-drying [10]. Both methods possess specific advantages as well as disadvantages. The iPrOH-H₂O-exchange preserves the pore structure [17–19] but the surface of the hydrated cement is morphed, carbonate-like phases are likely to form already after an exchange time of several minutes [10,16,20], and certain hydration products are damaged [10,11,17–19,21]. The latter is due to the mechanical mixing process of the solvent exchange leading to a perturbation of the cement matrix and dehydration of ettringite [10,18,19,22]. In contrast, by submerging the cementitious

* Corresponding author.

E-mail addresses: patrick.kissling@pci.uni-hannover.de (P.A. Kießling), franziska.luebke@pci.uni-hannover.de (F. Lübke), alexander.mundstock@pci.uni-hannover.de (A. Mundstock), lohaus@baustoff.uni-hannover.de (L. Lohaus), haist@baustoff.uni-hannover.de (M. Haist), juergen.caro@pci.uni-hannover.de (J. Caro), nadja.bigall@pci.uni-hannover.de (N.C. Bigall).<https://doi.org/10.1016/j.cemconres.2022.106841>

Received 17 August 2021; Received in revised form 12 May 2022; Accepted 12 May 2022

Available online 18 June 2022

0008-8846/© 2022 The Authors. Published by Elsevier Ltd. This is an open access article under the CC BY-NC-ND license (<http://creativecommons.org/licenses/by-nc-nd/4.0/>).

suspension in LN₂ no perturbation and thus no damage to the microstructure occurs [23–25]. It was also shown that the combination of both aforementioned techniques, meaning a gradual hydration stop by iPrOH-H₂O-exchange combined with subsequent freeze-drying, has the great potential to complement their distinct advantages, having a hydration-stopped sample whose cement matrix remained undisturbed and being completely dry [26]. Nevertheless, low pressure treatment is suspected to diminish the early stage hydration product ettringite [10,11,27–31] which is generated within the first 90 min of hydration of cement (Table S1) [7]. Based on our recent results [32] about the influence of low pressure on the crystal structure, morphology, and chemical composition of ettringite, freeze-drying as a potential hydration stop technique is further developed and optimized regarding duration and level of low-pressure treatment. Hence, all steps implementing vacuum or low pressure treatment were performed under conditions that are non-invasive to ettringite's morphological and compositional stability.

Therefore, in this work, we report on the influence of three different hydration stop techniques on cement and its hydration product ettringite to find both, the most non-invasive and complete, as well as the fastest hydration stop technique. Fig. 1 illustrates the synthesis route of the three hydration stop techniques: (1) solvent exchange with iPrOH (Iso), (2) freezing with LN₂ and subsequent freeze-drying (FD), and (3) gradual solvent exchange with iPrOH, freezing with LN₂ and subsequent freeze-drying (IFD). To assess changes in the crystal structures induced by these three hydration stop techniques X-ray diffraction analysis (XRD) was performed. The change in the chemical decomposition behaviour, as well as the bound water content, were evaluated by thermogravimetric analysis (TGA). As imaging technique for the morphology of the hydration-stopped and anhydrous cement particles, environmental scanning electron microscopy (ESEM) was applied. In this work, the aforementioned characterization techniques were carried out as time-dependent measurements to discuss the morphological changes at different hydration states (10 min, 30 min, 60 min, and 90 min) using three different hydration stop techniques.

2. Materials and methods

2.1. Materials

The main materials for this study were Portland cement CEM I 42.5 R from Heidelberg Cement AG (in the following referred to as cement or

CEM I), anhydrous isopropanol (≥99.95%) and anhydrous copper sulphate (≥98%) from Carl Roth, Millipore water (18.2 MΩ·cm) cleaned by an Arium 611DI from Sartorius (in the following referred to as water) and liquid nitrogen (≥99.999%) from Linde. As an internal standard for XRD measurements silicon (97.5%) from Riedel-de Haën was used. The cement was stored at ambient temperature (20 °C ± 2 °C) and humidity (18%–45%) for the whole study.

2.2. Methods

2.2.1. Cementitious suspension

Following the mixing program shown in Table 1, cementitious suspensions with a water to cement ratio w/c = 0.5 and a total volume of 500 mL were prepared. 610 g cement and 305 mL water (precooled to 10 °C) was mixed with a balloon whisk using a Kenwood KitchenAid KM336 S Chef Classic to simulate concrete mixing as usually performed at larger scales. During the first 10 min, the mixture's temperature rose to 20 °C. The last step of slow stirring at level 2 (approx. 72 rpm) was performed for different durations (6, 26, 56, and 86 min) to investigate the reaction kinetics. Afterwards, all samples were withdrawn for hydration stoppage, dried, and stored at 19.2 °C ± 0.4 °C in a dry nitrogen atmosphere for 0 to 2 d before characterization was performed.

2.2.2. Procedure for solvent exchanged samples (Iso)

After a total reaction duration of 10 min, 30 min, 60 min, and 90 min after adding water, 10 mL of the cementitious suspension were taken with an Eppendorf pipette, instantly transferred into 50 mL anhydrous isopropanol (precooled to 5 °C) in falcon tubes and agitated for 5 min at

Table 1
Mixing program for cementitious suspensions.

Step	Duration	Mode (Kenwood KitchenAid) [rpm]
Dry mixing of CEM I	60 s	Level 2 [approx. 72]
Adding water	30 s	Level 2 [approx. 72]
Pre-homogenisation	15 s	Level 2 [approx. 72]
Homogenisation	15 s	Maximum [approx. 220]
Stop and manually scraping off	60 s	Off
Homogenisation II	120 s	Maximum [approx. 220]
Slow stirring	Until stopped	Level 2 [approx. 72]

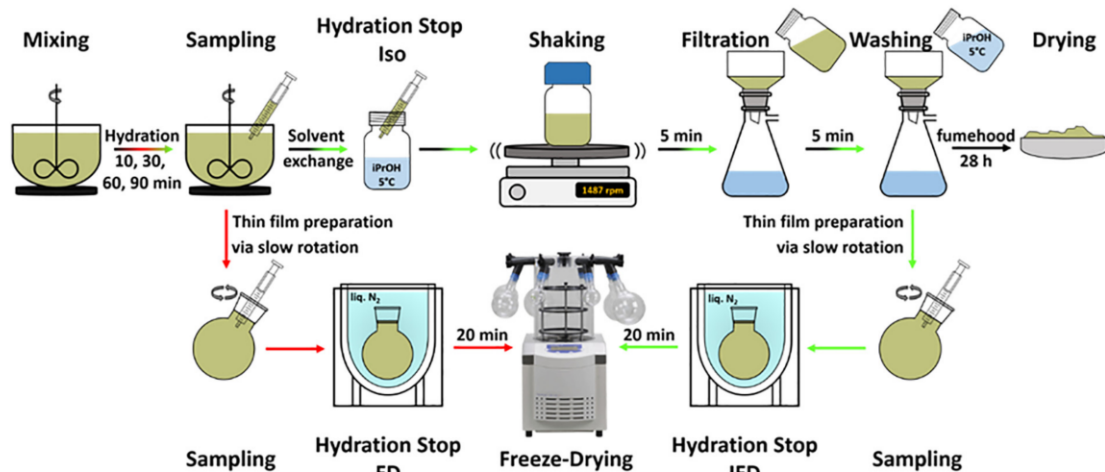


Fig. 1. Scheme of hydration stop by isopropanol-water exchange (Iso, synthesis route in black arrows), freezing with liquid nitrogen and subsequent freeze-drying (FD, synthesis route in red arrows), and isopropanol water exchange with subsequent freezing with liquid nitrogen and successive freeze-drying (IFD, synthesis route in green arrows). (For interpretation of the references to colour in this figure legend, the reader is referred to the web version of this article.)

1487 rpm with a shaker (Multi Reax by Heidolph Instruments GmbH & Co. KG), so no mechanical stirring was performed. Using a Buchner funnel the iPrOH-H₂O-suspension was filtrated using a fibreglass filter (retention 0.4 µm, MN-GF 5 by Macherey-Nagel GmbH & Co. KG). The sample was washed twice by adding 50 mL anhydrous isopropanol (precooled to 5 °C), filtrated for 5 min, and stored under ambient conditions (19.2 °C ± 0.4 °C) for 28 h in the fume hood (Fig. 1). This procedure is referred to as **Iso**. To address the possible influence of drying under ambient conditions instead of vacuum drying, five repetitions with vacuum-drying at 4 mbar for 3 h (**Iso**²) were done and analysed by TGA.

2.2.3. Procedure for subsequent freeze-drying (FD)

After a total reaction duration of 10 min, 30 min, 60 min, and 90 min after adding water, 10 mL of the cementitious suspension were taken with an Eppendorf pipette, transferred to a 250 mL flask, which was slowly rotated to get a homogenous thin layer of cementitious suspension, and transferred quickly into LN₂ (−196.15 °C) for 20 min. Each sample was freeze-dried using a freeze-dryer (Alpha 1–2 LDplus from Martin Christ Gefriertrocknungsanlagen GmbH) coupled with a two-stage rotary vane pump (RV 12 from Edwards Vacuum) for 3 h at 4 mbar (Fig. 1). This procedure is referred to as **FD**.

2.2.4. Procedure for solvent exchanged samples with subsequent freeze-drying (IFD)

After a total reaction duration of 10 min, 30 min, 60 min, and 90 min after adding water, 10 mL of the cementitious suspension were taken with an Eppendorf pipette, instantly transferred into 50 mL anhydrous isopropanol (precooled to 5 °C) in falcon tubes and agitated for 5 min at 1487 rpm with a shaker (Multi Reax), so no mechanical stirring was performed. Using a Buchner funnel the iPrOH-H₂O-suspension was filtrated using a fibreglass filter (retention 0.4 µm). The sample was washed twice by adding 50 mL anhydrous isopropanol (precooled to 5 °C) and filtrated for 5 min. Each humid sample was transferred first into a 100 mL flask and second quickly into LN₂ for 20 min. All samples were freeze-dried using a freeze-dryer (Alpha 1–2 LDplus) coupled with a two-stage rotary vane pump (RV 12) for 3 h at 4 mbar (Fig. 1). This procedure is referred to as **IFD**.

2.2.5. Dryness test

To assess the residual water content of the samples after the hydration stop, anhydrous copper sulphate [CuSO₄] (up to 5 mg for freeze-dried and 50 mg up to 200 mg for solvent exchanged samples) was added to 1.0 g of the samples. If the residual water content was at least five times the molar amount of CuSO₄, hydration to copper sulphate pentahydrate [CuSO₄ · 5 H₂O] [33–37], indicated by a deep blue colour, occurred.

2.2.6. X-ray diffraction

The crystallinity was investigated by X-ray diffraction (XRD) using a Bruker D8 Advance in reflection mode. It was operated at 20 °C, 40 kV, and 40 mA using Cu-K_α radiation. Each measurement was done in a 2θ-range from 5° to 85°, with a step size of 0.010540856°, and 4 s per step, resulting in a total measurement time of 8.75 h. Additionally, to ensure ettringite being present, a zoom-in of the diffractogram was done in a 2θ-range from 8° to 10°, with a step size of 0.010540856°, and 12 s per step, resulting in a total measurement time of 1.62 h. The powder of each sample was transferred into an X-ray amorphous PVC powder carrier and smoothed, to avoid sample displacement. The diffraction patterns were evaluated by the database of Powder Diffraction File (PDF-2) 2020 of the International Centre for Diffraction Data (ICDD).

Furthermore, the phase ratio in anhydrous cement was evaluated by Rietveld refinement [38,39] using literature data [40–54], the measured XRD data of this work, and the software TOPASv6 by Bruker.

2.2.7. Thermogravimetric analysis

To evaluate the content of bound water (mainly from ettringite) any dried sample was investigated by thermogravimetric analysis (TGA) using a TGA/DSC 3+ from Mettler-Toledo GmbH. The samples were transferred into aluminium oxide crucibles (70 µL), before measurement. It was operated in a temperature range from 20 °C to 1100 °C under a nitrogen flow of 25 mL/min, a heating ramp of 5 K/min followed by holding the temperature at 1100 °C for 15 min. The data was normalized by mass (mg), derived once by time (s), multiplied by 3600 (for plotting in h) and plotted against temperature (°C).

Based on the results of Jakob et al. [7] dealing with the content of C-S-H and ettringite at different hydration stages, we stated that the decomposition at 130 °C ± 80 °C is attributed solely to ettringite because at this point of hydration according to observations from literature [7,57,55–57], we assume that no detectable amount of C-S-H is formed. The right shoulder of this decomposition peak could also belong to gypsum [10,58,59]. Additionally, we always compared the decomposition integral at 127.5 °C ± 17.5 °C with the integral at 445 °C ± 25 °C, which both belong to gypsum. Its ratio stayed essentially identical, so its contribution to the integral at 130 °C ± 80 °C changed only marginal. Therefore, we used the integral at 130 °C ± 80 °C for comparison of decomposition behaviour of ettringite. Nevertheless, it was recently shown by Zhang et al. [16] that after a solvent exchange with iPrOH, the solvent could not be released under normal conditions, therefore, it has to be clarified, that in the cases of **Iso** and **IFD** the first decomposition peak might be influenced by the unknown amount of chemically bound iPrOH [10].

2.2.8. Nitrogen physisorption

To assess the specific surface area and the specific volume of hydrated cement, nitrogen (N₂) physisorption was performed at a NOVA 3000e from Quantachrome GmbH & Co KG operating at 77 K. Before physisorption measurements, the samples were degassed under vacuum at 298 K for 24 h. Specific surface area and specific volume were estimated by applying the Brunauer-Emmett-Teller (BET) [60] equation. Pore volume was estimated at p/p₀ = 0.95345 by applying Density Functional Theory (DFT) [61,62] as well as pore size distributions by applying DFT [61,62] and Barrett-Joyner-Halenda (BJH) [63].

2.2.9. Environmental scanning electron microscopy and particle size distribution

To assess the morphology of the dried samples, environmental scanning electron microscopy (ESEM) using a Zeiss Supra VP 55, equipped with a cold field emission gun and a 4 Quadrant Backscatter Electron Detector (QBSD) was used as an imaging method. The acceleration voltage was 10 kV, the current 6 nA, and the pressure 1.0 mbar for each measurement. The powder was transferred onto an adhesive carbon disk and was cleaned from an excess sample through a compressed air gun. Each sample was degassed in the antechamber for 2.5 min for safety reasons. At a pressure of 375 nbar in the antechamber, the “Variable Pressure” mode was started. The particle size distribution for each hydration state was achieved by the evaluation of eight ESEM micrographs with a magnification of 1000 times, wherein 1000 ± 50 particles from two out of five syntheses were measured with the software ImageJ 1.52a.

2.2.10. Prolonged hydration duration

To compare the four different hydration stop techniques (**Iso** [drying under ambient conditions for 28 h in the fumehood], **Iso**² [drying directly after filtration for 3 h @ 4 mbar], **FD**, and **IFD**) at later hydration states (9 h, 16.5 h, and 24 h) at which an appreciable amount C-S-H has formed, two repetitions were done, analysed by TGA and XRD, and evaluated. The results are shown and discussed in the Supplementary Data (Figs. S9 and S10).

3. Results and discussion

3.1. Portland cement CEM I 42.5 R

The anhydrous Portland cement CEM I 42.5 R was analysed using ESEM, TGA, and XRD to assess the state before hydration took place. ESEM micrograph (Fig. 2a) shows a non-homogeneous particle size distribution with a mean size of $d_{50} = 4.2 \mu\text{m} \pm 0.1 \mu\text{m}$. The TGA measurements were performed at three different heating ramps (5 K/min, 10 K/min, and 25 K/min) and the TGA spectra (Fig. 2b) show two aspects. Firstly, the usage of a steeper heating ramp leads to a decomposition slightly shifted to a higher temperature, as the system has less time to spread the thermal energy. Thus, all further TGA measurements were conducted using the lowest heating ramp of 5 K/min. Secondly, for the anhydrous cement, the following decomposition processes were identified: (1) dehydration of adsorbed water until roughly 100 °C, (2) decomposition of gypsum [$\text{CaSO}_4 \cdot 2 \text{H}_2\text{O}$] at $127.5 \text{ °C} \pm 17.5 \text{ °C}$ as well as at $445 \text{ °C} \pm 25 \text{ °C}$ [10,58,59,64–66], and (3) calcite [CaCO_3] at $645 \text{ °C} \pm 125 \text{ °C}$ [58,59,66,67].

Fig. 3 shows the diffractograms of CEM I (black), synthetic C_3S (Ca_3SiO_5 , green), synthetic C_3A ($\text{Ca}_3\text{Al}_2\text{O}_6$, red) and its most prominent reflections in a range of $10^\circ \leq 2\theta \leq 71^\circ$ ($I_{\text{reflection}} > 0.1 I_{\text{max}}$), which align with the literature data [40–54]. Further, the identified phases (C_3A orthorhombic, C_3A cubic, C_3S , C_2S , CaSO_4 , C_4AF , MgO , $\text{CaSO}_4 \cdot 0.5 \text{H}_2\text{O}$,

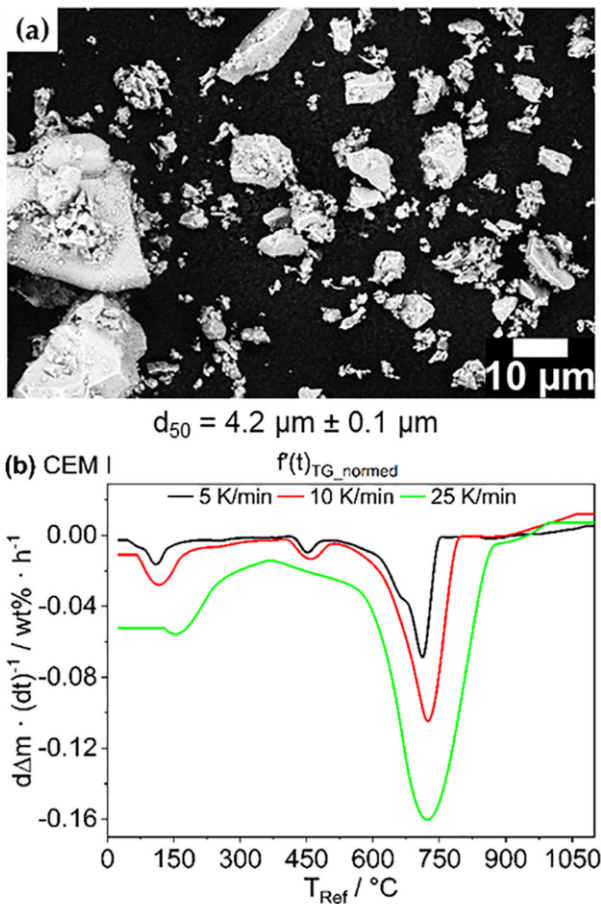


Fig. 2. (a) ESEM micrograph of anhydrous cement with mean particle size d_{50} and (b) TGA data plotted as normalized weight loss per hour against the temperature of anhydrous CEM I with different heating ramps (5 K/min, 10 K/min, and 25 K/min).

CaO , and SiO_2) and their ratio derived from Rietveld refinement (purple) [38,39] match the data shown by Lu et al. [68] with slight differences in their respective intensities (Fig. 3b).

3.2. Hydration stop of cementitious suspension

The hydration process of cementitious suspensions with a water to cement mass ratio of $w/c = 0.5$ was stopped at four defined times (10 min, 30 min, 60 min, and 90 min after the addition of water) by three different techniques (Iso, FD, and IFD). In order to demonstrate the reproducibility of all hydration stop techniques, five equal repetitions of the syntheses and characterisations with each analytical technique were conducted. The hydration stop enables the analysis of the cementitious suspension with slow techniques as N_2 physisorption, XRD, TGA, and ESEM to evaluate the influence of the hydration process on the chemical composition and morphology of cement. This includes information about the formation of the hydration product ettringite as well as the influence of the applied hydration stop method on the specific surface area, specific volume, porosity, crystal phases, morphology, and the content of bound water in the cementitious suspensions. To assess the possibility of further hydration processes after drying, a copper sulphate test was conducted. This test showed that in the case of solvent exchange (Iso), residual water was present, while methods involving freeze-drying (FD and IFD) yielded totally dry samples. Consequently, in the latter two cases further growth (after employing the hydration stop method) can be ruled out, while in the case of Iso, further hydration reactions might still occur.

3.2.1. Nitrogen physisorption

To gain knowledge about the anticipated changed morphology of cement grains after hydration, ad- and desorption behaviour during N_2 physisorption was examined. The isotherms (Figs. S1–S5) show small hysteresis, with varying width at different hydration durations and by different hydration stop techniques. The broadest hysteresis results from using the gradual IFD method. Fig. 4 summarizes the evaluation of the specific surface area (Fig. 4a), as well as specific volume (Fig. 4b), which shows a small increase for all techniques and durations of hydrated cement paste. It is noticeable that the combined technique IFD leads to the highest specific surface area and volume followed by Iso and FD, with a maximum after 30 min of hydration. This finding can be explained as the remaining water leads to further hydration of solvent exchanged samples (Iso), resulting in bigger ettringite crystals on the surface and therefore higher specific surface area and volume. The increasing specific surface area and volume itself can be explained by looking at the reaction's course. During hydration, early hydration products are formed on cement particles' surfaces, which leads to an increase of the specific surface area. It can be assumed that this process is more dominant than the agglomeration of the cement particles, which occurs simultaneously during the reaction and would possibly lead to a reduced specific surface area [69].

The pore size distribution (Fig. 5a–c) derived from N_2 physisorption measurement shows only a slight but homogenous increase of the mean pore size p_{50} relative to anhydrous cement (Fig. 5d+e). Compared to the starting material CEM I (0 min), the pore size distribution after hydration becomes broader independent of the applied hydration stop technique. This behaviour can be explained by the presence of various hydration products leading to larger surface roughness and hence to both a larger specific surface area and a larger amount of small pores.

For the sake of clarity, we note that the shown pore size distribution cannot directly be transferred to real cementitious materials, as it is most likely that the drying process leads to different pore sizes [70,71]. The reason is that during the first hours of cement hydration no robust structure occurs, which in turn conserves the pore structure during hydration. Furthermore, it can be derived that for cement samples the change of pore sizes in the nanometre range, as well as the change of surface area, is of the same order of magnitude for all three hydration

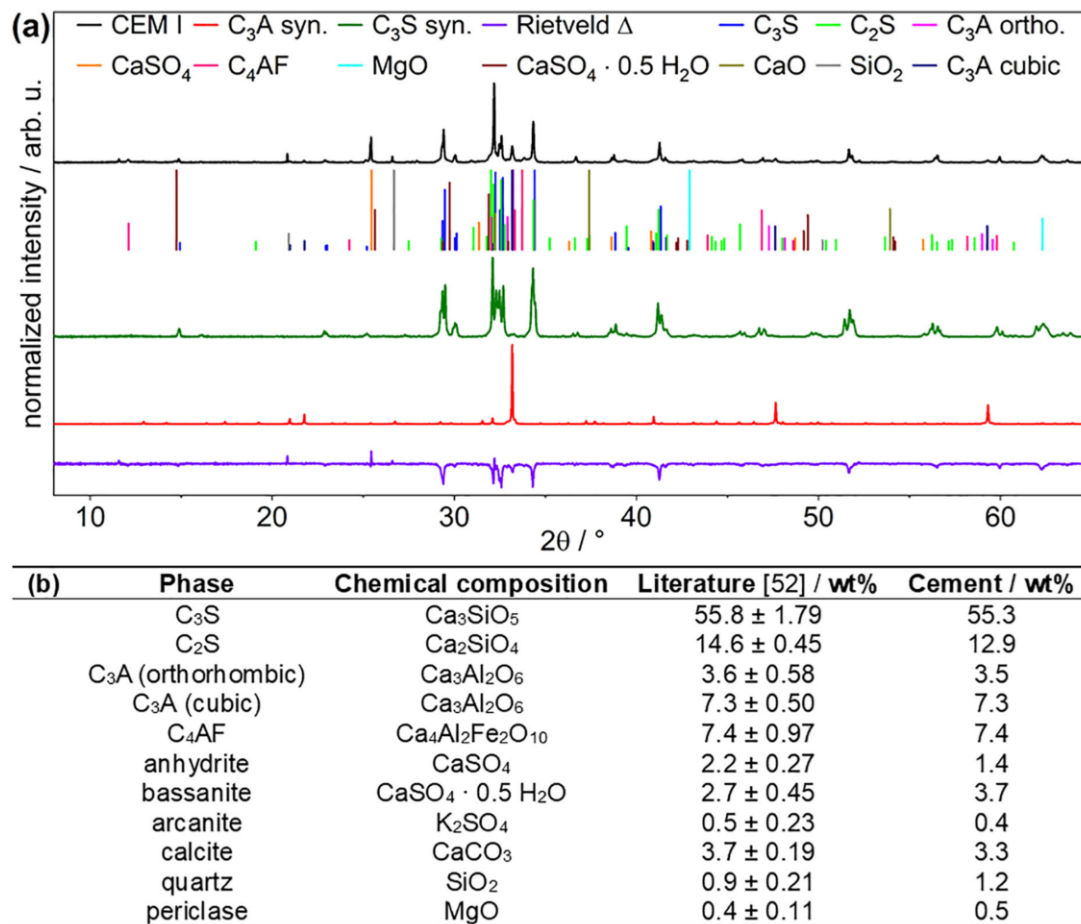


Fig. 3. (a) Powder X-ray diffraction pattern of anhydrous cement, its synthetic main components C₃S and C₃A, literature reflections for all identifiable phases [40–54], the result of Rietveld-refinement indicated by difference, and (b) phase content of anhydrous Portland cement CEM I 42.5 R derived by Rietveld-refinement compared to data by Lu et al. [68].

stop techniques. This indicates that all three methods indeed lead to a reaction stop.

Summarizing, evaluation of physisorption measurements showed at each specific duration and hydration stop technique the same direction of change of specific surface area, volume and pore size distribution of stopped cementitious suspensions relative to anhydrous cement. **Iso** has always the lowest value which could be an indication for the breakdown of ettringite occurring after a hydration duration of several hours [72].

3.2.2. X-ray diffraction

To link the aforementioned changes to the specific surface area, volume and pore size distribution with the presence of ettringite, XRD is employed. The diffractograms (Fig. 6) of the samples dried with the freeze-drying method (**FD**) proved their effectiveness, as all of the samples (100%, 20 of 20 measured samples), show, independent of the hydration duration, a distinct ettringite reflection in the range of $8^\circ \leq 2\theta \leq 10^\circ$ (Fig. 6b). Meanwhile, samples stopped by the state-of-the-art method **iPrOH-H₂O-exchange (Iso)** show a distinct (45%, 9 of 20 measured samples) and a weak noisy ettringite reflection (55%, 11 of 20 measured samples). The combination of both techniques (**IFD**) shows identical results as **Iso** (Fig. 6b).

Summarizing, the evaluation of XRD micrographs indicates that the hydration stop technique **FD** prevented the dehydration of ettringite in all 20 investigated samples, but in the case of **Iso** and **IFD** only 9 samples

(45%) had a distinct ettringite reflection. Therefore, XRD results seem to indicate that **FD** is possibly a more suited hydration stop technique to preserve ettringite, which can enable a time-variant analysis of cementitious suspensions. However, constant growth of ettringite's content in the cementitious suspensions could not be derived from the XRD data.

3.2.3. Thermogravimetric analysis

The results shown by XRD measurements are confirmed by thermogravimetric analysis (TGA) (Fig. 7). Evaluation of samples stopped by the **FD** method (Fig. 7b) shows, compared to anhydrous cement, an enhanced dehydration peak at $130^\circ\text{C} \pm 80^\circ\text{C}$, which aligns with preserved ettringite [32]. In contrast, the samples stopped by the **Iso** method as well as the **IFD** method show a less pronounced dehydration peak at $130^\circ\text{C} \pm 80^\circ\text{C}$, which is due to the lower ettringite content as also observed by aforementioned XRD investigations. The integral of this first dehydration peak varies depending on the applied hydration stop technique and hydration duration, i.e. **FD** > **Iso** > **IFD** and 90 min > 60 min > 30 min > 10 min. The anhydrous cement's degree of gypsum at $127.5^\circ\text{C} \pm 17.5^\circ\text{C}$ and $445^\circ\text{C} \pm 25^\circ\text{C}$ [10,58,59,64–66] as well as the content of calcite at $645^\circ\text{C} \pm 125^\circ\text{C}$ [58,59,66,67] did not change during hydration for each applied drying technique. In case of **Iso** and **IFD** it is not possible to state that the first dehydration peak at $130^\circ\text{C} \pm 80^\circ\text{C}$ belongs solely to ettringite because it was shown previous studies that adsorbed **iPrOH** is also released in this temperature range [15].

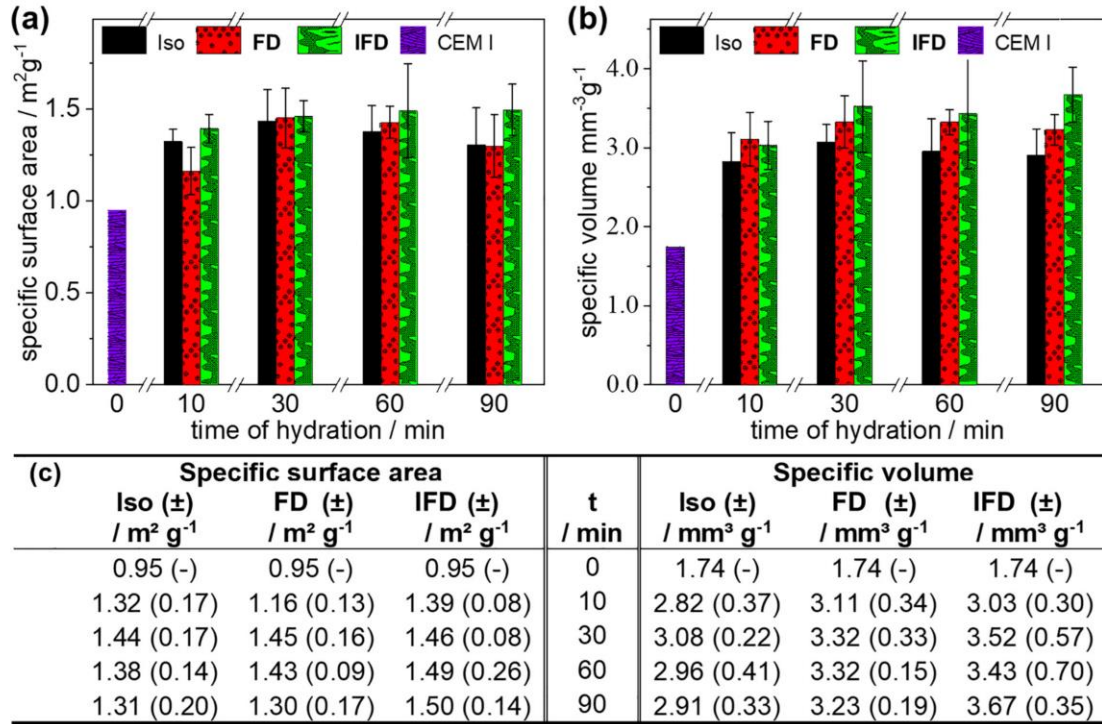


Fig. 4. N₂ physisorption data; (a) specific surface area, (b) specific volume of anhydrous and hydrated CEM I; stopped after various hydration durations (up to 90 min) by three different techniques (Iso, FD, and IFD), and (c) respective values; corresponding isotherms in Figs. S1–S5.

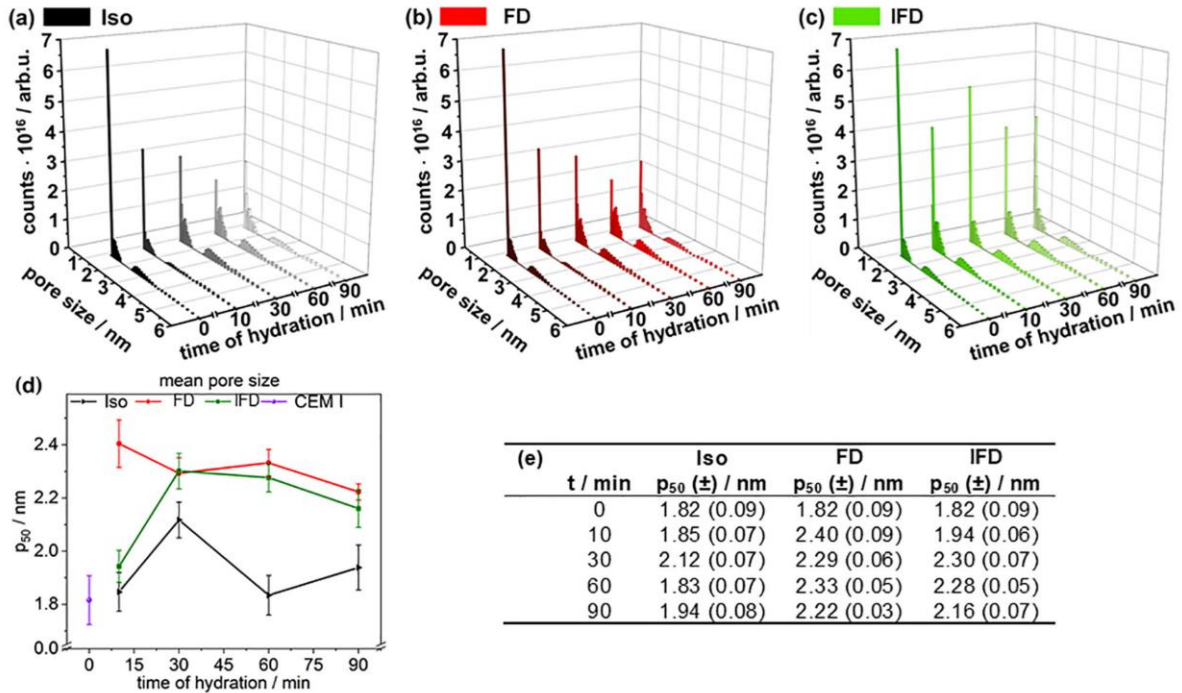


Fig. 5. N₂ physisorption measurement; pore size distribution of anhydrous and hydrated cement stopped after various hydration durations (up to 90 min) by three different techniques (a) Iso, (b) FD, and (c) IFD, (d) mean pore size p₅₀ of anhydrous and hydrated cement, and (e) corresponding mean values.

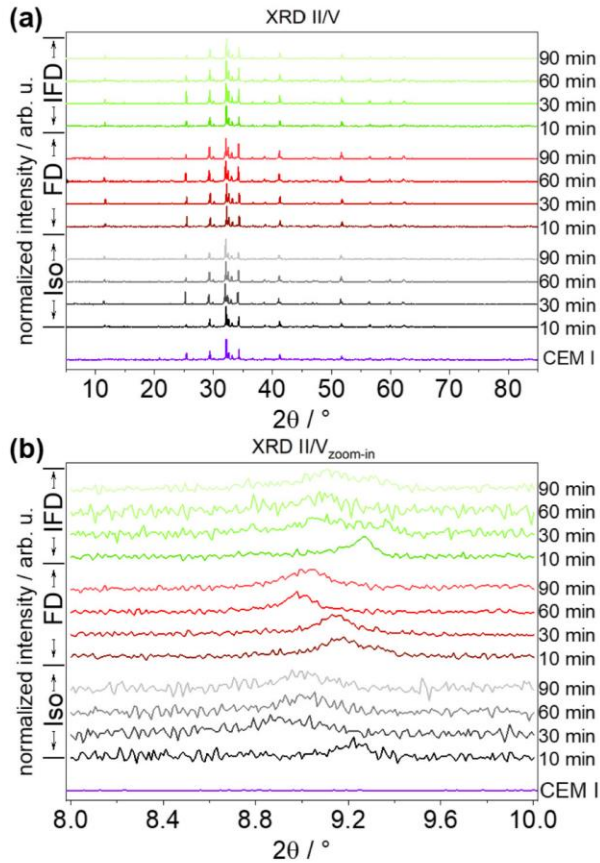


Fig. 6. Powder X-ray diffraction patterns of anhydrous and hydrated CEM I stopped after various hydration durations (up to 90 min) by three different techniques (Iso, FD, and IFD) in an angle range of (a) $5^\circ \leq 2\theta \leq 85^\circ$ and (b) $8^\circ \leq 2\theta \leq 10^\circ$; complete overview in Fig. S6.

Additionally, Trenwith [73] showed the decomposition of iPrOH being at $488^\circ\text{C} \pm 40^\circ\text{C}$, however, within the present work the described process has no significant influence in this temperature range.

These findings suggest that freeze-drying retains the highest amount of ettringite, which aligns with XRD results. Furthermore, FD has the advantage that one parameter less has to be considered, as in the proposed FD technique no solvent exchange is needed. Therefore, freeze-drying FD seems to be superior to or at least on par with the state-of-the-art iPrOH-H₂O-exchange technique Iso and the combined iPrOH-H₂O-exchange freeze-drying technique IFD.

To assess the influence of the drying technique after isopropanol-water exchange, two types of drying, (1) under ambient conditions ($19.2^\circ\text{C} \pm 0.4^\circ\text{C}$) for 28 h in the fume hood (Iso) and (2) vacuum drying at 4 mbar for 3 h (Iso²) were implemented and analysed by TGA (Fig. 8). Both techniques point to the same result that at this early stage of hydration no influence of the applied drying technique is distinguishable. The evaluation by TGA shows that the main decomposition peak of ettringite at $130^\circ\text{C} \pm 80^\circ\text{C}$ has nearly the same topology for both solvent exchange-based hydration stop techniques (Iso² and Iso). Differences are slightly visible at $445^\circ\text{C} \pm 25^\circ\text{C}$ belonging to gypsum [10,58,59,66,64–66] and more distinguishable at $645^\circ\text{C} \pm 125^\circ\text{C}$, wherein at hydration stages (up to 60 min) the integral of samples stopped by Iso² are steeper, indicating a higher amount of calcite [58,59,66,67] in these samples. Therefore, in our opinion the used drying under ambient conditions (Iso) is as applicable as vacuum drying at 4 mbar for 3 h or even better suited at these early hydration states.

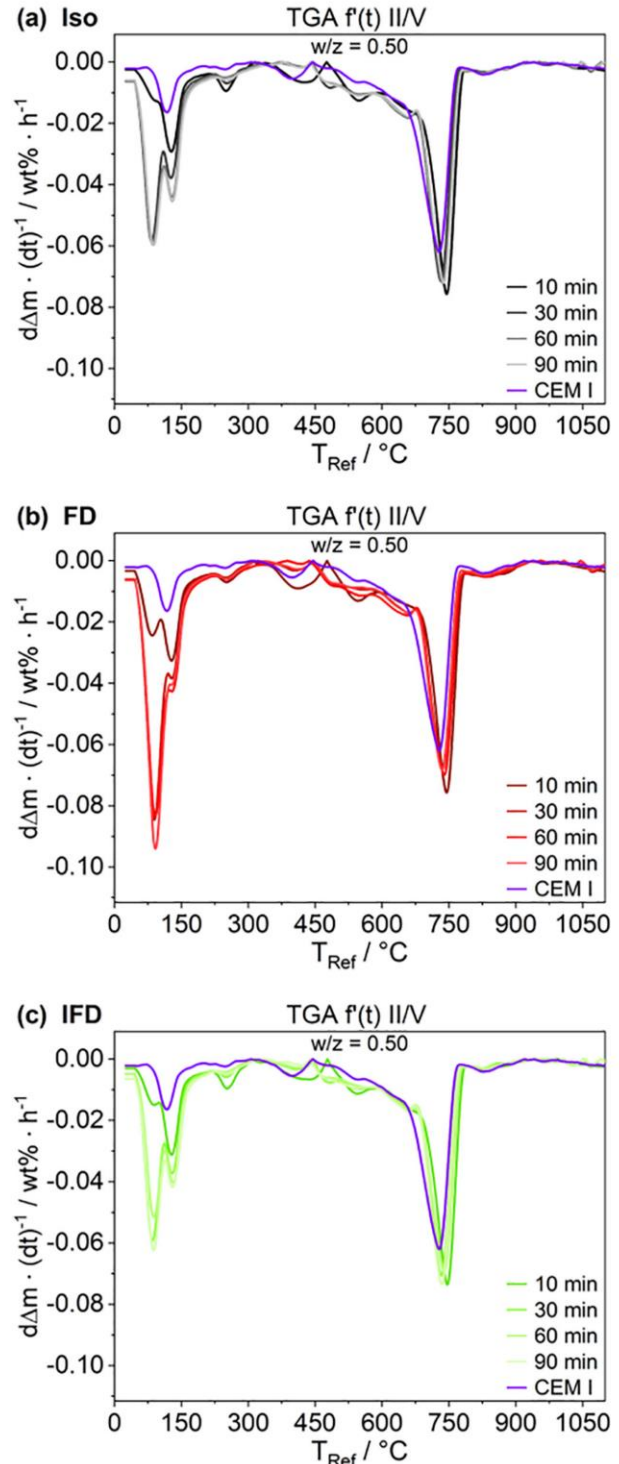


Fig. 7. TGA data plotted as mass normalized time derived weight loss ($d\Delta m \cdot (dt)^{-1} / \text{wt}\% \cdot \text{h}^{-1}$) against the reference temperature of anhydrous and hydrated CEM I with a heating rate of 5 K/min; stopped after various hydration durations (up to 90 min) by three different techniques (a) Iso, (b) FD, and (c) IFD; complete overview in Fig. S7.

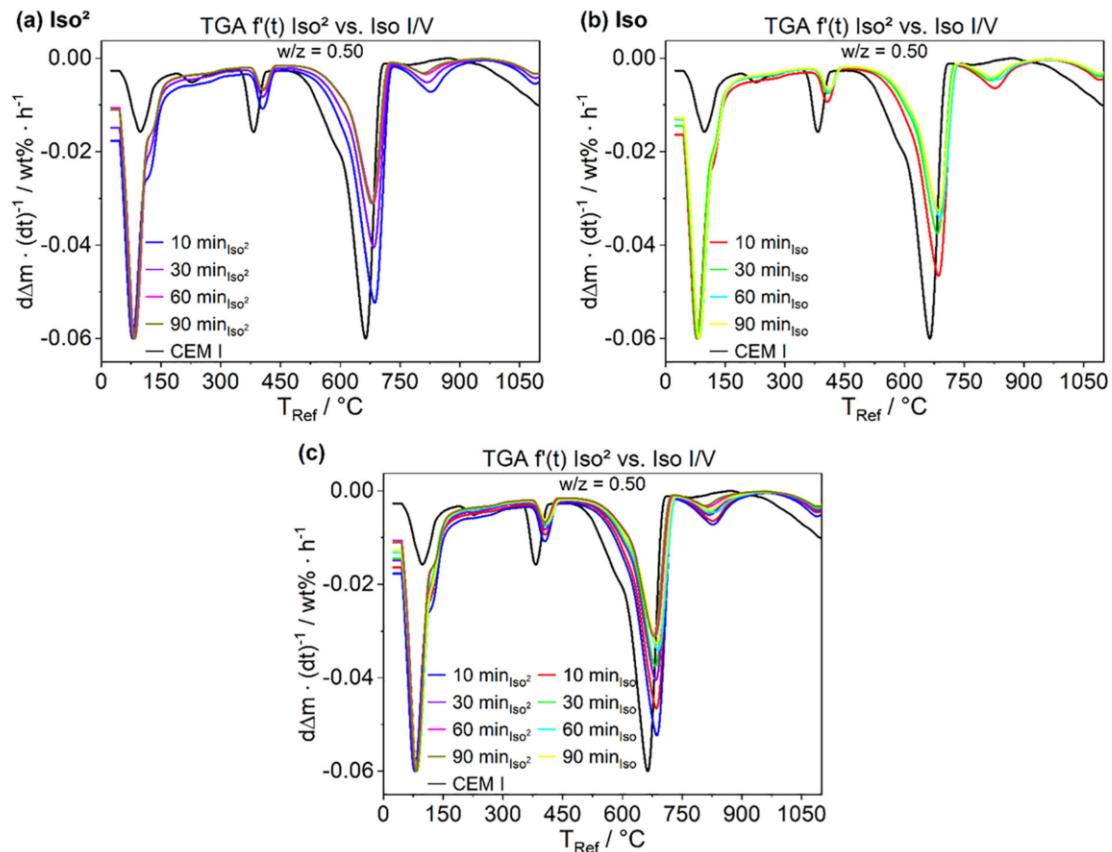


Fig. 8. TGA data plotted as mass normalized time derived weight loss ($d\Delta m \cdot (dt)^{-1}$) per hour against the reference temperature of anhydrous and hydrated CEM I with a heating rate of 5 K/min; stopped after various hydration durations (up to 90 min) Iso and Iso²; (a) Iso², (b) Iso, and (c) direct overlay; complete overview in Fig. S8.

3.2.4. Environmental scanning electron microscopy

Finally, to visualize the particles' morphology and texture environmental scanning electron microscopy (ESEM) was employed (Fig. 9). Their visual reproducibility was verified by taking micrographs of different syntheses of the same hydration state. It is noticeably that after different hydration durations (up to 90 min) independent of the applied hydration stop technique (Iso, FD, and IFD) the particles are non-homogeneously distributed, but a higher amount of small particles, relative to anhydrous cement (Fig. 2a), is detectable. The surfaces of the bigger particles seem to be less rough, leading to the assumption that these are non-reacted C₃S particles, as the hydration process of C₃S starts only after several hours [6,10,74–76].

Additionally, based on the ESEM micrographs, particle size distributions, as well as mean particle sizes, were evaluated (Fig. 10). Differences in the distribution of the particles, independent of the hydration stop technique applied, are marginal (Fig. 10a–c). The mean particle size (Fig. 10d+e) of freeze-dried samples (FD) decreases by 17% (from 4.21 μm to 3.49 μm , 0.83 $d_{50, \text{CEM I}}$) over the first 10 min, rises slightly by 6% (from 3.49 μm to 3.69 μm , 0.88 $d_{50, \text{CEM I}}$) to its maximum after 30 min of hydration, whereby the longest hydration duration of 90 min shows the smallest particles (2.99 μm , 0.71 $d_{50, \text{CEM I}}$). Solvent exchange (Iso) leads to a similar decrease by 20% (from 4.21 μm to 3.30 μm , 0.80 $d_{50, \text{CEM I}}$) over the first 10 min of hydration, rises by 18% (from 3.30 μm to 3.97 μm , 0.94 $d_{50, \text{CEM I}}$), decreases again by 7% (from 3.97 μm to 3.68 μm , 0.87 $d_{50, \text{CEM I}}$) and reaches its maximal particle size after 90 min (4.27 μm , 1.01 $d_{50, \text{CEM I}}$). The combination of both techniques (IFD) shows a less pronounced decrease by 12% (from 4.21 μm to 3.69 μm , 0.88 $d_{50, \text{CEM I}}$)

over the first 10 min, rises by 15% (from 3.69 μm to 4.25 μm , 1.01 $d_{50, \text{CEM I}}$) after 30 min and 60 min (4.20 μm), before a decay of 13% (from 4.20 μm to 3.67 μm , 0.87 $d_{50, \text{CEM I}}$) is visible. The stagnating growth could be explained as at the dormant stage, which has been reported to be between 30 min and 90 min [69], the hydration kinetics are reduced, which in turn means that the forming of hydration products on the surface of cement particles is in equilibrium with the agglomeration of the cement particles. After a short hydration period of 10 min, freeze-dried samples show a slightly higher d_{50} -value compared to samples treated with isopropanol (Iso and IFD). Although, the following hydration period shows larger particle sizes for solvent exchanged samples (Iso and IFD). The larger particles could be, as previously hypothesized [26], identified as agglomerations of smaller particles induced by iPrOH treatment, although the difference is less concise.

In summary, the imaging technique ESEM reveals, dependent on the applied hydration stop technique (Iso, FD, and IFD), small differences in the respective particle size distribution, and ESEM reveals growing particles with longer hydration duration and points out that solvent exchange with iPrOH leads to enlarged particles.

4. Conclusions

The method used to stop the hydration of cementitious suspensions, namely freeze-drying of samples frozen in liquid nitrogen (FD), solvent exchange with isopropanol (Iso), and solvent exchange with subsequent freeze-drying (IFD), has an impact on the mineralogical composition as well as the morphology of hydrated Portland cement (CEM I 42.5 R). It

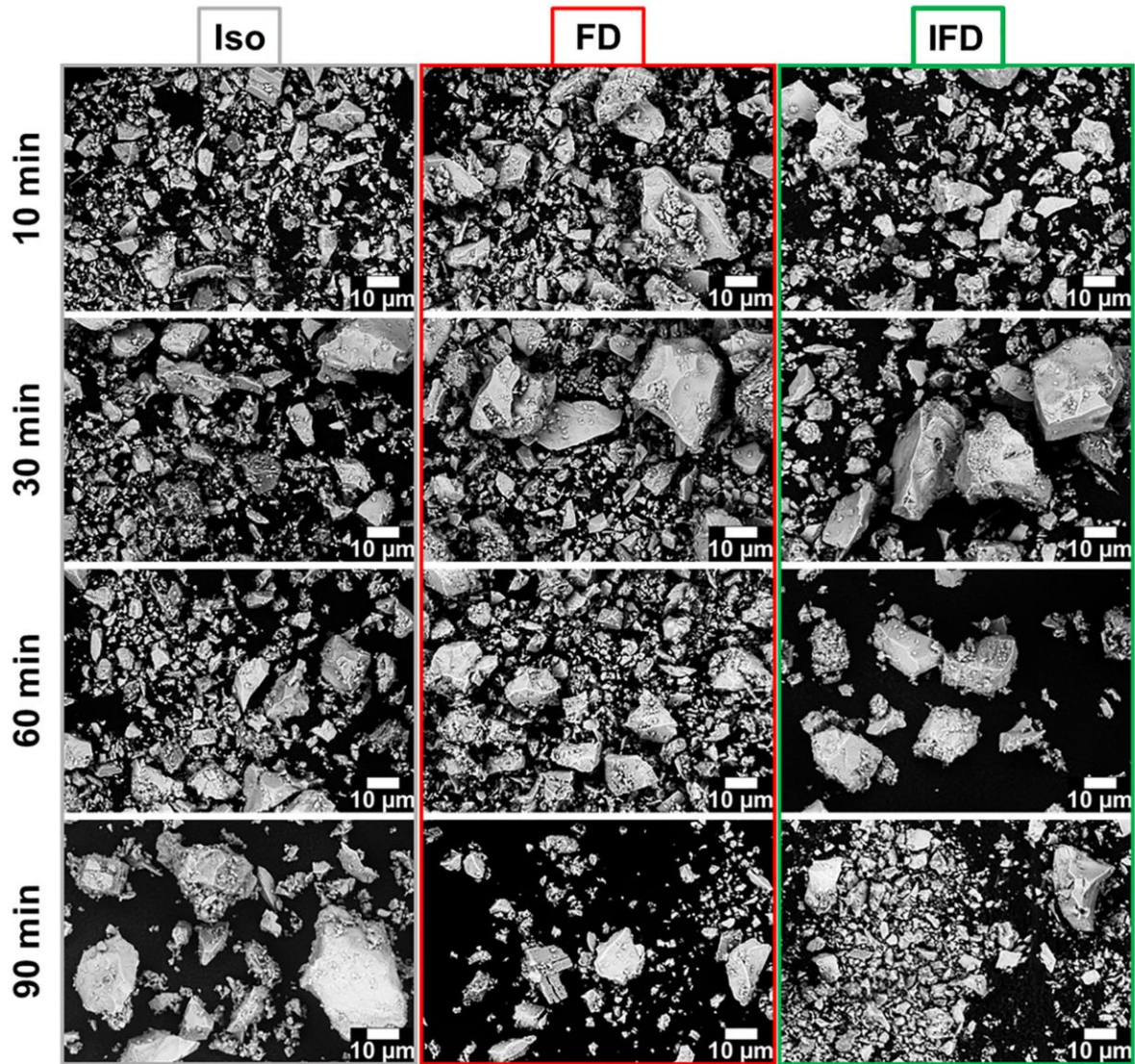


Fig. 9. ESEM micrographs of hydrated cement stopped after various hydration durations (up to 90 min) by three different techniques (Iso, FD, and IFD); 1.0 mbar, 6 nA, and 10 kV.

was shown by X-Ray diffraction (XRD) and thermogravimetric analysis (TGA) that the technique **FD** preserves the highest amount of ettringite at every hydration stage (10 min, 30 min, 60 min, and 90 min). Methods using solvent exchange with isopropanol (**Iso** and **IFD**) lead to an inconsistent degree of ettringite at the aforementioned hydration stages. These results are supported by nitrogen physisorption measurements of treated samples, wherein the specific surface area and the volume indicate the growth of ettringite. Noteworthy, **Iso** and **IFD** show their respective maxima earlier compared to **FD**. This can be explained by the fact that the use of **Iso** has the disadvantage that after the solvent exchange the samples are not water-free, which in turn might lead to further hydration of the cementitious suspension as well as undermines the idea of a time-variant analysis since it is not known in which hydration state the sample was stopped. The particle size distribution derived from environmental scanning electron microscopy (ESEM) showed only a slight change compared to anhydrous cement. Nevertheless, ESEM depicts, dependent on the applied hydration stop technique (**Iso**, **FD** and **IFD**), small differences in the respective particle size

distribution, shows growing particles with longer hydration duration, and points out that solvent exchange with iPROH leads to enlarged particles.

The freeze-drying technique (**FD**) shown in this article was optimized to the point that it is a suitable technique to stop the hydration process of cementitious suspensions nearly instantly without disturbing the cement matrix, damaging or morphing the surface of hydrated cement, as well as without changes to the chemical composition e.g. formation carbonate-like phases. The freeze-drying technique (**FD**) enables the hydration to be stopped completely after defined hydration durations, enabling a precise time-variant analysis of the hydrated cement. The proposed freeze-drying technique (**FD**) allows compared to **Iso** and **IFD** the preparation of more reproducible samples and further, has the advantage that one parameter less has to be considered as no solvent exchange is needed. Therefore, freeze-drying (**FD**) seems to be a superior alternative to the state-of-the-art method, solvent exchange with isopropanol (**Iso**).

Supplementary data to this article can be found online at <https://doi.org/10.1016/j.cemconres.2022.106841>.

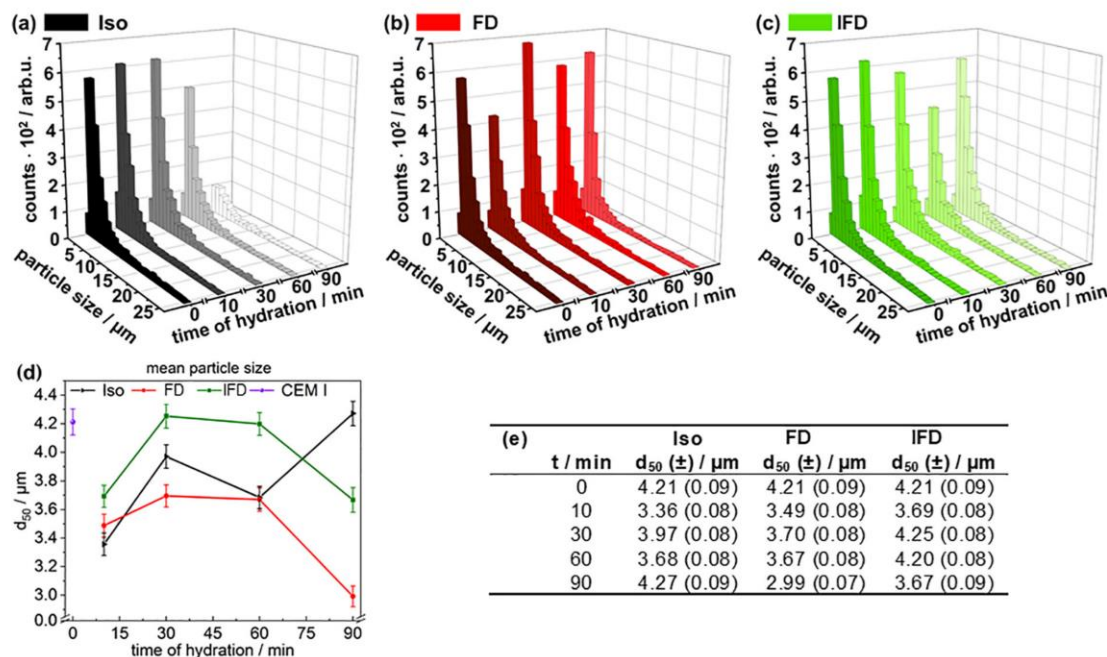


Fig. 10. Particle size distribution of anhydrous and hydrated cement derived from ESEM micrographs, stopped after various hydration durations (up to 90 min) by three different techniques, (a) Iso, (b) FD, and (c) IFD, and (d) corresponding mean particle size d_{50} , and (e) mean values.

[org/10.1016/j.cemconres.2022.106841](https://doi.org/10.1016/j.cemconres.2022.106841).

CRediT authorship contribution statement

Patrick A. Kießling: Conceptualization, XRD, TGA, BET, Formal analysis, Validation, Investigation, Data curation, Writing – original draft, Writing – review & editing, Visualization.

Franziska Lükemann: Writing – review & editing.

Alexander Mundstock: Writing – review & editing.

Ludger Lohaus: Resources, Writing – review & editing.

Jürgen Caro: Writing – review & editing.

Michael Haist: Writing – review & editing.

Nadja C. Bigall: Conceptualization, Resources, Writing – review & editing, Supervision, Funding acquisition.

Declaration of competing interest

The authors declare that they have no known competing financial interests or personal relationships that could have appeared to influence the work reported in this paper.

Acknowledgements

The study was funded by the Deutsche Forschungsgemeinschaft (DFG, German Research Foundation) – projects BI 1708/5-1, LO 751/26-1 [77] as well as by the project BI 1708/4-1. In addition, the project leading to these results has in part received funding from the European Research Council (ERC) under the European Union's Horizon 2020 research and innovation program (grant agreement No. 714429). The authors thank A. Feldhoff for access to XRD. The authors thank A. Krabbenhöft (IW) for ESEM measurements. The authors thank Heidelberg Cement AG for providing the cement during the DFG SPP 2005 priority program. The authors thank the Laboratory for Nano- and Quantum Engineering (LNQE) for support.

References

- [1] F. Winnefeld, A. Zingg, L. Holzer, J. Pakusch, S. Becker, The ettringite-superplasticizer interaction and its impact on ettringite distribution in cement suspensions, in: 9th ACI Int. Conf. Superplast. Other Chem. Admixtures Concr. Sevilla, Spain, Oct. 12-14, 2009, Sevilla, Spain, 2009, pp. 420.1–420.17.
- [2] G.H. Tattersall, Workability And Quality Control of Concrete, 1st ed., CRC Press, London, 2014 <https://doi.org/10.1201/9781482267006>.
- [3] J. Golaszewski, Influence of cement properties on rheology of fresh cement mortars without and with superplasticizer, *Archit. Civ. Eng. Environ.* 4 (2008) 49–66.
- [4] L.J. Struble, W.-G. Lei, Rheological changes associated with setting of cement paste, *Adv. Cem. Based Mater.* 2 (1995) 224–230, [https://doi.org/10.1016/1065-7355\(95\)90041-1](https://doi.org/10.1016/1065-7355(95)90041-1).
- [5] H. Uchikawa, K. Ogawa, S. Uchida, Influence of character of clinker on the early hydration process and rheological property of cement paste, *Cem. Concr. Res.* 15 (1985) 561–572, [https://doi.org/10.1016/0008-8846\(85\)90053-5](https://doi.org/10.1016/0008-8846(85)90053-5).
- [6] U. Pott, C. Ehm, C. Jakob, D. Stephan, in: Investigation of the Early Cement Hydration With a New Penetration Test, Rheometry And In-situ XRD, 2020, pp. 246–255, https://doi.org/10.1007/978-3-030-22566-7_29.
- [7] C. Jakob, D. Jansen, N. Ukrainczyk, E. Koenders, U. Pott, D. Stephan, J. Neubauer, Relating ettringite formation and rheological changes during the initial cement hydration: a comparative study applying XRD analysis, rheological measurements and modeling, *Materials (Basel)* 12 (2019) 2957, <https://doi.org/10.3390/ma12182957>.
- [8] M. Wyrzykowski, P. Lura, Effect of relative humidity decrease due to self-desiccation on the hydration kinetics of cement, *Cem. Concr. Res.* 85 (2016) 75–81, <https://doi.org/10.1016/j.cemconres.2016.04.003>.
- [9] R.J. Flatt, G.W. Scherer, J.W. Bullard, Why alite stops hydrating below 80% relative humidity, *Cem. Concr. Res.* 41 (2011) 987–992, <https://doi.org/10.1016/j.cemconres.2011.06.001>.
- [10] K. Scrivener, R. Snellings, B. Lothenbach, A Practical Guide to Microstructural Analysis of Cementitious Materials, CRC PR INC, 2015 (22. Dezember 2015).
- [11] J.M. Makar, T. Sato, The effect of drying method on ordinary Portland cement surfaces during the early stages of hydration, *Mater. Struct. Constr.* 46 (2013) 1–12, <https://doi.org/10.1617/s11527-012-9878-2>.
- [12] D.C. Hughes, The use of solvent exchange to monitor diffusion characteristics of cement pastes containing silica fume, *Cem. Concr. Res.* 18 (1988) 321–324, [https://doi.org/10.1016/0008-8846\(88\)90016-6](https://doi.org/10.1016/0008-8846(88)90016-6).
- [13] D.C. Hughes, N.L. Crossley, Pore structure characterisation of GGBS/OPC grouts using solvent techniques, *Cem. Concr. Res.* 24 (1994) 1255–1266, [https://doi.org/10.1016/0008-8846\(94\)90110-4](https://doi.org/10.1016/0008-8846(94)90110-4).
- [14] H.F.W. Taylor, A.B. Turner, Reactions of tricalcium silicate paste with organic liquids, *Cem. Concr. Res.* 17 (1987) 613–623.
- [15] Z. Zhang, G.W. Scherer, Evaluation of drying methods by nitrogen adsorption, *Cem. Concr. Res.* 120 (2019) 13–26, <https://doi.org/10.1016/j.cemconres.2019.02.016>.

- [16] G.W. Zhang, Scherer, physical and chemical effects of isopropanol exchange in cement-based materials, *Cem. Concr. Res.* 145 (2021), 106461, <https://doi.org/10.1016/j.cemconres.2021.106461>.
- [17] V. Kocaba, Development And Evaluation of Methods to Follow Microstructural Development of Cementitious Systems Including Slags, *École Polytechnique Fédérale de Lausanne*, 2009.
- [18] S. Mantellato, M. Palacios, R.J. Flatt, Reliable specific surface area measurements on anhydrous cements, *Cem. Concr. Res.* 67 (2015) 286–291, <https://doi.org/10.1016/j.cemconres.2014.10.009>.
- [19] S. Mantellato, M. Palacios, R.J. Flatt, Impact of sample preparation on the specific surface area of synthetic ettringite, *Cem. Concr. Res.* 86 (2016) 20–28, <https://doi.org/10.1016/j.cemconres.2016.04.005>.
- [20] L.D. Mitchell, J.C. Margeson, The effects of solvents on C-S-H as determined by thermal analysis, *J. Therm. Anal. Calorim.* 86 (2006) 591–594, <https://doi.org/10.1007/s10973-006-7712-1>.
- [21] A. Mezhev, D. Kulisch, A. Goncharov, S. Zhutovsky, in: Effect of Soaking Time in a Solvent on Hydration Stoppage of Cement, 2020, pp. 23–27, https://doi.org/10.1007/978-3-030-43332-1_5.
- [22] V. Kocaba, E. Gallucci, K.L. Scrivener, Methods for determination of degree of reaction of slag in blended cement pastes, *Cem. Concr. Res.* 42 (2012) 511–525, <https://doi.org/10.1016/j.cemconres.2011.11.010>.
- [23] C. Gallé, Effect of drying on cement-based materials pore structure as identified by mercury intrusion porosimetry, *Cem. Concr. Res.* 31 (2001) 1467–1477, [https://doi.org/10.1016/S0008-8846\(01\)00594-4](https://doi.org/10.1016/S0008-8846(01)00594-4).
- [24] M. Moukwa, P.C. Aitcin, The effect of drying on cement pastes pore structure as determined by mercury porosimetry, *Cem. Concr. Res.* 18 (1988) 745–752, [https://doi.org/10.1016/0008-8846\(88\)90098-1](https://doi.org/10.1016/0008-8846(88)90098-1).
- [25] A. Zingg, L. Holzer, A. Kaech, F. Winnefeld, J. Pakusch, S. Becker, L. Gauckler, The microstructure of dispersed and non-dispersed fresh cement pastes - new insight by cryo-microscopy, *Cem. Concr. Res.* 38 (2008) 522–529, <https://doi.org/10.1016/j.cemconres.2007.11.007>.
- [26] P.A. Kibling, D. Cotardo, T. von Bronk, L. Lohaus, N.C. Bigall, Comparison of water-isopropanol replacement and lyophilisation for hydration stop of cementitious suspensions, in: V. Mechtcherine, K. Khayat, E. Secieru (Eds.), *Rheol. Process. Constr. Mater. RheoCon 2019, SCC 2019*, Springer, Cham, 2020, pp. 610–618, https://doi.org/10.1007/978-3-030-22566-7_71.
- [27] J. Marchand, R. Pleau, R. Gagné, Deterioration of concrete due to freezing and thawing, in: *Mater. Sci. Concr. Vol. IV*, 1995, pp. 283–354.
- [28] R.L. Day, B.K. Marsh, Measurement of porosity in blended cement pastes, *Cem. Concr. Res.* 18 (1988) 63–73, [https://doi.org/10.1016/0008-8846\(88\)90122-6](https://doi.org/10.1016/0008-8846(88)90122-6).
- [29] N.N. Skoblinkaya, K.G. Krasnikov, Changes in crystal structure of ettringite on dehydration. 1, *Cem. Concr. Res.* 5 (1975) 381–394.
- [30] N.N. Skoblinkaya, K.G. Krasnikov, L.V. Nikitina, V.P. Varlamov, Changes in crystal structure of ettringite on dehydration. 2, *Cem. Concr. Res.* 5 (1975) 419–431, [https://doi.org/10.1016/0008-8846\(75\)90017-4](https://doi.org/10.1016/0008-8846(75)90017-4).
- [31] R. Snellings, J. Chwast, Ö. Cizer, N. De Belie, Y. Dhandapani, P. Durdzinski, J. Elsen, J. Haufe, D. Hooton, C. Patapy, M. Santhanam, K. Scrivener, D. Snoeck, L. Steger, S. Tongbo, A. Vollpracht, F. Winnefeld, B. Lothenbach, Report of TC 238-SCM: hydration stoppage methods for phase assemblage studies of blended cements—results of a round robin test, *Mater. Struct. Constr.* 51 (2018), <https://doi.org/10.1617/s11527-018-1237-5>.
- [32] P.A. Kibling, F. Lübke, T. von Bronk, D. Cotardo, L. Lei, A. Feldhoff, L. Lohaus, M. Haist, N.C. Bigall, Influence of low-pressure treatment on the morphological and compositional stability of microscopic ettringite, *Materials (Basel)* 14 (2021) 2720, <https://doi.org/10.3390/ma14112720>.
- [33] H. Bannwarth, B.P. Kremer, *Vom Stoffaufbau zum Stoffwechsel*, 2007.
- [34] K. Bernhauer, Einführung in die organisch-chemische Laboratoriumstechnik, Springer Berlin Heidelberg, Berlin, Heidelberg, 1942, <https://doi.org/10.1007/978-3-662-02148-4>.
- [35] J. Houben, *Die Methoden der Organischen Chemie*, 3rd ed., Georg Thieme Verlag, Stuttgart, 1925 <https://doi.org/10.1055/b-003-125733>.
- [36] A. Stähler, *Handbuch der Arbeitsmethoden in der anorganischen Chemie*, Walter de Gruyter, Berlin, 1913.
- [37] T. Wieland, L. Gattermann, *Die Praxis des organischen Chemikers*, De Gruyter, Berlin, Boston, 1952, <https://doi.org/10.1515/9783111722535>.
- [38] H.M. Rietveld, A profile refinement method for nuclear and magnetic structures, *J. Appl. Crystallogr.* 2 (1969) 65–71, <https://doi.org/10.1107/S0021889869006558>.
- [39] P. Paufler, R.A. Young (Eds.), *The Rietveld Method*. International Union of Crystallography, Oxford University Press, 1993, 298 p. Price £ 45.00. ISBN 0-19-855577-6, *Cryst. Res. Technol.* 30 (1995) 494–494. doi:10.1002/crat.2170300412.
- [40] Á.G. De La Torre, S. Bruque, J. Campo, M.A.G. Aranda, The superstructure of C3S from synchrotron and neutron powder diffraction and its role in quantitative phase analyses, *Cem. Concr. Res.* 32 (2002) 1347–1356, [https://doi.org/10.1016/S0008-8846\(02\)00796-2](https://doi.org/10.1016/S0008-8846(02)00796-2).
- [41] F.C. Hawthorne, R.B. Ferguson, Anhydrous sulfates II. Refinement of the crystal structure of anhydrite, *Can. Mineral.* 13 (1975) 289–292.
- [42] L. Desgranges, D. Grebille, G. Calvarin, G. Chevrier, N. Floquet, J.-C. Niecepe, Hydrogen thermal motion in calcium hydroxide: Ca(OH)₂, *Acta Crystallogr. Sect. B* 49 (1993) 812–817, <https://doi.org/10.1107/S0108768193003556>.
- [43] G.A. Lager, J.D. Jorgensen, F.J. Rotella, Crystal structure and thermal expansion of α-quartz SiO₂ at low temperatures, *J. Appl. Phys.* 53 (1982) 6751–6756, <https://doi.org/10.1063/1.330062>.
- [44] M.R. Hartman, R. Berliner, Investigation of the structure of ettringite by time-of-flight neutron powder diffraction techniques, *Cem. Concr. Res.* 36 (2006) 364–370, <https://doi.org/10.1016/j.cemconres.2005.08.004>.
- [45] M.I. McCarthy, N.M. Harrison, Ab initio determination of the bulk properties of MgO, *Phys. Rev. B* 49 (1994) 8574–8582, <https://doi.org/10.1103/PhysRevB.49.8574>.
- [46] T. Pilati, F. Demartin, C.M. Gramaccioli, Lattice-dynamical estimation of atomic displacement parameters in carbonates: calcite and aragonite CaCO₃, dolomite CaMg(CO₃)₂ and magnesite MgCO₃, *Acta Crystallogr. Sect. B Struct. Sci.* 54 (1998) 515–523, <https://doi.org/10.1107/S0108768197018181>.
- [47] J.A. McGinney, Redetermination of the structures of potassium sulphate and potassium chromate: the effect of electrostatic crystal forces upon observed bond lengths, *Acta Crystallogr. Sect. B Struct. Crystallogr. Cryst. Chem.* 28 (1972) 2845–2852, <https://doi.org/10.1107/S0567740872007022>.
- [48] C. Bezou, A. Nonat, J.-C. Mutin, A.N. Christensen, M.S. Lehmann, Investigation of the crystal structure of -CaSO₄, CaSO₄ · 0.5 H₂O, and CaSO₄ · 0.6 H₂O by powder diffraction methods, *J. Solid State Chem.* 117 (1995) 165–176, <https://doi.org/10.1006/jssc.1995.1260>.
- [49] W. Mumme, R. Hill, G. Bushnellwye, E. Segnit, Rietveld crystal structure refinements, crystal chemistry and calculated powder diffraction data for the polymorphs of dicalcium silicate and related phases, *NEUES Jahrb. Mineral.* 169 (1995) 35–68, <http://hdl.handle.net/102.100.100/230393?index=1>, <http://hdl.handle.net/102.100.100/230393?index=1>.
- [50] P. Mondal, J.W. Jeffery, The crystal structure of tricalcium aluminate, Ca₃Al₂O₆, *Acta Crystallogr. Sect. B Struct. Crystallogr. Cryst. Chem.* 31 (1975) 689–697, <https://doi.org/10.1107/S0567740875003639>.
- [51] F. Nishi, Y. Takéuchi, The Al₆O₁₈ rings of tetrahedra in the structure of Ca₈5NaAl₆O₁₈, *Acta Crystallogr. Sect. B Struct. Crystallogr. Cryst. Chem.* 31 (1975) 1169–1173, <https://doi.org/10.1107/S0567740875004736>.
- [52] A.A. Colville, S. Geller, The crystal structure of brownmillerite, Ca₂FeAlO₅, *Acta Crystallogr. Sect. B Struct. Crystallogr. Cryst. Chem.* 27 (1971) 2311–2315, <https://doi.org/10.1107/S056774087100579x>.
- [53] Q. Huang, O. Chmaissem, J.J. Capponi, C. Chailout, M. Marezio, J.L. Tholence, A. Santoro, Neutron powder diffraction study of the crystal structure of HgBa₂Ca₄Cu₅O₁₂ at room temperature and at 10 K, *Phys. C Supercond. Appl.* 227 (1994) 1–9, [https://doi.org/10.1016/0921-4534\(94\)90349-2](https://doi.org/10.1016/0921-4534(94)90349-2).
- [54] J.C.A. Boeyens, V.V.H. Ichharam, Redetermination of the crystal structure of calcium sulphate dihydrate, CaSO₄ · 2H₂O, *Z. Krist. New Cryst. Struct.* 217 (2002) 9–10, <https://doi.org/10.1524/nrcs.2002.217.jg.9>.
- [55] S.T. Bergold, F. Goetz-Neunhoeffer, J. Neubauer, Quantitative analysis of C-S-H in hydrating alite pastes by in-situ XRD, *Cem. Concr. Res.* 53 (2013) 119–126, <https://doi.org/10.1016/j.cemconres.2013.06.001>.
- [56] S.T. Bergold, F. Goetz-Neunhoeffer, J. Neubauer, Mechanically activated alite: new insights into alite hydration, *Cem. Concr. Res.* 76 (2015) 202–211, <https://doi.org/10.1016/j.cemconres.2015.06.005>.
- [57] C. Jakob, D. Jansen, U. Pott, J. Neubauer, in: Comparing Phase Development And Rheological Properties of OPC Paste Within the First Hour of Hydration, 2020, pp. 219–227, https://doi.org/10.1007/978-3-030-22566-7_26.
- [58] D.J. Morgan, D.N. Todor, *Thermal Analysis of Minerals*, Abacus Press, 1976, 256 pp. £12.50, *Clay Miner.* 13 (1978) 132–132. doi:10.1180/claymin.1978.013.1.11.
- [59] J. Dweck, P.M. Buchler, A.C.V. Coelho, F.K. Cartledge, Hydration of a Portland cement blended with calcium carbonate, *Thermochim. Acta* 346 (2000) 105–113, [https://doi.org/10.1016/S0040-6031\(99\)00369-X](https://doi.org/10.1016/S0040-6031(99)00369-X).
- [60] S. Brunauer, P.H. Emmett, E. Teller, Adsorption of gases in multimolecular layers, *J. Am. Chem. Soc.* 60 (1938) 309–319, <https://doi.org/10.1021/ja01269a023>.
- [61] R.M. Dreizler, E.K.U. Gross, *Density Functional Theory - An Approach to the Quantum Many-body Problem*, 1990.
- [62] L.D. Gelb, K.E. Gubbins, R. Radhakrishnan, M. Sliwinski-Bartkowiak, Phase separation in confined systems, *Rep. Prog. Phys.* 62 (1999) 1573–1659, <https://doi.org/10.1088/0034-4885/77/5/056502>.
- [63] E.P. Barrett, L.G. Joyner, P.P. Halenda, The determination of pore volume and area distributions in porous substances. I. Computations from nitrogen isotherms, *J. Am. Chem. Soc.* 73 (1951) 373–380, <https://doi.org/10.1021/ja01145a126>.
- [64] Q. Yu, H.J.H. Brouwers, Gypsum: an investigation of microstructure and mechanical properties, in: G. Fischer, M. Geiker, O. Hededa, L. Ottosen, H. Stang (Eds.), *Proc. 8th Fib Int. PhD Symp. Civ. Eng. Lyngby*, Technical University of Denmark, 2010, pp. 341–346.
- [65] C.G. Vassileva, S.V. Vassilev, Behaviour of inorganic matter during heating of Bulgarian coals, *Fuel Process. Technol.* 86 (2005) 1297–1333, <https://doi.org/10.1016/j.fuproc.2005.01.024>.
- [66] A. Bakolas, E. Aggelakopoulou, A. Moropoulou, Evaluation of pozzolanic activity and physico-mechanical characteristics in ceramic powder-lime pastes, *J. Therm. Anal. Calorim.* 92 (2008) 345–351, <https://doi.org/10.1007/s10973-007-8858-1>.
- [67] K. Wang, S.P. Shah, A. Mishulovich, Effects of curing temperature and NaOH addition on hydration and strength development of clinker-free CKD-fly ash binders, *Cem. Concr. Res.* 34 (2004) 299–309, <https://doi.org/10.1016/j.cemconres.2003.08.003>.
- [68] Z.C. Lu, M. Haist, D. Ivanov, C. Jakob, D. Jansen, S. Leinitz, J. Link, V. Mechtcherine, J. Neubauer, J. Plank, W. Schmidt, C. Schilde, C. Schröfl, T. Sowoidnich, D. Stephan, Characterization data of reference cement CEM 1 42.5 R used for priority program DFG SPP 2005 “Opus Fluidum Futurum – Rheology of reactive, multiscale, multiphase construction materials, *Data Br.* 27 (2019), 104699, <https://doi.org/10.1016/j.dib.2019.104699>.
- [69] F.W. Locher, *Zement - Grundlagen der Herstellung und Verwendung*, Bau + Technik, Düsseldorf, 2000.
- [70] E. Hering, R. Martin, M. Stohrer *Taschenbuch der Mathematik und Physik*, n.d.

- [71] E. Berodier, K. Scrivener, Understanding the filler effect on the nucleation and growth of C-S-H, *J. Am. Ceram. Soc.* 97 (2014) 3764–3773, <https://doi.org/10.1111/jace.13177>.
- [72] Verein Deutscher Zementwerke e.V., *Zement-Taschenbuch*, Verein Deutscher Zementwerke e.V., Düsseldorf, 2002.
- [73] A.B. Trenwith, Thermal decomposition of isopropanol, *J. Chem. Soc. Faraday Trans. 1 Phys. Chem. Condens. Phases* 71 (1975) 2405–2412, <https://doi.org/10.1039/F19757102405>.
- [74] J.W. Bullard, H.M. Jennings, R.A. Livingston, A. Nonat, G.W. Scherer, J. S. Schweitzer, K.L. Scrivener, J.J. Thomas, Mechanisms of cement hydration, *Cem. Concr. Res.* 41 (2011) 1208–1223, <https://doi.org/10.1016/j.cemconres.2010.09.011>.
- [75] T. Gutberlet, *Hydratation von Tricalciumsilikat – Die ersten 30 Stunden* 216, 2016.
- [76] C. Hesse, *Der Reaktionsverlauf der frühen Hydratation von Portlandzement in Relation zur Temperatur* 123, 2009, <https://doi.org/10.1021/bi050862i>. Dissertation.
- [77] DFG SPP 2005—Priority Programm Opus Fluidum Futurum—Rheology of Reactive, Multiscale, Multiphase Construction Materials., (n.d.).

Is freeze-drying an alternative to solvent exchange for the hydration stop of cementitious suspensions?

Patrick A. Kiffling^a, Franziska Lübke^a, Alexander Mundstock^a, Ludger Lohaus^b, Michael Haist^b, Jürgen Caro^a, Nadja C. Bigall^{a,*}

^a*Institute of Physical Chemistry and Electrochemistry, Leibniz Universität Hannover, Germany*

^b*Institute of Building Materials Science, Leibniz Universität Hannover, Germany*

Abstract

In order to understand the rheological properties of cementitious suspensions at early stages, among other phases, the formation of ettringite and its time-dependent influence, whether by amount or morphology, has to be examined in detail using a suitable method to stop the hydration process. It is state-of-the-art to exchange water with isopropanol, however, the water initially remains in the system possibly leading to reduced time resolution. Our group raised the question if freeze-drying or the combination of the water-isopropanol exchange with subsequent freeze-drying might be a suitable technique to achieve an almost complete hydration stop at any time. Recently, it was shown under which circumstances low-pressure characterization techniques can be employed without destroying the samples due to loss of crystal bound water. Here, by implementing these recent results, we show under which circumstances freeze-drying indeed can be employed as fast hydration stop method.

Keywords: Rheology, Hydration stop, Time-variant analysis, Cementitious suspension, Freeze-drying, Nitrogen-physisorption, Thermogravimetric analysis, X-Ray diffraction, Environmental scanning electron microscopy.

*Corresponding author

Email address: nadja.bigall@pci.uni-hannover.de (Nadja C. Bigall)

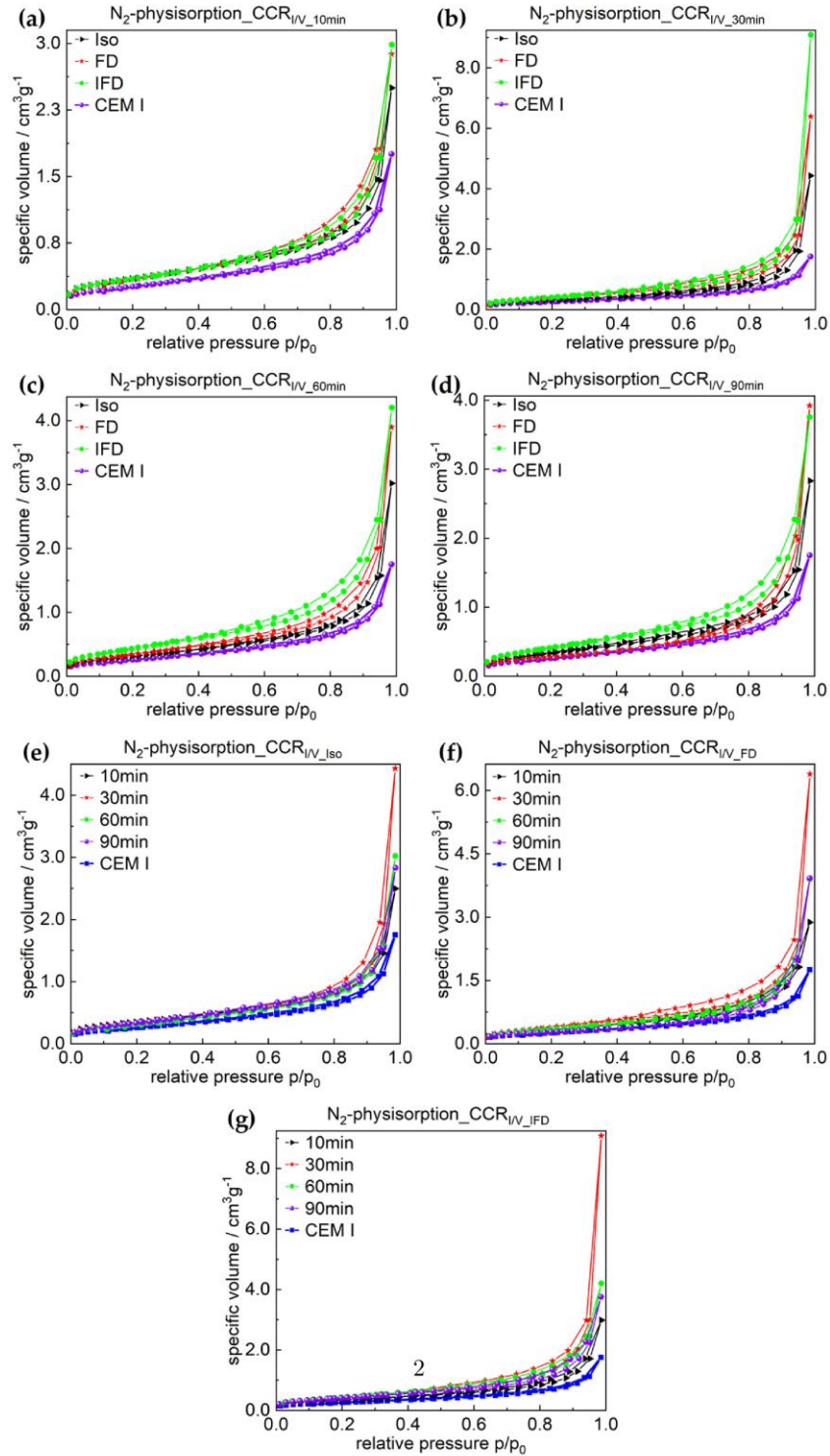


Fig. S1: N_2 -physorption measurement; isotherms of anhydrous and hydrated CEM I stopped at (a) 10 min, (b) 30 min, (c) 60 min, and (d) 90 min; stopped by (e) Iso, (f) FD, and (g) IFD; synthesis I/V.

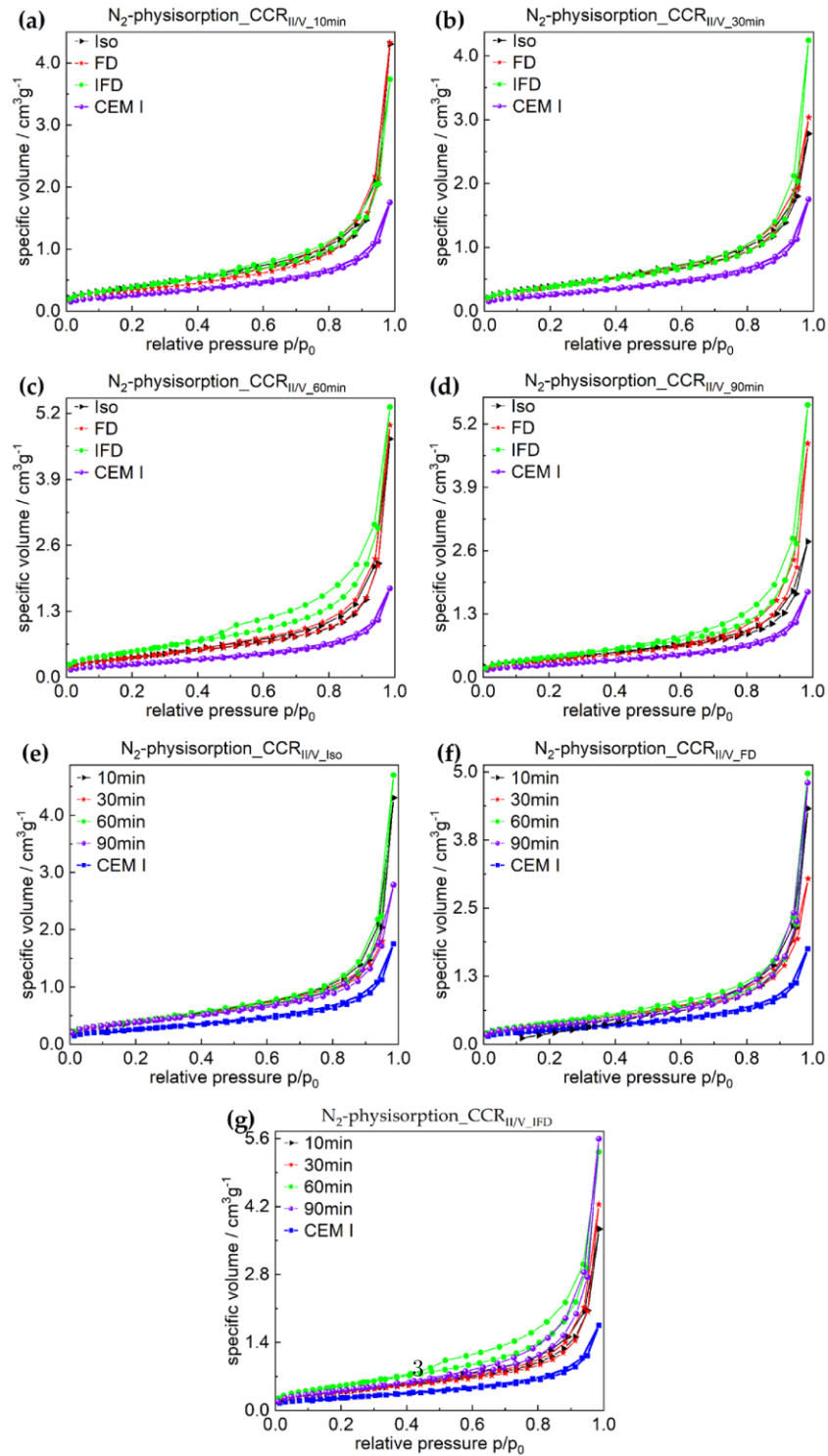


Fig. S2: N₂-physorption measurement; isotherms of anhydrous and hydrated CEM I stopped at (a) 10 min, (b) 30 min, (c) 60 min, and (d) 90 min; stopped by (e) Iso, (f) FD, and (g) IFD; synthesis II/V.

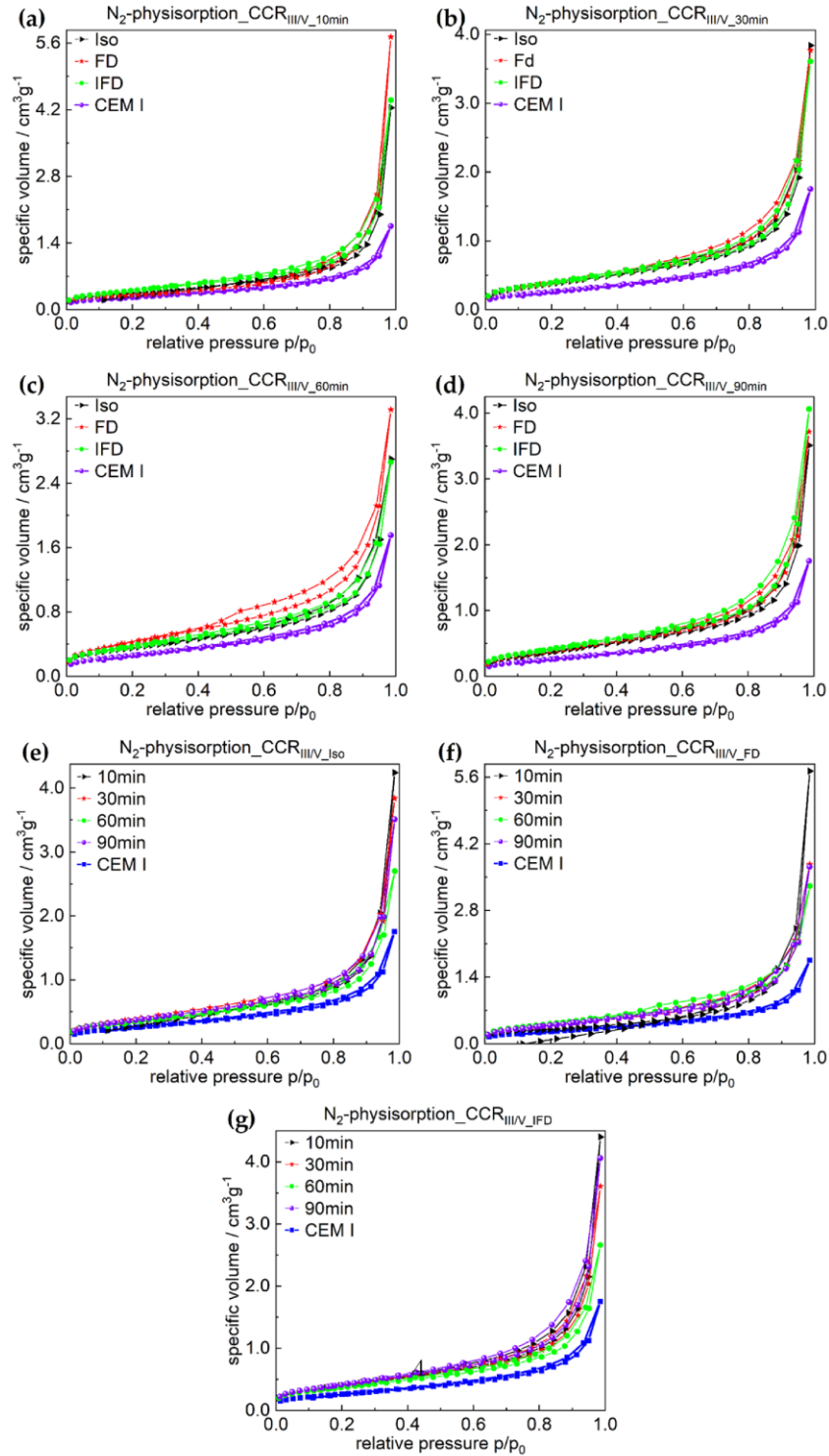


Fig. S3: N₂-physorption measurement; isotherms of anhydrous and hydrated CEM I stopped at (a) 10 min, (b) 30 min, (c) 60 min, and (d) 90 min; stopped by (e) Iso, (f) FD, and (g) IFD; synthesis III/V.

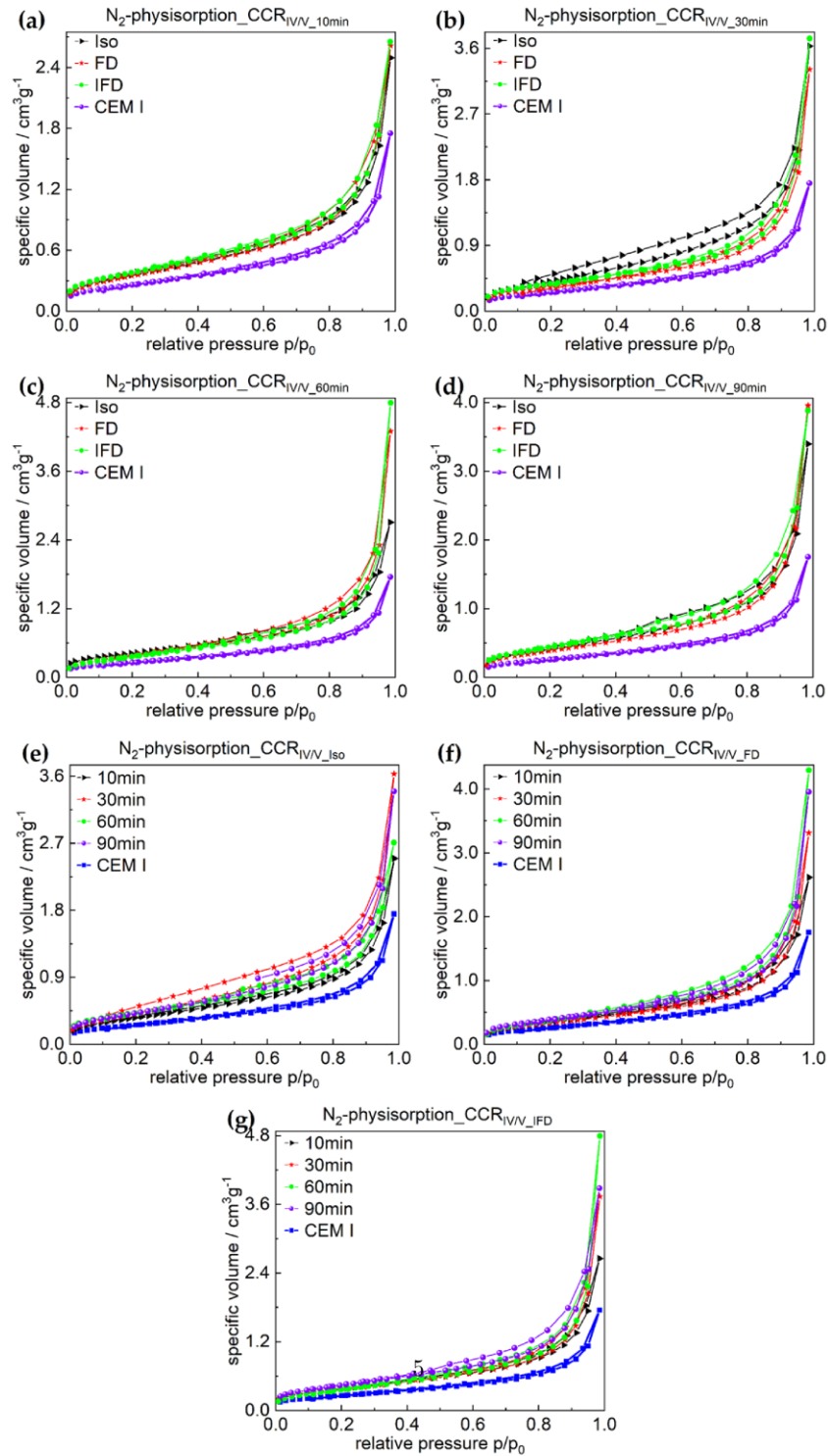


Fig. S4: N₂-physorption measurement; isotherms of anhydrous and hydrated CEM I stopped at (a) 10 min, (b) 30 min, (c) 60 min, and (d) 90 min; stopped by (e) Iso, (f) FD, and (g) IFD; synthesis IV/V.

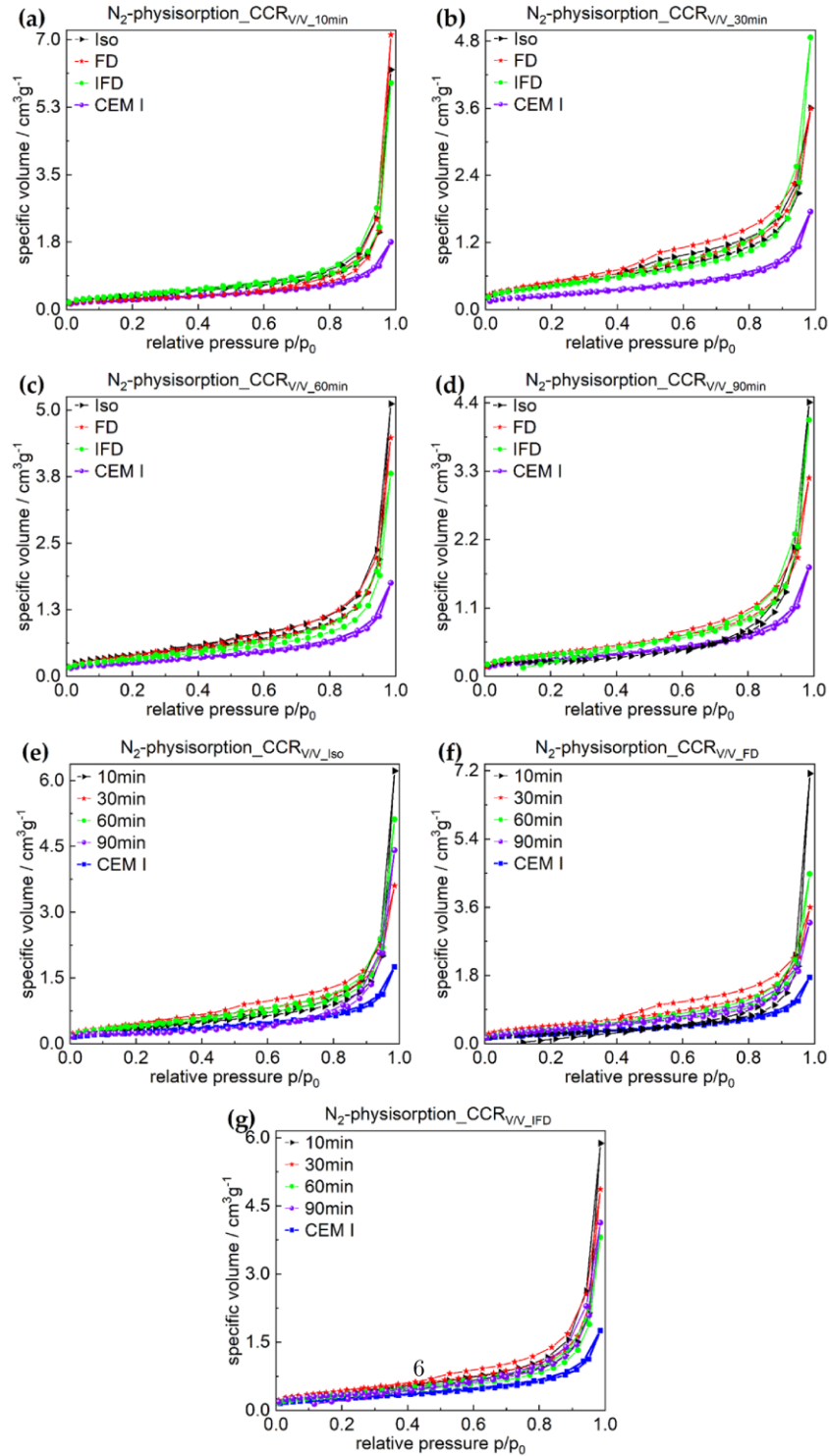


Fig. S5: N_2 -physorption measurement; isotherms of anhydrous and hydrated CEM I stopped at (a) 10 min, (b) 30 min, (c) 60 min, and (d) 90 min; stopped by (e) Iso, (f) FD, and (g) IFD; synthesis V/V.

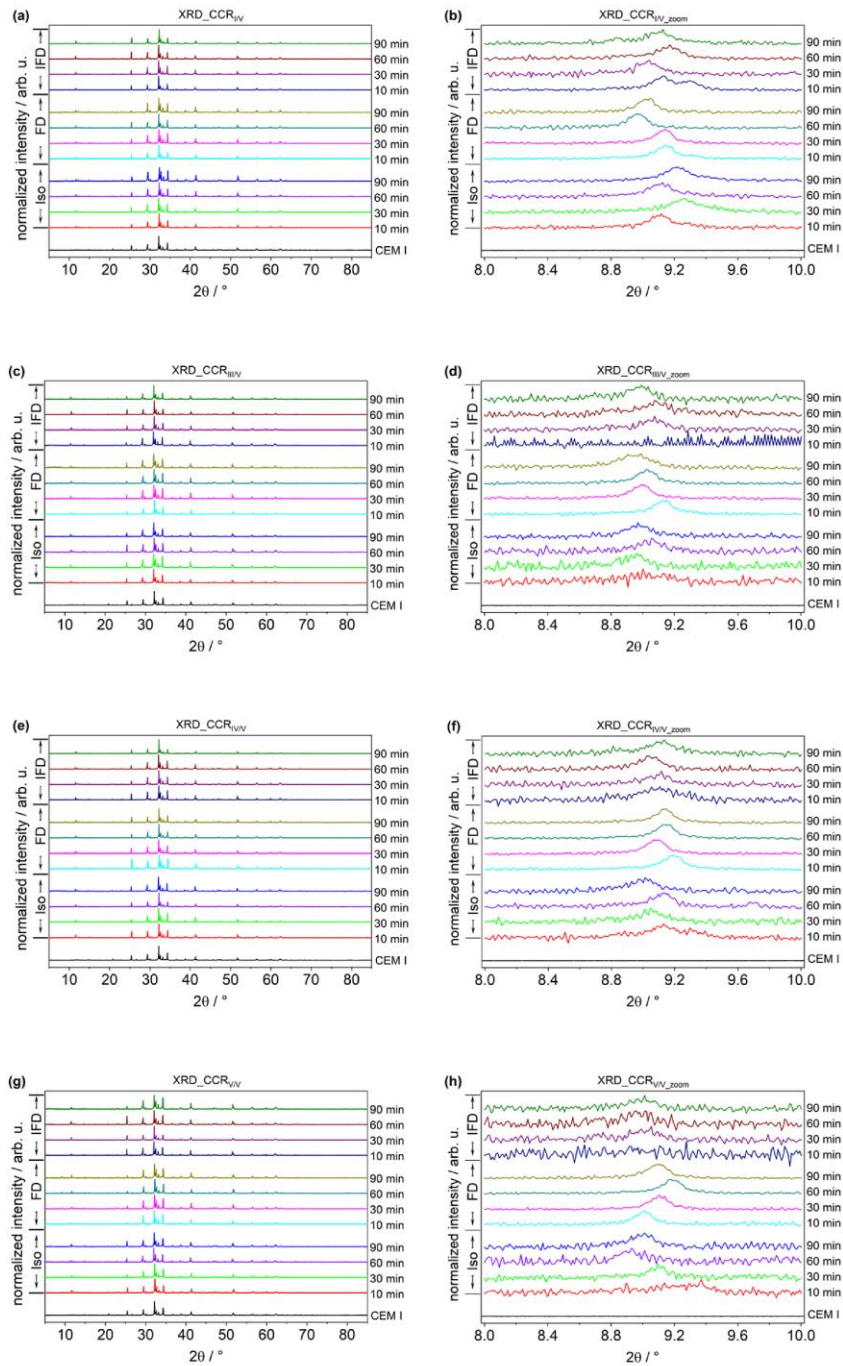


Fig. S6: Powder X-ray diffraction patterns of ⁷anhydrous and hydrated CEM I stopped by Iso, FD, and IFD in an angle range of (left) $5^\circ \leq 2\theta \leq 85^\circ$ and (right) $8^\circ \leq 2\theta \leq 10^\circ$; (a+b) synthesis I/V, (c+d) synthesis III/V, (e+f) synthesis IV/V, and (g+h) synthesis V/V.

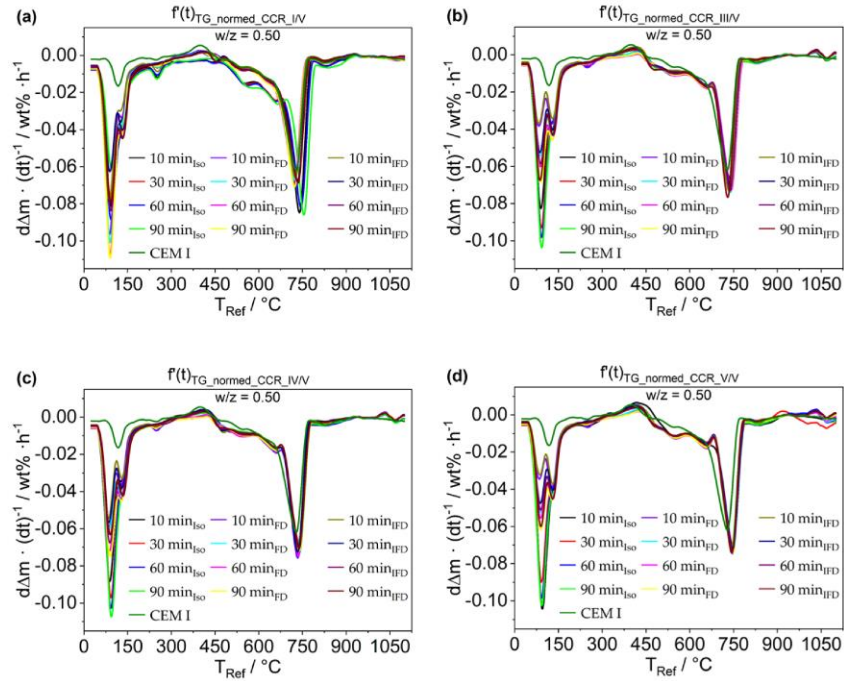


Fig. S7: Overview showing TGA data plotted as mass normalized time derived weight loss ($d\Delta m \cdot (dt)^{-1}$) per hour against the reference temperature of anhydrous and hydrated CEM I with a heating rate of 5 K/min; stopped after various hydration durations (10 min, 30 min, 60 min, and 90 min) by three different techniques (**Iso**, **FD**, and **IFD**); (a) synthesis I/V, (b) synthesis III/V, (c) synthesis IV/V, and (d) synthesis V/V.

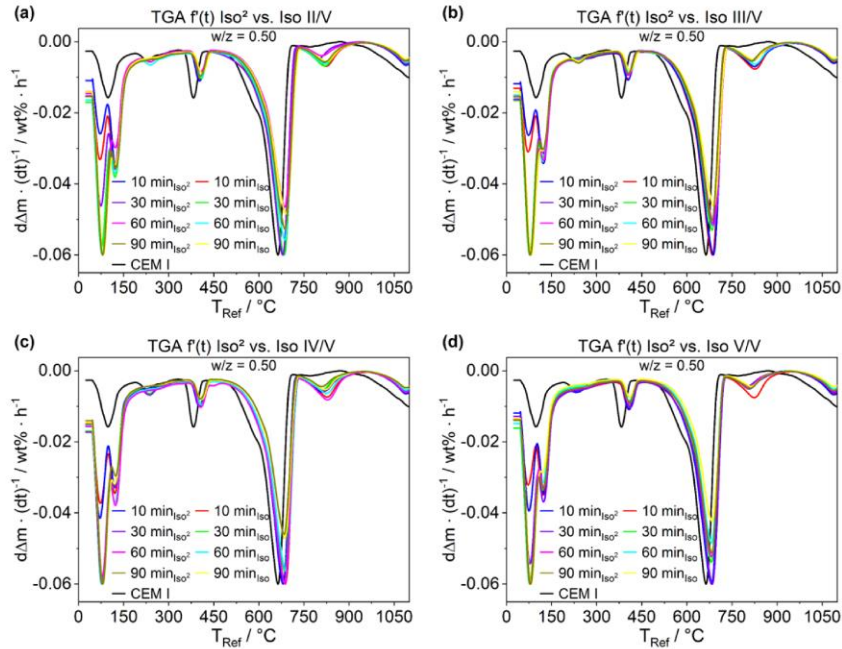


Fig. S8: Overview showing TGA data plotted as mass normalized time derived weight loss ($d\Delta m \cdot (dt)^{-1}$) per hour against the reference temperature of anhydrous and hydrated CEM I with a heating rate of 5 K/min; stopped after various hydration durations (10 min, 30 min, 60 min, and 90 min) by two techniques (**Iso** and **Iso**²); (a) synthesis II/V, (b) synthesis III/V, (c) synthesis IV/V, and (d) synthesis V/V.

From TGA (**Figure S9**) it is visible that the early decomposition peak at $130 \text{ }^\circ\text{C} \pm 80 \text{ }^\circ\text{C}$ increases with prolonged hydration time. This result is caused by the increasing amount of ettringite and C-S-H. Further, the right shoulder at around $130 \text{ }^\circ\text{C}$ that is accounted to the decomposition of gypsum is only slightly visible after 9 h of hydration and is visually lost afterwards. The overall mass loss increased over time due to more hydration products (basanite, portlandite, C-S-H, ettringite) being present. At this stage of hydration (9 h, 16.5 h, and 24 h), it is not possible to derive the content of ettringite and to evaluate one technique being better suited than another as easily as before. The copper sulphate test showed the same results at every stage that by implementing

freeze-drying no unbound water remains in the sample.

Through XRD (**Figure 10**), no significant changes to the amount of ettringite can be seen, as at all hydration states (9 h, 16.5 h, and 24 h) for all applied hydration stop techniques (**Iso**, **Iso**², **FD**, and **IFD**), a clear distinct
15 reflection corresponding to ettringite is visible. To address differences in their composition, Rietveld refinement might be a tool for assessment, which we do not have at hand, yet.

To summarize, at later hydration stages (9 h, 16.5 h, and 24 h), differences between various hydration stop techniques (**Iso**, **Iso**², **FD**, and **IFD**) are
20 marginal. All techniques show a distinct reflection for ettringite. Nevertheless, by TGA it might prove difficult to quantify the amount of ettringite as C-S-H phases show similar decomposition behavior at a temperature range of 130 °C ± 80 °C.

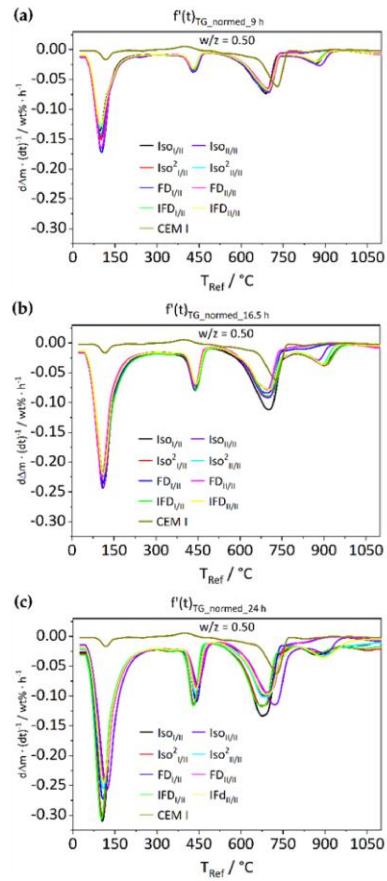


Fig. S9: TGA data plotted as mass normalized time derived weight loss ($d\Delta m \cdot (dt)^{-1}$) per hour against the reference temperature of anhydrous and hydrated CEM I with a heating rate of 5 K/min; stopped after various hydration durations ((a) 9 h, (b) 16.5 h, and (c) 24 h) by four different techniques (Iso, Iso², FD, and IFD)

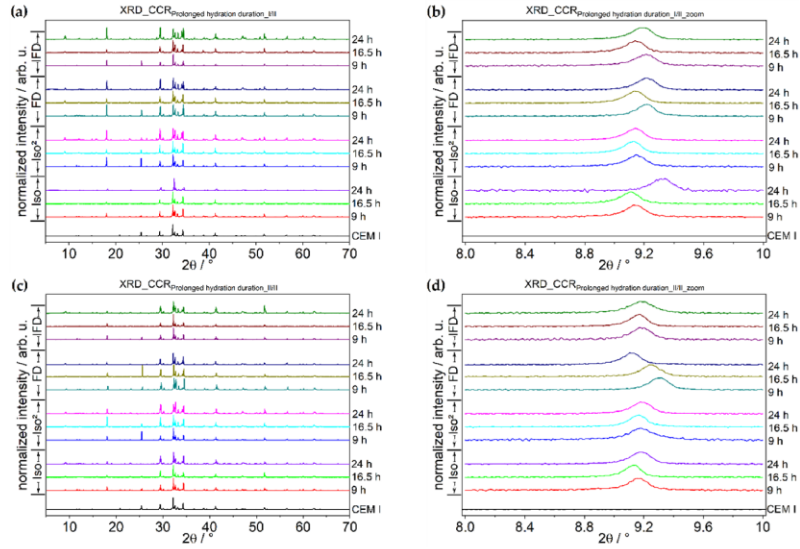


Fig. S10: Powder X-ray diffraction patterns of anhydrous and hydrated CEM I stopped after various hydration durations (up to 24 h) by four different techniques (**Iso**, **Iso**², **FD**, and **IFD**) in an angle range of (**a+c**) $5^\circ \leq 2\theta \leq 70^\circ$ and (**b+d**) $8^\circ \leq 2\theta \leq 10^\circ$; (**a+b**) synthesis 1 and (**c+d**) synthesis 2.

Table S1: Phase content of early hydration products dependent on hydration time [1].

Phase	wt% _{0min}	wt% _{10min}	wt% _{30min}	wt% _{60min}	wt% _{90min}
C_3S^1	41.0	41.17 ± 0.59	41.24 ± 0.44	40.81 ± 0.47	41.10 ± 0.14
C_3A^2	8.0	4.93 ± 0.12	4.88 ± 0.07	4.98 ± 0.24	4.93 ± 0.21
$C_3S_2H_4^3$	0.0	0.0 ± 0.0	0.0 ± 0.0	0.0 ± 0.0	0.0 ± 0.0
portlandite ⁴	0.0	0.10 ± 0.03	0.11 ± 0.02	0.11 ± 0.01	0.13 ± 0.01
anhydrite ⁵	1.7	1.81 ± 0.24	1.81 ± 0.18	1.88 ± 0.19	1.85 ± 0.25
gypsum ⁶	2.2	0.29 ± 0.08	0.47 ± 0.14	0.52 ± 0.13	0.48 ± 0.10
ettringite ⁷	0.0	4.28 ± 0.39	5.09 ± 0.12	5.27 ± 0.37	5.22 ± 0.25

¹ Ca_3SiO_5 , ² $Ca_3Al_2O_6$, ³ $Ca_3Si_2O_5 \cdot 4H_2O$, ⁴ $Ca(OH)_2$, ⁵ $CaSO_4$, ⁶ $CaSO_4 \cdot 2H_2O$,

⁷ $Ca_6Al_2(SO_4)_3(OH)_{12} \cdot 26H_2O$

References

- 25 [1] C. Jakob, D. Jansen, N. Ukrainczyk, E. Koenders, U. Pott, D. Stephan,
J. Neubauer, [Relating Ettringite Formation and Rheological Changes during](#)
the Initial Cement Hydration: A Comparative Study Applying XRD Analy-
sis, Rheological Measurements and Modeling, Materials 12 (18) (2019) 2957.
[doi:10.3390/ma12182957](#),
30 URL <https://www.mdpi.com/1996-1944/12/18/2957>

4 APPLICATION OF THE FREEZE-DRYING-BASED HYDRATION STOP TECHNIQUE

4.1 SUMMARY

One of the main issues encountered in modern cement-based works is insufficient knowledge about the rheological properties of cement-based suspensions during processing, as the rheological properties of cementitious suspensions are crucial tools for characterising fresh cement-based suspensions. Therefore, a hydration stop technique that enables a time-variant analysis of cementitious suspensions is needed. A hot candidate is utilising the freeze-drying method that was described in the previous **section 3**.

In the following **section 4.2**, fourth research article^{222}, this freeze-drying-based technique (**FD**) is in part used to evaluate the influence of *in situ* formed ettringite on the rheology of model suspensions consisting of quartz powder (SiO_2), since in cementitious suspensions diverse hydration processes co-occur (**section 2.2**) and might influence each other. Here, an up-scalable synthesis route of ettringite was introduced. Further, it was shown that higher amounts of ettringite in the quartz suspension lead to stiffening accompanied by an increase of plastic viscosity μ , yield stress τ_0 , and equilibrium dynamic viscosity η_{eq} during various shear rates. Furthermore, based on the obtained data sets, it might, in future works, be possible to distinguish between the influence of forming ettringite and other hydration processes in cementitious suspensions like the formation of calcium-silicate-hydrate (C-S-H). Due to the comparable particle size distribution of the used quartz powder and Portland cement (CEM I 42.5 R), these findings are likely transferable to cementitious suspensions and practical applications.

Besides the rheological aspects exists the challenge to adapt building materials to extrinsic factors like climate, resource scarcity, politics, and, recently, security requirements (tap-proofness).^{36} As previously mentioned, cement itself mainly consists of Ca_3SiO_5 , Ca_2SiO_4 , and $\text{Ca}_3\text{Al}_2\text{O}_6$ and acts as the binder or glue of the composite material concrete, which additionally contains coarse and fine aggregates (*exempli gratia* sand, gravel, or crushed stones).^{40} For this, most approaches work on the macroscopic or microscopic levels, *exempli*

²²² P.A. Kißling, J. Link, M. Heinemann, F. Lübke mann-Warwas, F. Rieck genannt Best, T. Sowoidnich, A. Mundstock, H.-M. Ludwig, L. Lohaus, M. Haist, N.C. Bigall, *Constr. Build. Mat.* **2023**, *408*, 133678. <https://doi.org/10.1016/j.conbuildmat.2023.133678>.

gratia by the addition of filler materials such as sand or slag to enhance the strength of hardened cement paste by compacting or adding superplasticiser to improve fluidity and pumpability of cementitious suspensions^{42,223-231}. Additionally, several approaches aim at the nanoscopic levels, wherein enhanced external compression and tensile strength^{215,232} as well as a reduction of the dormant period is observed. Besides an acceleration of the hydration of cement, a lowering of the initial as well as final setting time by 90 min to 100 min^{215} is induced by different types of nanoparticles *exempli gratia* tobermorite nanofibers^{233}, SiO₂^{215,234-239}, TiO₂^{232,240}, α -Fe₂O₃^{238,239}, ZnO^{232,241}, and carbon nanotubes^{242,243}. Hereby, the beforementioned specific modifications are observed on the paste level already, without additional aggregates.

-
- ²²³ H. Moosberg-Bustnes, B. Lagerblad, E. Forssberg, *Mater. Struct.* 37, **2004**, 74–81. <https://doi.org/10.1007/bf02486602>.
- ²²⁴ U.S. Department of Transportation, Fly Ash, Fed. Highw. Adm., **2007**. <http://www.fhwa.dot.gov/infrastructure/materialsgrp/flyash.htm>, January 12, **2022**.
- ²²⁵ U.S. Department of Transportation, Ground Granulated Blast-Furnace Slag, Fed. Highw. Adm., **2007**. <http://www.fhwa.dot.gov/infrastructure/materialsgrp/ggbfs.htm>, January 12, **2022**.
- ²²⁶ U.S. Department of Transportation, Silica Fume User's Manual, Fed. Highw. Adm., **2005**, 1–194.
- ²²⁷ T.R.S. Mullapudi, D. Gao, A. Ayoub, *Mag. Concr. Res.* 65, **2013**, 1081–1091. <https://doi.org/10.1680/mac.12.00187>.
- ²²⁸ H.E. Elyamany, A.E.M. Abd Elmoaty, B. Mohamed, *Alexandria Eng. J.* 53, **2014**, 295–307. <https://doi.org/10.1016/j.aej.2014.03.010>.
- ²²⁹ S.H. Kosmatka, B. Kerkhoff, W.C. Panarese, Design and Control of Concrete Mixtures, 14th edition, Portland Cement Association, Skokie, Illinois **2008**.
- ²³⁰ C.Y. Tuan, S. Yehia, *Aci Mater. J.* 101, **2004**, 287–293.
- ²³¹ E.A. Avallone, T.B. Iii, Marks' standard handbook for mechanical engineers, **1997**. <https://doi.org/10.5860/choice.34-3330>.
- ²³² L. Senff, D.M. Tobaldi, P. Lemes-Rachadel, J.A. Labrincha, D. Hotza, *Constr. Build. Mater.* 65, **2014**, 191–200. <https://doi.org/10.1016/j.conbuildmat.2014.04.121>.
- ²³³ M. Diez-Garcia, J.J. Gaitero, J.S. Dolado, C. Aymonier, *Angew. Chemie Int. Ed.* 56, **2017**, 3162–3167. <https://doi.org/10.1002/anie.201611858>.
- ²³⁴ K.J. Krakowiak, J.J. Thomas, S. Musso, S. James, A.-T. Akono, F.-J. Ulm, *Cem. Concr. Res.* 67, **2015**, 103–121. <https://doi.org/10.1016/j.cemconres.2014.08.008>.
- ²³⁵ M.S. El-Feky, P. Youssef, A.M. El-Tair, S. Ibrahim, M. Serag, *AIMS Mater. Sci.* 6, **2019**, 864–883. <https://doi.org/10.3934/mat.2019.6.864>.
- ²³⁶ B.B. Mukharjee, S. V. Barai, *Constr. Build. Mater.* 68, **2014**, 416–425. <https://doi.org/10.1016/j.conbuildmat.2014.06.074>.
- ²³⁷ D. Kong, H. Zhang, X. Du, Y. Yang, S.P. Shah, S. Wei, *Constr. Build. Mater.* 37, **2012**, 707–715. <https://doi.org/10.1016/j.conbuildmat.2012.08.006>.
- ²³⁸ H. Li, H. Xiao, J. Ou, *Cem. Concr. Res.* 34, **2004**, 435–438. <https://doi.org/10.1016/j.cemconres.2003.08.025>.
- ²³⁹ H. Li, H. Xiao, J. Yuan, J. Ou, *Compos. Part B Eng.* 35, **2004**, 185–189. [https://doi.org/10.1016/S1359-8368\(03\)00052-0](https://doi.org/10.1016/S1359-8368(03)00052-0).
- ²⁴⁰ D. Feng, N. Xie, C. Gong, Z. Leng, H. Xiao, H. Li, X. Shi, *Ind. Eng. Chem. Res.* 52, **2013**, 11575–11582. <https://doi.org/10.1021/ie4011595>.
- ²⁴¹ S.A. Ghahari, E. Ghafari, N. Lu, *Constr. Build. Mater.* 146, **2017**, 755–763. <https://doi.org/10.1016/j.conbuildmat.2017.04.165>.
- ²⁴² R. Siddique, A. Mehta, *Constr. Build. Mater.* 50, **2014**, 116–129. <https://doi.org/10.1016/j.conbuildmat.2013.09.019>.
- ²⁴³ M. Ghosal, A.K. Chakraborty, Influence of cement behavior with and without polymer nano composites, *Adv. Polym. Mater. Synth. Appl.*, **2018**, 121–142.

In the following **section 4.3**, fifth research article^{244}, the impact of not yet investigated type of nanoparticles, hard magnetic ϵ -Fe₂O₃, will be evaluated. Herefor, cementitious suspensions were blended with different amounts (≤ 10 wt%) of synthetic gallium substituted Fe₂O₃ (85% ϵ and 15% α) nanomagnets, and its influence on the hardened state ($t_{hyd} \geq 28$ d) was examined. The partial substitution of iron with gallium is needed to stabilise the normally metastable ϵ -phase of Fe₂O₃.^{218} It was shown how or to which extent the amount of nanoscopic gallium substituted iron oxide particles (Ga_{0.043}Fe_{1.957}O₃) influences properties relevant to the real-world application of hardened cement paste simultaneously using a cheap and easily mass-produced additive.

4.2 INFLUENCE OF *IN SITU* ETTRINGITE FORMATION ON THE RHEOLOGICAL PROPERTIES OF QUARTZ SUSPENSIONS

P.A. Kißling, J. Link, M. Heinemann, F. Lübke mann-Warwas, F. Rieck genannt Best, T. Sowoidnich, A. Mundstock, H.-M. Ludwig, M. Haist, N.C. Bigall, *Constr. Build. Mat.* **2023**, *408*, 133678.

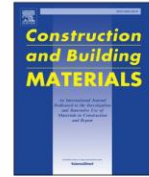
DOI: <https://doi.org/10.1016/j.conbuildmat.2023.133678> .

²⁴⁴ P.A. Kißling, M. Mahlbacher, C. Wesemann, A. Mundstock, F. Lübke mann-Warwas, S. Klimke, F. Renz L. Lohaus, M. Haist, N.C. Bigall, *Chemie Ing. Tech.*, **2023**. <https://doi.org/10.1002/cite.202300022>.



Contents lists available at ScienceDirect

Construction and Building Materials

journal homepage: www.elsevier.com/locate/conbuildmat

Influence of *in situ* ettringite formation on the rheological properties of quartz suspensions

Patrick A. Kißling^{a,b,1}, Julian Link^{b,1}, Melanie Heinemann^c, Franziska Lübke-Warwas^a, Felix Rieck genannt Best^a, Thomas Sowoidnich^c, Alexander Mundstock^a, Horst-Michael Ludwig^c, Michael Haist^{b,*}, Nadja C. Bigall^a

^a Institute of Physical Chemistry and Electrochemistry, Leibniz Universität Hannover, Callinstr. 3a, 30167 Hanover, Germany

^b Institute for Building Materials Science, Leibniz Universität Hannover, Appelstr. 9a, 30167 Hanover, Germany

^c F.A. Finger-Institute of Building Materials Science, Bauhaus Universität Weimar, Coudraystr. 11A, 99423 Weimar, Germany

ARTICLE INFO

Keywords:

Rheology

Ettringite

Cement model system

Quartz suspension

Analytics

ABSTRACT

Cement suspensions are subject to hydration processes causing dissolution of cement clinker, precipitation of hydration products and changes in the ion content of the carrier liquid. These mechanisms take place in parallel and control the workability of cement suspensions. The precipitation of nano-granular ettringite is currently believed to be one of the key influencing factors for rheological properties of fresh cement suspensions. In order to quantify the effect of ettringite precipitation from other precipitation or dissolution processes onto the rheological behaviour, a model suspension consisting of quartz powder and *in situ* formed ettringite is used, enabled by implementing a new upscalable synthesis route of ettringite. The quantity of formed ettringite in the model suspension is varied and derived qualitatively from X-ray diffraction as well as quantitatively from inductively coupled plasma optical emission spectrometry and thermogravimetric analysis. The influence of the ettringite content on the rheological properties is determined and linked to the specific surface of the formed ettringite particles. This allows a quantification of the controlling mechanism of ettringite and the dependency of these mechanisms on particle properties. The correlation of the results to a reference suspension without ettringite verifies the statement of influence.

1. Introduction

Portland cement consists of the clinker phases tri- and dicalcium silicate (alite, C_3S and belite, C_2S) as well as tricalcium aluminate (C_3A) and calcium aluminoferrite (C_4AF) at different mass fractions (note: the cement-chemistry notation with $C \equiv CaO$, $S \equiv SiO_2$, $A \equiv Al_2O_3$, $F \equiv Fe_2O_3$, $\bar{S} \equiv SO_3$, and $H \equiv H_2O$ is used) [1,2]. In contact with water, the aluminate phase C_3A undergoes a very rapid hydration process in which calcium aluminate hydrate (CAH) is formed, which will lead to a very rapid loss of workability. In order to control this process, sulphate is added in the form of gypsum ($C\bar{S}H_2$), hemihydrate ($C\bar{S}H_{0.5}$) or anhydrite ($C\bar{S}$), which reacts with C_3A forming ettringite ($C_6A\bar{S}_3H_{32}$). Ettringite

precipitates in the suspension as small needle-shaped particles [3–9], which significantly alter the rheological properties of the cement suspension by changing the solid phase content and by the formation of a new phase with different morphology and surface properties compared to existing phases. Based on several works [3–10], it was concluded that ettringite's precipitation is a major controlling factor of the rheological properties of cement pastes at early hydration state. With increasing content of ettringite, the workability is decreasing and yield stress, plastic viscosity and dynamic viscosity are increasing [3–10]. Other authors, q.v. ROUSSEL ET AL. [11] suggest, that the thixotropy of fresh cement paste is primarily controlled by a bridging of non-hydrated cement particles by precursor products of Calcium Silicate Hydrate (C-S-H), hereby rather excluding ettringite formation as possible origin of

* Corresponding author.

E-mail addresses: patrick.kissling@pci.uni-hannover.de (P.A. Kißling), j.link@baustoff.uni-hannover.de (J. Link), melanie.heinemann@uni-weimar.de (M. Heinemann), franziska.luebke-warwas@pci.uni-hannover.de (F. Lübke-Warwas), felix.best@pci.uni-hannover.de (F. Rieck genannt Best), thomas.sowoidnich@uni-weimar.de (T. Sowoidnich), alexander.mundstock@pci.uni-hannover.de (A. Mundstock), horst-michael.ludwig@uni-weimar.de (H.-M. Ludwig), haist@baustoff.uni-hannover.de (M. Haist), nadja.bigall@pci.uni-hannover.de (N.C. Bigall).

¹ These authors contributed equally to this work.

<https://doi.org/10.1016/j.conbuildmat.2023.133678>

Received 31 May 2023; Received in revised form 4 September 2023; Accepted 3 October 2023

Available online 17 October 2023

0950-0618/© 2023 Published by Elsevier Ltd.

these rheological changes during time. In reference [12] the authors of the paper at hand were able to disprove the theory, that the water consumption involved in the formation of ettringite and the subsequent change in phase content are the sole origin of changes in thixotropy, by showing that the thixotropy is strongly influenced by the shear history of the paste. If the phase change due to ettringite formation were to be the sole cause of thixotropy, this effect cannot be reversed by mere shearing of the paste, which however was observed in [12]. In a detailed analysis of the hydration products by BOGNER ET AL. [7] the individual hydration products were quantified during hydration and hints that both ettringite as well as C-S-H formation play a role in thixotropy were gained. A detailed modelling of these effects for early hydration times is not possible yet, however with beginning of setting C-S-H seems to control the rheological properties [7]. Since a combination between the influence of different hydration products is not feasible yet, this study presents an approach to quantify the influence of ettringite as a hydration product on the rheological behaviour of granular suspensions as cement paste. Hence, this study supports the detailed quantification of the effect of ettringite on rheology, in order to assess further influences of cement pastes to C-S-H formation.

In order to measure the isolated influence of ettringite on rheology, a model system was selected in this study to exclude the majority of other intrinsic and extrinsic influencing factors as e.g. dissolution and precipitation processes with accompanying changes in phase content of individual cementitious phases or changes in the ionic composition of the carrier liquid. The model system consisted of a quartz powder suspension with a polydisperse particle size distribution similar to cement suspension and *in situ* precipitated ettringite. There are existing studies on the influence of phase content, particle sizes and specific surface areas of individual components of a suspension (see e.g. KRIEGER ET AL. [13], GUY ET AL. [14], CASTLE ET AL. [15], and LUCKHAM ET AL. [16]), however with a clear lack on studies with new particles forming *in situ* in the suspension due to chemical reaction processes. In the chosen approach, the quartz powder particles can be considered quasi non-reactive (also considering the time scale of ettringite formation). Thus, with this setup we study the effect of ettringite formation onto rheology exclusively. The ettringite formation was controlled by the amount of added aluminium sulphate octadecahydrate ($\text{Al}_2(\text{SO}_4)_3 \bullet 18 \text{H}_2\text{O}$) which was varied to reach different contents of ettringite. The resulting rheological behaviour of ettringite containing model suspension is referred to a reference suspension without ettringite precipitation to separate the pure influence of ettringite onto rheology. All characterisation techniques were carried out as composition-dependent measurements to discuss the impact of ettringite on quartz suspensions' rheological properties.

2. Materials and methods

2.1. Materials

The main materials for this study were quartz powder D6400 from Quarzwerke Frechen (in the following referred to as SiO_2 with a density $\rho = 2.65 \text{ g cm}^{-3}$), aluminium sulphate octadecahydrate ($\geq 98 \%$, $\text{Al}_2(\text{SO}_4)_3 \bullet 18 \text{H}_2\text{O}$, $\rho = 1.72 \text{ g cm}^{-3}$), nitric acid (65 %, HNO_3 , zA, $\rho = 1.41 \text{ g cm}^{-3}$), and anhydrous isopropanol ($\geq 99.95 \%$, $\rho = 0.79 \text{ g cm}^{-3}$) from Carl Roth, calcium chloride ($\geq 98 \%$, CaCl_2 , $\rho = 2.15 \text{ g cm}^{-3}$) as well as sodium hydroxide ($\geq 99.9 \%$, NaOH , $\rho = 2.13 \text{ g cm}^{-3}$) from Merck, ethanol ($\geq 99.8 \%$, $\rho = 0.789 \text{ g cm}^{-3}$) from Sigma-Aldrich, Millipore water ($18.2 \text{ M}\Omega\cdot\text{cm}$) cleaned by an Arium mini from Sartorius (in the following referred to as water), argon ($\geq 99.999 \%$, Ar) and liquid nitrogen ($\geq 99.999 \%$) from Linde. All densities ρ are taken from the suppliers. The quartz powder was stored at ambient temperature ($20 \text{ }^\circ\text{C} \pm 2 \text{ }^\circ\text{C}$) and humidity ($65 \pm 2 \%$) by the laboratory's climate control for the whole study.

Table 1

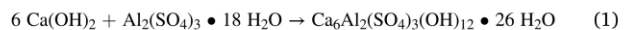
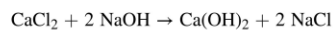
Mixing method for quartz suspensions using a Kenwood Patissier.

step	duration / min	mode / approx. rpm
dry mixing of SiO_2	1.0	level 4 / 72
adding aqueous CaCl_2 solution	1.0	level 4 / 72
stop and manual homogenisation	0.5	off
adding aqueous NaOH solution	1.0	level 4 / 72
stop and manual homogenisation	1.0	off
adding aqueous $\text{Al}_2(\text{SO}_4)_3 \bullet 18 \text{H}_2\text{O}$ solution	2.0	level 12 / 220
stop and manual homogenisation	1.0	off
homogenisation	13	level 12 / 220

2.2. Methods

2.2.1. Synthesis of ettringite

Derived from STRUBLE [17], three aqueous solutions were prepared: (1) $\text{Al}_2(\text{SO}_4)_3 \bullet 18 \text{H}_2\text{O}$ (0.383 M, 1 eq.), (2) NaOH (4.595 M, 12 eq.), and (3) CaCl_2 (2.298 M, 6 eq.). Right after the mixture of solutions (2) and (3) within 30 s, solution (1) was added fast (30 s) under vigorous stirring (500 rpm, Hei-Torque Precision 400 by Heidolph Instruments GmbH, Co. KG; anchor AR 19 PTFE, $d_{\text{shaft}} = 8 \text{ mm}$) and followed by slow stirring (50 rpm) for 3 min (see Eq. (1)). The alkaline solution was filtered using a Buchner funnel with a glass fibre filter (retention $0.4 \mu\text{m}$, $d = 125 \text{ mM}$; MN-GF 5 by Macherey-Nagel GmbH, Co. KG) and after centrifugation (60 min, 10,000 G, Sigma 3-18KS, $20 \text{ }^\circ\text{C}$), the precipitate was decanted. To remove the adsorbed water or rather the remaining reaction medium, the precipitate was dried in a vacuum furnace (Vakuumschrank VO29 by Memmert GmbH & Co. KG) for 24 h at $25 \text{ }^\circ\text{C}$ under inert conditions (1.015 bar Ar). These parameters were chosen for drying with neither a phase transition ($25 \text{ }^\circ\text{C}$, 1.015 bar) nor formation of limestone (CaCO_3) (Ar atmosphere). Analysis see section S1.



2.2.2. Particle size distribution by laser diffraction

The particle size distribution of anhydrous quartz powder was measured by laser diffraction using an LS 230 combined with polarized intensity differential scanning (PIDS) from Beckman Coulter, Inc.. For this purpose, the sample was diluted in the dispersing agent isopropanol and sonicated (1000 W, 2 min) directly before the measurement to disperse the particles. Device-specific deviation at $d_{50} = 0.58 \mu\text{m} \pm 0.012 \mu\text{m}$.

2.2.3. Quartz suspension preparation

Following the mixing method shown in Table 1, SiO_2 (477.0 g) was consecutively mixed with an aqueous solution made of CaCl_2 (25.31 g in 116 mL), a solution of NaOH (18.24 g in 116 mL) in water, resulting in the formation of calcium hydroxide ($\text{Ca}(\text{OH})_2$, 16.90 g, $\rho = 2.24 \text{ g cm}^{-3}$ [18,19]) and one of five differently concentrated aqueous solutions of $\text{Al}_2(\text{SO}_4)_3 \bullet 18 \text{H}_2\text{O}$ (0 g, 6.33 g, 12.66 g, 19.00 g, and 25.33 g in 88 mL) using a Kenwood Kitchen Aid KSM90 Patissier resulting in mass fractions of ettringite ($\rho = 1.77 \text{ g cm}^{-3}$ [19]) of 0.0 wt%, 2.4 wt%, 4.7 wt%, 6.9 wt%, and 9.1 wt% (corresponding to the mass of formed ettringite $m_{\text{ettringite}} = 0.0 \text{ g}$, 11.93 g, 23.85 g, 35.78 g, and 47.70 g), respectively (Table 2). The values of mass fractions are calculated as mass of ettringite $m_{\text{ettringite}}$ divided by the combined mass of SiO_2 m_{SiO_2} and $m_{\text{ettringite}}$ (see Eq. (2)). Each suspension at the time of mixture had a solution-to-quartz mass ratio of 0.67 (Table 1). The reaction duration was previously ascertained as described in section S2 in the Supplementary Material (Table S1, Fig. S3).

Table 2

Composition of model and reference suspensions with and without the precipitation of ettringite, wherein in the latter case, $\Phi_{\text{ettringite}}$ was replaced by $\Phi_{\text{Ca(OH)}_2}$ and Φ_{SiO_2} ; details on calculation see **section S3** in the Supplementary Materials.

desired amount of ettringite / wt%	model suspensions with ettringite					reference suspension without ettringite					total phase content Φ_{total}
	m / g					m / g					
	H ₂ O	SiO ₂	CaCl ₂	NaOH	Al ₂ (SO ₄) ₃ • 18 H ₂ O	H ₂ O	SiO ₂	CaCl ₂	NaOH	Al ₂ (SO ₄) ₃ • 18 H ₂ O	
0.0	320.0	477.0	25.31	18.24	0.00	320.0	477.0	25.31	18.24	0.00	0.370
2.4					6.33	494.3	19.67	14.18			0.376
4.7					12.66	512.0	13.58	9.79			0.381
6.9					19.00	530.0	7.03	5.07			0.387
9.1					25.33	548.4	0.00	0.00			0.392

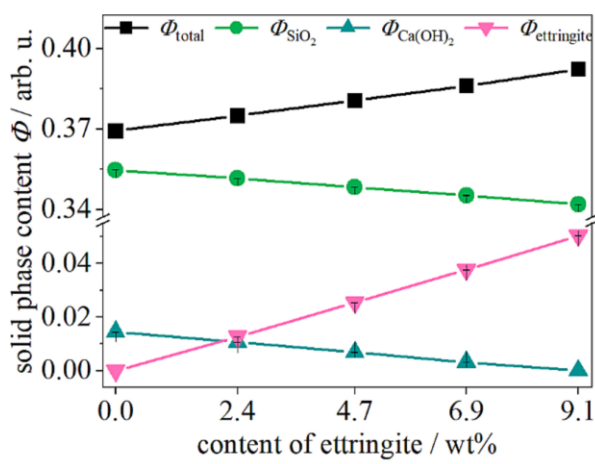


Fig. 1. Calculated composition of different phase contents within the model suspension for changing content of ettringite.

Table 3

Data for **Fig. 1**; quartz powder model suspension with increasing amount of in situ formed ettringite (up to 9.1 wt%); samples' composition changing underlying phase contents Φ of total, SiO₂, Ca(OH)₂, and ettringite.

sample name	phase content Φ / arb. u.			
	total	SiO ₂	Ca(OH) ₂	ettringite*
0.0 wt%	0.37 ± 0.00	0.35 ± 0.00	0.01 ± 0.00	0.00 ± 0.00
2.4 wt%	0.37 ± 0.00	0.35 ± 0.00	0.01 ± 0.00	0.01 ± 0.00
4.7 wt%	0.38 ± 0.00	0.35 ± 0.00	0.01 ± 0.00	0.03 ± 0.00
6.9 wt%	0.39 ± 0.00	0.35 ± 0.00	0.00 ± 0.00	0.04 ± 0.00
9.1 wt%	0.39 ± 0.00	0.34 ± 0.00	0.00 ± 0.00	0.05 ± 0.00

*Ca₆Al₂(SO₄)₃(OH)₁₂ • 26 H₂O.

$$\text{mass fraction of ettringite} \equiv \frac{m_{\text{ettringite}}}{m_{\text{ettringite}} + m_{\text{SiO}_2}} \quad (2)$$

A reference quartz suspension was prepared without the precipitation of ettringite in order to quantify the impact of ettringite compared to a reference suspension with the same phase content and same ratio of $\Phi_{\text{Ca(OH)}_2} / \Phi_{\text{SiO}_2}$. The composition of the reference suspension is detailed in **Table 2** and the corresponding calculation of the mass to use is shown in **section S3** in the **Supplementary Material**. Mixing of this suspension was performed to ensure an identical shear history as described in **Table 1**.

The composition of the model suspension in terms of phase content is given in **Fig. 1**. With increasing amount of ettringite the phase the phase contents of quartz powder and Ca(OH)₂ are slightly decreasing, whereas the total volumetric phase content Φ_{total} is increasing as well (**Table 3**).

2.2.4. Solvent exchange with isopropanol (Iso)

After a reaction time of 15 min, 10 mL of the mixed suspension were taken with an Eppendorf pipette, instantly transferred into 50 mL anhydrous isopropanol (precooled to 5 °C) in centrifuge tubes (50 mL) and agitated for 10 min by hand. Using a Buchner funnel the isopropanol-H₂O-suspension was filtered via a cellulose filter (retention 3 to 5 μm, ROTILABO® Type 14A by Carl Roth GmbH + Co. KG). The sample was washed twice by adding 50 mL anhydrous isopropanol (precooled to 5 °C), filtered, dried in an oven at 45 °C for 6 h, and pulverized with a mortar (**Fig. 2**). This procedure is referred to as **Iso**.

2.2.5. Inductively coupled plasma optical emission spectrometry

To determine both the chemical composition of the filtrate (**Fig. 2**) as a function of the preset amount of ettringite in the quartz suspensions formed and to check whether the preset amount of ettringite was correctly formed, inductively coupled plasma optical emission spectrometry (ICP-OES) was employed using an Activa M with the radial observation from Horiba Jobin Yvon GmbH. For this, the filtrate was gravimetrically diluted 13:1 with nitric acid (HNO₃, 1 %). Here, the deviation of the device has two areas, at a ion concentration below 50 mg L⁻¹ ± 1 mg L⁻¹ and above 50 mg L⁻¹ ± 2 %.

2.2.6. X-ray diffraction

The crystallinity and composition of all educts, products, and dried samples were investigated by X-ray diffraction (XRD) using a Bruker D8

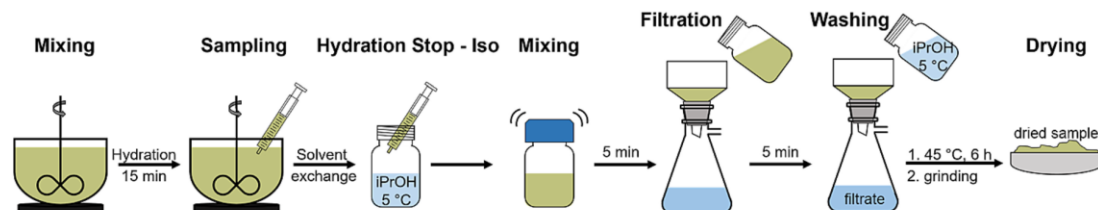


Fig. 2. Scheme of hydration stop by solvent exchange with isopropanol (Iso).

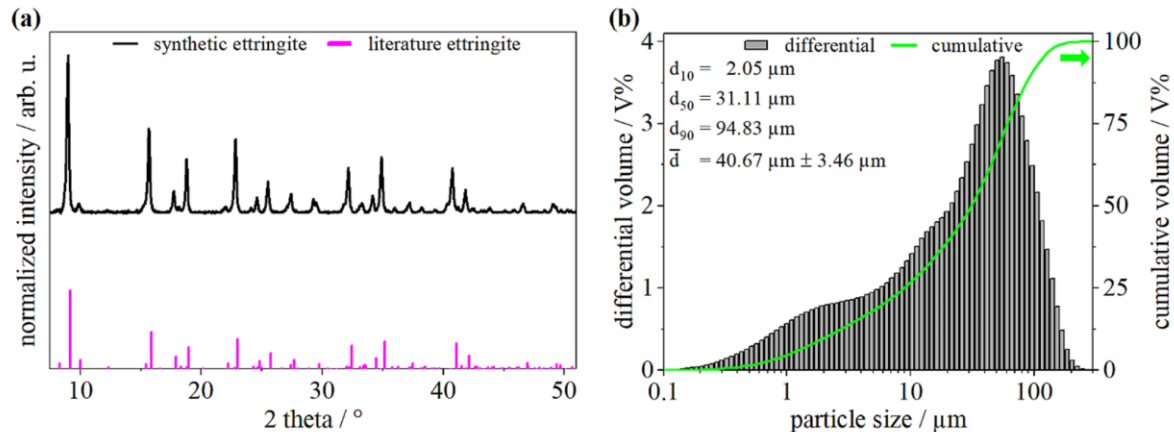


Fig. 3. (a) Powder X-ray diffraction pattern of synthetic ettringite (black) and its literature data reflections (PDF code: 01-074-9855, pink) [24,25] and (b) particle size distribution of anhydrous quartz powder SiO_2 derived from laser diffraction; further characterisation in Figs. S1 + S2.

Advance in reflection mode including a LynxEye detector. It was operated at 20 °C, 40 kV, and 40 mA using $\text{Cu-K}\alpha$ radiation. Each measurement was done in a 2θ -range from 5° to 70°, with a step size of 0.010540856°, and 4 s per step, resulting in a total measurement time of 7.25 h per sample. Additionally, to ensure the presence of ettringite, a zoom-in diffractogram was done in a 2θ -range from 8° to 10°, with a step size of 0.010540856°, and 12 s per step, resulting in a total measurement time of 1.62 h per sample. The powder of each sample was transferred into an X-ray amorphous PVC powder carrier and smoothed to avoid sample displacement. Their diffraction patterns were evaluated via the database of Powder Diffraction File (PDF-2) 2020 of the International Centre for Diffraction Data (ICDD).

2.2.7. Thermogravimetric analysis

To evaluate the content of physically and chemically bound water, mainly from ettringite, as well as the change in the decomposition behaviour every dried sample (Fig. 2), SiO_2 , $\text{Ca}(\text{OH})_2$, $\text{Al}_2(\text{SO}_4)_3 \cdot 18 \text{H}_2\text{O}$, and synthetic ettringite were investigated by thermogravimetric analysis (TGA) using aluminium oxide crucibles (70 μL) in a TGA/DSC 3+ from Mettler-Toledo GmbH with a device-specific deviation of $\pm 0.005\%$ (min. 1 μg) and a relative temperature deviation of 0.4%. It was operated in a temperature range from 20 °C to 1100 °C under a nitrogen flow of 25 mL/min and a heating ramp of 5 °C/min, followed by holding the temperature at 1100 °C for 15 min.

2.2.8. Scanning electron microscopy

For scanning electron microscopy (SEM), a FEI Nova NanoSEM 230, equipped with a through-the-lens-detector was used as an imaging tool, with a deviation of 0.5 nm at 30 kV. The acceleration voltage was 2 kV, the current 8 pA, and the pressure 525 nbar for each measurement, the powder (i.e. anhydrous SiO_2 and dried sample (Fig. 2)) was transferred on an adhesive carbon disk and cleaned from the excess sample through a compressed air gun. For the analysis of the particle size d of $\text{Ca}(\text{OH})_2$ as well as the morphology (length l , width w , and aspect ratio $AR = lw^{-1}$) of ettringite ten SEM micrographs of each preset amount were taken and manually measured. Via the software ImageJ 1.53 s, each micrograph was enlarged by 200%, thus dividing one micrograph into four sub-micrographs, measured by taking two values for each particle, in case of ettringite the longest distance was counted as length l and the shortest as width w and for $\text{Ca}(\text{OH})_2$ both values were nearly identical, being noted as particle size d . The total amount of counted particles is indicated on the y-axis in Fig. 6 and ranged from 400 to 2500 particles.

2.2.9. Nitrogen physisorption

To assess the specific surface area of anhydrous quartz powder SiO_2

as well as the dried samples (Fig. 2), nitrogen (N_2) physisorption was performed at an Analysator SA 3100 from Beckman Coulter Inc. operating at -196.15 °C. Before physisorption measurements, the samples were degassed under vacuum at 150 °C for 4 h. Specific surface area was estimated by applying the BRUNAUER-EMMETT-TELLER (BET) [20] equation.

2.2.10. Rheological measurements

The rheological properties of the suspensions were investigated by a ThermoFisher Haake MARS 60 rheometer using a cylindrical building materials cell (details on measurement set-up, device-specific resolution accuracy, and data conversion see [18,19]) actively conditioned to 20 °C by a tempering unit. The performed stress-controlled measurement sequence consisted of a linearly increasing shear ramp from 0 Pa to 1024 Pa within 90 s. When the rotational velocity reached $\Omega = 80$ rpm, the shear stress τ was kept constant for 15 s and followed by a linear, stress controlled decreasing ramp to 0 Pa. To evaluate yield stress τ_0 and plastic viscosity μ , the data of the decreasing ramp between $\dot{\gamma} = 50 \text{ s}^{-1}$ and the corresponding maximum shear rate (up to $\dot{\gamma} = 500 \text{ s}^{-1}$) was selected for a BINGHAM evaluation [21].

To connect the rheological results to a building practical application the workability of the suspensions with different amounts of ettringite was investigated via a spread flow test according to DIN EN 1015-3 without shocks [22]. For further correlations to established methods, the yield stress $\tau_{0,calc}$ is calculated from the spread flow diameter SF according to the approach by ROUSSEL ET AL. [23] (Eq. (3)). As a sufficient flow of the samples is a precondition for the application of this conversion, all samples with a spread flow $SF > 200$ mm were selected.

$$\tau_{0,calc} = \frac{225 \cdot \rho \cdot g \cdot V^2}{128 \cdot \pi^2 \cdot R^5} \quad (3)$$

ρ = specific weight / $\text{kg} \cdot \text{m}^{-3}$

V = sample's volume / m^3 (HÄGERMANN cone: $3.44 \cdot 10^{-4} \text{ m}^3$)

g = gravitational acceleration / $\text{m} \cdot \text{s}^{-2}$

R = spread flow radius without shocks / m.

3. Results and discussion

3.1. Structural characterisation

3.1.1. Synthetic ettringite and anhydrous quartz powder (educts)

For investigation of the influence of ettringite onto the rheological properties of the quartz powder suspension, it is necessary to form enough ettringite *in situ* in order to achieve a sufficient variation of contents in the suspension. During the early hydration process of cement

Table 4

Desired preset amount of ettringite in quartz powder suspensions and the respective amount derived by ICP-OES and TGA; the standard deviation noted as 0.0 was in all cases in the order of $1 \cdot 10^{-4}$, rounded according to DIN 1333 [26].

desired amount of ettringite / wt %	measured content of ettringite / wt % derived by		determined mass m / g by			
			ICP-OES		TGA	
			ICP-OES	TGA	Ca (OH) ₂	ettringite
0.0	0.0 ± 0.0	0.0 ± 0.0	16.45 ± 0.05	0.0 ± 0.0	16.9 ± 0.0	0.0 ± 0.0
2.4	2.3 ± 0.0	2.4 ± 0.0	12.19 ± 0.03	11.58 ± 0.03	12.7 ± 0.0	11.9 ± 0.0
4.7	4.6 ± 0.0	4.7 ± 0.0	7.97 ± 0.04	23.17 ± 0.05	8.4 ± 0.0	23.9 ± 0.0
6.9	6.7 ± 0.0	6.9 ± 0.0	3.74 ± 0.06	34.76 ± 0.12	4.2 ± 0.0	35.8 ± 0.0
9.1	9.0 ± 0.0	9.1 ± 0.0	0.0 ± 0.0	46.98 ± 0.13	0.0 ± 0.0	47.7 ± 0.0

suspensions, the ettringite content increases very rapidly from 0 wt% to approx. 5 wt% and remains at this content for the time relevant to processing [5]. Based on this information, the ettringite contents for this study were selected in order to be able to investigate the influence of lower and higher ettringite content. As the synthesis route introduced by STRUBLE [17] requires a big reaction volume, it is not suitable for our investigations. Therefore, the route was optimized by replacing the saturated aqueous solution of Ca(OH)₂ with solutions of NaOH and CaCl₂ to form Ca(OH)₂ (Eq. (S1)) *in situ*, which more correctly mirrors cementitious systems since during the hydration of cement, Ca(OH)₂ is also formed *in situ*. Analysis of the resulting synthetic powder (subsection 2.2.1) by XRD (Fig. 3a), TGA, and IR confirmed the successful synthesis of ettringite via the up-scalable synthesis route developed in this study (subsection S1.1 in the Supplementary Material (Fig. S1)). The powder diffractogram depicted in Fig. 3a shows the comparison of the measured 2θ data with its most prominent reflections ($I_{\text{reflection}} > 0.1 I_{\text{max}}$) in the angular range of $7.5^\circ \leq 2\theta \leq 51^\circ$ [24], which correlates with the data by HARTMAN ET AL. [24] (PDF code: 01–074-9855). The only two

discrepancies in comparison with literature, regarding the intensity of the reflections at $2\theta = 32.03^\circ$ and $2\theta = 34.84^\circ$, are most likely induced by the faceting of the crystals. In order to identify changes to anhydrous quartz powder SiO₂ after synthetic ettringite is formed on the surface as well as to analyse these, the state before mixing with aqueous solutions (subsection 2.2.3) is assessed via TGA, XRD, IR (subsection S1.2 in the Supplementary Material (Fig. S2)). The analysis of the particle size distribution shows a broad distribution of the SiO₂ with a mean size $\bar{d} = 40.67 \mu\text{m} \pm 3.46 \mu\text{m}$ (Fig. 3b). Both this model system and a cement paste show a polydisperse particle size distribution and with the precipitation of hydration products (e.g. ettringite) the polydispersity significantly increases.

3.1.2. Model suspensions

To demonstrate reproducibility, three repetitions of the syntheses and characterisations were conducted. Hereby, the main focus lay on correlating the flow behaviour of the suspension with the content of ettringite contained therein. Each desired preset amount of ettringite in the suspension (Table 4) was achieved by the employed synthesis method (subsection 2.2.1) with a yield of nearly 100 % (i.e. the added mass of Al₂(SO₄)₃ • 18 H₂O was nearly 100 % transformed) as indicated quantitatively by two analytical methods (ICP-OES and TGA) and qualitatively by XRD, IR, and SEM described in subsection 2.2. The mean of the quantified content of ettringite by ICP-OES and TGA was used for all further correlation of rheological properties and content of ettringite. The detailed data and their evaluation are shown in section S5 in the Supplementary Material.

To visualize changes on the surface of quartz particles with different content of precipitated ettringite, scanning electron microscopy (SEM) was used (Fig. 4). At a content of 0.0 wt% ettringite (Fig. 4b) the surface shows only crystallized Ca(OH)₂. It is obvious that with rising content of ettringite an increasing number of small needle-shaped ettringite crystals appears which show pronounced interconnections for ettringite contents above 4.7 wt% (Fig. 4c-f). Consequently, with increasing ettringite content the total specific surface of all particles in the suspensions should significantly rise. Furthermore, the SEM investigations show a needle-like shape for the precipitated ettringite particle.

The verification of the development of the specific surface area within suspensions with different contents of ettringite was performed by nitrogen physisorption measurements. The evaluation shows an increase of the specific surface area with rising ettringite content (Fig. 5a),

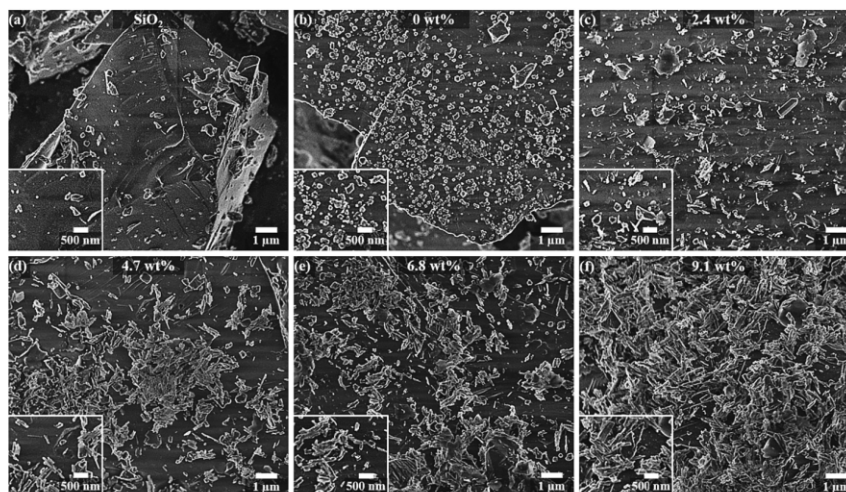


Fig. 4. SEM micrographs of (a) anhydrous quartz powder SiO₂ with the increasing amount of *in situ* formed ettringite (b) 0.0 wt%, (c) 2.4 wt%, (d) 4.7 wt%, (e) 6.8 wt%, and (f) 9.1 wt%) stopped after 15 min of hydration by Iso; 525 nbar, 8 pA, and 2 kV; estimated particle size d of Ca(OH)₂ as well as ettringite's crystal's length l , width w , and aspect ratio $AR = l w^{-1}$ derived from the SEM micrographs see Fig. 6.

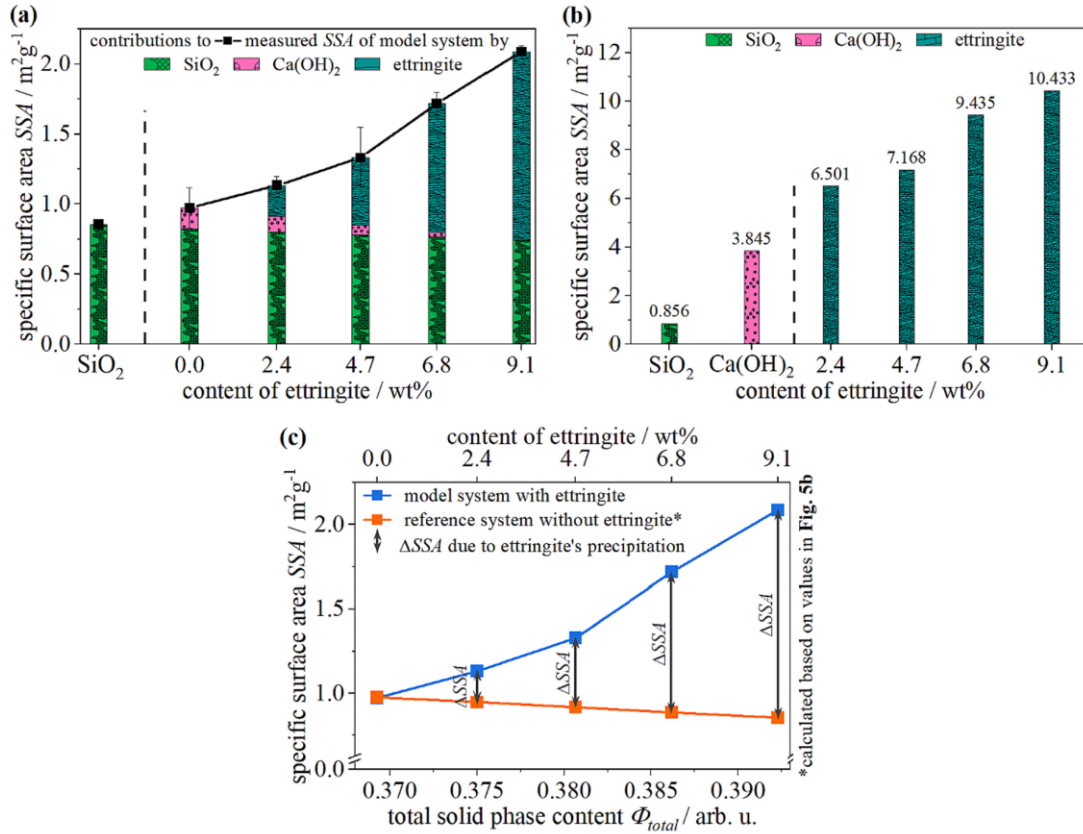


Fig. 5. N₂ physisorption data; (a) specific surface area SSA of anhydrous quartz powder SiO₂ with the increasing amount of in situ formed ettringite; reaction stopped after 15 min of hydration by Iso, respective values in Table S9, and corresponding data in Table S10, (b) recalculated (Eq. (4)) SSA of SiO₂, Ca(OH)₂, and in the case of ettringite dependent on the model suspensions' composition, and (c) comparison of SSA of model suspension with ettringite precipitation and reference suspension without ettringite precipitation to determine the SSA contribution corresponding to ettringite formation.

exhibiting a non-linear nature. It is expected that this slope results from the fact that due to the reaction velocity being proportional to the concentrations of the reactants [27], more and smaller needle-like shaped ettringite is formed with higher concentrations of Al₂SO₄ • 18 H₂O.

$x \equiv$ content of ettringite in the model suspension / wt%

$$SSA_x = SSA_{SiO_2} \frac{\Phi_{SiO_2,x}}{\Phi_{total,x}} + SSA_{Ca(OH)_2} \frac{\Phi_{Ca(OH)_2,x}}{\Phi_{total,x}} + SSA_{ettringite,x} \frac{\Phi_{ettringite,x}}{\Phi_{total,x}} \quad (4)$$

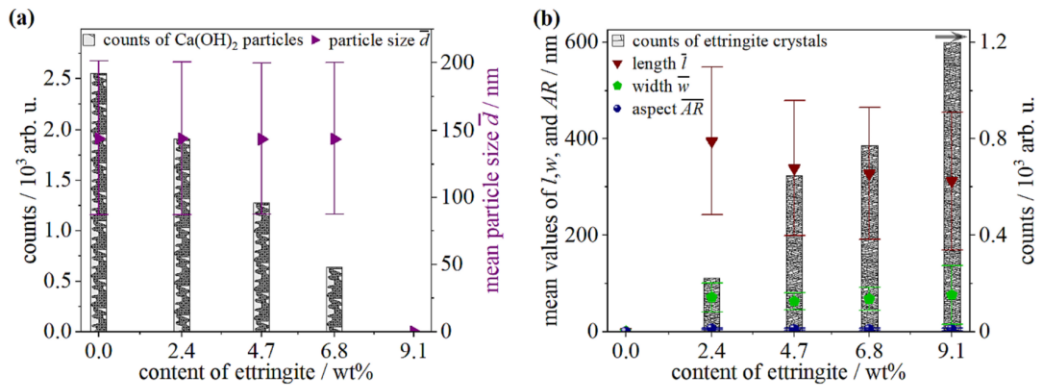


Fig. 6. SEM results; (a) mean particle size \bar{d} of Ca(OH)₂ with respective counts and (b) mean length \bar{l} , width \bar{w} , and aspect ratio \bar{AR} with respective counts of ettringite dependent on preset content of ettringite in the model suspension; values rounded according to DIN 1333 [26] and distributions shown in Fig. S12.

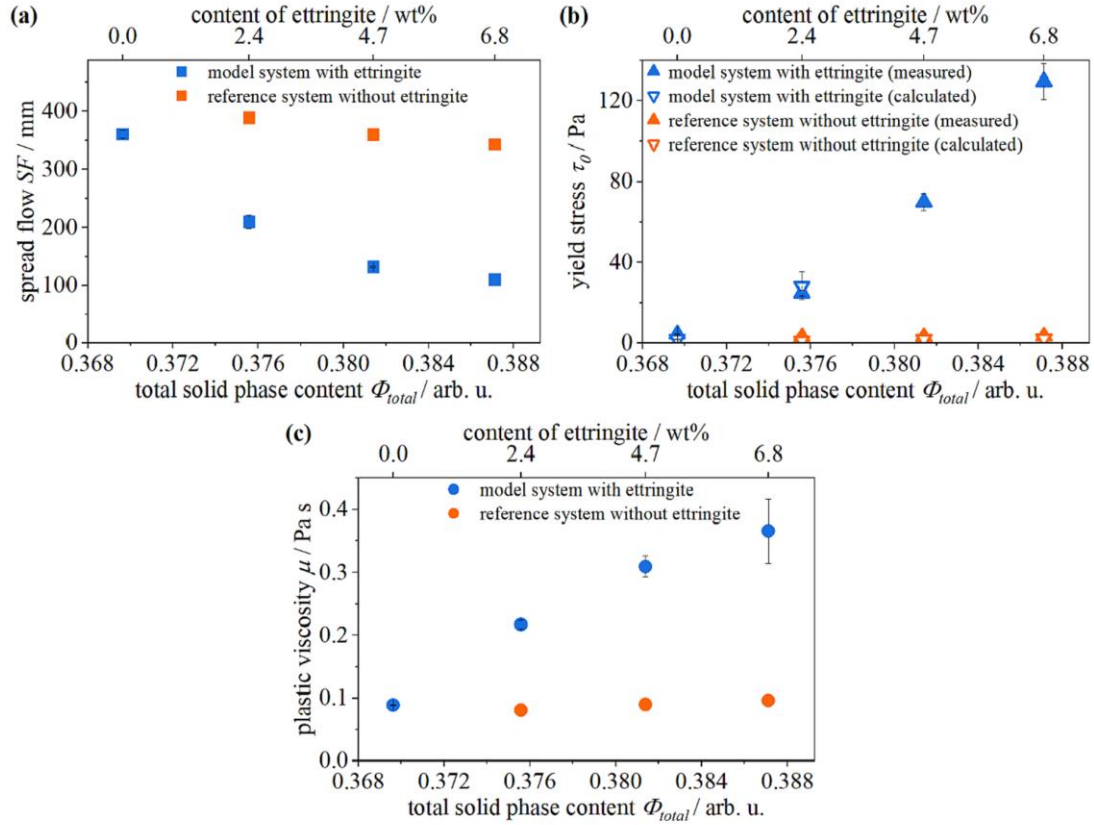


Fig. 7. Results of rheological measurements on the suspensions with and without ettringite; (a) spread flow SF , (b) yield stress τ_0 , and (c) plastic viscosity μ ; for the yield stress τ_0 in addition to the rheometer results also the yield stress τ_0 calculated from the spread flow SF results by Eq. (3) is given and designated as “calculated”.

$$SSA_{Ca(OH)_2} = \frac{SSA_{0.0} - SSA_{SiO_2} \frac{\Phi_{SiO_2}}{\Phi_{total,0.0}}}{\frac{\Phi_{Ca(OH)_2}}{\Phi_{total,0.0}}} = 3.845 \text{ m}^2 \text{ g}^{-1}$$

$$SSA_{ettringite,x} = \frac{SSA_x - SSA_{SiO_2} \frac{\Phi_{SiO_2,x}}{\Phi_{total,x}} - SSA_{Ca(OH)_2} \frac{\Phi_{Ca(OH)_2,x}}{\Phi_{total,x}}}{\frac{\Phi_{ettringite,x}}{\Phi_{total,x}}}$$

Derived from the solid phase content ratios ($\Phi_x \Phi_{total,x}^{-1}$) the different contributions of each component (i.e. SiO_2 , $Ca(OH)_2$, and ettringite) to the measured specific surface area were calculated. Note that due to the different densities of the materials, the volumetric phase content (solids fraction) of the suspension increases with increasing ettringite content. The specific surface area for SiO_2 and $Ca(OH)_2$ are deviated from the sample SiO_2 and 0.0 wt%, as the first is a single-phase system and the second two phase system with known SiO_2 and unknown $Ca(OH)_2$. From these, the specific surfaces SSA of the pure phases in the model system were assessed as $0.856 \text{ m}^2/\text{g}$ and $3.845 \text{ m}^2/\text{g}$ for SiO_2 , $Ca(OH)_2$ (Eq. (4)). Here, both SiO_2 and $Ca(OH)_2$ are considered to be constant due to the following reasoning. The amount of quartz powder is identical (Table 2) for each suspension, inert, and thus the particle size distribution remains unchanged. Derived from SEM micrographs it is seen that both the particle size distribution of $Ca(OH)_2$ (Fig. S12a) and its mean particle size \bar{d} stay approximately identical $\bar{d} = 144 \text{ nm} \pm 57 \text{ nm}$ (Fig. 6a) while only the counts of particles sinks (Figs. 6a). Thus, the SSA of portlandite is considered to be constant. In parallel, the counts of needle-shaped ettringite particles grows while their size decreases slightly with higher content of ettringite in the model suspension (Figs. 6b).

The calculated specific surface area $SSA(\Phi_{total})$ for the reference

suspension without ettringite precipitation is shown in Fig. 5c and correlated to the ettringite containing model suspension. Here, the solid phase content ratios $\Phi_{SiO_2}^* \Phi_{total}^{-1}$ and $\Phi_{Ca(OH)_2}^* \Phi_{total}^{-1}$ were multiplied with the previously assessed specific surface areas of SiO_2 ($SSA_{SiO_2} = 0.856 \text{ m}^2/\text{g}$) and $Ca(OH)_2$ ($SSA_{Ca(OH)_2} = 3.845 \text{ m}^2/\text{g}$) (Eq. (5)). The visible declining trend for the system without ettringite is due to less amount of $Ca(OH)_2$ in the reference suspension, as the content of ettringite was exchanged by SiO_2 and $Ca(OH)_2$ and at a higher total solid phase content Φ_{total} more ettringite and less $Ca(OH)_2$ is in the corresponding model system (Table 2).

$$SSA_{\Phi_{total},x} = SSA_{SiO_2} \frac{\Phi_{SiO_2,x}^*}{\Phi_{total,x}} + SSA_{Ca(OH)_2} \frac{\Phi_{Ca(OH)_2,x}^*}{\Phi_{total,x}} \quad (5)$$

$$\Phi_{SiO_2}^* \Phi_{ettringite,x} = \Phi_{SiO_2,x} + \Phi_{ettringite,x} \left(1 - \frac{\Phi_{Ca(OH)_2,x}}{\Phi_{SiO_2,x}} \right)$$

$$\Phi_{Ca(OH)_2}^* \Phi_{ettringite,x} = \Phi_{Ca(OH)_2,x} + \Phi_{ettringite,x} \left(\frac{\Phi_{Ca(OH)_2,x}}{\Phi_{SiO_2,x}} \right)$$

The difference between the specific surface area between both suspensions is directly caused by ettringite precipitation and thus indicating the additional formed surface.

3.2. Rheological characterisation

After the preset amount of ettringite in the model suspension (i.e. the suspension containing quartz, ettringite and $Ca(OH)_2$) was successfully formed, the rheological properties of the suspension were assessed. Due to changes in the total solid phase content Φ_{total} with variation in ettringite content (Fig. 1), the rheological properties are a function of

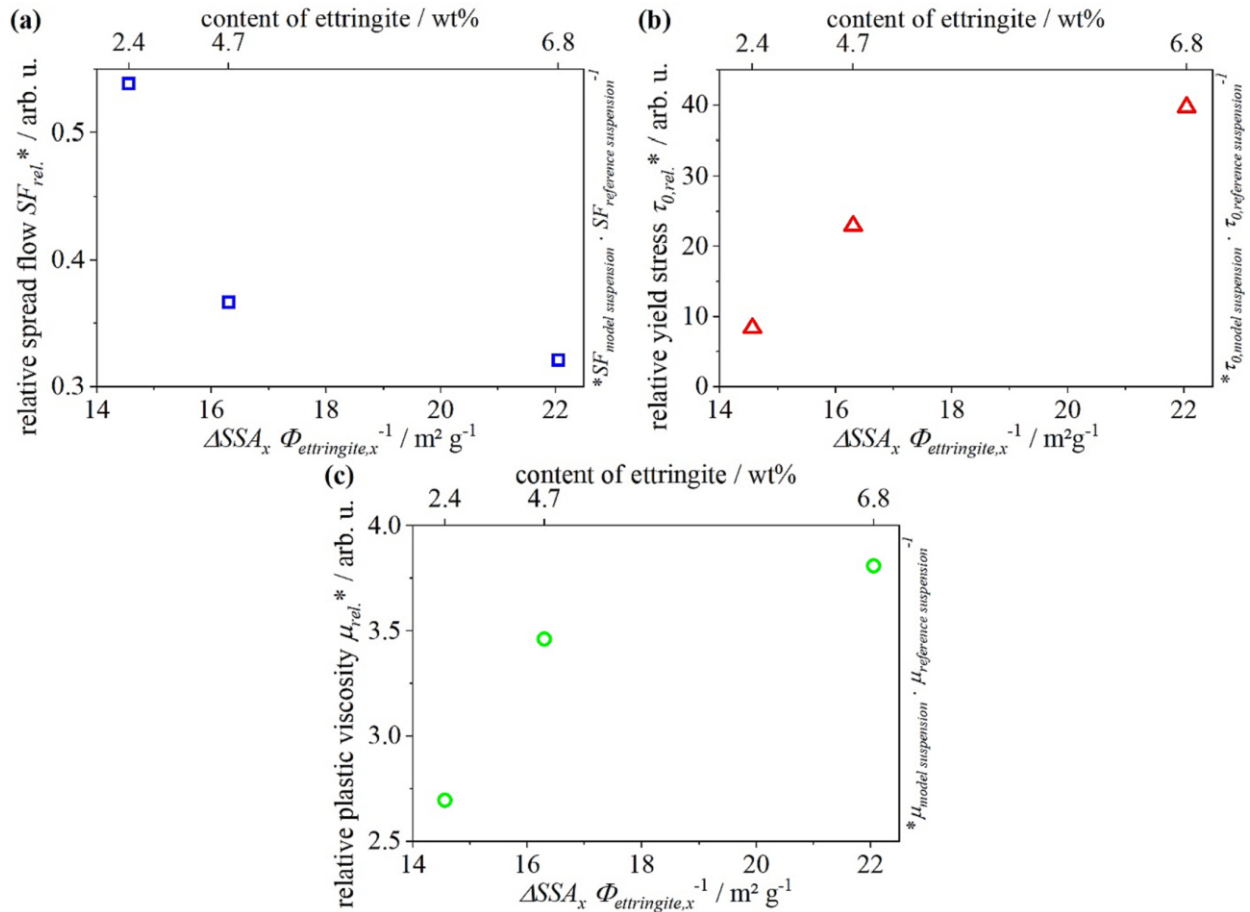


Fig. 8. Quantification of the impact of particle properties of ettringite on rheology of model suspensions normalized by the corresponding property of the reference suspension plotted as a function of the specific surface area created by ettringite and normalized by the solid phase content of ettringite $\Delta SSA_x \Phi_{ettringite,x}^{-1}$; (a) relative spread flow SF_{rel} , (b) relative yield stress $\tau_{0,rel}$, and (c) relative plastic viscosity μ_{rel} .

combined changes in Φ_{total} and ettringite content (Fig. 7). A higher amount of ettringite reduces the flowability of the model suspension resulting in a non-linear decrease of the spread flow SF (Fig. 7a). The yield stress τ_0 (Fig. 7b), and in parallel, the plastic viscosity μ increase with increasing ettringite content within the model suspension (Fig. 7c). The rheological behaviour of the samples with 9.1 wt% ettringite content strongly resembles a solid instead of a liquid, showing no yielding in spread flow tests and exhibiting significant slippage layers in the rheometer measurements. Consequently, the samples with 9.1 wt% ettringite are not considered for rheological evaluations. Calculation of the yield stress τ_0 based on the spread flow SF according to ROUSSEL ET AL. [21] shows a good correlation to the yield stress τ_0 determined by rheometer measurement (Fig. 7b). Model suspensions with ettringite content higher than 2.4 wt% show a spread flow $SF < 200$ mm, for which Eq. (3) is not validated. The values are thus not reported here.

In order to evaluate to what extent, the influences on rheology of the model suspension can be attributed to the ettringite precipitation or the changing solid phase content, a reference suspension is investigated with the same solid phase contents, however without ettringite precipitation. The rheological behaviour of the reference suspension also shows a decrease in workability (Fig. 7a) and an increase in both yield stress τ_0 and plastic viscosity μ with increasing phase content (Fig. 7b and 7c). However, the rheological changes of the reference suspension are significantly smaller compared to the model suspensions with ettringite. Since the total solid phase content Φ_{total} of both suspensions is

similar, it can be safely concluded, that the changes observed for the model (quartz, ettringite, $\text{Ca}(\text{OH})_2$) suspension are primarily caused by ettringite precipitation and not by the changes in the solid phase content Φ_{total} .

Since the difference between the rheological properties of the model suspension and the reference suspension is induced by ettringite, in a next step, the impact of the varying particle properties of ettringite has to be considered. As pointed out in subsection 3.1.2, the non-linearity of the specific surface area of the granular inventory of the suspensions (Fig. 5a) is primarily caused by changing particle properties of ettringite due to hydration kinetics. Since kinetic principles are applied, a higher ettringite content is related to more ettringite particles with smaller sizes and a lower ettringite content resulting in less particles with a larger elongated structure (Fig. 6b). Note however, that the detailed mechanisms responsible for these changes are not totally clear yet (see subsection 3.1.2). The influence of the properties of ettringite onto the rheology is shown in Fig. 8. Therefore, the additional specific surface ΔSSA formed due to ettringite precipitation (see Fig. 5b) is normalized by the volumetric ettringite phase content $\Phi_{ettringite}$ (i.e. the volume of ettringite solids divided by the total volume of the suspension).

With rising ettringite content the ratio $\Delta SSA_x \cdot \Phi_{ettringite,x}^{-1}$ increases confirming a very pronounced influence of the ettringite particle properties onto the rheology. Therefore, in Fig. 8 the rheological properties spread flow SF , yield stress and plastic viscosity of the model suspension each are normalized by the respective value of the reference suspension.

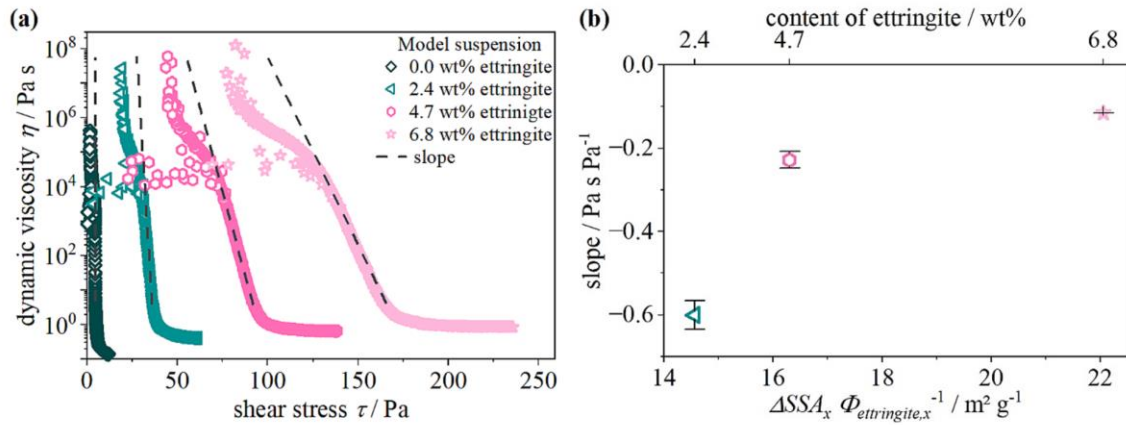


Fig. 9. Impact of the content and specific surface of ettringite particles on the rheology in dependence of the applied shear stress τ ; (a) dynamic viscosity η measured in downward ramp for different ettringite contents and (b) dependency of slope of η -curves on $\Delta SSA_x \Phi_{etringtone,x}^{-1}$.

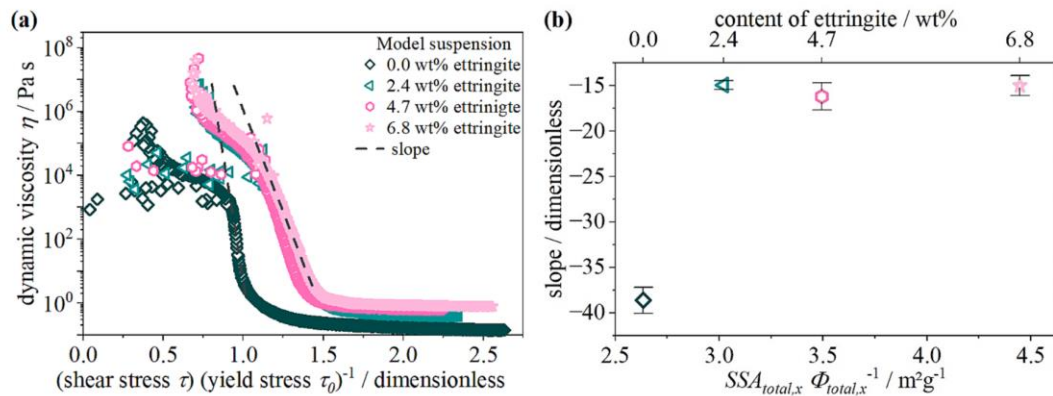


Fig. 10. Impact of the content and specific surface of ettringite particles on the rheology in dependence of the applied shear stress normalized by the respective yield stress of the sample; (a) dynamic viscosity η measured in downward ramp for different ettringite contents as a function of the applied shear stress normalized by the respective yield stress τ_0 of the sample and (b) dependency of slope of the viscosity curves from (a) on the normalized total specific surface area $SSA_{total,x} \Phi_{total,x}^{-1}$.

The higher the specific surface (and most likely the smaller) of the ettringite particles, the higher the decline of spread flow (Fig. 8a) and the increase of both yield stress τ_0 (Fig. 8b) and plastic viscosity μ (Fig. 8c). Unfortunately, the model suspension with $\Phi_{total} = 0.370$ contains no ettringite and cannot be plotted, i.e. $\Phi_{etringtone} = 0$.

Comparing Fig. 8b and 8c, the effect of the ettringite properties seem to be significantly more pronounced with regard to the relative yield stress $\tau_{0,rel}$ than for relative plastic viscosity μ_{rel} . This can be explained by the dominant influence of the particle's needle-like morphology on the yielding behaviour of the suspension occurring at low shear stress. This can be proven by evaluating the dynamic viscosity of the suspensions in the stress controlled downward ramp, which shows different slopes at low shear stresses τ close to the respective yield stresses τ_0 (Fig. 9a). This absolute value of the slope decreases with increasing $\Delta SSA_x \Phi_{etringtone,x}^{-1}$, indicating a significantly increased interparticle friction over a larger shear stress area before yielding (Fig. 9b). The data at $0.5 \cdot 10^{-1} \text{ s}^{-1} \leq \dot{\gamma} \leq 10^{-3} \text{ s}^{-1}$ was selected to quantify the slopes.

Normalizing the shear stress τ in Fig. 9 by the respective yield stress τ_0 of each sample results in master curves as shown in Fig. 10a. The behaviour of the two-phase system with 0 wt% ettringite (SiO_2 and $\text{Ca}(\text{OH})_2$) differs significantly from the three-phase system (SiO_2 , $\text{Ca}(\text{OH})_2$ and ettringite). The determination of the slopes of the viscosity curves (see Fig. 10b) shows that the coagulation process upon unloading (and thus the yielding process upon loading) is fundamentally altered by

ettringite, leading to a much more 'ductile' yielding. This finding clearly underlines the previous conclusion, that the needle-like ettringite seems to have a much better stabilization effect on the system, stabilizing the individual quartz-particles.

The results show that the influence of ettringite is very pronounced on the yield stress τ_0 at very low loadings and respective low shear rates $\dot{\gamma}$, also shown by the investigations of JAKOB ET AL. [5]. At high shear rates $\dot{\gamma}$, a disproportionately lower influence of the ettringite content onto the rheological properties is found, which is consistent with the results published by LINK ET. AL. [13]. Consequently, the influence of ettringite on the rheological parameters is also related to the applied level of shear stress τ .

4. Conclusions

Quartz powder suspensions were chosen as a model system for cement suspensions to investigate the impact of different quantities of *in situ* formed ettringite on their rheological properties. To enable this study, an up-scalable synthesis route of ettringite was introduced in this work. The growing amount of formed ettringite was derived qualitatively from X-ray diffraction (XRD), scanning electron microscopy (SEM), and nitrogen physisorption as well as quantitatively from inductively coupled plasma optical emission spectrometry (ICP-OES) and thermogravimetric analysis (TGA). With increasing amount of

precipitated ettringite the workability decreases and yield stress and plastic viscosity increase, consequently. This is due on the one hand due to the change in phase content, but primarily due to the significant increase in specific surface of the ettringite particles formed. Further it was found, that with increasing total amount of ettringite, the specific surface of the particles increases, indicating a shift to smaller particles, which can be explained by their formation mechanism. The effect of the fineness is much more pronounced for the yield stress than for the plastic viscosity, proofing similar observations made on cement suspensions. Further, the ettringite morphology has pronounced effect on the yielding behaviour itself, leading to a much more ductile behaviour.

CRedit authorship contribution statement

Patrick A. Kjöbling: Writing – review & editing, Writing – original draft, Visualization, Validation, Methodology, Investigation, Formal analysis, Data curation, Conceptualization. **Julian Link:** Writing – review & editing, Writing – original draft, Methodology, Investigation, Conceptualization. **Melanie Heinemann:** Writing – review & editing. **Franziska Lübke** **Mann-Warwas:** Writing – review & editing. **Felix Rieck** **genannt Best:** Writing – review & editing. **Thomas Sowoidnich:** Writing – review & editing. **Alexander Mundstock:** Writing – review & editing, Visualization. **Horst-Michael Ludwig:** Writing – review & editing. **Michael Haist:** Writing – review & editing, Supervision, Resources, Funding acquisition, Conceptualization. **Nadja C. Bigall:** Conceptualization, Funding acquisition, Resources, Supervision, Writing – review & editing.

Declaration of Competing Interest

The authors declare the following financial interests/personal relationships which may be considered as potential competing interests: Nadja-Carola Bigall reports financial support was provided by German Research Foundation. Michael Haist reports financial support was provided by German Research Foundation. Horst-Michael Ludwig reports was provided by German Research Foundation..

Data availability

Data will be made available on request.

Acknowledgements

The study was funded by the Deutsche Forschungsgemeinschaft (DFG, German Research Foundation) – projects BI 1708/5-1, HA 7917/3-1, and LU 1652/32-1 [28] as well as by the project BI 1708/4-1. The authors thank A. Feldhoff and J. Caro for access to XRD (PCI, LUH). The authors thank J. Caro for access to IR (PCI, LUH). The authors thank C. Matthes (F.A., Weimar) for SEM measurements, A. Schulz (F.A., Weimar) for nitrogen physisorption as well as laser diffraction measurement, and G. Bohne (F.A., Weimar) for ICP-OES measurements. The authors thank the Laboratory for Nano- and Quantum Engineering (LNQE) for support.

Appendix A. Supplementary data

Supplementary data to this article can be found online at <https://doi.org/10.1016/j.conbuildmat.2023.133678>.

References

- [1] G.A. Rankin, The ternary system CaO-Al₂O₃-SiO₂, with optical study by F. E. Wright, *Am. J. Sci.* XXXIX (1915) 1–79. <https://doi.org/10.2475/ajs.4-39.229.1>.
- [2] R.H. Bogue, *The chemistry of Portland cement*, Reinhold Publishing Corp, New York, 1947.
- [3] H. Uchikawa, K. Ogawa, S. Uchida, Influence of character of clinker on the early hydration process and rheological property of cement paste, *Cem. Concr. Res.* 15 (1985) 561–572, [https://doi.org/10.1016/0008-8846\(85\)90053-5](https://doi.org/10.1016/0008-8846(85)90053-5).
- [4] J. Golaszewski, Influence of cement properties on rheology of fresh cement mortars without and with superplasticizer, *Archit. Civ. Eng. Environ.* 4 (2008) 49–66.
- [5] C. Jakob, D. Jansen, N. Ukrainczyk, E. Koenders, U. Pott, D. Stephan, J. Neubauer, Relating Ettringite Formation and Rheological Changes during the Initial Cement Hydration: A Comparative Study Applying XRD Analysis, Rheological Measurements and Modeling, *Materials (basel)*. 12 (2019) 2957, <https://doi.org/10.3390/ma12182957>.
- [6] F. Winnefeld, A. Zingg, L. Holzer, J. Pakusch, S. Becker, The Ettringite-superplasticizer interaction and its impact on ettringite distribution in cement suspensions, in: 9th ACI Int. Conf. Superplast. Other Chem. Admixtures Concr. Sevilla, Spain, Oct. 12–14, 2009, Sevilla, Spain, 2009; pp. 420.1–420.17.
- [7] A. Bogner, J. Link, M. Baum, M. Mahlbacher, T. Gil-Diaz, J. Lützenkirchen, T. Sowoidnich, F. Heberling, T. Schäfer, H.M. Ludwig, F. Dehn, H.S. Müller, M. Haist, Early hydration and microstructure formation of Portland cement paste studied by oscillation rheology, isothermal calorimetry, 1H NMR relaxometry, conductance and SAXS, *Cem. Concr. Res.* 130 (2020), 105977, <https://doi.org/10.1016/j.cemconres.2020.105977>.
- [8] L.J. Struble, W.-G. Lei, Rheological changes associated with setting of cement paste, *Adv. Cem. Bas. Mat.* 2 (1995) 224–230, [https://doi.org/10.1016/1065-7355\(95\)90041-1](https://doi.org/10.1016/1065-7355(95)90041-1).
- [9] G.H. Tattersall, *Workability and Quality Control of Concrete*, 1st ed., CRC Press, London, 2014. <https://doi.org/10.1201/9781482267006>.
- [10] U. Pott, C. Ehm, C. Jakob, D. Stephan, Investigation of the Early Cement Hydration with a New Penetration Test, Rheometry and In-Situ XRD, in: V. Mechtcherine, K. Khayat, E. Secrieru (Eds.), *Rheol. Process. Constr. Mater. RheoCon 2019, SCC 2019*, Springer, Cham, 2020; pp. 246–255. https://doi.org/10.1007/978-3-030-22566-7_29.
- [11] N. Roussel, G. Ovarlez, S. Garrault, C. Brumaud, The origins of thixotropy of fresh cement pastes, *Cem. Concr. Res.* 42 (2012) 148–157, <https://doi.org/10.1016/j.cemconres.2011.09.004>.
- [12] J. Link, T. Sowoidnich, C. Pfitzner, T. Gil-Diaz, F. Heberling, J. Lützenkirchen, T. Schäfer, H.M. Ludwig, M. Haist, The influences of cement hydration and temperature on the thixotropy of cement paste, *Materials (basel)*. 13 (2020) 1–20, <https://doi.org/10.3390/MA13081853>.
- [13] I.M. Krieger, T.J. Dougherty, A Mechanism for Non-Newtonian Flow in Suspensions of Rigid Spheres, *Trans. Soc. Rheol.* 3 (1959) 137–152, <https://doi.org/10.1122/1.548848>.
- [14] B.M. Guy, M. Hermes, W.C.K. Poon, Towards a Unified Description of the Rheology of Hard-Particle Suspensions, *Phys. Rev. Lett.* 115 (2015), 088304, <https://doi.org/10.1103/PhysRevLett.115.088304>.
- [15] J. Castle, A. Farid, L. V. Woodcock, The effect of surface friction on the rheology of hard-sphere colloids, in: *Trends Colloid Interface Sci. X*, Steinkopff, Darmstadt, n. d.; pp. 259–265. <https://doi.org/10.1007/BFb0115790>.
- [16] P.F. Luckham, M.A. Ukeje, Effect of Particle Size Distribution on the Rheology of Dispersed Systems, *J. Colloid Interface Sci.* 220 (1999) 347–356, <https://doi.org/10.1006/jcis.1999.6515>.
- [17] L.J. Struble, Synthesis and characterization of ettringite and related phases, in: *Proc. 8th Int. Congr. Chem. Cem.*, 6th ed., Rio de Janeiro, 1986; pp. 582–588.
- [18] Institut für Arbeitsschutz der Deutschen Gesetzlichen Unfallversicherung, GESTIS-Stoffdatenbank, (n.d.). <https://gestis.dguv.de/data?name=001150>.
- [19] M.C. Anthony, J.W. Bideaux, R.A. Bladh, K.W. Nichols, *The Handbook of Mineralogy* (2001). <http://www.handbookofmineralogy.org/>.
- [20] S. Brunauer, P.H. Emmett, E. Teller, Adsorption of Gases in Multimolecular Layers, *J. Am. Chem. Soc.* 60 (1938) 309–319, <https://doi.org/10.1021/ja01269a023>.
- [21] E.C. Bingham, *An Investigation of the Laws of Plastic Flow*, *Bull. Bur. Stand.* 13 (1916) 309–353.
- [22] DIN German Institute for Standardization., DIN EN 1015-3:2007-05, Methods of test for mortar for masonry — Part 3: Determination of consistence of fresh mortar (by flow table); German version EN 1015-3:1999+A1:2004+A2:2006, Beuth Verlag GmbH, Berlin, Germany, 2007.
- [23] N. Roussel, P. Coussot, “Fifty-cent rheometer” for yield stress measurements: From slump to spreading flow, *J. Rheol. (N. Y. N. Y.)*. 49 (2005) 705–718, <https://doi.org/10.1122/1.1879041>.
- [24] M.R. Hartman, R. Berliner, Investigation of the structure of ettringite by time-of-flight neutron powder diffraction techniques, *Cem. Concr. Res.* 36 (2006) 364–370, <https://doi.org/10.1016/j.cemconres.2005.08.004>.
- [25] A.E. Moore, H.F.W. Taylor, Crystal structure of ettringite, *Acta Crystallogr. Sect. B Struct. Crystallogr. Cryst. Chem.* 26 (1970) 386–393, <https://doi.org/10.1107/S0567740870002443>.
- [26] DIN German Institute for Standardization, DIN 1333:1992-02, Beuth Verlag GmbH, Berlin, Germany, Presentation of numerical data, 1992.
- [27] A.F. Hollemann, E. Wiberg, N. Wiberg, *Lehrbuch der anorganischen chemie*, 102nd ed., Walter de Gruyter, 2017.
- [28] Deutsche Forschungsgesellschaft (DFG), DFG SPP 2005—Priority Programm ‘Opus Fluidum Futurum—Rheology of Reactive, Multiscale, Multiphase Construction Materials’, (2018). <https://www.spp2005.de/> (accessed 31 October 2021).

Supporting Data

Influence of *in situ* ettringite formation on the rheological properties of quartz suspensions

Patrick A. Kießling^{a,b,†}, Julian Link^{b,†}, Melanie Heinemann^c, Franziska Lübke^a, Felix Rieckgenannt Best^a, Thomas Sowoidnich^c, Alexander Mundstock^a, Horst-Michael Ludwig^c, Michael Haist^{b,*}, and Nadja C. Bigall^a

^a Institute of Physical Chemistry and Electrochemistry, Leibniz Universität Hannover, Callinstr. 3a, 30167 Hanover, Germany; patrick.kissling@pci.uni-hannover.de, franziska.luebke@pci.uni-hannover.de, felix.best@pci.uni-hannover.de, alexander.mundstock@pci.uni-hannover.de, nadja.bigall@pci.uni-hannover.de

^b Institute of Building Materials Science, Leibniz Universität Hannover, Appelstr. 9a, 30167 Hanover, Germany; j.link@baustoff.uni-hannover.de

^c F.A. Finger-Institute of Building Materials Science, Bauhaus Universität Weimar, Coudraystr. 11A, 99423 Weimar, Germany; melanie.heinemann@uni-weimar.de, thomas.sowoidnich@uni-weimar.de, horst-michael.ludwig@uni-weimar.de

[†] These authors contributed equally to this work.

^{*} Correspondence: haist@baustoff.uni-hannover.de (+49-511-762-3772)

Received: date; Accepted: date; Published: date

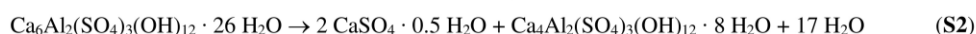
Abstract: Cement suspensions are subject to hydration processes causing dissolution of cement clinker, precipitation of hydration products and changes in the ion content of the carrier liquid. These mechanisms take place in parallel and control the workability of cement suspensions. The precipitation of nano-granular ettringite is currently believed to be one of the key influencing factors for rheological properties of fresh cement suspensions. In order to quantify the effect of ettringite precipitation from other precipitation or dissolution processes onto the rheological behaviour, a model system consisting of quartz powder and *in situ* formed ettringite is used, enabled by implementing a new upscalable synthesis route of ettringite. The quantity of formed ettringite in the model suspension is varied and derived qualitatively from X-ray diffraction as well as quantitatively from inductively coupled plasma optical emission spectrometry and thermogravimetric analysis. The influence of the ettringite content on the rheological properties are determined and also correlated to differing sizes of ettringite particles. This allows a quantification of the controlling mechanism of ettringite and the dependency of these mechanisms on particle properties. The correlation of the results to a reference suspension without ettringite verifies the statement of influence.

Keywords: Rheology, Ettringite, Cement model system, Quartz suspension, Analytics.

S1 Characterization of synthetic ettringite and anhydrous quartz powder

S1.1 Synthetic ettringite

Analysis of the resulting synthetic colourless powder implementing thermogravimetric analysis (TGA), X-ray diffraction (XRD), and infrared spectroscopy (IR) confirmed the successful synthesis of ettringite [Ca₆Al₂(SO₄)₃(OH)₁₂ · 26 H₂O]. **Fig. S1a** displays the TGA measurement wherein a large mass loss of 34.6% can be seen between 50 °C and 210 °C. As previously described by HALL ET AL. [1], this is attributed to the decomposition of ettringite to hemihydrate [CaSO₄ · 0.5 H₂O] and calcium aluminate monosulphate [AFm-14H; Ca₄Al₂(SO₄)₃(OH)₁₂ · 8 H₂O] (Eq. (S2)):



Further dehydration of hemihydrate at 225 °C ± 25 °C, dehydration of AFm-14H at 775 °C ± 125 °C, as well as ettringite's complete decomposition to calcium aluminate [(CaO)_x(Al₂O₃)_y], quicklime [CaO], and anhydrite [CaSO₄] at 900 °C [2–4] are discernible. The total mass loss of 46.4% closely matches the bound water content of ettringite (45.9%). The powder diffractogram depicted in **Fig. S1b** shows the comparison of the measured 2θ data with its most prominent reflections (I_{reflection} > 0.1 I_{max}) in the angular range of 7.5° ≤ 2θ ≤ 51° [5], which correlates with the data by HARTMAN ET AL. [5] (PDF code: 01-074-9855). The only two discrepancies in comparison with literature, regarding the intensity of the reflections at 2θ = 32.03° and 2θ = 34.84°, are most likely induced by the

faceting of the crystals. This is especially prominent for the reflection at $2\theta = 34.84^\circ$, which is most probably due to two different underlying crystal planes ($(10\bar{1}8)$ and $(30\bar{1}5)$) [5], here given by their BRAVAIS-MILLER indices according to a trigonal symmetry in a hexagonal cell. **Fig. S1c** shows the corresponding IR spectrum, wherein respective IR bands of ettringite in the mid-IR region align with the literature [6]. The bands are assigned as follows: (1) broad band at $3375\text{ cm}^{-1} \pm 375\text{ cm}^{-1}$ due to stretching vibrations of hydroxide groups and water molecules, (2) the latter's bending vibrations at 1650 cm^{-1} , 1460 cm^{-1} , and 870 cm^{-1} , as well as (3) the strong and sharp band at 1115 cm^{-1} corresponds with vibrations of sulphate groups.

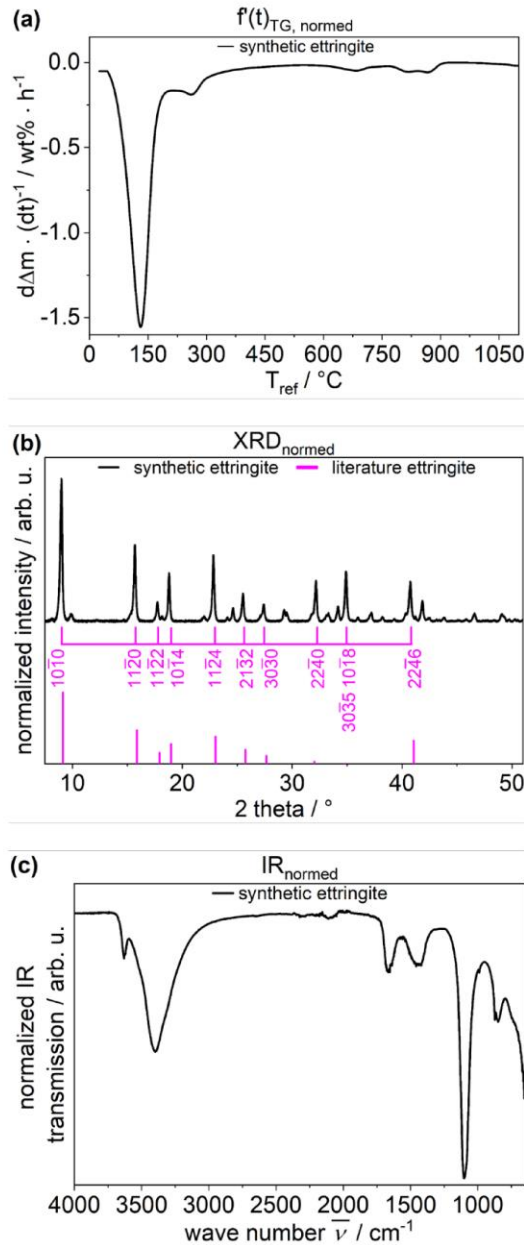


Fig. S1. (a) TGA data of synthetic ettringite plotted as mass normalized time derived weight loss ($d\Delta m \cdot (dt)^{-1}$) per hour against the reference temperature with a heating rate of $5\text{ }^\circ\text{C}/\text{min}$, (b) Powder X-ray diffraction pattern of synthetic ettringite (black) and its literature data reflections (PDF code: 01-074-9855, pink) [5,7] indexed using BRAVAIS-MILLER indices according to a trigonal symmetry in a hexagonal cell, and (c) IR spectrum in a range of $4000\text{ cm}^{-1} \leq \bar{\nu} \leq 700\text{ cm}^{-1}$.

S1.2 Quartz powder

Anhydrous quartz powder was analysed using TGA, XRD, and IR to assess the state before synthetic ettringite is formed on the surface. TGA measurement (Fig. S2a) shows the desorption of water up to roughly 100 °C and the condensation of silanol groups both at 230 °C ± 65 °C and 532 °C ± 136 °C [8]. Fig. S2b exhibits the respective diffractogram comparing the measured 2θ data with the most prominent reflections ($I_{\text{reflection}} > 0.1 \cdot I_{\text{max}}$) in the angular range of $5^\circ \leq 2\theta \leq 70^\circ$ [26], which align with the data by LAGER ET AL. [9]. Small differences in the respective intensity could be induced by different particle sizes, as smaller crystals display broader reflections [10–13]. Fig. S2c shows the corresponding IR spectrum, wherein found bands in the mid-IR region align with literature data [14]. Quartz powder's particle size distribution (Fig. S2d) was evaluated using laser diffraction, showing a similar yet coarser distribution as cement (CEM I 42.5 R).

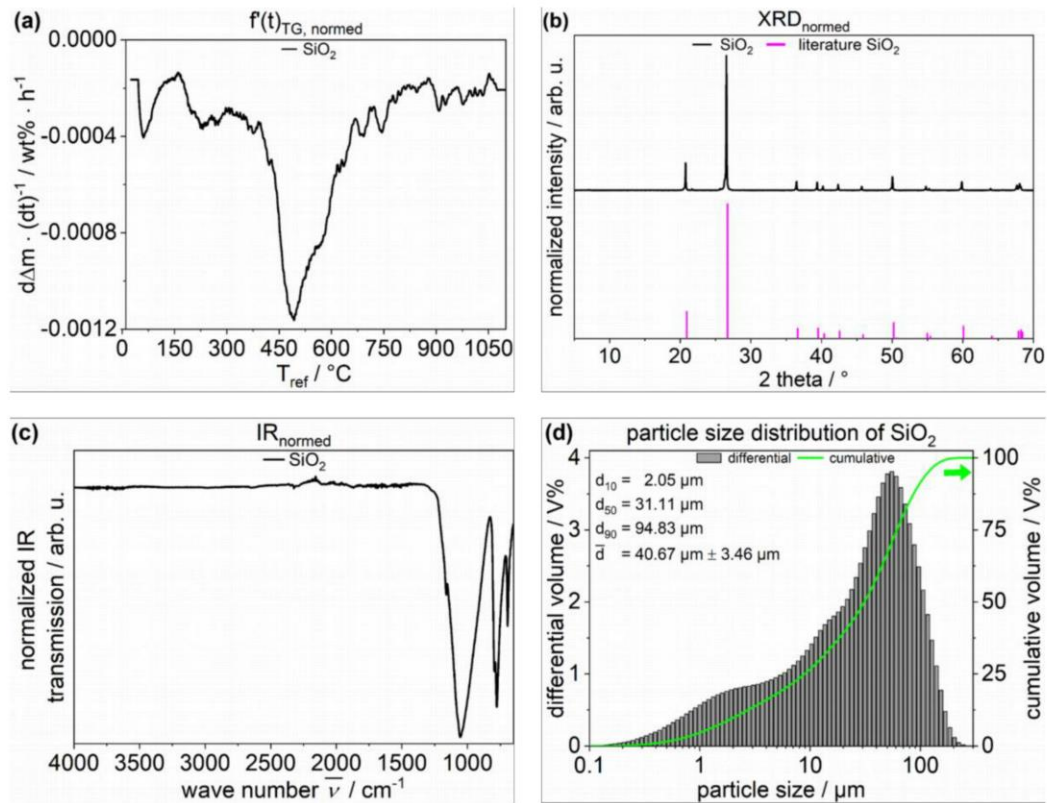


Fig. S2. (a) TGA data of anhydrous quartz powder plotted as mass normalized time derived weight loss ($d\Delta m \cdot (dt)^{-1}$) per hour against the reference temperature with a heating rate of 5 °C/min, (b) its powder X-ray diffraction pattern in an angular range of $7^\circ \leq 2\theta \leq 70^\circ$ compared against literature reflections (pink) [9], (c) respective IR spectrum in a range of 4000 cm^{-1} to 650 cm^{-1} , and (d) its particle size distribution derived from laser diffraction.

S2 Ascertainment of reaction duration

The essential time needed for a complete chemical conversion of $\text{Ca}(\text{OH})_2$ and $\text{Al}_2(\text{SO}_4)_3 \cdot 18 \text{H}_2\text{O}$ to ettringite in the quartz system was ascertained by XRD, TGA, and IR (Fig. S3). For this, following the mixing program shown in Table S1, a quartz suspension with a water to quartz ratio of $w/q = 0.67$, a phase content of $\Phi = 0.36$, a total volume of 1.2 L, and 9.1 wt% of *in situ* formed ettringite was prepared. SiO_2 (1144.8 g, 19.05 M) was consecutively mixed under stirring with an aqueous solution of CaCl_2 (279 mL, 1.96 M), a solution of NaOH (279 mL, 3.92 M) in water, and an aqueous solution of $\text{Al}_2(\text{SO}_4)_3 \cdot 18 \text{H}_2\text{O}$ (210 mL, 0.43 M) using a Kenwood KitchenAid KM336 S Chef Classic. After various reaction durations (up to 7 h) following the addition of $\text{Al}_2(\text{SO}_4)_3 \cdot 18 \text{H}_2\text{O}$, 10 mL of the quartz suspension were taken with an Eppendorf pipette, transferred to a 250 mL flask, which was slowly rotated to get a homogenous thin layer of quartz suspension, and transferred quickly into liquid nitrogen for 30 min. Each sample was freeze-dried using a freeze-dryer (Alpha 1-2 LDplus from Martin Christ Gefriertrocknungsanlagen GmbH) including the vacuum transducer VCP63MV (Thyracont Vacuum Instruments GmbH, device-specific deviation: 10 % in a range of 10 – 0.01 mbar) coupled with a two-stage rotary vane pump (RV 12 from Edwards Vacuum) for 11 h at 4 mbar (Fig. S4). The dried samples were stored at 19.2 °C ± 0.4 °C in a dry nitrogen atmosphere for up to 2 d before characterisation. This hydration stop process was derived from KIBLING ET AL.[15].

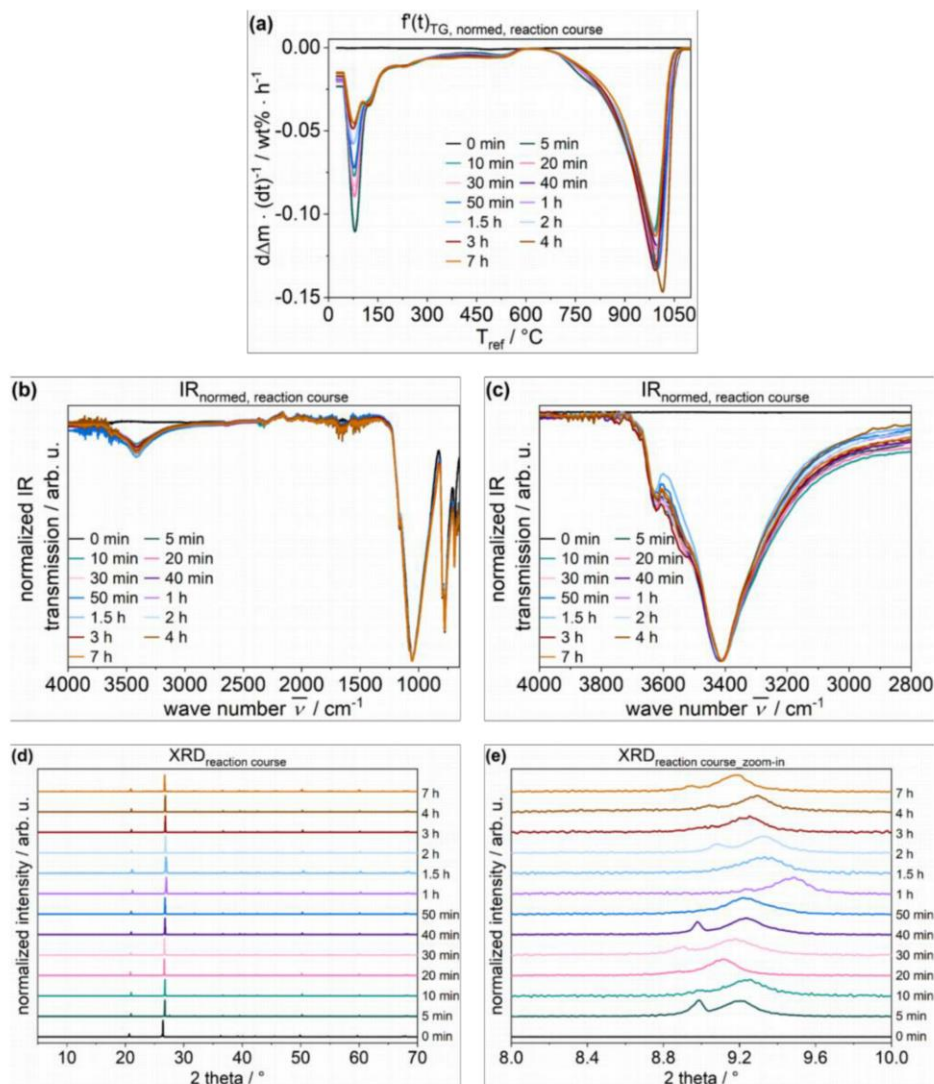


Fig. S3. (a) TGA data plotted as mass normalized time derived weight loss ($d\Delta m \cdot (dt)^{-1}$) per hour against the reference temperature of anhydrous and hydrated quartz powder with a heating rate of $5^\circ\text{C}/\text{min}$; reaction stopped after 15 min with various contents of *in situ* formed ettringite (up to 9.1 wt%) by lyophilisation technique; IR-spectrum in a range of (b) $4000\text{ cm}^{-1} \leq \tilde{\nu} \leq 650\text{ cm}^{-1}$ and (c) $4000\text{ cm}^{-1} \leq \tilde{\nu} \leq 2800\text{ cm}^{-1}$, and Powder X-ray diffraction patterns as well as their literature reflections [5,9,16] in an angular range of (d) $7^\circ \leq 2\theta \leq 70^\circ$ and (e) $8^\circ \leq 2\theta \leq 10^\circ$.

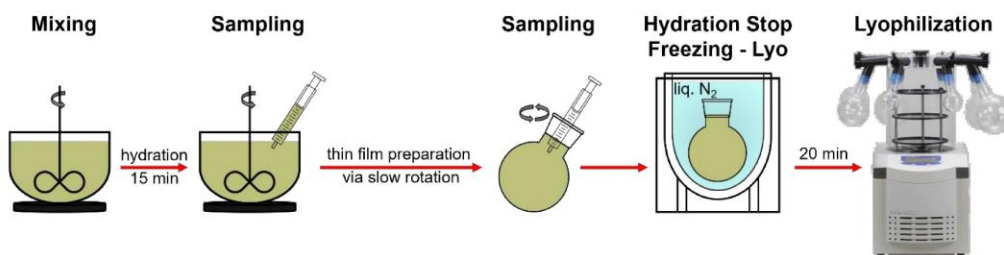


Fig. S4. Scheme of hydration stop by freezing with liquid nitrogen and subsequent lyophilization (Lyo).

Table S1. Mixing program for cementitious suspensions using a Kenwood KitchenAid.

step	duration / min	mode / approx. rpm
------	----------------	--------------------

dry mixing of SiO ₂	1.0	level 2 / 72
adding aqueous CaCl ₂ solution	1.0	level 2 / 72
stop and manually scraping off	1.0	off
adding aqueous NaOH solution	1.0	level 2 / 72
stop and manually scraping off	1.0	off
adding aqueous Al ₂ (SO ₄) ₃ · 18 H ₂ O solution	2.0	level max / 220
stop and manually scraping off	0.5	off
homogenisation	until stopped	level 2 / 72

S3 Calculation of mass fractions for reference suspension shown in Table 2

Table S2a. Details on mix design for a quartz suspension with a phase content of 0.36, a total volume of 500 mL and a maximum precipitated amount of ettringite of 10 wt% of the mass of SiO₂ resulting in a absolute mass fraction of 9.1 wt%*.

chemical	Al ₂ (SO ₄) ₃ · 18 H ₂ O	CaCl ₂	NaOH	Ca(OH) ₂	ettringite	SiO ₂	H ₂ O
molar ratio	1	6	12	6	1	209	467
density ρ / g cm ⁻³	1.72	2.15	2.16	2.24	1.77	2.65	1.00
mass m / g	25.33	25.31	18.24	16.90	47.70	477.0	320.0
molar mass M / g mol ⁻¹	666.42	110.98	40.00	74.1	1255.11	60.083	18.01
amount of substance n / mmol	38	228	456	228	38	7939	17763

*calculated via $(m_{\text{ettringite}}) (m_{\text{SiO}_2} m_{\text{ettringite}})^{-1} = (47.70 \text{ g}) (477.0 \text{ g} + 47.70 \text{ g}) = 9.1 \text{ wt\%}$.

Table S2b. Composition of model quartz suspensions with different preset amounts of ettringite.

desired amount of ettringite / wt%	SiO ₂		H ₂ O	NaOH	CaCl ₂	Al ₂ (SO ₄) ₃ · 18 H ₂ O	Ca(OH) ₂ *		ettringite ^o
	m / g	V / mL	V / mL	m / g	m / g	m / g	m ⁽¹⁾ / g	m ⁽²⁾ / g	m / g
0.0						0.00		16.90	0.0
2.4						6.33		12.67	11.9
4.7	477	180	320	18.24	25.31	12.66	16.90	8.45	23.9
6.9						19.00		4.22	35.8
9.1						25.33		0.0	47.7

*formed *in-situ* via the reaction of NaOH and CaCl₂; ⁽¹⁾previous to formation of ettringite; ⁽²⁾ post formation of ettringite
^oformed *in-situ* via the reaction of Ca(OH)₂ and Al₂(SO₄)₃ · 18 H₂O.

Table S2c. Total, solids', and fluids' volume of model quartz suspensions with different preset amounts of ettringite including the phase content of SiO₂, Ca(OH)₂, ettringite, and total phase content.

desired amount of ettringite / wt%	V _{solid} / mL			V _{fluid} / mL		V _{total} * / mL	phase content Φ			
	SiO ₂	Ca(OH) ₂	ettringite	H ₂ O		V _{total}	SiO ₂	Ca(OH) ₂	ettringite	total
0.0		7.5	0.0			507.5	0.35	0.01	0.00	0.37
2.4		5.7	6.7			512.4	0.35	0.01	0.01	0.38
4.7	180	3.8	13.5	320		517.2	0.35	0.01	0.03	0.38
6.9		1.9	20.2			522.1	0.35	0.00	0.04	0.39
9.1		0.0	26.9			526.9	0.34	0.00	0.05	0.39

*V_{total} = V_{solids} + V_{fluid}.

To derive a reference suspension without the precipitation of ettringite, the preset amount of ettringite was exchanged with SiO₂ and Ca(OH)₂ with the same phase content and same ratio of $\Phi_{\text{Ca(OH)}_2} / \Phi_{\text{SiO}_2}$.

Table S2d. Total, solids', and fluids' volume of model quartz suspensions with different preset amounts of ettringite.

desired amount of ettringite / wt%	phase ratio	V _{total} / mL	H ₂ O	SiO ₂		Ca(OH) ₂	
	$\Phi_{\text{Ca(OH)}_2} / \Phi_{\text{SiO}_2}$	V _{total}	V / mL	m / g	V* / mL	m / g	V ^o / mL
0.0	0.04	507.5		477	180	16.9	7.5
2.4	0.03	512.4		494.3	186.5	13.1	5.9
4.7	0.02	517.2	320	512	193.2	9.1	4.0
6.9	0.01	522.1		530	200	4.7	2.1
9.1	0.00	526.9		548.4	206.9	0.0	0.0

*calculated via $V_{\text{SiO}_2} = (V_{\text{total}} - V_{\text{H}_2\text{O}}) (1 + \Phi_{\text{Ca(OH)}_2} / \Phi_{\text{SiO}_2})^{-1}$

^ocalculated via $V_{\text{Ca(OH)}_2} = V_{\text{SiO}_2} (\Phi_{\text{Ca(OH)}_2} / \Phi_{\text{SiO}_2})$

S4 Ideal behaviour of quartz suspension with various contents of ettringite and Ca(OH)₂

To allow for a quantification of the amount of *in situ* formed ettringite, reference samples were produced and analysed. Here, anhydrous quartz powder D6400 was mixed with a combination of calcium hydroxide ($\text{Ca}(\text{OH})_2$) and anhydrous ettringite (**Table S3** and **Fig. S5**).

Table S3. Composition of the investigated idealised quartz suspension.

content / wt%			m / mg		
SiO_2	$\text{Ca}(\text{OH})_2$	ettringite	SiO_2	$\text{Ca}(\text{OH})_2$	ettringite
96.6	3.4	0	1000	35.42	0.00
95.0	2.6	2.4	1000	27.53	25.0
93.5	1.8	4.7	1000	19.01	50.0
92.2	0.9	6.9	1000	9.84	75.0
90.9	0.0	9.1	1000	0.00	100

Analysis of defined combinations of calcium hydroxide [$\text{Ca}(\text{OH})_2$] (up to 9.1 wt%) and synthetic ettringite ($\text{Ca}_6\text{Al}_2(\text{SO}_4)_3(\text{OH})_{12} \cdot 26 \text{H}_2\text{O}$) (up to 9.1 wt%) in quartz powder [SiO_2 , D6400] was done by XRD, TGA, and IR, which are described in the following paragraphs.

Thermogravimetric analysis (TGA) (**Fig. S5a**) shows that the integral of the main decomposition peak of $\text{Ca}(\text{OH})_2$ at $500 \text{ }^\circ\text{C} \pm 80 \text{ }^\circ\text{C}$ [17] decreases with rising content of ettringite in the same order as the first peak of ettringite at $130 \text{ }^\circ\text{C} \pm 80 \text{ }^\circ\text{C}$ increases (**Fig. S5b**). The same behaviour can be observed by infrared spectroscopy (IR) (**Fig. S5c and d**), wherein the strong band at 3643 cm^{-1} belonging to the hydroxide group of $\text{Ca}(\text{OH})_2$ [18] is step-wise diminished with higher ettringite content while the respective broad band of the bound water of ettringite at $3300 \text{ cm}^{-1} \pm 300 \text{ cm}^{-1}$ grows. Evaluation of X-ray diffraction measurements allows the distinction between two aspects rooted in the growing ettringite content. On the one hand, the relative intensity of the main reflection corresponding to $\text{Ca}(\text{OH})_2$ at $2\theta = 31.8^\circ$ ($I_{\text{reflection}} = 0.05 I_{\text{max,quartz}}$) gets diminished (highest intensity $I_{\text{reflection}} = 0.05 I_{\text{max,quartz}}$ at 0.0 wt% to lowest $I_{\text{reflection}} \cong 0.00 I_{\text{max,quartz}}$ at 9.1 wt%) and on the other hand, the relative intensity of ettringite's main reflection at $2\theta = 8.9^\circ$ rises (lowest intensity $I_{\text{reflection}} = 0.00 I_{\text{max,quartz}}$ at 0.0 wt% to highest $I_{\text{reflection}} \cong 0.05 I_{\text{max,quartz}}$ at 9.1 wt%) (**Fig. S5e and f**).

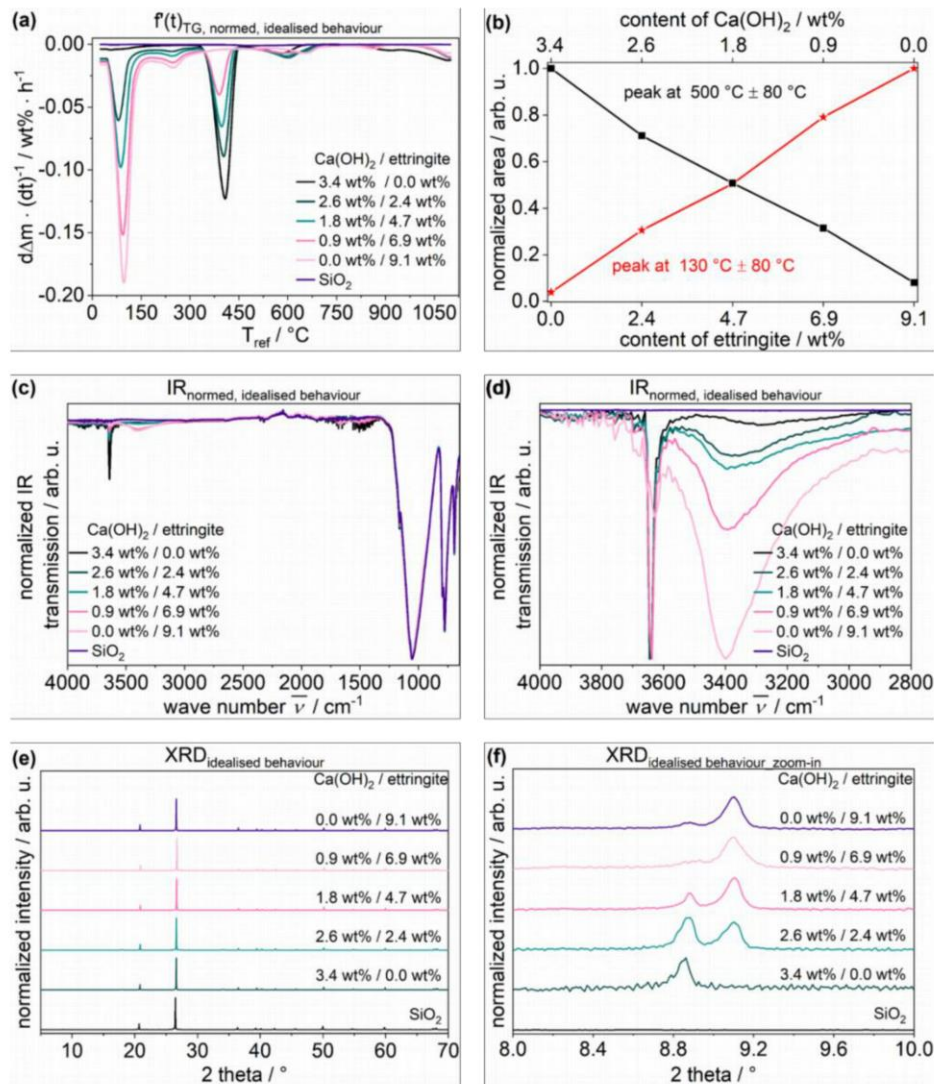


Fig. S5. (a) TGA data of anhydrous quartz powder with various contents of Ca(OH)₂ (up to 9.1 wt%) and anhydrous ettringite (up to 9.1 wt%) plotted as mass normalized time derived weight loss ($d\Delta m \cdot (dt)^{-1}$) per hour against the reference temperature with a heating rate of 5 °C/min, (b) linear regression of Ca(OH)₂ content (up to 9.1 wt%) against the content of ettringite (up to 9.1 wt%), IR-spectrum in a range of (c) 4000 cm⁻¹ to 650 cm⁻¹ and (d) 4000 cm⁻¹ to 2800 cm⁻¹, and Powder X-ray diffraction patterns as well as their literature reflections [5,9,16] in an angular range of (e) $7^\circ \leq 2\theta \leq 70^\circ$ and (f) $8^\circ \leq 2\theta \leq 10^\circ$.

S5 Mass fractions

S5.1 Quantitatively

S5.1.1 Inductively coupled plasma optical emission spectrometry

To determine both the chemical composition of the filtrate as a function of the preset amount of ettringite (up to 9.1 wt%) in the quartz suspensions formed and to check whether the preset amount of ettringite was formed, inductively coupled plasma optical emission spectrometry (ICP-OES) was employed. While the concentration c in the aqueous media of the dissolved sodium (Na⁺), calcium (Ca²⁺), aluminium (Al³⁺), and sulphate (SO₄²⁻) was assessed by ICP-OES, the hydroxide (OH⁻) concentration $c(\text{OH}^-)$ was derived from conductivity measurements (Tables S4 to S6) and calculations (Eqs. (S3 to S6)). The evaluation (Table S4) showed that only up to 40% (0.48 g · dm⁻³) of the maximal amount (1.26 g · dm⁻³) of dissolved Ca(OH)₂ [19] is present in the suspension even without the formation of ettringite (0.0 wt%), while $c(\text{Na}^+)$ is in the desired range of 30 g · dm⁻³. Furthermore, the $c(\text{Al}^{3+})$ for suspensions with different preset amounts (0.0 to 6.9 wt%) is at 1.0 mg · dm⁻³ ± 0.1 mg · dm⁻³ and for 9.1 wt% at 10 mg · dm⁻³ ± 5.4 mg · dm⁻³, indicating that less than 0.01% unreacted Al₂(SO₄)₃ · 18 H₂O remained

in the suspension. Additionally, it has to be pointed out that even without adding the $\text{Al}_2(\text{SO}_4)_3 \cdot 18 \text{H}_2\text{O}$ solutions, Al^{3+} and SO_4^{2-} have been detected and stayed in the same range except for the highest amount of ettringite (9.1 wt%). Adjusted to the results by ICP-OES and conductivity measurements, the preset amount of ettringite was as desired (**Table S4**).

Table S4. Calculated and measured concentrations of Na^+ , Ca^{2+} , Al^{3+} , SO_4^{2-} , and OH^- derived by ICP-OES, conductivity measurements and recalculations; full data in **Table S7**.

Al^{3+}	measured concentration / $\text{mg} \cdot \text{dm}^{-3}$				content of ettringite / wt%	calculated $c(\text{OH}^-)$ / $\text{mg} \cdot \text{dm}^{-3}$
	Ca^{2+}	Na^+	SO_4^{2-}			
1.0 ± 0.1	403 ± 182	28576 ± 2065	41.8 ± 24.6	0.0 ± 0.0	442 ± 0.04	
0.9 ± 0.1	440 ± 44.5	32319 ± 349	56.3 ± 14.7	2.3 ± 0.0	481 ± 0.03	
0.9 ± 0.1	410 ± 27.6	29991 ± 605	57.0 ± 7.7	4.6 ± 0.0	478 ± 0.03	
1.0 ± 0.3	333 ± 73.0	30974 ± 1687	63.4 ± 19.9	6.7 ± 0.0	478 ± 0.05	
10.0 ± 5.4	64.1 ± 15.9	32309 ± 1209	178 ± 25.9	9.0 ± 0.0	252 ± 0.04	

S5.1.2 Thermogravimetric analysis

The results shown by the evaluation of ICP-OES are confirmed and quantified by TGA (**Fig. S6**). Compared to anhydrous quartz powder all samples show enhanced dehydration peaks, which correspond to the decomposition of anhydrous ettringite [1–4] and $\text{Ca}(\text{OH})_2$ at $500 \text{ }^\circ\text{C} \pm 80 \text{ }^\circ\text{C}$ [17]. Both, the decomposition peak of anhydrous $\text{Ca}(\text{OH})_2$ decreases linearly (**Fig. S5b**) with rising ettringite content and a lack of decomposition of anhydrous $\text{Al}_2(\text{SO}_4)_3 \cdot 18 \text{H}_2\text{O}$ is visible (**Fig. S6**). Further, the first peak at $130 \text{ }^\circ\text{C} \pm 80 \text{ }^\circ\text{C}$, belonging to the main decomposition of ettringite, grows in the same order as the preset content of *in situ* formed ettringite in the quartz suspension (**Fig. S6b**). This result indicates the complete conversion of $\text{Al}_2(\text{SO}_4)_3 \cdot 18 \text{H}_2\text{O}$ to ettringite. The broad decomposition peak at $863 \text{ }^\circ\text{C} \pm 187 \text{ }^\circ\text{C}$ aligns with two processes, first the complete decomposition of ettringite to $(\text{CaO})_x(\text{Al}_2\text{O}_3)_y$, CaO , and CaSO_4 [2–4] as well as second the resulting eutectic mixture of these decompositions products, SiO_2 , and the by-product NaCl (Eq. (5)) [20]. By comparing the integrals of the main decomposition peak of ettringite in a temperature range of $45 \text{ }^\circ\text{C}$ and $170 \text{ }^\circ\text{C}$ [1,21] and the main peak of $\text{Ca}(\text{OH})_2$ in a range from $335 \text{ }^\circ\text{C}$ to $450 \text{ }^\circ\text{C}$ of both the ideal model system (**section S4**, **Table S3**, and **Fig. S5**) and the model system, it was possible to quantify the amount of ettringite (**Table S8**). It was shown that the measured amount of ettringite was as intended (**Tables 4 + S4**).

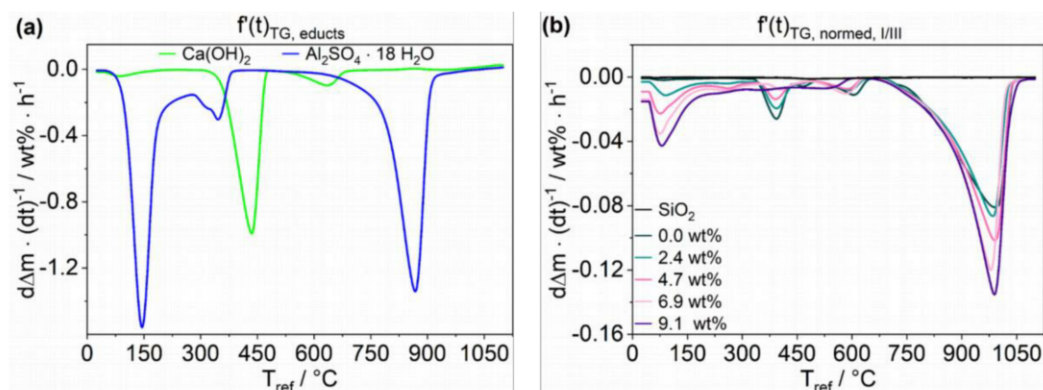


Fig. S6. TGA data plotted as mass normalized time derived weight loss ($d\Delta m \cdot (dt)^{-1}$) per hour against the reference temperature of (a) anhydrous reactants $\text{Ca}(\text{OH})_2$ and $\text{Al}_2(\text{SO}_4)_3 \cdot 18 \text{H}_2\text{O}$ and (b) anhydrous as well as hydrated quartz powder with a heating rate of $5 \text{ }^\circ\text{C}/\text{min}$; reaction stopped after 15 min with various contents of *in situ* formed ettringite (up to 9.1 wt%) by Iso; synthesis I/III and complete overview in **Fig. S9**.

S5.2 Qualitatively

S5.2.1 X-ray diffraction

To confirm the formation of ettringite as aforementioned, XRD is employed. The diffractograms (**Fig. S7**) of all dried samples except for 0.0 wt% show a distinct ettringite reflection in the angular range of $8^\circ \leq 2\theta \leq 10^\circ$, which is only visible in a zoom-in (**Fig. S7b**). Further, the ratio of portlandite ($\text{Ca}(\text{OH})_2$) to ettringite in the zoom-in aligns concordantly to the ideal behaviour shown in **Fig. S5f**, wherein the reflection at $2\theta \cong 8.8^\circ$ becomes less intense with rising content of ettringite while ettringite's main reflection at $2\theta \cong 9.1^\circ$ corresponding to crystal plane $(10\bar{1}0)$ [5] becomes dominant, so qualitatively, the amount of ettringite was as desired.

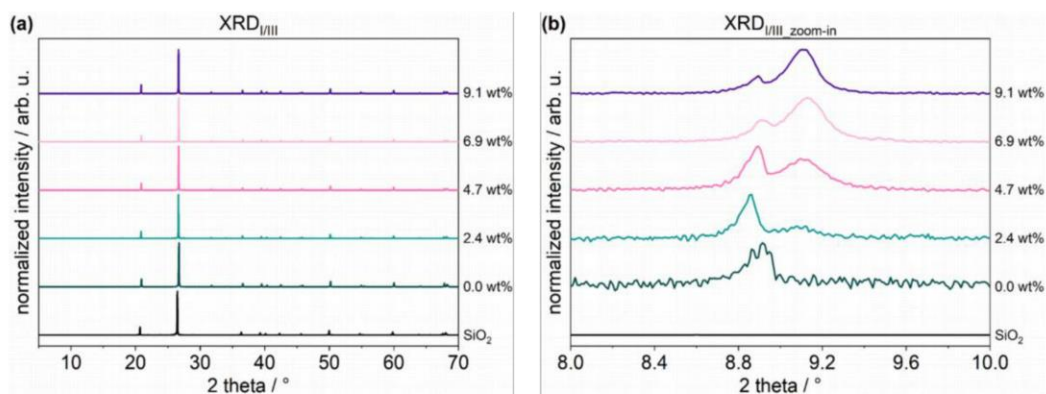


Fig. S7. Powder X-ray diffraction patterns of anhydrous quartz powder with the increasing amount of *in situ* formed ettringite (up to 9.1 wt%) stopped after 15 min of hydration by Iso in an angular range of (a) $7^\circ \leq 2\theta \leq 70^\circ$ and (b) $8^\circ \leq 2\theta \leq 10^\circ$; synthesis I/III and complete overview in Fig. S10.S5.2.2 Infrared spectroscopy

To re-evaluate and confirm the content of ettringite derived from TGA, IR spectroscopy is employed (Fig. S8). As previously indicated by TGA, with a rising preset content of ettringite in the suspension the quantity of non-reacted $\text{Ca}(\text{OH})_2$ decreases. This is indicated by the stepwise diminishment of the strong band at 3643 cm^{-1} belonging to the hydroxide group of $\text{Ca}(\text{OH})_2$ [18]. In parallel, both the respective bands of ettringite grow to the same extent as the aforementioned bands of $\text{Ca}(\text{OH})_2$ diminishes, further no bands corresponding to the reactant $\text{Al}_2(\text{SO}_4)_3 \cdot 18 \text{ H}_2\text{O}$ are found (Fig. S8c and d). Therefore, it can be concluded that the preset content of *in situ* formed ettringite was achieved and this, in turn, confirms that possible changes to the rheological properties are solely induced by ettringite's formation and not by unreacted reactants.

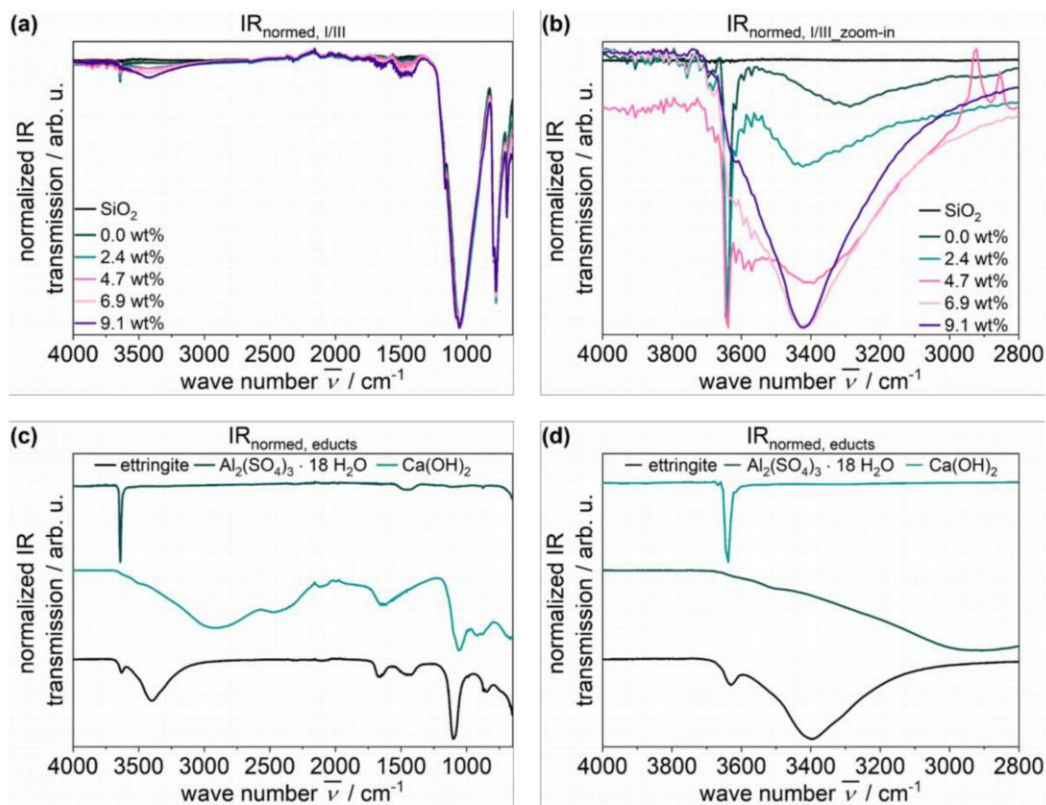


Fig. S8. IR spectra of (a and b) anhydrous and hydrated quartz powder as well as (c and d) anhydrous reactants $\text{Ca}(\text{OH})_2$ and $\text{Al}_2(\text{SO}_4)_3 \cdot 18 \text{ H}_2\text{O}$ in a range of (left) 4000 cm^{-1} to 650 cm^{-1} and (right) 4000 cm^{-1} to 2800 cm^{-1} ; reaction stopped after 15 min with various contents of *in situ* formed ettringite (up to 9.1 wt%) by Iso; synthesis I/III and complete overview in Fig. S11.

S6 Additional data for used model system

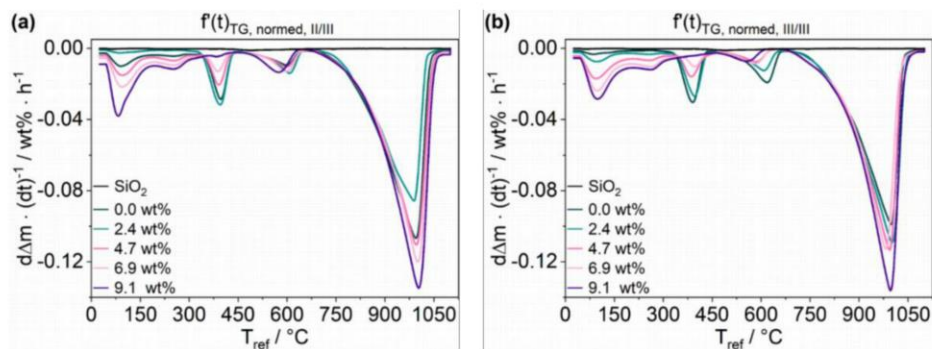


Fig. S9. TGA data plotted as mass normalized time derived weight loss ($d\Delta m \cdot (dt)^{-1}$ per hour against the reference temperature of anhydrous and hydrated quartz powder with a heating rate of $5^\circ\text{C}/\text{min}$; reaction stopped after 15 min with various contents of *in situ* formed ettringite (up to 9.1 wt%) by isopropanol-water exchange (**Iso**); (**a**) synthesis II/III and (**b**) synthesis III/III.

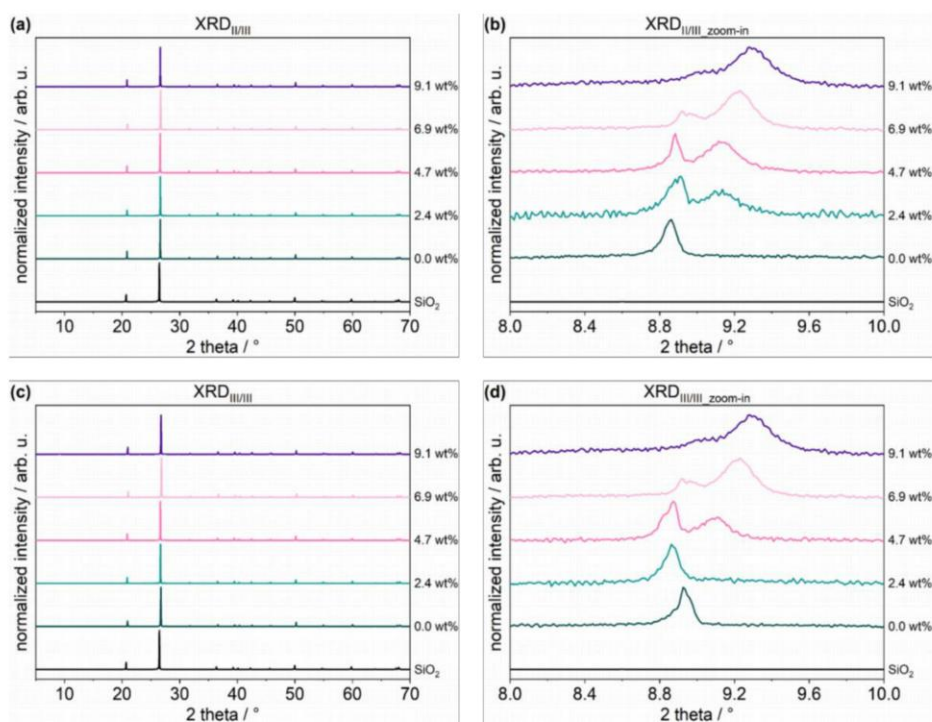


Fig. S10. Powder X-ray diffraction patterns of anhydrous quartz powder with growing *in situ* formed ettringite content (up to 9.1 wt%) stopped after 15 min of hydration by lyophilisation technique in an angular range of (**left**) $7^\circ \leq 2\theta \leq 70^\circ$ and (**right**) $8^\circ \leq 2\theta \leq 10^\circ$; (**a and b**) synthesis II/III and (**c and d**) synthesis III/III.

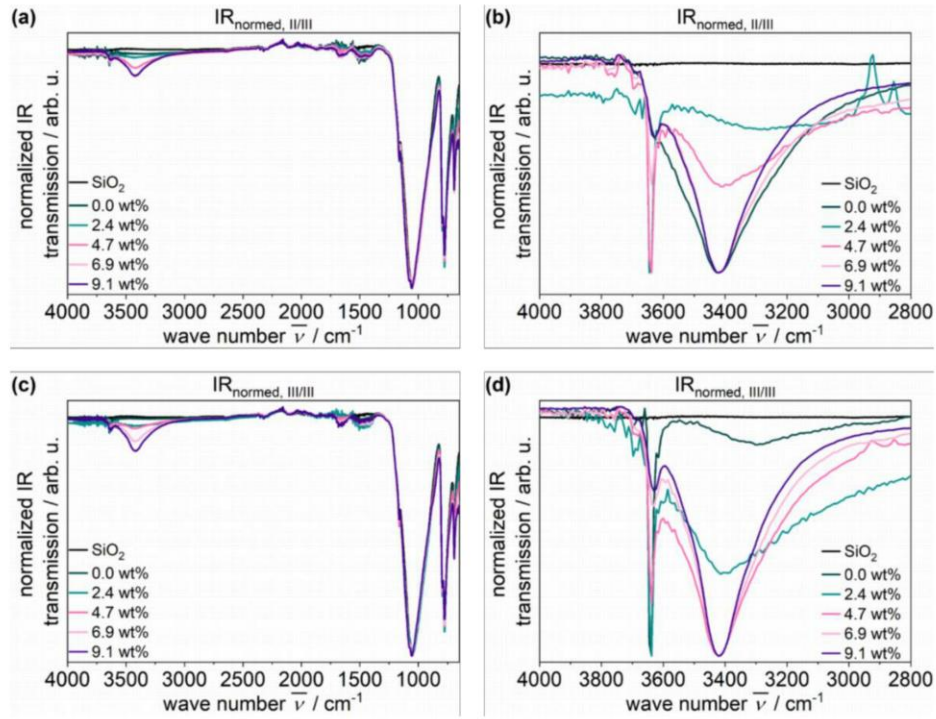


Fig. S11. IR spectra of anhydrous and hydrated quartz powder in a range of (left) $4000 \text{ cm}^{-1} \leq \tilde{\nu} \leq 650 \text{ cm}^{-1}$ and (right) $4000 \text{ cm}^{-1} \leq \tilde{\nu} \leq 2800 \text{ cm}^{-1}$; reaction stopped after 15 min with various contents of *in situ* formed ettringite (up to 9.1 wt%) by isopropanol-water exchange; (a and b) synthesis II/III and (c and d) synthesis III/III.

Table S5. Samples' measured potential differences ΔE (mV), conductivities σ ($\text{mS} \cdot \text{cm}^{-1}$), temperature Θ ($^{\circ}\text{C}$), as well as calculated pH using Eqs. (S3) and (S4).

measured			sample name	calculated		
ΔE / mV	σ / $\text{mS} \cdot \text{cm}^{-1}$	Θ / $^{\circ}\text{C}$		pH Eq. (S3)	pH Eq. (S4)	ΔpH / %
-116.3	–	24.6	Buffer pH = 9.18	9.18	9.24	0.7
-220.2	–	24.3	Buffer pH = 11	11.01	11.00	0.1
-302.0	–	24.2	Buffer pH = 12.454	12.45	12.39	0.5
-312.0	120.0	24.9	I/III_0.0 wt%	12.63	12.56	0.5
-313.0	124.5	25.0	I/III_2.4 wt%	12.64	12.58	0.5
-309.6	115.7	25.5	I/III_4.7 wt%	12.58	12.52	0.5
-314.2	116.6	25.9	I/III_6.9 wt%	12.67	12.60	0.6
-298.0	116.6	25.4	I/III_9.1 wt%	12.38	12.32	0.5
-307.3	103.0	24.7	II/III_0.0 wt%	12.54	12.48	0.5
-309.6	114.0	20.7	II/III_2.4 wt%	12.58	12.52	0.5
-313.1	109.5	21.0	II/III_4.7 wt%	12.65	12.58	0.5
-307.6	103.2	21.1	II/III_6.9 wt%	12.55	12.48	0.5
-288.6	113.1	23.8	II/III_9.1 wt%	12.21	12.16	0.4
-307.2	103.8	22.0	III/III_0.0 wt%	12.54	12.48	0.5
-310.2	118.9	25.0	III/III_2.4 wt%	12.60	12.53	0.5
-309.6	109.8	20.5	III/III_4.7 wt%	12.58	12.52	0.5
-310.5	117.3	21.4	III/III_6.9 wt%	12.60	12.53	0.5
-298.3	113.7	21.2	III/III_9.1 wt%	12.39	12.33	0.5
-308.8 ± 2.2	108.9 ± 7.8	23.9 ± 1.3	mean_0.0 wt%	554.33 ± 0.53	1.63 ± 0.0	0.5 ± 0.0
-310.9 ± 1.5	119.1 ± 4.3	23.6 ± 2.0	mean_2.4 wt%	565.55 ± 1.09	1.66 ± 0.0	0.5 ± 0.0
-310.8 ± 1.6	111.7 ± 2.9	22.3 ± 2.2	mean_4.7 wt%	568.69 ± 1.17	1.67 ± 0.0	0.5 ± 0.0
-310.8 ± 2.7	112.4 ± 6.5	22.8 ± 2.2	mean_6.9 wt%	572.78 ± 0.52	1.68 ± 0.0	0.5 ± 0.0
-295.0 ± 4.5	114.5 ± 1.5	23.5 ± 1.7	mean_9.1 wt%	572.49 ± 0.03	1.68 ± 0.0	0.5 ± 0.0

Table S6. Sample composition for ICP-OES.

sample name	m _{sample} / g	m _{HNO₃} / mg
I/III_0.0 wt%	5.568	246.5
I/III_2.4 wt%	5.040	217.5
I/III_4.7 wt%	5.150	216.9
I/III_6.9 wt%	5.115	200.0
I/III_9.1 wt%	5.175	206.8
II/III_0.0 wt%	5.041	197.8
II/III_2.4 wt%	5.308	121.8
II/III_4.7 wt%	5.278	210.7
II/III_6.9 wt%	5.268	200.5
II/III_9.1 wt%	5.186	219.8
III/III_0.0 wt%	5.344	217.1
III/III_2.4 wt%	5.278	216.7
III/III_4.7 wt%	5.049	231.9
III/III_6.9 wt%	5.305	212.4
III/III_9.1 wt%	5.238	213.6

Table S7. Samples' measured ionic concentrations by ICP-OES and calculated OH⁻ concentration *c*(OH⁻) derived from pH using Eqs. (S5 and S6) [19].

measured concentration / mg · dm ⁻³				sample name	calculated [19]	
Al ³⁺	Ca ²⁺	Na ⁺	SO ₄ ²⁻		pOH	<i>c</i> (OH ⁻) / mg · dm ⁻³
1.0	521	30844	13.4	I/III_0.0 wt%	1.37	503
0.8	389	31953	73.3	I/III_2.4 wt%	1.36	523
0.9	431	29339	61.5	I/III_4.7 wt%	1.42	456
1.0	260	30685	86.2	I/III_6.9 wt%	1.33	549
6.9	71.3	31931	167	I/III_9.1 wt%	1.62	285
0.9	193	26806	55.1	II/III_0.0 wt%	1.46	415
1.0	468	32355	46.7	II/III_2.4 wt%	1.42	456
0.9	379	30535	61.4	II/III_4.7 wt%	1.35	525
1.3	333	29450	49.2	II/III_6.9 wt%	1.45	420
6.9	75.2	31334	160	II/III_9.1 wt%	1.79	194
1.1	495	28078	57.0	III/III_0.0 wt%	1.46	414
1.0	464	32648	49.0	III/III_2.4 wt%	1.40	467
1.0	421	30098	48.1	III/III_4.7 wt%	1.42	456
0.7	406	32786	54.9	III/III_6.9 wt%	1.40	473
16.3	45.9	33661	208	III/III_9.1 wt%	1.61	288
1.0 ± 0.1	403 ± 182	28576 ± 2065	41.8 ± 24.6	mean_0.0 wt%	1.43 ± 0.04	442 ± 0.04
0.9 ± 0.1	440 ± 44.5	32319 ± 349	56.3 ± 14.7	mean_2.4 wt%	1.39 ± 0.03	481 ± 0.03
0.9 ± 0.1	410 ± 27.6	29991 ± 605	57.0 ± 7.7	mean_4.7 wt%	1.39 ± 0.03	478 ± 0.03
1.0 ± 0.3	333 ± 73.0	30974 ± 1687	63.4 ± 19.9	mean_6.9 wt%	1.39 ± 0.05	478 ± 0.05
10.0 ± 5.4	64.1 ± 15.9	32309 ± 1209	178 ± 25.9	mean_9.1 wt%	1.67 ± 0.08	252 ± 0.04

Table S8. From TGA derived integrals of quartz powder containing different amounts of Ca(OH)₂ and ettringite in two temperature regions; region **A** (45 °C to 170 °C; ettringite) and **B** (335 °C to 450 °C);
left: idealised behaviour and **right:** syntheses I to III.

idealised behaviour				sample name content / wt% Ca(OH) ₂ / Ettringite	syntheses I to III			
absolute area		normalized area			absolute area		normalized area	
A	B	A	B		A	B	A	B
0.01	0.01	0.00	0.00	SiO ₂	0.01	0.00	0.00	0.00
0.05	6.18	0.01	1.00	3.5 / 0.0				
1.93	4.25	0.25	0.69	2.6 / 2.4				
3.60	2.88	0.46	0.47	1.8 / 4.7				
6.06	1.53	0.78	0.25	0.9 / 6.9				
7.80	0.06	1.00	0.01	0.0 / 9.1				
				I/III_0.0 wt%	0.06	1.13	0.03	1.00
				I/III_2.4 wt%	0.49	0.81	0.28	0.72
				I/III_4.7 wt%	0.87	0.47	0.49	0.42
				I/III_6.9 wt%	1.28	0.15	0.72	0.14
				I/III_9.1 wt%	1.76	0.00	1.00	0.01
				II/III_0.0 wt%	0.12	1.53	0.08	1.00
				II/III_2.4 wt%	0.32	1.19	0.24	0.78
				II/III_4.7 wt%	0.77	0.75	0.59	0.50
				II/III_6.9 wt%	1.07	0.34	0.82	0.23
				II/III_9.1 wt%	1.31	0.00	1.00	0.01
				III/III_0.0 wt%	0.10	1.38	0.05	1.00
				III/III_2.4 wt%	0.42	1.20	0.25	0.87
				III/III_4.7 wt%	0.68	0.58	0.40	0.42
				III/III_6.9 wt%	0.98	0.25	0.58	0.19
				III/III_9.1 wt%	1.68	0.00	1.00	0.01
				mean_0.0 wt%	0.09 ± 0.02	1.35 ± 0.16	0.05 ± 0.02	1.00 ± 0.00
				mean_2.4 wt%	0.41 ± 0.07	1.07 ± 0.18	0.25 ± 0.02	0.79 ± 0.06
				mean_4.7 wt%	0.77 ± 0.07	0.60 ± 0.12	0.49 ± 0.08	0.45 ± 0.04
				mean_6.9 wt%	1.11 ± 0.12	0.25 ± 0.08	0.71 ± 0.10	0.19 ± 0.04
				mean_9.1 wt%	1.58 ± 0.20	0.00 ± 0.00	1.00 ± 0.00	0.01 ± 0.00

Table S9. Data for Fig. 5; specific surface area values derived from N₂ physisorption; rounded according to DIN 1333 [22].

content of ettringite / wt%	specific surface area SSA (±) / m ² · g ⁻¹							
	model system (SiO ₂ , Ca(OH) ₂ + ettringite)					reference mixture* (Ca(OH) ₂ + ettringite)		
	measured/sum	SiO ₂	Ca(OH) ₂	ettringite	calculated/sum	SiO ₂	Ca(OH) ₂	
SiO ₂	0.856 (0.006)	0.856	0.00	0.00				not applicable
0.0	0.97 (0.15)	0.82	0.15	0.00	0.976	0.822	0.155	
2.4	1.14 (0.07)	0.80	0.11	0.22	0.947	0.830	0.117	
4.7	1.33 (0.22)	0.78	0.07	0.48	0.917	0.838	0.079	
6.9	1.72 (0.09)	0.77	0.03	0.92	0.887	0.847	0.040	
9.1	2.09 (0.05)	0.75	0.00	1.34	0.856	0.856	0.000	

*calculated based on the evaluated specific surface area of SiO₂ = 0.856 m² · g⁻¹ and Ca(OH)₂ = 3.845 m² · g⁻¹.

Table S10. N₂-physorption data for **Fig. 5**; specific surface area of anhydrous quartz powder and quartz powder suspensions with the increasing amount of *in situ* formed ettringite (up to 9.1 wt%).

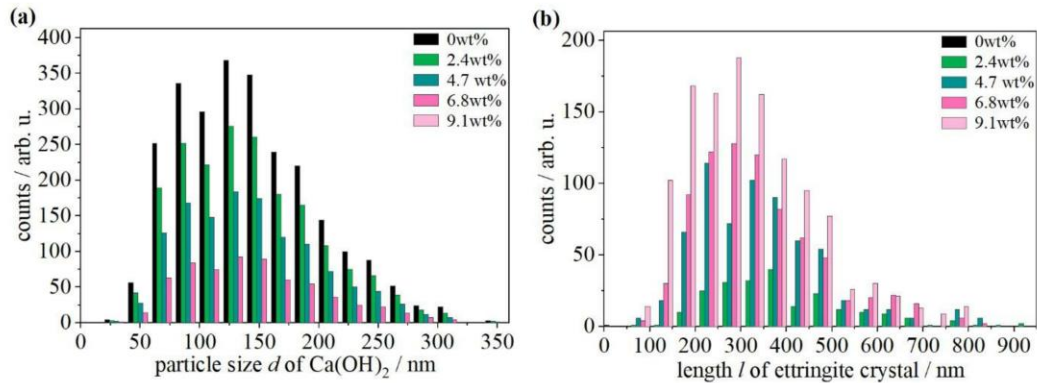
sample name	specific surface area / m ² g ⁻¹	
	measurement I/II	measurement II/II
SiO ₂	0.862	0.850
I/III_0.0 wt%	0.845	0.925
I/III_2.4 wt%	1.076	1.137
I/III_4.7 wt%	1.122	1.3
I/III_6.9 wt%	1.173	1.818
I/III_9.1 wt%	2.071	2.12
II/III_0.0 wt%	1.183	1.159
II/III_2.4 wt%	1.126	1.051
II/III_4.7 wt%	1.147	1.162
II/III_6.9 wt%	1.634	1.605
II/III_9.1 wt%	2.120	1.994
III/III_0.0 wt%	0.879	0.848
III/III_2.4 wt%	1.250	1.159
III/III_4.7 wt%	1.619	1.632
III/III_6.9 wt%	1.810	1.709
III/III_9.1 wt%	2.092	2.123
mean_SiO ₂	0.856 ± 0.006	
mean_0.0 wt%	0.973 ± 0.143	
mean_2.4 wt%	1.133 ± 0.064	
mean_4.7 wt%	1.330 ± 0.216	
mean_6.9 wt%	1.718 ± 0.080	
mean_9.1 wt%	2.087 ± 0.045	

$$\Delta E = -0.059 \text{ V} \cdot (\text{pH} - 7.27) \Leftrightarrow \text{pH} = -0.059 \text{ V} \cdot \Delta E^{-1} + 7.27 \quad (\text{S3})$$

$$\text{pH} = (7.13 \pm 1.63 \cdot 10^{-2}) + (-1.76 \cdot 10^{-2} \pm 7.31 \cdot 10^{-5}) \cdot \Delta E \quad (\text{S4})$$

$$\text{pOH} = 14 - \text{pH} \quad (\text{S5})$$

$$c(\text{OH}^-) = 10^{-\text{pOH}} \quad (\text{S6})$$



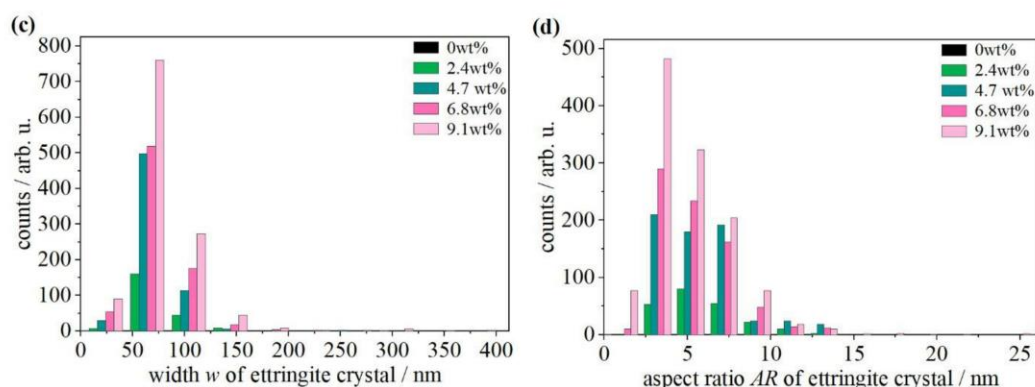


Fig. S12. Data for Fig. 6; distributions derived from SEM micrographs of (a) particle size d of $\text{Ca}(\text{OH})_2$, ettringite crystals' (b) length l , (c) width w , and (d) aspect ratio AR dependent on preset content of ettringite in the model suspension.

References

- [1] C. Hall, P. Barnes, A.D. Billimore, A.C. Jupe, X. Turrillas, Thermal decomposition of ettringite $\text{Ca}_6[\text{Al}(\text{OH})_6]_2(\text{SO}_4)_3 \cdot 26\text{H}_2\text{O}$, *J. Chem. Soc., Faraday Trans. 92* (1996) 2125–2129. <https://doi.org/10.1039/FT9969202125>.
- [2] H.F.W. Taylor, *Cement chemistry*, Thomas Telford Publishing, 1997. <https://doi.org/10.1680/cc.25929>.
- [3] IUCLID-CD-ROM, IUCLID-CD-ROM, Year 2000 edition; European Commission, Joint Research Centre, Institute for Health and Consumer Protection, European Chemicals Bureau; Ispra, Italy, (n.d.).
- [4] L. Roth, U. Weller, *Gefährliche chemische Reaktionen : Stoffinformationen, Reaktionstabellen, Unfallberichte / Roth; Weller ; 1, ecomed-Verl.-Ges., 1982.*
- [5] M.R. Hartman, R. Berliner, Investigation of the structure of ettringite by time-of-flight neutron powder diffraction techniques, *Cem. Concr. Res.* 36 (2006) 364–370. <https://doi.org/10.1016/j.cemconres.2005.08.004>.
- [6] S.K. Deb, M.H. Manghnani, K. Ross, R.A. Livingston, P.J.M. Monteiro, Raman scattering and X-ray diffraction study of the thermal decomposition of an ettringite-group crystal, *Phys. Chem. Miner.* 30 (2003) 31–38. <https://doi.org/10.1007/s00269-002-0279-x>.
- [7] A.E. Moore, H.F.W. Taylor, Crystal structure of ettringite, *Acta Crystallogr. Sect. B Struct. Crystallogr. Cryst. Chem.* 26 (1970) 386–393. <https://doi.org/10.1107/S0567740870002443>.
- [8] H.G. Hong, D.D. Sackett, T.E. Mallouk, Adsorption of Well-Ordered Zirconium Phosphonate Multilayer Films on High Surface Area Silica, *Chem. Mater.* 3 (1991) 521–527. <https://doi.org/10.1021/cm00015a030>.
- [9] G.A. Lager, J.D. Jorgensen, F.J. Rotella, Crystal structure and thermal expansion of α -quartz SiO_2 at low temperatures, *J. Appl. Phys.* 53 (1982) 6751–6756. <https://doi.org/10.1063/1.330062>.
- [10] P. Debye, P. Scherrer, Interferenz an regellos orientierten Teilchen im Röntgenlicht. I., in: *Nachrichten von Der Königlichen Gesellschaft Der Wissenschaften Zu Göttingen, Math. Klasse, Weidmannsche Buchhandlung, Berlin, 1916: pp. 1–26.*
- [11] P. Scherrer, Bestimmung der Größe und der inneren Struktur von Kolloidteilchen mittels Röntgenstrahlen, in: *Nachrichten von Der Königlichen Gesellschaft Der Wissenschaften Zu Göttingen, Math. Klasse, Weidmannsche Buchhandlung, Berlin, 1918: pp. 98–100. http://eudml.org/doc/59018.*
- [12] J.I. Langford, A.J.C. Wilson, Scherrer after sixty years: A survey and some new results in the determination of crystallite size, *J. Appl. Crystallogr.* 11 (1978) 102–113. <https://doi.org/10.1107/S0021889878012844>.
- [13] P. Kasten, Strukturauflösung von Kristallpulver, *Phys. Unserer Zeit.* 46 (2015) 174–179. <https://doi.org/10.1002/piuz.201401405>.
- [14] S. Vahur, A. Teearu, P. Peets, L. Joosu, I. Leito, ATR-FT-IR spectral collection of conservation materials in the extended region of 4000–80 cm^{-1} , *Anal. Bioanal. Chem.* 408 (2016) 3373–3379. <https://doi.org/10.1007/s00216-016-9411-5>.
- [15] P.A. Kießling, F. Lübckemann, A. Mundstock, L. Lohaus, M. Haist, J. Caro, N.C. Bigall, Is freeze-drying an alternative to solvent exchange for the hydration stop of cementitious suspensions?, *Cem. Concr. Res.* 159 (2022) 106841. <https://doi.org/10.1016/j.cemconres.2022.106841>.
- [16] L. Desgranges, D. Grebille, G. Calvarin, G. Chevrier, N. Floquet, J.-C. Niece, Hydrogen thermal motion in calcium hydroxide: $\text{Ca}(\text{OH})_2$, *Acta Crystallogr. Sect. B.* 49 (1993) 812–817. <https://doi.org/10.1107/S0108768193003556>.
- [17] Institut für Arbeitsschutz der Deutschen Gesetzlichen Unfallversicherung, GESTIS-Stoffdatenbank, (n.d.). <https://gestis.dguv.de/data?name=001150>.
- [18] M. Galván-Ruiz, J. Hernández, L. Baños, J. Noriega-Montes, M.E. Rodríguez-García, Characterization of Calcium Carbonate, Calcium Oxide, and Calcium Hydroxide as Starting Point to the Improvement of Lime for Their Use in Construction, *J. Mater. Civ. Eng.* 21 (2009) 694–698. [https://doi.org/10.1061/\(ASCE\)0899-1561\(2009\)21:11\(694\)](https://doi.org/10.1061/(ASCE)0899-1561(2009)21:11(694)).
- [19] A.F. Hollemann, E. Wiberg, N. Wiberg, *Lehrbuch der anorganischen chemie*, 102nd ed., Walter de Gruyter, 2017.
- [20] A.L. Sihm, Melting points of binary and ternary eutectic chloride salts MD simulations on LiCl-NaCl-KCl and its binary constituents salts, (2019).
- [21] P.A. Kießling, F. Lübckemann, T. von Bronk, D. Cotardo, L. Lei, A. Feldhoff, L. Lohaus, M. Haist, N.C. Bigall, Influence of Low-Pressure Treatment on the Morphological and Compositional Stability of Microscopic Ettringite, *Materials (Basel)*. 14 (2021) 2720. <https://doi.org/10.3390/ma14112720>.
- [22] DIN German Institute for Standardization, DIN 1333:1992-02, Presentation of numerical data, Beuth Verlag GmbH, Berlin, Germany, 1992.

4.3 IMPACT OF HARD MAGNETIC NANOCRYSTALS ON THE PROPERTIES OF HARDENED CEMENT PASTE

P. A. Kißling, M. Mahlbacher, C. Wesemann, A. Mundstock, F. Lübke-
mann-Warwas, S. Klimke, F. Renz, L. Lohaus, M. Haist, N. C. Bigall, *Chemie Ing. Tech.*, **2023**.
<https://doi.org/10.1002/cite.202300022>.

Impact of Hard Magnetic Nanocrystals on the Properties of Hardened Cement Paste

Patrick A. Kießling, Markus Mahlbacher, Christoph Wesemann, Alexander Mundstock, Franziska Lübke-Warwas, Stephen Klimke, Franz Renz, Ludger Lohaus, Michael Haist, and Nadja C. Bigall*

DOI: 10.1002/cite.202300022

This is an open access article under the terms of the Creative Commons Attribution License, which permits use, distribution and reproduction in any medium, provided the original work is properly cited.



Supporting Information
available online

In this work, nano-sized hard magnetic gallium-substituted iron oxide crystals, wherein gallium is used to stabilize the metastable epsilon iron oxide phase, were added to cement-water suspensions at different ratios, which were subsequently hydrated for at least 28 days. It is shown that higher contents of such nanocrystals in the hardened cement paste introduce a magnetic moment, whereas the mechanical properties remain unchanged compared to non-blended hardened cement paste for a wide concentration range.

Keywords: Analytical methods, Hydrated and hardened cement paste, Material science, Hard magnetic nanocrystals

Received: February 13, 2023; *revised:* July 21, 2023; *accepted:* September 01, 2023

1 Introduction

In our modern society, the most common building material is concrete [1], which is made from coarse and fine aggregates (e.g., sand, gravel, or crushed stones), Portland cement (in this case CEM I 42.5 R), water, and various admixtures. Cement itself mainly consists of Ca_3SiO_5 , Ca_2SiO_4 , and $\text{Ca}_3\text{Al}_2\text{O}_6$ and acts as the binder or glue of the composite material [2]. Over time, the requirements of building materials change as extrinsic factors like climate, resource scarcity, and politics rise up, with adaptations of the composite system becoming necessary [3]. Most approaches to modify the properties of cementitious suspensions, hydrated cement, and hardened cement paste, work on the macroscopic or microscopic level, e.g., by adding fillers such as sand or quartz powder to increase packing density and reduce the amount of binder or superplasticizer to improve fluidity and pumpability of concrete [4–13]. Alternatively, nano-scaled additives (TiO_2 [14, 15], ZnO [15, 16], carbon nanotubes [17, 18], $\alpha\text{-Fe}_2\text{O}_3$ [19–22], SiO_2 [21–27], and tobermorite nanofibers [28]), can be incorporated. This leads to enhanced external compression and tensile strength [15, 23], a reduction of the dormant period while accelerating the hydration of cement, as well as lowering the initial and final setting time by 90–100 min [23], respectively. Hereby, specific modifications are observed on the paste level already, without additional aggregates.

Previously, Ohkoshi et al. [29] synthesized hard-magnetic $\epsilon\text{-Fe}_2\text{O}_3$ nanocrystals (NCs) demonstrating their capability

to absorb millimeter waves due to a high coercive field H_c . They showed that the partial substitution of iron atoms by gallium stabilizes the metastable phase of $\epsilon\text{-Fe}_2\text{O}_3$ and changes coercive field H_c as a function of the substitution rate, changing the absorption wavelength or rather the resonance frequency f_r as follows by

$$f_r \approx \frac{\gamma}{2\pi\sqrt{1-A^2}} \sqrt{4\pi M_s(H_a + 4\pi E M_s)} \quad (1)$$

where γ corresponds to the gyromagnetic ratio of an electron ($1.76 \cdot 10^{11} \text{ T}^{-1}\text{s}^{-1}$) [30], A to the damping constant, H_a

^{1,2}Patrick A. Kießling <https://orcid.org/0000-0001-5596-9976>,

²Markus Mahlbacher, ¹Christoph Wesemann,

¹Dr. rer. nat. Alexander Mundstock, ¹Dr. rer. nat. Franziska

Lübke-Warwas, ³Dr. rer. nat. Stephen Klimke,

^{3,4}Prof. Dr. rer. nat. Franz Renz, ²Prof. Dr.-Ing. Ludger Lohaus,

²Prof. Dr.-Ing. Michael Haist, ^{1,4}Prof. Dr. rer. nat. Nadja C. Bigall

<https://orcid.org/0000-0003-0171-1106>

(nadja.bigall@pci.uni-hannover.de)

¹Leibniz University Hannover, Institute of Physical Chemistry and Electrochemistry, Callinstr. 3a, 30167 Hanover, Germany.

²Leibniz University Hannover, Institute of Building Materials Science, Appelstraße 9a, 30167 Hanover, Germany.

³Leibniz University Hannover, Institute of Inorganic Chemistry, Callinstr. 3–9, 30167 Hanover, Germany.

⁴Leibniz University Hannover, Laboratory of Nano and Quantum Engineering (LNQE), Schneiderberg 39, 30167 Hanover, Germany.

Online in color, print in grayscale unless the author(s) contribute to the costs.

✓✓ These are not the final page numbers!

2

Research Article

Chemie
Ingenieur
Technik

to the uniaxial anisotropy field of an unpatterned film, E to the effective demagnetization factor, and $4\pi M_s$ to the saturation magnetization according to Kittel (1) [31].

In the present work, these new magnetic properties are induced into hardened cement paste. By doing so, the general properties, such as porosity and compressive strength should be maintained or improved.

The crux of the matter being whether the magnetic properties of the NCs stay the same in this matrix is answered by evaluating the magnetic properties. We investigate which structure-properties hardened cement pastes blended or functionalized with $\text{Ga}_{0.043}\text{Fe}_{1.957}\text{O}_3$ nanomagnets exhibit compared to non-blended hardened cement paste. To better quantify these aspects, aggregates and other additives, such as sand or slag, were neglected and only the change in the properties of hardened cement paste cuboids were studied, which for example showed a tremendous increase of magnetic remanence M_R by a factor of about 750. Here, different amounts (≤ 10 wt%, namely 0, 1, 5, and 10 wt%) of self-synthesized $\text{Ga:Fe}_2\text{O}_3$ (85% ϵ and 15% α) NCs were added to CEM I 42.5 R (Fig. 1), which already contains 2–5 wt% Fe_2O_3 present as part of brownmillerite (C_4AF) (Fig. S1b in the Supporting Information SI). The blending values were chosen to be comparable to previous studies [14–16, 21–27].

2 Experimental

The experimental details (Sect. S1) as well as the characterization (Sect. S2.1) of all educts and intermediates (where necessary) can be found in Supporting Information SI. Characterization of the as-synthesized NCs by Mössbauer spectroscopy, superconducting quantum interference device (SQUID), powder X-ray diffraction (XRD) reveals the presence of two $\text{Ga:Fe}_2\text{O}_3$ phases (85% ϵ and 15% α) and from TEM micrographs (Fig. 2a) it can be observed that $\text{Ga:Fe}_2\text{O}_3$ NCs were polydisperse with a size of $22 \text{ nm} \pm 11 \text{ nm}$. For a detailed characterization see SI Sect. S2.1.2.

3 Results and Discussion

The evaluation of the hardened cement paste samples is divided into two distinct topics: (1) The structural characterization split into the analysis of the chemical composition and morphological appearance and (2) the investigation of mechanical and magnetic properties.

3.1 Structural Characterization

For the chemical composition analysis of hardened cement paste cuboids with an admixture of $\text{Ga:Fe}_2\text{O}_3$ NCs (≤ 10 wt%, namely 0, 1, 5 and 10 wt%), XRD, thermal

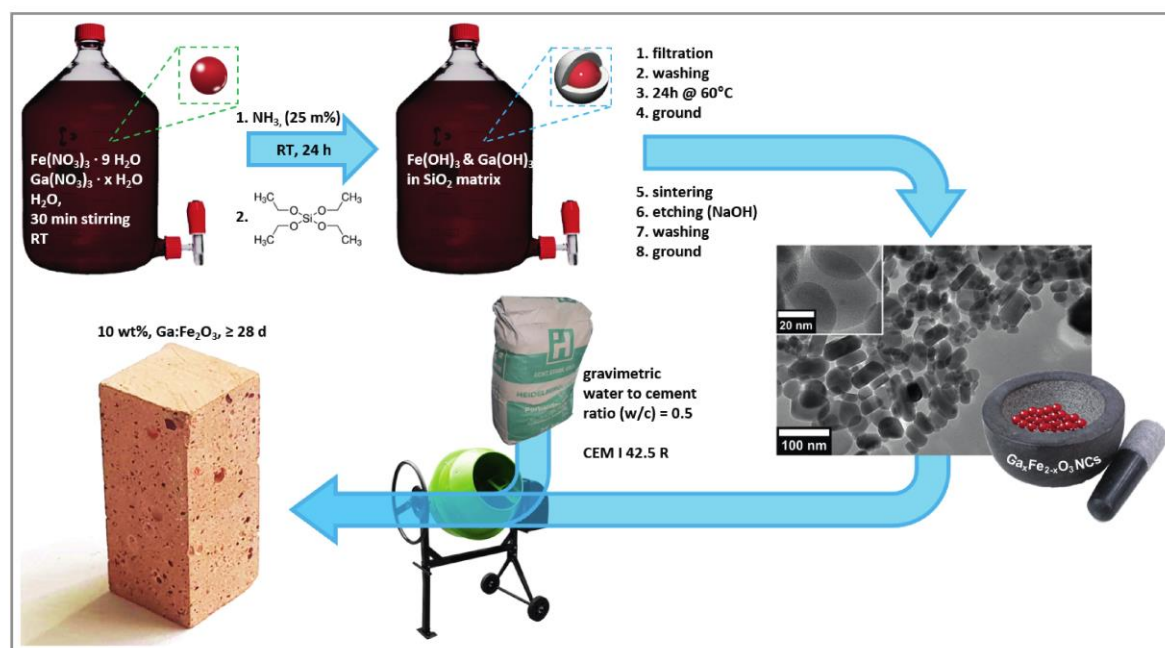


Figure 1. Schematic illustration of the synthetic pathway and preparation of $\text{Ga:Fe}_2\text{O}_3$ NCs, blending of CEM I 42.5 R with a gravimetric water-to-cement ratio (w/c) of 0.5 with $\text{Ga:Fe}_2\text{O}_3$ NCs, preparation of hardened cement paste cuboids.

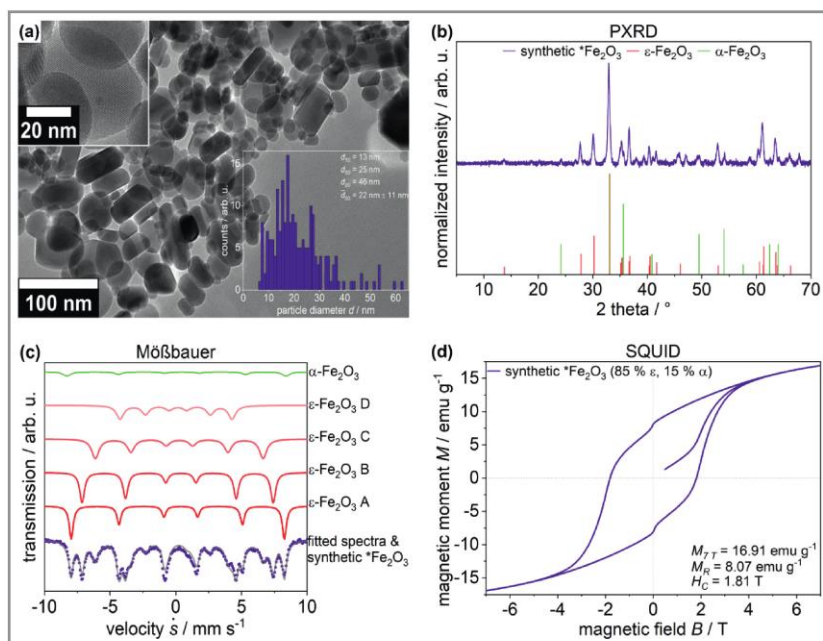


Figure 2. Evaluation of synthesized NCs. a) TEM micrograph with PSD and zoom-in as insets, b) PXRD pattern including reference patterns of ϵ - Fe_2O_3 and α - Fe_2O_3 [32], c) Mössbauer spectroscopy showing the fitted spectra including five sextets, one of α - Fe_2O_3 and four of ϵ - Fe_2O_3 (A to D), and d) SQUID including maximal magnetization at $B = 7 \text{ T } M_{7T}$, remanence M_R , and coercive field H_C .

gravimetric analysis (TGA), and scanning electron microscopy coupled with energy dispersive X-ray spectroscopy (SEM-EDXS) were used. While the first two techniques (PXRD and TGA) show only slight deviations concerning the impact of different amounts of $\text{Ga}:\text{Fe}_2\text{O}_3$ NCs on the hydration products (see SI Figs. S2 and S3). SEM-EDXS enabled the spatially resolved validation of the $\text{Ga}:\text{Fe}_2\text{O}_3$ NCs distribution in the hardened cement paste blocks ($10 \text{ mm} \times 4 \text{ mm} \times 1 \text{ mm}$) (Fig. 3 and S4 in SI). The micrographs exhibit a non-aggregated homogenous distribution in all samples, with the number of Fe fractions increasing with a higher mass fraction of $\text{Ga}:\text{Fe}_2\text{O}_3$ NCs, which qualitatively indicates an increasing Fe content in the samples. Significant deviations from the morphology cannot be detected, as the surface of all samples shows almost evenly distributed hydration products in form of flower-like portlandite, while the recorded oxygen values differ between the samples (Fig. S4 in SI), possibly induced by the oxygen of $\text{Ga}:\text{Fe}_2\text{O}_3$ NCs.

After showing the impact of the incorporated $\text{Ga}:\text{Fe}_2\text{O}_3$ NCs on the chemical composition, the pore structure of the hardened cement paste blocks was investigated via nitrogen physisorp-

tion (Fig. 4a and S5a–c in SI), and mercury intrusion porosimetry (Fig. 4b and S5d in SI). In the case of building materials, such knowledge is of utmost importance, since the porosity influences the mass transport, strength, durability, and thermal properties. A higher porosity could lead to less strength as well as higher mass and lower thermal transport and durability of concrete. The evaluation of nitrogen physisorption of all investigated samples presents no significant deviation in terms of the specific surface area (80 to $83 \text{ m}^2 \text{ g}^{-1}$) and specific volume (100 to $120 \text{ mm}^3 \text{ g}^{-1}$). The mean pore diameter \bar{d}_{pore} shows enlarged pores by up to 28% in comparison to pure hardened cement paste and 15% to anhydrous cement with the addition of $\text{Ga}:\text{Fe}_2\text{O}_3$ NCs with increasing proportion. The isotherms (Fig. S5c in SI) exhibit H4-type hysteresis loops for all mass fractions with a strong decrease of the desorption branch in the

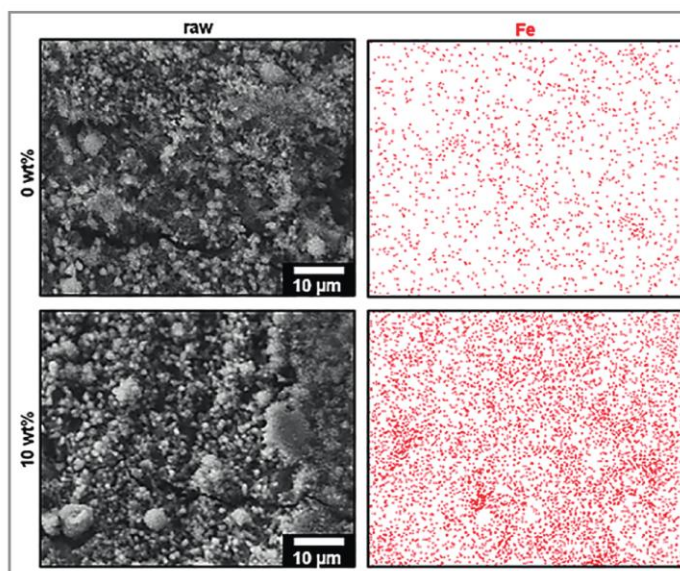


Figure 3. SEM-EDXS data of hardened cement pastes made from anhydrous cement mixed with different mass fractions of $\text{Ga}:\text{Fe}_2\text{O}_3$ NCs ($\leq 10 \text{ wt } \%$, namely 0, 1, 5, and 10 wt %); exemplary shown for non-blended hardened cement paste (0 wt %) and highest amount of Fe_2O_3 NCs (10 wt %); depicted are (left) micrograph and (right) Fe spots (red).

Online in color, print in grayscale unless the author(s) contribute to the costs.

✓✓ These are not the final page numbers!

4

Research Article

Chemie
Ingenieur
Technik

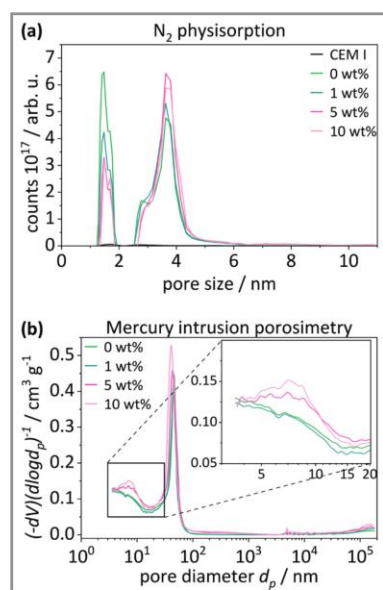


Figure 4. Evaluation of hardened cement paste s of anhydrous cement mixed with different mass fractions of Ga:Fe₂O₃ NCs; pore size distribution derived from a) nitrogen physisorption and b) mercury intrusion porosimetry.

range of $0.4 \leq p/p_0 \leq 0.5$, as expected when using a wetting adsorbate such as nitrogen [33].

Furthermore, the H4-type hysteresis' shape indicates non-rigid aggregated crystals and not completely filled voids with pore condensate. With a mass fraction of 1, 5, and 10 wt % Ga:Fe₂O₃ NCs the hysteresis width is increased by 8.5 %, 17 %, and by 12 % compared to the reference composition of 0 wt %. This indicates a change in the pore structure to a higher amount of pores. Simultaneously less completely filled pores, resulting in a decreasing density, which was calculated via weight and volume of the hardened cement paste blocks, of 1.85, 1.79, 1.76, and 1.70 g cm⁻³ with an increasing amount of filler, is observed (see Sect. S1.2.11 in SI). This phenomenon is most probably due to a high concentration of water around Ga:Fe₂O₃ NCs, because of the high surface-to-volume ratio of nanoparticles [34], during the early solidification process. Similar effects are observed in mercury intrusion porosimetry, with samples showing increasing porosity with increasing Ga:Fe₂O₃ NCs content, visible in the specific intrusion volume (Fig. S5d in SI) for the low ($p \leq 3.45$ bar) and high-pressure range ($p \leq 4000$ bar). Utilizing the Washburn equation [35] and analysis procedure according to DIN ISO 15901-1:2019-03 [36], this corresponds to larger pore volumes at two ranges of pore diameter d_{pore} , 5–15 nm (Fig. 4b inset) and 50–200 μ m (Fig. 4b). Both methods indicate that the porosity or the number of pores increases with rising Ga:Fe₂O₃ content, both at the nano- and microscale.

The changes of porosity induced by the hydration products formed, which in turn were influenced by the amount

of admixed Ga:Fe₂O₃ NCs and evaluated via PXRD and TGA, led to a variance in the pore size distribution and density of the samples.

3.2 Investigation of Mechanical and Magnetic Properties

Due to both, the observed increased porosity detected by nitrogen physisorption and mercury intrusion porosimetry as well as the influence of Ga:Fe₂O₃ NCs, the mechanical and magnetic properties are assumed to change accordingly. Therefore, the mechanical properties were determined by compressive strength test as well as micro- and nanoindentation, and the magnetic properties by SQUID measurements.

3.2.1 Mechanical Properties

The strength of hardened cement paste cubes (40 mm) was examined via a compressive strength test derived from DIN EN 12390-3:2019-10 [37] after 28 d of hydration (Fig. 5). It can be seen that increasing the share of NCs lowers the characteristic compressive strength f_{ck} by up to 28 %, while the change due to 1 wt % is marginal (–1.9 %). At a content of 10 wt % Ga:Fe₂O₃ NCs, the compressive strength f_{ck} decreases below $f_{ck} = 39.4$ N mm⁻², which has to be considered for the application in construction as a building material, but is negligible in regards to non-structural coatings for e.g. tap-proofness [38]. The lowered compressive strength f_{ck} could be due to the enhanced porosity, see calculated density in the previous section as well as the pore volumes in nitrogen physisorption and mercury intrusion porosimetry, caused by the admixture of Ga:Fe₂O₃ NCs. In addition to this macroscopic investigation, the hardness and stiffness of hardened cement paste on the micro- and nanoscale were determined from micro- and nanoindentation tests (Fig. 6). Force-displacement curves of a Berkovich (nano) and Vickers (micro) indenter are measured and analyzed for indentation hardness H_{IT} and modulus M_{IT} [39].

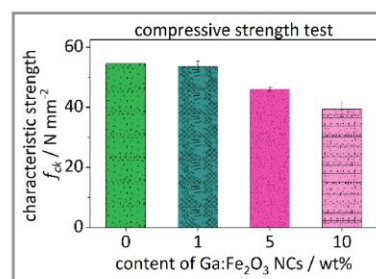


Figure 5. Evaluation of mechanical properties of hardened cement pastes mixed with different mass fractions of Ga:Fe₂O₃ NCs by compressive strength test at 28 d.

While a clear trend is distinguishable in compressive strength f_{ck} , the micro indentation hardness H_{IT} and modu-

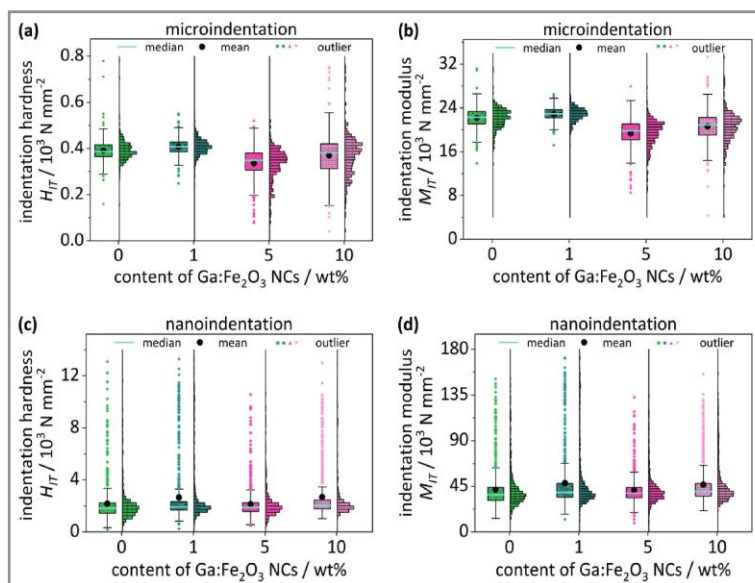


Figure 6. Evaluation of mechanical properties of hardened cement pastes mixed with different mass fractions of Ga:Fe₂O₃ NCs by indentation hardness H_{IT} derived from a) microindentations and b) nanoindentation as well as indentation modulus M_{IT} derived from c) microindentation and d) nanoindentation.

lulus M_{IT} show only minor differences, whereby the latter is dependent on the material's stiffness. Its respective median decreases slightly from approximately 23 to 20 kN mm⁻², while overall distribution width increases from approximately ± 2 to ± 3 kN mm⁻² (Fig. 6a,b). Hardly any changes are visible for the nano indentation hardness H_{IT} and modulus M_{IT} (Fig. 6c,d), where median values and distribution widths remain the same. The size of nano additive Ga:Fe₂O₃ (22 nm \pm 11 nm) is rather small compared to the volumes probed by nano-indentation, i.e., penetration depth of 250 nm, and no impact on the micro-scale mechanics arises. The same applies to micro-indentation with a penetration depth of 24 μ m.

It can be concluded that an increasing mass fraction of Ga:Fe₂O₃ NCs leads to a loss in macroscopic strength, while the mechanical properties (hardness and stiffness) on the micro- and nano-scale hardly change. Therefore, loss in mechanical strength seems to arise from increased porosity rather than alteration of cement paste's matrix incorporating Ga:Fe₂O₃ NCs.

3.2.2 Magnetic Properties

To appraise the magnetic character of hardened cement paste mixed with different mass fractions of Ga:Fe₂O₃ NCs, SQUID measurements were conducted (Fig. 7), where the magnetic moment M was measured against an external magnetic field \vec{H} in a range of $-7\text{ T} \leq B \leq 7\text{ T}$ and evaluated regarding the maximum magnetization at $B = 7\text{ T}$ M_{7T} , remanence M_R and coercive field H_C .

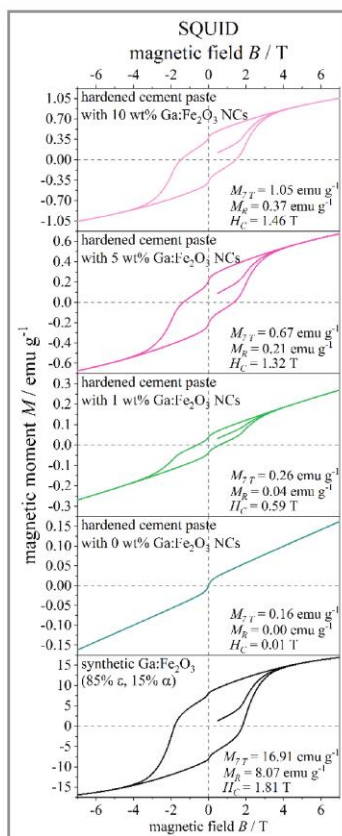


Figure 7. SQUID data of hardened cement paste s mixed with different mass fractions of Ga:Fe₂O₃ NCs measured at 27 °C in an external field H of $-7\text{ T} \leq B \leq 7\text{ T}$ with $B'(t) = 5\text{ Oe s}^{-1}$; with $H_c \equiv$ coercive field, $M_R \equiv$ remanence, and $M_{7T} \equiv$ maximum magnetization at $B = 7\text{ T}$.

Online in color, print in grayscale unless the author(s) contribute to the costs.

✓✓ These are not the final page numbers!

6

Research Article

Chemie
Ingenieur
Technik

ened cement paste) to $H_c = 1.46$ T (blended with 10 wt % Ga:Fe₂O₃ NCs), which is relatively close to that of the pure nanocrystals ($H_c = 1.81$ T). A possible explanation for this might be a magnetic exchange bias between the nanocrystal grains and the cement matrix. Due to the high magnetocrystalline anisotropy of Ga:Fe₂O₃ NCs, the nanocrystal grains keep their magnetic moment M undirected to the external magnetic field \vec{H} , increasing the energy needed to align the spins of the surrounding matrix (Fig. 8). We assume that, by lowering the external magnetic field \vec{H} , at first only the spins of the cement matrix furthest away from the NCs de-align and at an external magnetic field $\vec{H} \cong 0$ T only the NCs are still fully aligned. To achieve the ground state, a negative external magnetic field \vec{H} has to be applied.

In the case of maximum magnetization at $B = 7$ T M_{7T} , the sample with the highest mass fraction (10 wt %) exhibits only approximately 6 % of maximum magnetization at $B = 7$ T M_{7T} of the native Ga:Fe₂O₃ NCs, while the coercive field H_c is approximately 81 %, which is attributed to the lower amounts of unpaired electron spins per mole. Further, the remanence M_R of the blended hardened cement paste samples increases linearly with the added amount of Ga:Fe₂O₃ NCs. At the same time, the remanence M_R value normalized by the magnetic mass ($M_R = 3.9 \text{ emu g}^{-1} \pm 0.3 \text{ emu g}^{-1}$) is in all cases half of the synthetic Ga:Fe₂O₃ NCs ($M_R = 8.07 \text{ emu g}^{-1}$) probably due to the interaction with the cement matrix (Figs. 7 and 8).

In summary, the addition of different mass fractions (1–10 wt %) of Ga:Fe₂O₃ NCs enhanced coercive field H_c , maximum magnetization at $B = 7$ T M_{7T} , and remanence M_R compared to pure hardened cement paste, wherein the extrapolated remanence M_R was approximately half of the native Ga:Fe₂O₃ NCs'. This effect was attributed to the interaction between the electron spins of residue calcium aluminum ferrite (brownmillerite, C₄AF) with a low coercive field H_c and the electron spins of Ga:Fe₂O₃ with strong magnetic anisotropy. Cement seems to be a good matrix to isolate the Ga:Fe₂O₃ NCs, although halving the remanence M_R while not interfering with their maximum magnetization at $B = 7$ T M_{7T} .

4 Conclusion

Hardened cement pastes were prepared from a standard Portland cement (CEM I 42.5R) and different amounts of hard magnetic nanocrystals, and their structure-property relationships have been tested. Decisive physical properties of hardened cement paste were affected by the addition of this type of NCs:

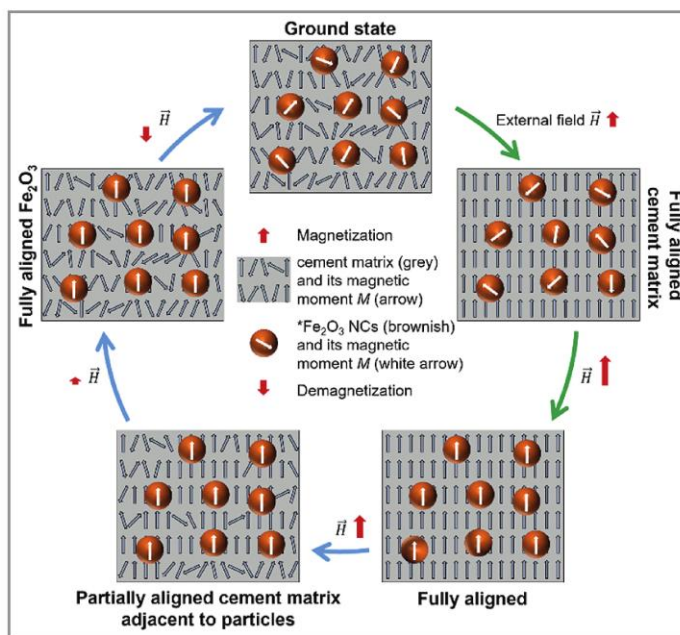


Figure 8. Scheme of alignment of the magnetic moment M in hardened cement pastes mixed with Ga:Fe₂O₃ NCs in an external field H of $-7 \text{ T} \leq B \leq 7 \text{ T}$.

- The higher the Ga:Fe₂O₃ content, the higher the porosity and, consequently, the lower the sample density.
- Coercive field H_c and magnetic remanence M_R are proportionally enhanced with rising Ga:Fe₂O₃ content, while the maximum magnetization at $B = 7$ T M_{7T} was only slightly affected.
- Micro- and nanoscale mechanical properties remain unaffected, no matter how much Ga:Fe₂O₃ is added, while compressive strength decreases.

In this work, we showed how and to which extent the amount of Ga:Fe₂O₃ NCs influences properties relevant to the practice of hardened cement paste, hence also the concrete properties, using a cheap and easily mass-producible nanoscale additive. The shown properties of blended hardened cement paste might make it a promising material for coatings of facades or interior walls, when it comes to niche applications like the demand for protection against wireless eavesdropping. Implementing these properties into concrete might enable constructions to protect sensitive machinery that is negatively influenced by radio waves, like magnetic resonance tomography in the medical field, to ensure greater lifetime and efficiency. At the same time, sensitive data can be protected by blocking the external access from third parties, i.e., enhanced tap-proofness or protection against wireless eavesdropping, but this will be in focus of investigation of future works.

Supporting Information

Supporting Information for this article can be found under DOI: <https://doi.org/10.1002/cite.202300022>. This document includes all experimental procedures, additional measurements as well as additional references to primary literature relevant for this study [43–80].

Acknowledgment

The authors thank A. Feldhoff for access to PXRD and SEM. The authors thank Heidelberger Cement AG for providing the cement in the DFG SPP 2005 priority program “Opus Fluidum Futurum – Rheology of Reactive, Multi-scale, Multiphase Construction Materials” [43]. The authors of this study are grateful for the financial support of the Deutsche Forschungsgemeinschaft (DFG, German Research Foundation – projects BI1708/5-1, HA 7917/3-1, and LO 751/26-1 [43]) and the German Federal Ministry for Economic Affairs and Energy (BMWf funding code 03ET1557A). Open access funding enabled and organized by Projekt DEAL.

Symbols used

A	[-]	damping constant
B	[T, or 10^5 Oe]	magnetic field
$B'(t)$	[Oe s ⁻¹]	alteration rate of magnetic field
C_C	[mm]	lenses' chromatic aberration in TEM
C_S	[mm]	lenses' spherical aberration in TEM
d	[m]	diameter
d_{10}	[m]	10 % are below this diameter
d_{50}	[m]	50 % are below this diameter or median
d_{90}	[m]	90 % are below this diameter or 10 % above
d_{pore}	[m]	pore size
d_{shaft}	[m]	diameter of mixing shaft
\bar{d}	[m]	mean diameter or average diameter
\bar{d}_{pore}	[m]	mean pore size or average pore size
$d\Delta m/(dt)$	[wt % h ⁻¹]	time derived weight loss in TGA
E	[-]	effective demagnetization factor
f_{ck}	[N mm ⁻²]	compressive strength
f_r	[s ⁻¹]	resonance frequency
\bar{H}	[T]	external magnetic field
H_a	[T]	uniaxial anisotropy field of the unpatterned film
H_C	[T]	coercive field
H_{IT}	[N mm ⁻²]	hardness of indentation
$I_{reflection}$	[-]	intensity of reflection in XRD

M	[emu g ⁻¹]	magnetic moment
M_{7T}	[emu g ⁻¹]	maximal magnetization at $B = 7$ T
M_{IT}	[N mm ⁻²]	modulus of indentation
M_R	[emu g ⁻¹]	remanence
p	[10 ⁵ Pa]	pressure
p/p_0	[-]	relative pressure for nitrogen physisorption
p_{intr}	[10 ⁸ Pa]	pressure of intrusion for Hg-porosimetry
\dot{s}	[mm s ⁻¹]	velocity
T_{ref}	[°C]	reference temperature
V	[mL]	volume
V_p	[μL]	pore volume
$V_{p,total}$	[μL]	total pore volume
V_{sample}	[μL]	sample volume
w/c	[-]	gravimetric water to cement ratio

Greek letters

α	[-]	crystal phase
γ	[T ⁻¹ s ⁻¹]	gyromagnetic ratio; $1.76 \cdot 10^{11}$
δ	[°]	contact angle
ε	[-]	crystal phase
η	[N m ⁻¹]	surface tension
θ	[°]	annular position of source and detector in XRD, relative to sample

Abbreviations

AR	aspect ratio
BET	Brunauer-Emmert-Teller
BJH	Barrett-Joyner-Halenda
C-S-H	calcium silicate hydrate; $m \text{ CaO} \cdot \text{SiO}_2 \cdot n \text{ H}_2\text{O}$
DFT	density functional theory
eq.	equivalent
EDXS	energy-dispersive X-ray spectroscopy
Ga:Fe ₂ O ₃	gallium substituted iron oxide [$\text{Ga}_{0.043}\text{Fe}_{1.957}\text{O}_3$]
NC	nanocrystals
r _{cf}	relative centrifugal force
SEM	scanning electron microscopy
SQUID	superconducting quantum interference device
TEM	transmission electron microscopy
TGA	thermogravimetric analysis
XRD	X-ray diffraction

References

- [1] J. Rieger, M. Kellermeier, L. Nicoleau, *Angew. Chem., Int. Ed.* **2014**, *53* (46), 12380–12396. DOI: <https://doi.org/10.1002/anie.201402890>
- [2] DIN EN 197-1:2011-11, *Cement – Part 1: Composition, Specifications and Conformity Criteria for Common Cements; German Version EN 197-1:2011*, Beuth Verlag, Berlin **2011**.

Online in color, print in grayscale unless the author(s) contribute to the costs.

✓ These are not the final page numbers!

8

Research Article

Chemie
Ingenieur
Technik

- [3] E. D. Hondros, E. Bullock, *Angew. Chem., Int. Ed.* **1989**, *28* (8), 1088–1097. DOI: <https://doi.org/10.1002/anie.198910881>
- [4] *Zement-Taschenbuch*, Vol. 50, Verein Deutscher Zementwerke e.V., Düsseldorf **2002**.
- [5] H. Moosberg-Bustnes, B. Lagerblad, E. Forssberg, *Mater. Struct.* **2004**, *37* (2), 74–81. DOI: <https://doi.org/10.1007/bf02486602>
- [6] *Blast Furnace Slag*, Federal Highway Administration, U.S. Department of Transportation, Washington, DC **2007**. <https://www.fhwa.dot.gov/publications/research/infrastructure/pavements/97148/010.cfm>
- [7] *Chapter 3 – Fly Ash in Portland Cement Concrete*, in *Fly Ash Facts for Highway Engineers*, Federal Highway Administration, U.S. Department of Transportation, Washington, DC **2007**. <https://www.fhwa.dot.gov/pavement/recycling/fach03.cfm>
- [8] *Silica Fume User's Manual*, Federal Highway Administration, U.S. Department of Transportation, Washington, DC **2007**, 1–194. <https://silicafume.org/concrete-manual.html>
- [9] T. R. S. Mullapudi, D. Gao, A. Ayoub, *Mag. Concr. Res.* **2013**, *65* (18), 1081–1091. DOI: <https://doi.org/10.1680/macrc.12.00187>
- [10] H. E. Elyamany, A. E. M. Abd Elmoaty, B. Mohamed, *Alexandria Eng. J.* **2014**, *53* (2), 295–307. DOI: <https://doi.org/10.1016/j.aej.2014.03.010>
- [11] S. H. Kosmatka, B. Kerkhoff, W. C. Panarese, *Design and Control of Concrete Mixtures*, 14th ed., Portland Cement Association, Washington, DC **2008**.
- [12] C. Y. Tuan, S. Yehia, *Acta Mater.* **2004**, *101*, 287–293.
- [13] E. A. Avallone, T. B. Iii, *Marks' Standard Handbook for Mechanical Engineers*, Vol. 34, McGraw Hill, New York **1997**.
- [14] D. Feng, N. Xie, C. Gong, Z. Leng, H. Xiao, H. Li, X. Shi, *Ind. Eng. Chem. Res.* **2013**, *52* (33), 11575–11582. DOI: <https://doi.org/10.1021/ie4011595>
- [15] L. Senff, D. M. Tobaldi, P. Lemes-Rachadel, J. A. Labrincha, D. Hotza, *Constr. Build. Mater.* **2014**, *65*, 191–200. DOI: <https://doi.org/10.1016/j.conbuildmat.2014.04.121>
- [16] S. A. Ghahari, E. Ghafari, N. Lu, *Constr. Build. Mater.* **2017**, *146*, 755–763. DOI: <https://doi.org/10.1016/j.conbuildmat.2017.04.165>
- [17] R. Siddique, A. Mehta, *Constr. Build. Mater.* **2014**, *50*, 116–129. DOI: <https://doi.org/10.1016/j.conbuildmat.2013.09.019>
- [18] M. Ghosal, A. K. Chakraborty, *Adv. Polym. Mater. Synth. Appl.* **2018**, *July*, 121–142.
- [19] M. Heikal, *J. Therm. Anal. Calorim.* **2016**, *126* (3), 1077–1087. DOI: <https://doi.org/10.1007/s10973-016-5715-0>
- [20] M. Heikal, M. E. A. Zaki, S. M. Ibrahim, *Constr. Build. Mater.* **2021**, *269*, 121310. DOI: <https://doi.org/10.1016/j.conbuildmat.2020.121310>
- [21] H. Li, H. Xiao, J. Yuan, J. Ou, *Compos. Part B Eng.* **2004**, *35* (2), 185–189. DOI: [https://doi.org/10.1016/S1359-8368\(03\)00052-0](https://doi.org/10.1016/S1359-8368(03)00052-0)
- [22] H. Li, H. Xiao, J. Ou, *Cem. Concr. Res.* **2004**, *34* (3), 435–438. DOI: <https://doi.org/10.1016/j.cemconres.2003.08.025>
- [23] M. H. Zhang, J. Islam, *Constr. Build. Mater.* **2012**, *29*, 573–580. DOI: <https://doi.org/10.1016/j.conbuildmat.2011.11.013>
- [24] K. J. Krakowiak, J. J. Thomas, S. Musso, S. James, A.-T. Akono, F.-J. Ulm, *Cem. Concr. Res.* **2015**, *67*, 103–121. DOI: <https://doi.org/10.1016/j.cemconres.2014.08.008>
- [25] M. S. El-Feky, P. Youssef, A. M. El-Tair, S. Ibrahim, M. Serag, *AIMS Mater. Sci.* **2019**, *6* (6), 864–883. DOI: <https://doi.org/10.3934/mat.2019.6.864>
- [26] B. B. Mukharjee, S. V. Barai, *Constr. Build. Mater.* **2014**, *68*, 416–425. DOI: <https://doi.org/10.1016/j.conbuildmat.2014.06.074>
- [27] D. Kong, H. Zhang, X. Du, Y. Yang, S. P. Shah, S. Wei, *Constr. Build. Mater.* **2012**, *37*, 707–715. DOI: <https://doi.org/10.1016/j.conbuildmat.2012.08.006>
- [28] M. Diez-Garcia, J. J. Gaitero, J. S. Dolado, C. Aymonier, *Angew. Chem., Int. Ed.* **2017**, *56* (12), 3162–3167. DOI: <https://doi.org/10.1002/anie.201611858>
- [29] S. Ohkoshi, S. Kuroki, S. Sakurai, K. Matsumoto, K. Sato, S. Sasaki, *Angew. Chem., Int. Ed.* **2007**, *46* (44), 8392–8395. DOI: <https://doi.org/10.1002/anie.200703010>
- [30] S. J. Barnett, *Rev. Mod. Phys.* **1935**, *7* (2), 129–166. DOI: <https://doi.org/10.1103/RevModPhys.7.129>
- [31] C. Kittel, *Phys. Rev.* **1948**, *73* (2), 155–161. DOI: <https://doi.org/10.1103/PhysRev.73.155>
- [32] K. Kelml, W. Maderl, *Z. Anorg. Allg. Chem.* **2005**, *631* (12), 2383–2389. DOI: <https://doi.org/10.1002/zaac.200500283>
- [33] M. Thommes, K. Kaneko, A. V. Neimark, J. P. Olivier, F. Rodriguez-Reinoso, J. Rouquerol, K. S. W. Sing, *Pure Appl. Chem.* **2015**, *87* (9–10), 1051–1069. DOI: <https://doi.org/10.1515/pac-2014-1117>
- [34] *Ultrafeine Aerosole und Nanopartikel am Arbeitsplatz*, Deutsche Gesetzliche Unfallversicherung, Berlin. <https://www.dguv.de/ifa/fachinfos/nanopartikel-am-arbeitsplatz/index.jsp>
- [35] E. W. Washburn, *Phys. Rev.* **1921**, *17* (3), 273–283. DOI: <https://doi.org/10.1103/PhysRev.17.273>
- [36] DIN ISO 15901-1:2019-03, *Evaluation of Pore Size Distribution and Porosity of Solid Materials by Mercury Porosimetry and Gas Adsorption – Part 1: Mercury Porosimetry (ISO 15901-1:2016)*, Beuth Verlag, Berlin **2019**.
- [37] DIN EN 12390-3:2019-10, *Testing Hardened Concrete – Part 3: Compressive Strength of Test Specimens; German Version EN 12390-3:2019*, Beuth Verlag, Berlin **2019**.
- [38] D. Neumann, U. Weinbrenner, U. Hestermann, L. Rongen, *Frick/Knöll Baukonstruktionslehre 2*, Vieweg+Teubner Verlag, Wiesbaden **2003**.
- [39] W. Oliver, G. Pharr, *J. Mater. Res.* **1992**, *7* (6), 1564–1583.
- [40] L. Khanna, N. K. Verma, *J. Magn. Magn. Mater.* **2013**, *336*, 1–7. DOI: <https://doi.org/10.1016/j.jmmm.2013.02.016>
- [41] Z. C. Lu et al., *Data Br.* **2019**, *27*, 104699. DOI: <https://doi.org/10.1016/j.dib.2019.104699>
- [42] F. D. Tamás, A. Vértes, *Cem. Concr. Res.* **1973**, *3* (5), 575–581. DOI: [https://doi.org/10.1016/0008-8846\(73\)90095-1](https://doi.org/10.1016/0008-8846(73)90095-1)
- [43] DFG SPP 2005, *Priority Program "Opus Fluidum Futurum – Rheology of Reactive, Multiscale, Multiphase Construction Materials"*, **2018**. www.spp2005.de/
- [44] H. M. Rietveld, *J. Appl. Crystallogr.* **1969**, *2* (2), 65–71. DOI: <https://doi.org/10.1107/S0021889869006558>
- [45] P. Paufler, *Cryst. Res. Technol.* **1995**, *30* (4), 494–494. DOI: <https://doi.org/10.1002/crat.2170300412>
- [46] F. Nishi, Y. Takéuchi, *Acta Crystallogr.* **1975**, *B31* (4), 1169–1173. DOI: <https://doi.org/10.1107/S0567740875004736>
- [47] A. A. Colville, S. Geller, *Acta Crystallogr.* **1971**, *B27* (12), 2311–2315. DOI: <https://doi.org/10.1107/s056774087100579x>
- [48] Q. Huang, O. Chmaissem, J. J. Capponi, C. Chailout, M. Marezio, J. L. Tholence, A. Santoro, *Physica C* **1994**, *227* (1–2), 1–9. DOI: [https://doi.org/10.1016/0921-4534\(94\)90349-2](https://doi.org/10.1016/0921-4534(94)90349-2)
- [49] J. C. A. Boeyens, V. V. H. Ichharam, *Z. Kristallogr. – New Cryst. Struct.* **2002**, *217*, 9–10. DOI: <https://doi.org/10.1524/nocr.2002.217.jg.9>
- [50] L. Desgranges, D. Grebille, G. Calvarin, G. Chevrier, N. Floquet, J.-C. Niepce, *Acta Crystallogr., Sect. B: Struct. Sci.* **1993**, *49* (5), 812–817. DOI: <https://doi.org/10.1107/S0108768193003556>
- [51] G. A. Lager, J. D. Jorgensen, F. J. Rotella, *J. Appl. Phys.* **1982**, *53* (10), 6751–6756. DOI: <https://doi.org/10.1063/1.330062>
- [52] M. R. Hartman, R. Berliner, *Cem. Concr. Res.* **2006**, *36* (2), 364–370. DOI: <https://doi.org/10.1016/j.cemconres.2005.08.004>
- [53] M. I. McCarthy, N. M. Harrison, *Phys. Rev. B.* **1994**, *49* (13), 8574–8582. DOI: <https://doi.org/10.1103/PhysRevB.49.8574>

- [54] T. Pilati, F. Demartin, C. M. Gramaccioli, *Acta Crystallogr., Sect. B Struct. Sci.* **1998**, *54* (5), 515–523. DOI: <https://doi.org/10.1107/S0108768197018181>
- [55] Á. G. De La Torre, S. Bruque, J. Campo, M. A. G. Aranda, *Cem. Concr. Res.* **2002**, *32* (9), 1347–1356. DOI: [https://doi.org/10.1016/S0008-8846\(02\)00796-2](https://doi.org/10.1016/S0008-8846(02)00796-2)
- [56] F. C. Hawthorne, R. B. Ferguson, *Can. Mineral.* **1975**, *13*, 289–292.
- [57] J. A. McGinnety, *Acta Crystallogr., Sect. B Struct. Crystallogr. Cryst. Chem.* **1972**, *28* (5), 2845–2852. DOI: <https://doi.org/10.1107/S0567740872007022>
- [58] C. Bezou, A. Nonat, J.-C. Mutin, A. N. Christensen, M. S. Lehmann, *J. Solid State Chem.* **1995**, *117* (1), 165–176. DOI: <https://doi.org/10.1006/jssc.1995.1260>
- [59] W. Mumme, R. Hill, G. Bushnellwye, E. Segnit, *Neues Jahrb. Mineral.* **1995**, *169* (1), 35–68.
- [60] P. Mondal, J. W. Jeffery, *Acta Crystallogr., Sect. B Struct. Crystallogr. Cryst. Chem.* **1975**, *31* (3), 689–697. DOI: <https://doi.org/10.1107/S0567740875003639>
- [61] S. Brunauer, P. H. Emmett, E. Teller, *J. Am. Chem. Soc.* **1938**, *60* (2), 309–319. DOI: <https://doi.org/10.1021/ja01269a023>
- [62] R. M. Dreizler, E. K. U. Gross, in *Density Funct. Theory*, Springer, Heidelberg **1990**.
- [63] L. D. Gelb, K. E. Gubbins, R. Radhakrishnan, M. Sliwinski-Bartkowiak, *Rep. Prog. Phys.* **1999**, *62*, 1573–1659. DOI: <https://doi.org/10.1088/0034-4885/77/5/056502>
- [64] NOVA[®]-e Series Models 25 and 26 NovaWin/NovaWin-CFR, Operating Manual, Version 11.01/11.02, Quantachrome Instruments, Boynton Beach, FL **2012**, 124–126. <https://dokumen.tips/documents/gas-sorption-system-operating-manual.html?page=124>
- [65] E. P. Barrett, L. G. Joyner, P. P. Halenda, *J. Am. Chem. Soc.* **1951**, *73* (1), 373–380. DOI: <https://doi.org/10.1021/ja01145a126>
- [66] T. J. Mays, *Stud. Surf. Sci. Catal.* **2007**, *160*, 57–62. DOI: [https://doi.org/10.1016/S0167-2991\(07\)80009-7](https://doi.org/10.1016/S0167-2991(07)80009-7)
- [67] *A Practical Guide to Microstructural Analysis of Cementitious Materials* (Eds: K. Scrivener, R. Snellings, B. Lothenbach), CRC Press, Boca Raton, FL **2015**.
- [68] Q. Yu, H. J. H. Brouwers, in *Proc. 8th fib Int. PhD Symposium in Civil Engineering* (Eds: G. Fischer, M. Geiker, O. Hededa, L. Ottoson, H. Stang), Technical University of Denmark, Lyngby **2010**.
- [69] C. G. Vassileva, S. V. Vassilev, *Fuel Process. Technol.* **2005**, *86* (12–13), 1297–1333. DOI: <https://doi.org/10.1016/j.fuproc.2005.01.024>
- [70] J. Dweck, P. M. Buchler, A. C. V. Coelho, F. K. Cartledge, *Thermochim. Acta* **2000**, *346* (1–2), 105–113. DOI: [https://doi.org/10.1016/S0040-6031\(99\)00369-X](https://doi.org/10.1016/S0040-6031(99)00369-X)
- [71] D. J. Morgan, *Clay Miner.* **1978**, *13* (1), 132–132. DOI: <https://doi.org/10.1180/claymin.1978.013.1.11>
- [72] A. Bakolas, E. Aggelakopoulou, A. Moropoulou, *J. Therm. Anal. Calorim.* **2008**, *92* (1), 345–351. DOI: <https://doi.org/10.1007/s10973-007-8858-1>
- [73] K. Wang, S. P. Shah, A. Mishulovich, *Cem. Concr. Res.* **2004**, *34* (2), 299–309. DOI: <https://doi.org/10.1016/j.cemconres.2003.08.003>
- [74] R. Zboril, M. Mashlan, D. Petridis, *Chem. Mater.* **2002**, *14* (3), 969–982. DOI: <https://doi.org/10.1021/cm0111074>
- [75] E. Tronc, C. Chanéac, J. P. Jolivet, *J. Solid State Chem.* **1998**, *139* (1), 93–104. DOI: <https://doi.org/10.1006/jssc.1998.7817>
- [76] H. Tokoro, W. Tarora, A. Namai, M. Yoshikiyo, S. Ohkoshi, *Chem. Mater.* **2018**, *30* (9), 2888–2894. DOI: <https://doi.org/10.1021/acs.chemmater.7b03708>
- [77] A. Namai et al., *Nat. Commun.* **2012**, *3* (1), 1035. DOI: <https://doi.org/10.1038/ncomms2038>
- [78] C. Jakob, D. Jansen, N. Ukrainczyk, E. Koenders, U. Pott, D. Stephan, J. Neubauer, *Materials (Basel)* **2019**, *12* (18), 2957. DOI: <https://doi.org/10.3390/ma12182957>
- [79] C. Jakob, D. Jansen, U. Pott, J. Neubauer, Comparing Phase Development and Rheological Properties of OPC Paste Within the First Hour of Hydration, in *Rheology and Processing of Construction Materials* (Eds: V. Mechtcherine, K. Khayat, E. Secrieru), vol. 23, Springer, Cham **2019**. DOI: https://doi.org/10.1007/978-3-030-22566-7_26
- [80] P. A. Kifling et al., *Constr. Build. Mater.*, submitted.

Online in color, print in grayscale unless the author(s) contribute to the costs.

✓✓ These are not the final page numbers!

10

Research Article

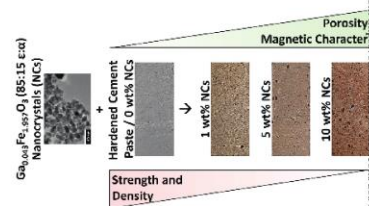
Chemie
Ingenieur
Technik

DOI: 10.1002/cite.202300022

Impact of Hard Magnetic Nanocrystals on the Properties of Hardened Cement Paste

Patrick A. Kießling, Markus Mahlbacher, Christoph Wesemann, Alexander Mundstock, Franziska Lübke, Franziska Warwas, Stephen Klimke, Franz Renz, Ludger Lohaus, Michael Haist, Nadja C. Bigall*

Research Article: The impact of different amounts of incorporated hard magnetic $\text{Ga}_{0.043}\text{Fe}_{1.957}\text{O}_3$ (85% ϵ and 15% α phase) nanocrystals (NCs) on the physical properties of hardened cement paste is shown. By adding these Fe_2O_3 NCs it is possible to modify the manifold properties simultaneously, thus, enabling fine-tuned buildings or coatings. ■



Supporting Information

Impact of hard Magnetic Nanocrystals on the Properties of Hardened Cement Paste

Patrick A. Kißling^{1,2}, Markus Mahlbacher², Christoph Wesemann¹, Dr. rer. nat. Alexander Mundstock¹, Dr. rer. nat. Franziska Lübke¹, Dr. rer. nat. Stephen Klimke³, Prof. Dr. rer. nat. Franz Renz^{3,4}, Prof. Dr.-ing. Ludger Lohaus², Prof. Dr.-ing. Michael Haist², and Prof. Dr. rer. nat. Nadja C. Bigall^{1,4,*}

DOI: 10.1002/cite.202300022

Correspondence: Nadja C. Bigall (nadja.bigall@pci.uni-hannover.de), Leibniz University, Institut für Physikalische Chemie und Elektrochemie, Callinstr. 3a, 30167 Hannover, Germany.

Table of Contents

S1 Experimental Procedures	2
S1.1 Materials.....	2
S1.2 Methods	2
S1.2.1 Synthesis of Gallium Substituted Iron Oxide Nanocrystals	2
S1.2.2 Gallium Substitution Rate Determination	2
S1.2.3 Transmission Electron Microscopy.....	3
S1.2.4 MÖSSBAUER Spectroscopy.....	3
S1.2.5 Superconducting Quantum Inference Device	3
S1.2.6 Thermogravimetric Analysis.....	3
S1.2.7 Powder X-Ray Diffraction	3
S1.2.8 Scanning Electron Microscopy and Electron Dispersive X-Ray Spectroscopy	4
S1.2.9 Preparation of Cementitious Suspension and Test Specimen	4
S1.2.10 Nitrogen Physisorption	5
S1.2.11 Calculation of Density.....	5
S1.2.12 Mercury Porosimetry.....	6
S1.2.13 Micro- and Nanoindentation.....	6
S2 Results and Discussion.....	6
S2.1 Characterization of Educts.....	6
S2.1.1 Pristine Portland Cement CEM I 42.5 R.....	6
S2.1.2 Synthesis of Gallium Substituted Iron Oxide Nanocrystals	7
S2.2 Structural Characterization.....	8
References.....	10

S1 Experimental Procedures**S1.1 Materials**

The main materials for this study were ordinary Portland cement CEM I 42.5 R from HeidelbergCement AG (in the following referred to as cement or CEM I), iron(III) nitrate nonahydrate ($\geq 98\%$ metals basis, $\text{Fe}(\text{NO}_3)_3 \cdot 9 \text{H}_2\text{O}$) and gallium(III) nitrate hydrate (99.999% metals basis, $\text{Ga}(\text{NO}_3)_3 \cdot x \text{H}_2\text{O}$) from Alfa Aesar, tetraethyl orthosilicate (98%, TEOS) from Merck, ammonia solution ($\geq 25\%$, p.a., NH_3) from Carl Roth, Millipore water ($18.2 \text{ M}\Omega \cdot \text{cm}$) cleaned by Arium Mini from Sartorius (in the following referred to as water), and liquid nitrogen ($\geq 99.999\%$) from Linde. The anhydrous cement was stored at ambient temperature ($20^\circ\text{C} \pm 2^\circ\text{C}$) and humidity (18% - 45%) for the whole study.

S1.2 Methods**S1.2.1 Synthesis of Gallium Substituted Iron Oxide Nanocrystals**

Following OHKOSHI ET AL. [29] gallium substituted epsilon iron oxide nanocrystals ($\epsilon\text{-Ga}_x\text{Fe}_{2-x}\text{O}_3$ NCs) were prepared by a sol-gel-method. $\text{Fe}(\text{NO}_3)_3 \cdot 9 \text{H}_2\text{O}$ (30 eq., 495.11 mmol, 200.00 g) as well as $\text{Ga}(\text{NO}_3)_3 \cdot x \text{H}_2\text{O}$ (1 eq., 16.50 mmol, 4.22 g) were dissolved in 9.25 L water and stirred (350 rpm) for 30 min at room temperature (RT). This yellow to orange solution was mixed with an aqueous solution of NH_3 (25 m%, 1.2 eq., 19.70 mol, 387.48 mL, 349.90 g) over a course of 20 min, resulting in a murky dark brown color, and stirred (350 rpm) for 30 min at RT. After that, TEOS (6 eq., 238.24 mmol, 357.68 mL, 336.21 g) was added slowly over 15 min and stirred for 24 h. In the next step, the solution was filtrated using a fiberglass filter (retention 0.4 μm , MN-GF 5 by Macherey-Nagel GmbH & Co. KG) in a Buchner funnel and washed once with 4.5 L of water. The residue was dried for 24 h at 60°C , ground until the color changed to reddish-brown, sieved (particles smaller 125 μm) and sintered in a ceramic bowl, implementing a five-step process: (1) applying a heating rate of 4°C min^{-1} reaching 200°C , (2) holding time of 10 min at 200°C , (3) applying a heating rate of 4°C min^{-1} reaching 1100°C , (4) holding time of 4 h at 1100°C , and (5) cooling with 4°C min^{-1} to room temperature. Afterwards, these sintered particles' silicon shell (740 g) was etched away by stirring in NaOH (0.5 M, 10 L) (350 rpm, Hei-Torque Precision 400 by Heidolph Instruments GmbH, Co. KG; collapsible-blade BR 14 stainless steel, $d_{\text{shaft}} = 8 \text{ mm}$, blade size = $90 \times 10 \text{ mm}$) for 96 h at RT, transferred into centrifugation tubes (80 mL PPCO-AOR from Herolab GmbH), centrifuged (20500 g, 10 min, 3-18KS by Sigma Laborzentrifugen GmbH equipped with a fixed angle rotor (30°) 12155-H), washed up to five times with water until the supernatant was at least pH = 8. After decanting the supernatant, the particle solution was dispersed uniformly on a PTFE plate, dried for 96 h at 60°C , ground manually via agate mortars and pistils (standard form, depths: 8 mm and 20 mm, inner diameters: 20 mm and 80 mm, and outer diameters: 25 mm and 95 mm) by Merck KGaA, and sieved (particles smaller than 125 μm ; test sieve ISO 3310-1 Body 316L Mesh S-steel/RF Body: 200 mm x 50 mm by Retsch GmbH with mesh sizes of 1.4 mm, 1 mm, 710 μm , 500 μm , 160 μm , 125 μm , and 100 μm).

S1.2.2 Gallium Substitution Rate Determination

The substitution rate x of the synthesized nanocrystals was determined via a microwave digestion and a subsequent analysis using an inductively coupled plasma optical emission spectroscopy (ICP-OES). For this, aliquots (approx. 23 mg) of the as-synthesized material were placed in a teflon microwave vessel and mixed with aqua regia (25 mL; $\text{HNO}_3:\text{HCl}$ 3:1). The sample was heated in the microwave (MLS Start by MLS GmbH) with an output of up to 750 W. Within 15 min, the mixture was heated to 160°C , remained there for 30 min, cooled to 40°C over 60 min, and filled up to 100 mL with water. In the last step, the diluted samples were measured via ICP-OES by 3P instruments GmbH.

S1.2.3 Transmission Electron Microscopy

Aspect ratio (AR), size, and morphology of $\text{Ga}_{0.043}\text{Fe}_{1.957}\text{O}_3$ (Ga:Fe₂O₃) NCs were investigated by transmission electron microscopy (TEM) using a Fei Tecnai G2 F20 electron microscope ($C_s = 0.5$ mm and $C_c = 0.5$ mm), equipped with a field-emission gun working at an acceleration voltage of 200 kV and a pressure of 0.137 nbar for each measurement. The nanocrystals were dispersed in water and transferred on a carbon-coated copper TEM grid.

S1.2.4 MÖSSBAUER Spectroscopy

The phase of Ga:Fe₂O₃ NCs was evaluated by MÖSSBAUER spectroscopy using a modified transmission MÖSSBAUER spectrometer by Wissenschaftliche Elektronik GmbH Starnberg/Germany (WissEL). The powder was finely ground manually via agate mortars and pistils (standard form, depths: 8 mm and 20 mm, inner diameters: 20 mm and 80 mm, and outer diameters: 25 mm and 95 mm) by Merck KGaA to sizes below 125 μm before measurement. Data acquisition was carried out using a self-build drive control and data acquisition unit at 25 °C while a proportional counter was used as a detector with a gamma radiation source, ⁵⁷Co isotope embedded in a rhodium matrix.

S1.2.5 Superconducting Quantum Interference Device

To assess the magnetic properties of Ga:Fe₂O₃ NCs as well as anhydrous cement mixed with different mass fractions an MPMS3 superconducting quantum interference device (SQUID) magnetometer from Quantum Design operating in a range of $-7 \text{ T} \leq B \leq 7 \text{ T}$ at 27 °C and an alteration rate $B'(t) = 5 \text{ Oe s}^{-1}$ was used to measure the MH curves of the iron oxide cement mixtures. The samples were finely ground via agate mortars and pistils (standard form, depths: 8 mm and 20 mm, inner diameters: 20 mm and 80 mm, and outer diameters: 25 mm and 95 mm) by Merck KGaA manually to sizes below 125 μm and fixed inside plastic containers mounted inside brass holders.

S1.2.6 Thermogravimetric Analysis

To evaluate the content of bound water, at early stages of hydration (≤ 90 min) mainly from ettringite, as well as the change in the decomposition behavior, any synthesized or dried sample was investigated by thermogravimetric analysis (TGA) using a TGA/DSC 3+ from Mettler-Toledo GmbH. It was operated in a temperature range from 20 °C to 1100 °C under a nitrogen flow of 25 mL min⁻¹, a heating rate of 5 °C min⁻¹ followed by holding the temperature at 1100 °C for 15 min. The data was normalized by mass (mg), derived once by time (s), multiplied by 3600 (for plotting in hours), and plotted against temperature (°C). The samples were transferred into aluminum oxide crucibles (70 μL) before measurement.

S1.2.7 Powder X-Ray Diffraction

The crystallinity was investigated by powder X-ray diffraction (PXRD) using a Bruker D8 Advance in reflection mode. It was operated at 20 °C, 40 kV, and 40 mA using Cu-K α radiation. Each measurement was done in a 2θ -range from 5° to 70°, with a step size of 0.010540856°, and 4 s per step, resulting in a total measurement time of 7.25 h. Additionally, to ensure ettringite being present, a zoom-in diffractogram was done in a 2θ -range from 8° to 10°, with a step size of 0.010540856°, and 12 s per step, resulting in a total measurement time of 1.62 h. The powder of each sample (≤ 90 min and ≥ 28 d) was transferred into an X-ray amorphous PVC powder carrier and smoothed, to have no sample displacement. Their diffraction patterns were evaluated by the database of Powder Diffraction File (PDF-2) 2020 of the International Centre for Diffraction Data (ICDD).

Furthermore, the phase ratio in anhydrous cement and as-synthesized particles were evaluated by Rietveld refinement [44,45] using literature data [46–60], the measured XRD data of this work, and the software TOPASv6 by Bruker.

S1.2.8 Scanning Electron Microscopy and Electron Dispersive X-Ray Spectroscopy

The local distribution of elements was investigated by scanning electron microscopy coupled with electron dispersive X-ray spectroscopy (SEM-EDXS) using a JEOL JSM 6700F equipped with a cold field emission gun and a 4 Quadrant Backscatter Electron Detector. The acceleration voltage was 20 kV, the current 10 μ A, the working distance 8.0 mm, and the pressure 375 nbar for each measurement. Before EDXS, micrographs were taken with an acceleration voltage of 2 kV. The sample block (≥ 28 d) (10 mm x 4 mm x 1.2 mm; **section S1.2.9**) was transferred onto an adhesive carbon disk.

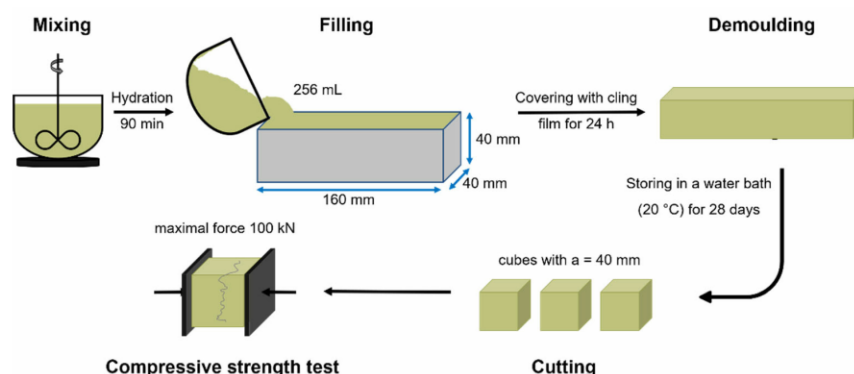
S1.2.9 Preparation of Cementitious Suspension and Test Specimen

Following the mixing program shown in **Table S1**, cementitious suspensions with a water to cement ratio (w/c) w/c = 0.5, a total volume of 600 mL, and four different concentrations of Ga:Fe₂O₃ NCs (0 wt% \equiv 0.00 g, 1 wt% \equiv 7.32 g, 5 wt% \equiv 36.61 g, and 10 wt% \equiv 73.22 g) were prepared. Therefore, 732 g cement and 366 mL water (precooled to 10 °C), resulting in w/c = 0.5, and a final temperature of 20 °C, was mixed with a balloon whisk using a Kenwood KitchenAid KM336 S Chef Classic to simulate concrete mixing as usually performed at larger scales. During the first ten minutes, the mixture's temperature rose to 20 °C.

Table S1. Mixing method for cementitious suspensions using a Kenwood KitchenAid.

Step	Duration / min	Mode / approx. rpm
adding of water	0.5	level 2 / 72
pre-homogenization	1.0	level 2 / 72
homogenization	1.0	maximum / 220
stop and manual homogenization	1.0	Off
homogenization II	2.0	maximum / 220
slow stirring	86	level 2 / 72
homogenization II	2.0	maximum / 220
slow stirring	86	level 2 / 72

90 min after adding water (related to slow stirring at level 2 for 86 min), four moulds (160 mm x 40 mm x 40 mm, 256 mL) were filled with the cementitious suspension, compacted manually, covered by cling film to prevent carbonation and evaporation of water over time, and stored under ambient conditions (20 °C \pm 1 °C). On the second day of hydration, the test specimen were demoulded, and transferred to a water bath (20 °C \pm 1 °C), and stored for 27 d before performing a compressive strength test derived from DIN EN 12390-3:2019-10 [37] (**Scheme S1**).



Scheme S1. Test specimen preparation for an age of 28 d and compressive strength test derived from DIN EN 12390-3:2019-10 [37].

S1.2.10 Nitrogen Physisorption

To assess the specific surface area and the specific volume of hardened cement paste (*HCP*) (≥ 28 d) mixed with Ga:Fe₂O₃ NCs, nitrogen (N₂) physisorption was performed in a NOVA 3000e from Quantachrome GmbH & Co KG operating at -196.15 °C. Before physisorption measurements, the powder samples and the split specimen were degassed under vacuum (100 mbar) at 40 °C for 4 h. *HCP* (≥ 28 d) specimen were split and sieved (particle size 1 mm to 2 mm; test sieve ISO 3310-1 Body 316L Mesh S-steel/RF Body: 200 mm x 50 mm by Haver & Boecker GmbH with mesh sizes of 2.0 mm and 1.0 mm). Subsequently, solvent exchange with isopropanol was performed for 3 d at a water to solvent ratio of 1:50. Samples were vacuum dried at 40 °C for 4 d to a final pressure of 15 μ bar. Specific surface area and specific volume were estimated by applying the BRUNAUER-EMMETT-TELLER (BET) [61] equation. Pore volume was estimated at $p/p_0 = 0.9489$, pore size distributions by applying by applying Density Functional Theory (DFT) [62,63] (non local density functional theory – N₂ - carbon equilibrium transition kernel at 77K based on a *slit-pore model*) [64] and BARRETT-JOYNER-HALENDA (BJH) [65] using the software NovaWin from Quantachrome GmbH & Co KG.

S1.2.11 Calculation of Density

In order to determine the density of *HCP* mixed with Ga:Fe₂O₃ NCs small rectangular blocks were taken, weighed using a high precision balance from Sartorius AG and measured via a digital caliper from Vorel. The density was calculated via the division of the small blocks with the volume, see **Table S2**.

Table S2. Data for the calculation of the density of *HCP* mixed with Ga:Fe₂O₃ NCs.

Content of Ga:Fe ₂ O ₃ NCs / wt%	Mass / g	Length / mm	Width / mm	Height / mm	Volume / cm ³	Density / g cm ⁻³
0	4.5345	24.38	10.06	10.00	2.45	1.85
1	4.3520	23.30	10.25	10.18	2.43	1.79
5	3.2189	17.95	10.07	10.11	1.83	1.76
10	3.7847	21.84	10.06	10.14	2.23	1.70

S1.2.12 Mercury Porosimetry

To assess the porous character, ranging from super-nanopores to super-micropores (10 nm to 100 μ m) [68], of *HCP* (≥ 28 d) mixed with Ga:Fe₂O₃ NCs, mercury (Hg) intrusion porosimetry (MIP) was

performed with a Poremaster 60 GT from Anton Paar Germany GmbH. Before measurements, the test specimens (≥ 28 d) were split and sieved (particle size 2 mm to 4 mm; test sieve ISO 3310-1 Body 316L Mesh 5-steel/RF Body: 200 mm x 50 mm by Haver & Boecker GmbH with mesh sizes of 4.0 mm and 2.0 mm). Subsequently, solvent exchange with isopropanol was performed for 3 d at a water to solvent ratio of 1:50. Samples were vacuum dried at 40 °C for 4 d to a final pressure of 15 μ bar. Low pressure intrusion was performed at $p \leq 3.45$ bar and subsequent high pressure up to $p = 4000$ bar. Pore size distributions for the intrusion branch were calculated from the WASHBURN [35] equation using a contact angle $\delta = 140^\circ$ and a surface tension $\eta = 480$ mN/m.

S1.2.13 Micro- and Nanoindentation

Mechanical properties on the micro- and nanoscales of HCP (≥ 28 d) mixed with Ga:Fe₂O₃ NCs, were assessed from micro- and nanoindentation testing. Here, cross sections (20 mm x 30 mm) were cut from the specimen's center of each mix after approximately 30 days. Subsequently, all samples were polished until the surface turned reflective, cleaned with pressurized air, and stored in a box containing silica gel as drying agent without direct contact before measurement. Microindentation was performed with an Anton Paar Micro Combi Tester (MCT³) and a VICKERS indenter, for a square grid size of 20 x 20 indents spaced at 400 μ m. Loading and unloading rate was set to 3 N min⁻¹ for a maximum penetration depth of 24 μ m with a pause of 10 s at maximum loading. Nano indentation was performed with an Anton Paar Ultra Nanoindentation Tester (UNHT³) and a BERKOVICH indenter, for a square grid size of 25 x 25 indents spaced at 10 μ m. Loading and unloading rate was set to 20 mN min⁻¹ for a maximum penetration depth of 250 nm with a pause of 10 s at maximum loading. Data analysis of indentation hardness H_{IT} and indentation modulus M_{IT} was performed for the unloading branch of the force-displacement curve according to the approach of OLIVER ET AL. [39].

S2 Results and Discussion

S2.1 Characterization of Educts

S2.1.1 Pristine Portland Cement CEM I 42.5 R

To assess the state before hydration and addition of iron oxide NCs, the pristine Portland cement CEM I 42.5 R was characterized via PXRD, TGA, and particle size distribution derived from SEM micrographs. **Figure S1a** shows the diffractograms of CEM I (black), synthetic C₃S (Ca₃SiO₅, yellow), synthetic C₃A (Ca₃Al₂O₆, red) and its most prominent reflections in a range of $10^\circ \leq 2\theta \leq 71^\circ$ ($I_{reflection} > 0.1 I_{max}$), which align with the literature data [46–60]. Further, the identified phases (C₃A orthorhombic, C₃A cubic, C₃S, C₂S, CaSO₄, C₄AF, MgO, CaSO₄ · 0.5 H₂O, CaO, and SiO₂) and their ratio derived from Rietveld refinement (grey) [44,45] match the data shown by LU ET AL. [41] with slight differences in their respective intensities (**Figure S1b**). Derived from several SEM micrographs, anhydrous CEM I shows a non-homogeneous particle size distribution (PSD) with a mean size of $\bar{d} = 4.3 \mu\text{m} \pm 0.1 \mu\text{m}$ (**Figure S1c**). The TGA measurement (**Figure S1d**) shows as expected three decomposition processes: (1) desorption of adsorbed water until roughly 100 °C, (2) decomposition of gypsum (CaSO₄ · 2 H₂O) at 127.5 °C \pm 17.5 °C as well as at 445 °C \pm 25 °C [67–72], and (3) calcite (CaCO₃) at 645 °C \pm 125 °C [70–73].

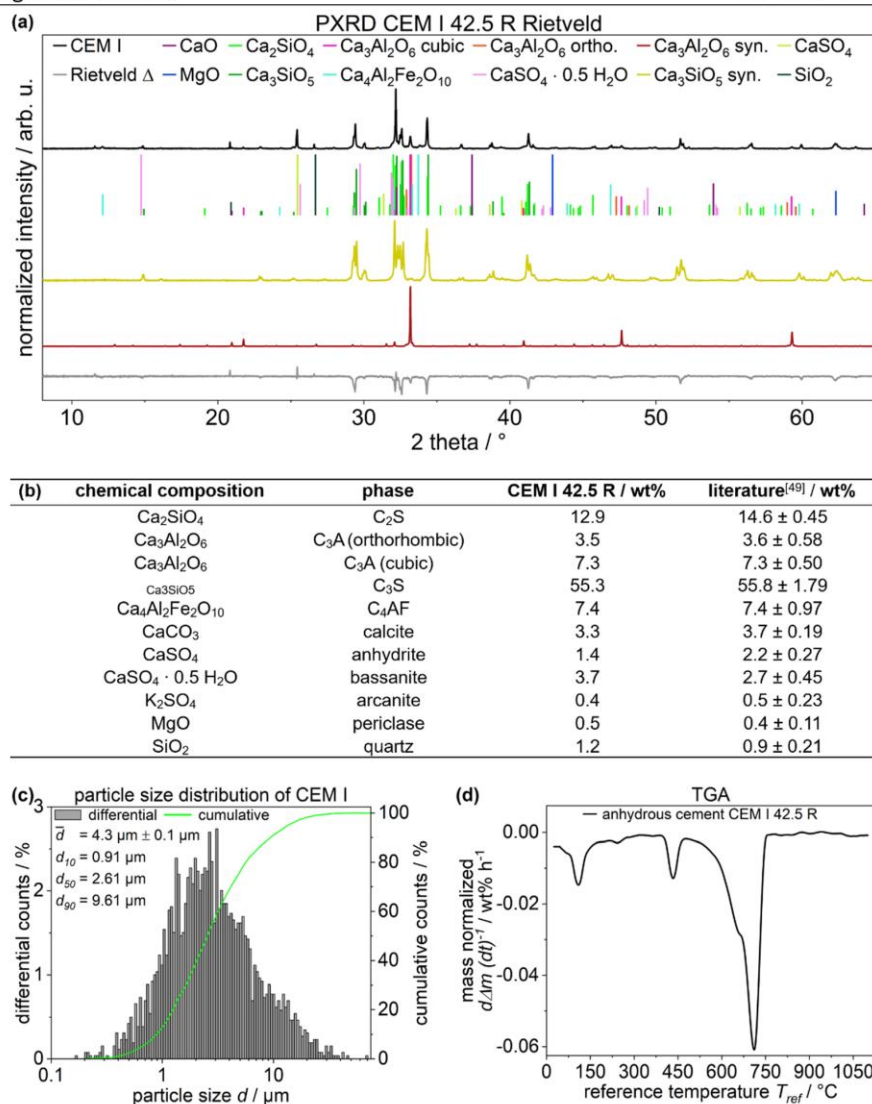


Figure S1. (a) PXRD pattern of anhydrous cement (black), its synthetic main components C₃S (yellow) and C₃A (red), literature reflections for all identifiable phases [46–60], the result of Rietveld-Refinement indicated by difference (grey), (b) phase content of anhydrous Portland cement CEM I 42.5 R derived by Rietveld-Refinement compared to data from LU ET AL. [41], (c) particle size distribution derived from several SEM micrographs, and (d) TGA data plotted as normalized weight loss ($d\Delta m / (dt)^{-1}$) per hour against the reference temperature T_{ref} with a heating rate of $5\text{ }^{\circ}\text{C min}^{-1}$.

S2.1.2 Synthesis of Gallium Substituted Iron Oxide Nanocrystals

The nanoparticles used in this work were spherical Ga_xFe_{2-x}O₃ NCs synthesized according to the procedure of OHKOSHI ET AL. [29]. The substitution rate x of Fe by gallium was determined as $x = 0.043$ via ICP-OES by 3P Instruments GmbH, resulting in Ga_{0.043}Fe_{1.957}O₃ named as Ga:Fe₂O₃. In order to determine the actual phases of the Fe₂O₃ NCs PXRD (Figure 2b), Rietveld-Refinement [44,45], and MÖSSBAUER spectroscopy (Figure 2c) were performed. Comparison of diffractogram with literature data [32] and subsequent RIETVELD-Refinement [44,45] indicate that the synthesized particles are ϵ -Fe₂O₃ and α -Fe₂O₃ in a ratio of 85:15, as the most prominent reflections in a range of $10^{\circ} \leq 2\theta \leq 71^{\circ}$ ($I_{reflection} > 0.1 I_{max}$) align with the

literature data [50–53] (Figure 2b). The formation and ratio of ϵ -Fe₂O₃ and α -Fe₂O₃ is further supported by MÖSSBAUER spectroscopy (Figure 2c), with five different sextets from the measurement showing a good agreement with literature data [74,75].

The highest sextet with a hyperfine splitting of 51.69 T can be assigned to the hematite modification (α -Fe₂O₃) [79], where, derived from its overall peak area, a mass fraction of approx. 15 % was assumed to have resulted from further reactions during the sintering process [76,77]. The remaining four sextets were assigned to the epsilon modification of iron oxide (ϵ -Fe₂O₃), as it is known that four different iron sites can be distinguished inside its crystal structure, usually designated as A to D sites. Its crystal sites A-C follow octahedral coordination from the oxygen atoms, while the D-site is tetragonally coordinated, which aligns with the shown data, as the hyperfine splitting of the D site is much smaller with 26.41 T compared to the other three sites with 50.29 T, 45.09 T, and 39.58 T, respectively [75]. The addition of gallium nitrate mainly replaces the Fe³⁺ of site D with Ga³⁺ cations and hence shows smaller intensities or peak area compared to the other sites, as shown by OHKOSHI ET AL. [29], smaller Ga³⁺ ions prefer to substitute Fe³⁺ in the D-site of Fe₂O₃ with a moderate rate for site C, while sites A and B stay mainly largely unsubstituted. Using the MÖSSBAUER spectrum, it was demonstrated that the ϵ -crystal structure is the main component with small impurities of the α -phase, while the particles remain in the ferromagnetic region because the sextets do not collapse due to the reduced particle size. The magnetic properties were evaluated by SQUID (Figure 2d) and showed indeed hard magnetic character as described by OHKOSHI ET AL. [29]. The nanoparticle composite (ϵ -Ga:Fe₂O₃: α -Ga:Fe₂O₃ 85:15) showed a coercive field of 1.81 T, which is lower than that of pure ϵ -Ga:Fe₂O₃, but can be explained by the antiferromagnetic α -phase, resulting in the step at $B \approx 0$ T, and the integration of Ga³⁺ cations into the crystal lattice, whose effect has been extensively explained by OHKOSHI ET AL. [29].

S2.2 Structural Characterization

The evaluation of the PXRD diffractograms of hardened paste (Figure S2) showed a correlation between a higher mass fraction of Ga:Fe₂O₃ NCs and a more intense reflection at $2\theta \cong 9.2^\circ$, indicating that a higher amount of ettringite [52] is present in the sample compared to pure hydrated cement paste. Regardless of the addition of NCs, the decrease in the main reflections of C₃S and C₂S in a range of $29.5^\circ \leq 2\theta \leq 34.3^\circ$ is due to their hydration and the formation of portlandite [Ca(OH)₂] [4,78,79], the latter being indicated by new reflections at $2\theta = 18.2^\circ, 28.9^\circ, 34.3^\circ, 47.3^\circ, \text{ and } 51.0^\circ$ [45].

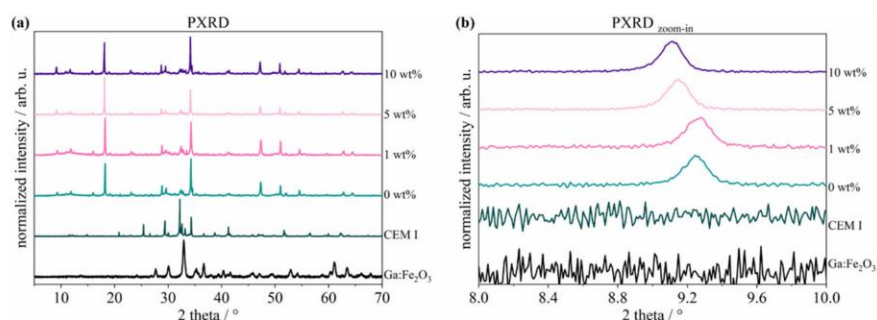


Figure S2. PXRD; evaluation of HCPs (≤ 28 d) made from anhydrous cement mixed with different mass fractions of Ga:Fe₂O₃ NCs; patterns in an angular range of (a) $5^\circ \leq 2\theta \leq 70^\circ$, (b) $8^\circ \leq 2\theta \leq 10^\circ$.

To gain insights into the chemical composition TGA (Figure S3) was used to assess the decomposition behaviour providing insight into the chemical composition of HCP. As shown by PXRD (Figure S2), the TGA (Figure S3) verifies the formation of portlandite, visible in the decomposition peaks characteristic of Ca(OH)₂ at $398^\circ\text{C} \pm 60^\circ\text{C}$ and $588^\circ\text{C} \pm 72^\circ\text{C}$ [80], as well as a high content of ettringite and CSH at temperature up to 225 °C, with no discernible deviation from pure HCP due to a higher mass fraction of Ga:Fe₂O₃ NCs is distinguishable.

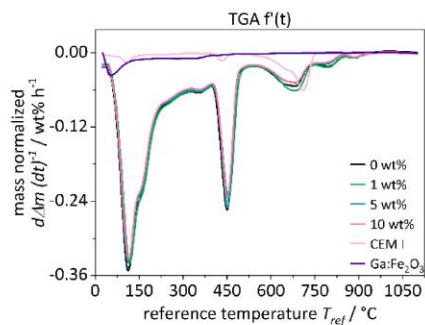


Figure S3. TGA data plotted as mass normalized time derived weight loss ($d\Delta m (dt)^{-1} / \text{wt}\% \cdot \text{h}^{-1}$) per hour against the reference temperature with a heating rate of $5 \text{ }^\circ\text{C min}^{-1}$ of HCP ($\leq 28 \text{ d}$) made from anhydrous cement mixed with different mass fractions of Ga:Fe₂O₃ NCs.

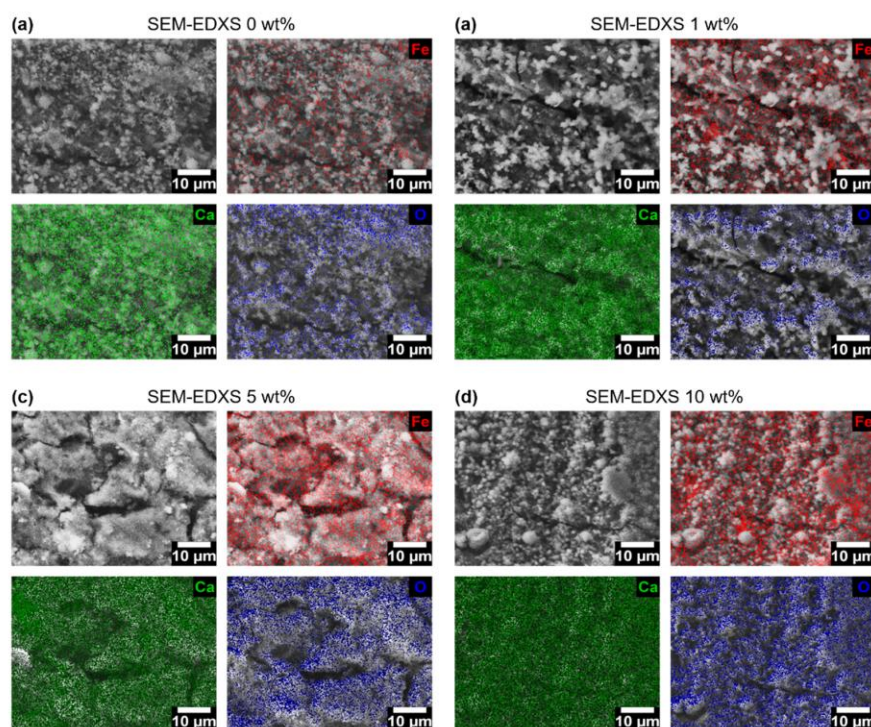


Figure S4. SEM-EDXS data of HCPs made from anhydrous cement mixed with different mass fractions of Ga:Fe₂O₃ NCs; depicted are Fe (red), Ca (green), and O (blue); (a) 0 wt%, (b) 1 wt%, (c) 5 wt%, and (d) 10 wt% Ga:Fe₂O₃ NCs content.

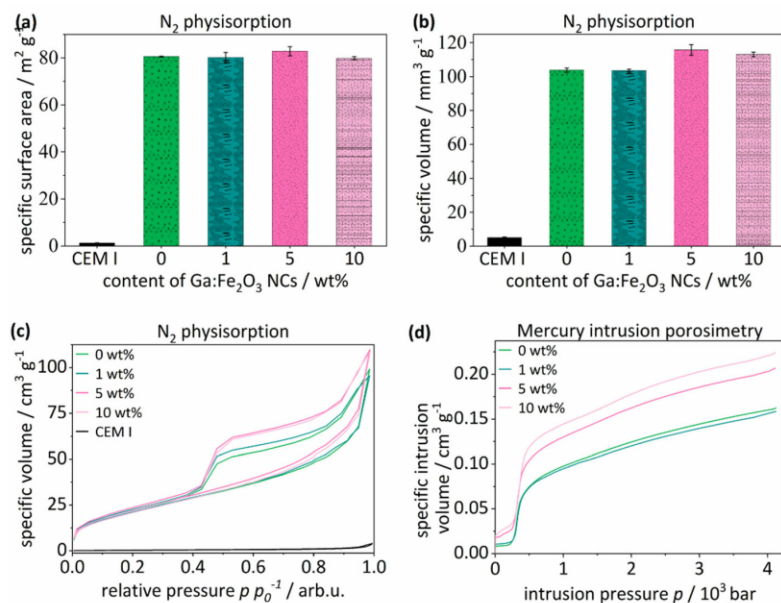


Figure S5. Evaluation of HCPs of anhydrous cement mixed with different mass fractions of Ga:Fe₂O₃ NCs; (a to c) N₂ physisorption data, (a) specific surface area, (b) specific volume, (c) isotherms, and (d) MIP intrusion.

References

- [4] Verein Deutscher Zementwerke e.V., *Zement-Taschenbuch*, Vol. 50, Verein Deutscher Zementwerke E.V., Düsseldorf **2002**.
- [29] S. Ohkoshi, S. Kuroki, S. Sakurai, K. Matsumoto, K. Sato, S. Sasaki, *Angew. Chemie Int. Ed.* **2007**, *46* (44), 8392–8395. DOI: 10.1002/anie.200703010.
- [32] K. Kelm, W. Mader, *Zeitschrift für Anorg. und Allg. Chemie.* **2005**, *631* (12), 2383–2389. DOI: 10.1002/zaac.200500283.
- [35] E. W. Washburn, *Phys. Rev.* **1921**, *17* (3), 273–283. DOI: 10.1103/PhysRev.17.273.
- [37] DIN German Institute for Standardization., *DIN EN 12390-3:2019-10, Testing Hardened Concrete - Part 3: Compressive Strength of Test Specimens; German Version EN 12390-3:2019*, Beuth Verlag GmbH, Berlin, Germany **2019**.
- [39] W. Oliver, G. Pharr, *J. Mater. Res.* **1992**, *7* (6), 1564–1583.
- [41] Z. C. Lu, M. Haist, D. Ivanov, C. Jakob, D. Jansen, S. Leinitz, J. Link, V. Mechtcherine, J. Neubauer, J. Plank, et al., *Data Br.* **2019**, *27*, 104699. DOI: 10.1016/j.dib.2019.104699.
- [44] H. M. Rietveld, *J. Appl. Crystallogr.* **1969**, *2* (2), 65–71. DOI: 10.1107/S0021889869006558.
- [45] P. Paufler, *Cryst. Res. Technol.* **1995**, *30* (4), 494–494. DOI: 10.1002/crat.2170300412.
- [46] F. Nishi, Y. Takéuchi, *Acta Crystallogr. Sect. B Struct. Crystallogr. Cryst. Chem.* **1975**, *31* (4), 1169–1173. DOI: 10.1107/S0567740875004736.
- [47] A. A. Colville, S. Geller, *Acta Crystallogr. Sect. B Struct. Crystallogr. Cryst. Chem.* **1971**, *27* (12), 2311–2315. DOI: 10.1107/s056774087100579x.
- [48] Q. Huang, O. Chmaissem, J. J. Capponi, C. Chaillout, M. Marezio, J. L. Tholence, A. Santoro, *Phys. C Supercond. its Appl.* **1994**, *227* (1–2), 1–9. DOI: 10.1016/0921-4534(94)90349-2.
- [49] J. C. A. Boeyens, V. V. H. Ichharam, *Zeitschrift für Krist. - New Cryst. Struct.* **2002**, *217* (JG), 9–10.

- DOI: 10.1524/ncrs.2002.217.jg.9.
- [50] L. Desgranges, D. Grebille, G. Calvarin, G. Chevrier, N. Floquet, J. -C Niepce, *Acta Crystallogr. Sect. B.* **1993**, 49 (5), 812–817. DOI: 10.1107/S0108768193003556.
- [51] G. A. Lager, J. D. Jorgensen, F. J. Rotella, *J. Appl. Phys.* **1982**, 53 (10), 6751–6756. DOI: 10.1063/1.330062.
- [52] M. R. Hartman, R. Berliner, *Cem. Concr. Res.* **2006**, 36 (2), 364–370. DOI: 10.1016/j.cemconres.2005.08.004.
- [53] M. I. McCarthy, N. M. Harrison, *Phys. Rev. B.* **1994**, 49 (13), 8574–8582. DOI: 10.1103/PhysRevB.49.8574.
- [54] T. Pilati, F. Demartin, C. M. Gramaccioli, *Acta Crystallogr. Sect. B Struct. Sci.* **1998**, 54 (5), 515–523. DOI: 10.1107/S0108768197018181.
- [55] Á. G. De La Torre, S. Bruque, J. Campo, M. A. G. Aranda, *Cem. Concr. Res.* **2002**, 32 (9), 1347–1356. DOI: 10.1016/S0008-8846(02)00796-2.
- [56] F. C. Hawthorne, R. B. Ferguson, *Can. Mineral.* **1975**, 13, 289–292.
- [57] J. A. McGinney, *Acta Crystallogr. Sect. B Struct. Crystallogr. Cryst. Chem.* **1972**, 28 (9), 2845–2852. DOI: 10.1107/s0567740872007022.
- [58] C. Bezou, A. Nonat, J.-C. Mutin, A. N. Christensen, M. S. Lehmann, *J. Solid State Chem.* **1995**, 117 (1), 165–176. DOI: 10.1006/jssc.1995.1260.
- [59] W. Mumme, R. Hill, G. Bushnellwye, E. Segnit, *NEUES Jahrb. FÜR Mineral.* **1995**, 169 (1), 35–68.
- [60] P. Mondal, J. W. Jeffery, *Acta Crystallogr. Sect. B Struct. Crystallogr. Cryst. Chem.* **1975**, 31 (3), 689–697. DOI: 10.1107/S0567740875003639.
- [61] S. Brunauer, P. H. Emmett, E. Teller, *J. Am. Chem. Soc.* **1938**, 60 (2), 309–319. DOI: 10.1021/ja01269a023.
- [62] R. M. Dreizler, E. K. U. Gross, in *Density Funct. Theory*, Springer Berlin Heidelberg, Berlin, Heidelberg **1990**.
- [63] L. D. Gelb, K. E. Gubbins, R. Radhakrishnan, M. Sliwinska-Bartkowiak, *Rep. Prog. Phys.* **1999**, 62, 1573–1659. DOI: 10.1088/0034-4885/77/5/056502.
- [64] Quantachrome Instruments, 'DFT MODELS LIBRARY OF DFT AND GCMC METHODS IN QUANTACHROME'S DATA REDUCTION SOFTWARE', available at <https://www.quantachrome.com/technical/dft.html>, n.d.
- [65] E. P. Barrett, L. G. Joyner, P. P. Halenda, *J. Am. Chem. Soc.* **1951**, 73 (1), 373–380. DOI: 10.1021/ja01145a126.
- [66] T. J. Mays, *Stud. Surf. Sci. Catal.* **2007**, 160 (0), 57–62. DOI: 10.1016/s0167-2991(07)80009-7.
- [67] K. Scrivener, R. Snellings, B. Lothenbach, *A Practical Guide to Microstructural Analysis of Cementitious Materials*, CRC PR INC (22. Dezember 2015) **2015**.
- [68] Q. Yu, H. J. H. Brouwers, in *Proc. 8th Fib Int. PhD Symp. Civ. Eng. Lyngby* (Eds: G. Fischer, M. Geiker, O. Hededa, L. Ottoson, H. Stang), Technical University Of Denmark **2010**.
- [69] C. G. Vassileva, S. V. Vassilev, *Fuel Process. Technol.* **2005**, 86 (12–13), 1297–1333. DOI: 10.1016/j.fuproc.2005.01.024.
- [70] J. Dweck, P. M. Buchler, A. C. V. Coelho, F. K. Cartledge, *Thermochim. Acta.* **2000**, 346 (1–2), 105–113. DOI: 10.1016/S0040-6031(99)00369-X.
- [71] D. J. Morgan, *Clay Miner.* **1978**, 13 (1), 132–132. DOI: 10.1180/claymin.1978.013.1.11.
- [72] A. Bakolas, E. Aggelakopoulou, A. Moropoulou, *J. Therm. Anal. Calorim.* **2008**, 92 (1), 345–351. DOI:

- 10.1007/s10973-007-8858-1.
- [73] K. Wang, S. P. Shah, A. Mishulovich, *Cem. Concr. Res.* **2004**, *34* (2), 299–309. DOI: 10.1016/j.cemconres.2003.08.003.
- [74] R. Zboril, M. Mashlan, D. Petridis, *Chem. Mater.* **2002**, *14* (3), 969–982. DOI: 10.1021/cm0111074.
- [75] E. Tronc, C. Chanéac, J. P. Jolivet, *J. Solid State Chem.* **1998**, *139* (1), 93–104. DOI: 10.1006/jssc.1998.7817.
- [76] H. Tokoro, W. Tarora, A. Namai, M. Yoshikiyo, S. Ohkoshi, *Chem. Mater.* **2018**, *30* (9), 2888–2894. DOI: 10.1021/acs.chemmater.7b03708.
- [77] A. Namai, M. Yoshikiyo, K. Yamada, S. Sakurai, T. Goto, T. Yoshida, T. Miyazaki, M. Nakajima, T. Suemoto, H. Tokoro, et al., *Nat. Commun.* **2012**, *3* (1), 1035. DOI: 10.1038/ncomms2038.
- [78] C. Jakob, D. Jansen, N. Ukrainczyk, E. Koenders, U. Pott, D. Stephan, J. Neubauer, *Materials (Basel)*. **2019**, *12* (18), 2957. DOI: 10.3390/ma12182957.
- [79] C. Jakob, D. Jansen, U. Pott, J. Neubauer, **2020**.
- [80] P. A. Kißling, J. Link, M. Heinemann, F. Lübke-Warwas, F. Rieck genannt Best, T. Sowoidnich, A. Mundstock, H.-M. Ludwig, L. Lohaus, M. Haist, et al., submitted to *Constr. Build. Mater.*.

5 SUMMARY OF THE WHOLE WORK

Focus of this thesis and its five associated publications was to elicit how the early hydration product ettringite influences the rheological properties at an early state of hydration. This included the query of how the morphology and chemical composition of ettringite itself are affected by different methods to stop the hydration process of cementitious suspensions as well as by the addition of hard magnetic nanocrystals. Moreover, the question arose whether no alternative way for hydration stoppage exists that is at least on par with the state-of-the-art technique isopropanol water exchange but less invasive, less mechanically disruptive, as well as more reproducible.

Both latter issues directly correlate to **section 3** of this thesis, wherein, at first, two well-known techniques, solvent exchange with isopropanol (**I**) and lyophilisation also known as freeze-drying (**L**), as well as, for the first time, their combination (**IL**) was used to assess the effect of hydration stoppage on samples at an early hydration stage ($t_{hyd} \leq 90$ min). Characterisation included scanning electron microscopy as an imaging technique and nitrogen physisorption to assess changes to porosity Ψ via the specific surface area SSA , specific volume SV , and pore size distribution PSD . Although the results were too ambiguous to crown a superior technique, the combined method could be identified as a jack-of-all-trades, master of none, since all characterisation results ended up in the middle/between the results of the pure techniques.

In order to optimise the freeze-drying-based method, the influence of the levels of low-pressure and the duration of treatment at these levels on ettringite were examined in detail, wherein ettringite was synthesised and thoroughly characterised before further studies. Three degrees of low-pressure p (400 Pa, 6 Pa, and 90 μ Pa or 3.53 mPa) and a treatment duration of up to $t_{l-p} = 72$ h were implemented to account for low-pressure levels, which are representative of scanning electron microscopy transmission electron microscopy and for freeze-drying, as well as to test out, if a low-pressure near the triple-point of water is sufficient for lyophilisation. Examination of morphological and compositional changes showed that no significant changes occur at $p = 400$ Pa over 72 h of drying. At $p = 6$ Pa significant changes occur already after $t_{l-p} = 5$ h, and at the lowest pressure p $t_{l-p} = 20$ min are sufficient for a drastic change of ettringite's crystal structure, morphology, and chemical composition.

Based on these results, the freeze-drying-based hydration stop was optimised to such an extent that it enables a nearly instantly hydration stop without significant changes to morphology, crystal structure, and chemical composition of ettringite. This, in turn, improves not only the reproducibility of the stopped samples but also eliminates the problematic chemisorption of isopropanol, making an energy- and time-consuming desorption or drying step unnecessary.

The developed technique's utilisation enabled the study of the influence of ettringite on the rheological properties of cementitious suspensions. Since those are very complex and include several hydration processes happening simultaneously/in parallel, investigations were carried out on a model system consisting of quartz powder and different pre-set amounts of *in situ* formed ettringite. It was analytically shown that the pre-set amount of precipitated ettringite was achieved in each analysed suspension. Rheological measurements facilitated the correlation between the amount of precipitated ettringite and changes to rheological properties, wherein these change exponentially with the linear rising content of ettringite.

Besides the studies at an early state of hydration ($t_{hyd} \leq 90$ min), modifications induced by mixing with a nanoscopic additive were evaluated. Addition of nanoscopic gallium substituted epsilon iron oxide ($Ga:Fe_2O_3$) (≤ 10 wt%), wherein the gallium is needed to stabilise the metastable ϵ -phase of iron oxide, introduces magnetic moment to the hardened cement paste and a higher porosity Ψ with higher amount of additive, leading to a decreased characteristic compressive strength with no changes to the hardness of the material. These shown properties of blended hardened cement paste, using a cheap and easily mass-producible nanoscale additive, might make it a promising material for coatings of facades or interior walls when it comes to the protection of sensitive machinery that is negatively influenced by radio waves, *exempli gratia* magnetic resonance tomography in the medical field, to ensure greater lifetime and efficiency.

6 CRITICAL DISCUSSION AND OUTLOOK

Although the newly developed freeze-drying-based technique proved its reproducibility during a round-robin test performed at three universities, access to a freeze-dryer or vacuum device with a distinct level of low-pressure is essential to make this technique work. In this regard, it was already assessed that fluctuations in a range of $90 \text{ Pa} \leq p \leq 450 \text{ Pa}$ did not change the results in the desired drying time range of 3 h. Nevertheless, the method is optimised for the utilisation of liquid nitrogen (LN_2) and requires a contact area as big as possible with the freezing medium, *exempli gratia* in this case, a volume $V = 10 \text{ mL}$ of the suspension ($w/c = 0.5$) distributed as a thin layer over the inner surface of a 250 mL flask. For higher amounts of suspensions or more liquid suspensions, either a bigger contact area is needed, or the pressure needs to be optimised, wherein it has to be noted that the time of sublimation of up to 100 mL pure bulk water in a 250 mL flask varies by only up to 10 min at $p = 400 \text{ Pa}$ compared to $p = 6 \text{ Pa}$. At this point, this procedure is not suited for large-scale amounts of cementitious suspension since the cooling rate of liquid nitrogen (LN_2) is not fast enough to instantly freeze thick samples due to the LEIDENFROST effect^{192}. Changing the freezing media to 2-methoxy-2-methylpropane (MTBE) in liquid nitrogen (LN_2) is possible. Still, the temperature right before freezing of MTBE is not easily achievable, not constant, and seems to dehydrate ettringite at least partly. Therefore, the developed method has to be examined and optimised to freeze thicker samples, ideally via another series of round-robin-tests. Alternatively, if the amount of cementitious suspension that has to be frozen is small enough, *id est* thinner layers or tiny droplets ($V \leq 4 \text{ mL}$, $w/c = 0.5$), this developed technique is indeed usable on large-scale, *exempli gratia* when a batch of a cementitious suspension is dispersed via spray into liquid nitrogen (LN_2) and dried afterwards.

Even after achieving the goal of being able to derive the properties of hardened cement paste directly from the microstructure or rheology of the early hydration state, many requirements for buildings cannot be solved by cement alone, *exempli gratia* the strength of a wall made exclusively of hardened cement paste is inferior to a wall that also contains aggregates. Other issues are financial, environmental, or political, so highly functionalised additives are needed. Furthermore, in our increasingly technological world, a solid and reliable wireless signal becomes increasingly essential for daily life (*exempli gratia* “smart home”) and modern production facilities, which opens the electronic back door for cyber-attacks. As many of us know, regular concrete is quite a hindrance for wireless applications. By adding iron oxide intentionally, as *exempli gratia* in reinforced concrete, in order to enhance stability,

the signal is even more diminished. This effect might be even more substantial in the case of nanoscopic iron oxide. Exclusive of these issues, in the case of hardened cement paste, iron oxide nanoparticles could lower thermal conductivity κ and enhance thermal capacity c_p , *id est* thermal energy is not so easily stored, and if stored, does not dissipate as fast as without this additive. Such thermal properties could *exempli gratia* allow inertia against temperature fluctuations during the day or reduce heating demands on cold nights. It is not yet ascertained which types or modifications of iron oxide and particle size could be used or are most suitable to introduce these effects mainly due to an enhanced porosity Ψ . These problems should or could be addressed in a subsequent study because if the currently used insulating materials, primarily based on polystyrene, could be replaced by a less polluting material, why hesitate?

During the last centuries, many composite materials were developed and even more guidelines on handling the materials have been implemented. Still, from a historical perspective, the progress seems to be less or more stagnant in the past decades. Indeed, climate protection might also be a reason to broaden the perspective of what can be used as an additive to concrete. But is cement or concrete still the construction material of the future? From an environmental perspective, bamboo could be an alternative, as each type of wood consumes more CO₂ than it produces. By purposeful arboriculture, it might also be possible to use seawater, whose level will constantly be rising in the following decades, for bamboo's hydration.

Will humanity's future be built on sand, water, or bamboo?

APPENDIX

GREEK LETTERS

Table A1: List of Greek letters.

Greek letter	explanation / unit
α	crystal phase
$\dot{\gamma}$	shear rate / s^{-1}
γ	crystal phase
ε	crystal phase
η	dynamic viscosity / Pa·s
η_{eq}	equilibrium dynamic viscosity / Pa·s
κ	thermal conductivity / $W \cdot m^{-1} \cdot K^{-1}$
μ	plastic viscosity / Pa·s
ρ	density or specific weight / $kg \cdot m^{-3}$
τ_0	yield stress / Pa
Ψ	porosity / %

SYMBOLS

Table A2: List of symbols.

symbol	explanation / unit
a	cell parameter / \AA
atm	atmosphere; 1 atm \equiv 101.325 kPa
\AA	1 \AA = 10^{-10} m
b	cell parameter / \AA
c	cell parameter / \AA
c_p	specific heat capacity / $J \cdot g^{-1} \cdot K^{-1}$
d	diameter / nm or μm or mm or cm
D	diffusivity / $m^2 \cdot s^{-1}$
f_{ck}	compressive strength / $N \cdot mm^2$
p	pressure / Pa
t	time / min
t_E	diffusion equilibrium time / s
t_{hyd}	hydration time / min or h or d
t_{l-p}	time of low-pressure treatment / h
T	Temperature / $^{\circ}C$
V	volume / mL or cm^3
x	characteristic length / m

ABBREVIATIONS

Table A3: List of abbreviations.

abbreviation	explanation / unit
A	Al_2O_3
AFm	$\text{Ca}_2(\text{Al,Fe})(\text{OH})_6]_2 \text{X n H}_2\text{O}$, mainly $\text{X} \equiv \text{OH}^-$, SO_4^{2-} , or CO_3^{2-} or calcium aluminate hydrate
AFm-14H	$\text{Ca}_4\text{Al}_2(\text{SO}_4)_3(\text{OH})_{12} \cdot 8 \text{H}_2\text{O}$ or calcium aluminate monosulphate
AR	aspect ratio
C	CaO
$\bar{\text{C}}$	CO_2
$\text{C}_2(\text{A,F})\text{H}_8$	$\text{Ca}_2\text{Al}_{2-x}\text{Fe}_x\text{O}_5 \cdot 8 \text{H}_2\text{O}$ or di calcium aluminate ferrite hydrate
C_2AH_8	$\text{Ca}_2\text{Al}_2\text{O}_5 \cdot 8 \text{H}_2\text{O}$ or di calcium aluminate hydrate
C_2S	Ca_2SiO_4 or belite
C_3A	$\text{Ca}_3\text{Al}_2\text{O}_6$ or tricalcium aluminate
C_3AH_6	$\text{Ca}_3\text{Al}_2\text{O}_6 \cdot 6 \text{H}_2\text{O}$ or cubic hydrogarnet or tri calcium aluminate hydrate
$\text{C}_3(\text{A,F})\text{H}_6$	$\text{Ca}_3\text{Al}_{2-x}\text{Fe}_x\text{O}_6 \cdot 6 \text{H}_2\text{O}$ or tri calcium aluminate ferrite hydrate
C_3S	Ca_3SiO_5 or alite
C_4AF	$\text{Ca}_4\text{Al}_2\text{Fe}_2\text{O}_{10}$ or brownmillerite
$\text{C}_4(\text{A,F})\text{H}_{19}$	$\text{Ca}_4\text{Al}_{2-x}\text{Fe}_x\text{O}_7 \cdot 19 \text{H}_2\text{O}$ or tetra calcium aluminate ferrite hydrate
C_4AH_{19}	$\text{Ca}_4\text{Al}_2\text{O}_7 \cdot 19 \text{H}_2\text{O}$ or tetra calcium aluminate hydrate
$\text{C}_6(\text{A,F})\bar{\text{S}}_3\text{H}_{32}$	$\text{Ca}_6\text{Al}_{2-x}\text{Fe}_x(\text{SO}_4)_3(\text{OH})_{12} \cdot 26 \text{H}_2\text{O}$ or iron ettringite or calcium trisulfoaluminate ferrite hydrate
$\text{C}_6\text{A}\bar{\text{S}}_3\text{H}_{32}$	$\text{Ca}_6\text{Al}_2(\text{SO}_4)_3(\text{OH})_{12} \cdot 26 \text{H}_2\text{O}$ or ettringite or calcium trisulfoaluminate hydrate
CAH	calcium aluminate hydrate
CCN	Cement Chemistry Notation
CH	$\text{Ca}(\text{OH})_2$ or portlandite
C.N.	coordination number
C-S-H	$m \text{CaO} \cdot \text{SiO}_2 \cdot n \text{H}_2\text{O}$; $1.2 \leq m \leq 2.3$ or calcium silicate hydrate
$\bar{\text{C}}\bar{\text{S}}\text{H}_2$	$\text{CaSO}_4 \cdot 2 \text{H}_2\text{O}$ or gypsum
D	silica fume
Eq.	equation
F	Fe_2O_3
FD	hydration stop technique based on freeze-drying
$\text{Ga:Fe}_2\text{O}_3$	gallium substituted iron oxide; $\text{Ga}_{0.043}\text{Fe}_{1.957}\text{O}_3$
H	H_2O
IFD	hydration stop technique based on gradual isopropanol-water exchange and freeze-drying
IL	hydration stop technique based on gradual isopropanol-water exchange and lyophilisation
iPrOH	isopropanol
Iso	hydration stop technique based on isopropanol-water exchange
K	K_2O

abbreviation	explanation / unit
K	Portland cement clinker
L	Li_2O
L	limestone with an organics' content $\text{TOC} \leq 0.50$ wt%
LL	limestone with an organics' content $\text{TOC} \leq 0.20$ wt%
LN_2	liquid nitrogen
Lyo	hydration stop technique based on lyophilisation
M	MgO
MTBE	2-methoxy-2-methylpropane
N	Na_2O
Nr.	number
P	natural pozzolan
PCE	polycarboxylate ether superplasticiser
Q	tempered pozzolan
SSA	specific surface area / $\text{m}^2 \cdot \text{g}^{-1}$
SV	specific volume / $\text{mm}^3 \cdot \text{g}^{-1}$
$\bar{\text{S}}$	SO_3
S	SiO_2
S	blast furnace slag
SEM	scanning electron microscopy
SQUID	superconducting quantum interference device
T	TiO_2
T	burnt slate
TEM	transmission electron microscopy
V	siliceous fly ash
w/c	gravimetric water to cement ratio
wt%	weight percentage
W	calcareous fly ash
XRD	X-ray diffraction

FIGURES

Table A4: List of figures.

Nr.	title	page
1	Evolution of compressive strength f_{ck} of cement's main components (C_3S , C_2S , C_3A , and C_4AF) in a cementitious suspension with $w/c = 0.5$; derived from BOGUE ET AL. ^{57} .	- 9 -
2	Scheme of particle interaction (a) without, resulting in coagulation/agglomeration, and (b) with superplasticiser, resulting in dispersion due to COULOMB ^{63,64} forces.	- 10 -
3	Dynamic viscosity η dependent on applied shear rate $\dot{\gamma}$, of a cementitious suspension exhibiting a viscoelastic (magenta), plastic (navy), and dilatant (dark yellow) flow behaviour.	- 11 -
4	(a) Theoretical crystal structure of the so-called "three chain" building blocks in calcium silicate hydrate (C-S-H) on the example of tobermorite 11Å (ICSD-92941) ^{122} in the $[10\bar{1}0]$ projection with edge-sharing octahedrally coordinated Ca^{2+} , and either bridging or pairing corner-sharing tetrahedrally Si^{4+} ; crystal structure of (b) jennite (ICSD-151413) ^{120} in the $[\bar{5}141]$ projection with edge-sharing octahedrally coordinated Ca^{2+} , and (c) tobermorite 14Å (ICSD-152489) ^{121} in the $[10\bar{1}0]$ projection with alternating edge-sharing Ca-O trigonal prisms and capped trigonal prisms; projection given in BRAVAIS-MILLER indices ^{123} .	- 15 -
5	Crystal structure of ettringite following HARTMAN ET AL. ^{128} ; (left) part of a single column in the $[10\bar{1}0]$ projection and (right) build-up in the $[0001]$ projection showing columns and channels parallel to c-axis; BRAVAIS-MILLER indices ^{123} according to a trigonal symmetry in a hexagonal cell.	- 17 -
6	Scheme for pressure-based hydration stop techniques; (a) vacuum-drying, (b) D-drying, (c) P-drying, and (d) freeze-drying.	- 22 -

TABLES

Table A5: List of tables

nr.	title	page
1	Composition of the five main types of cement and their modifications according to DIN EN 197-1 ^[40] .	- 8 -
2	Overview of the previously described hydration stop and drying techniques, including a short introduction, their respective advantages, as well as disadvantages.	- 23 -
3	Large-scale additives in cementitious suspensions and their respective impact. ^[199]	- 25 -
4	Changes to the previously used hydration stop techniques ^[219] .	- 28 -
A1	List of Greek letters.	IX
A2	List of symbols.	IX
A3	List of abbreviations.	X
A4	List of figures.	XII
A5	List of tables.	XIII
A6	List of equations.	XIII

EQUATIONS

Table A6: List of equations.

nr.	equation	page
(1)	$C_3S + n H_2O \rightarrow C_xS_yH_z + (3-x) Ca(OH)_2 + (n-z-(3-x)) H_2O$	- 13 -
(2)	$C_2S + n H_2O \rightarrow C_xS_yH_z + (2-x) Ca(OH)_2 + (n-z-(2-x)) H_2O$	- 13 -
(3)	$C_3A + 3 C\bar{S}H_2 + 26 H \rightarrow C_6A\bar{S}_3H_{32}$	- 16 -
	$Ca_3Al_2O_6 + 3 CaSO_4 \cdot 2 H_2O + 26 H_2O \rightarrow Ca_6Al_2(SO_4)_3(OH)_{12} \cdot 26 H_2O$	
(4)	$2 C_3A + 3 C_6A\bar{S}_3H_{32} + 4 H \rightarrow 3 C_4A\bar{S}H_{12}$	- 17 -
	$2 Ca_3Al_2O_6 + Ca_6Al_2(SO_4)_3(OH)_{12} \cdot 26 H_2O + 4 H_2O \rightarrow 3 Ca_4Al_2SO_4(OH)_8 \cdot 8 H_2O$	
(5)	$t_E \cong x^2 \cdot (2D)^{-1}$	- 19 -

CURRICULUM VITAE

Name	Patrick André Kißling
Date, place of birth	May 12 th 1993, Nuremberg
since 10/23	Scientific Assistant at the Institute of Chemical Reaction Engineering (CRT) at Hamburg University of Technology Supervisor: Prof. Dr. rer. nat. Raimund Horn
07/22 – 07/23	Academic assistant at the Institute of Building Materials Science (IfB) at the Gottfried Wilhelm Leibniz University Hannover Supervisor: Prof. Dr.-Ing. Michael Haist
07/22 – 09/22	Academic assistant at the Institute of Physical Chemistry and Electrochemistry (PCI) at the Gottfried Wilhelm Leibniz University Hannover Supervisor: apl. Prof. Dr. rer. nat. Dirk Dorfs
01/22 – 07/22	Scholarship holder of Graduate Academy at the Gottfried Wilhelm Leibniz University Hannover
09/21 – 12/21	Pre-doctoral fellow at the Institute of Physical Chemistry and Electrochemistry (PCI) at the Gottfried Wilhelm Leibniz University Hannover Supervisor: Prof. em. Dr. rer. nat. Jürgen Caro
06/18 – 08/21	Pre-doctoral fellow at the Institute of Physical Chemistry and Electrochemistry (PCI) at the Gottfried Wilhelm Leibniz University Hannover Supervisor: Prof. Dr. rer. nat. Nadja-Carola Bigall
06/18 – 11/23	Doctoral student at the Institute of Physical Chemistry and Electrochemistry (PCI) at the Gottfried Wilhelm Leibniz University Hannover Supervisor: Prof. Dr. rer. nat. Nadja-Carola Bigall Doctoral thesis title: “ <i>A freeze-drying-based hydration stop technique for the time-variant analysis of the early hydration products of cementitious suspensions</i> ”
10/15 – 04/18	Study of chemistry at the University of Hamburg. Degree: Master of Science (M.Sc.) Master thesis title: “ <i>Phosponsäuren mit zwitterionischer Endgruppe zur Stabilisierung von superparamagnetischen Eisenoxid-Nanopartikeln (SPIOs) – (Phosphonic acids with zwitterionic head group for stabilization of superparamagnetic iron oxide nanoparticles (SPIOs))</i> ” Supervisor: Dr. rer. nat. Theo Schotten, CAN GmbH, Prof. Dr. rer. nat. Horst Weller at the Institute of Physical Chemistry (PCI) at the University of Hamburg
10/11 – 09/15	Study of chemistry and polymer- and colloidal chemistry at the University of Bayreuth Degree: Bachelor of Science (B. Sc.) Bachelor thesis title: “ <i>Herstellung von TEM- und Cryo-TEM Proben unter Verwendung von Inkjet-Technologien</i> ” Supervisor: Dr. rer. nat. Stephan Hauschild, Prof. Dr. rer. nat. Stephan Förster at the Institute of Physical Chemistry I (PCI I) at the University of Bayreuth
09/02 – 05/11	General University Entrance Qualification at Hans-Sachs-Gymnasium Nürnberg with advanced studies in Latin and Physics

PUBLICATIONS AND CONFERENCES

Publications included in this Thesis

- 1 **Impact of hard magnetic nanocrystals on the properties of hardened cement paste.** P.A. Kißling, M. Mahlbacher, C. Wesemann, A. Mundstock, F. Lübkeemann-Warwas, S. Klimke, F. Renz, L. Lohaus, M. Haist, N.C. Bigall; *Chemie Ing. Tech.* **2023**.
DOI: <https://doi.org/10.1002/cite.202300022>.
- 2 **Influence of *in situ* ettringite formation on the rheological properties of quartz suspensions.** P.A. Kißling, J. Link, M. Heinemann, F. Lübkeemann-Warwas, F. Rieck genannt Best, T. Sowoidnich, A. Mundstock, H.-M. Ludwig, M. Haist, N.C. Bigall, *Constr. Build. Mat.* **2023**, *408*, 133678.
DOI: <https://doi.org/10.1016/j.conbuildmat.2023.133678>.
- 3 **Is freeze-drying an alternative to solvent exchange for hydration stop of cementitious suspensions?** P.A. Kißling, F. Lübkeemann, A. Mundstock, L. Lohaus, M. Haist, J. Caro, N.C. Bigall; *Cem. Concr. Res.* **2022**, *159*, 106841.
DOI: <https://doi.org/10.1016/j.cemconres.2022.106841>.
- 4 **Influence of low-pressure treatment on the morphological and compositional stability of microscopic ettringite.** P.A. Kißling, F. Lübkeemann, T. von Bronk, D. Cotardo, L. Lei, A. Feldhoff, L. Lohaus, M. Haist, N.C. Bigall; *Materials* **2021**, *14*, 11, 2720.
DOI: <https://doi.org/10.3390/ma14112720>.
- 5 **Comparison of water-isopropanol replacement and lyophilisation for hydration stop of cementitious suspensions.** P.A. Kißling, D. Cotardo, T. von Bronk, L. Lohaus, N.C. Bigall, in: V. Mechtcherine, K. Khayat, E. Secieru (Eds.) *Rheol. Process. Constr. Mater. RheoCon 2019, SCC2019*, Springer, Cham, **2020**: pp. 610–618.
DOI: https://doi.org/10.1007/978-3-030-22566-7_71.

Publications not included in this Thesis

- 6 **Multiplying oxygen permeability of a Ruddlesden-Popper oxide by orientation control via magnets.** Z. Zhao, G. Chen, G. Escobar Cano, P.A. Kißling, O. Stölting, B. Breidenstein, S. Polarz, N.C. Bigall, A. Weidenkaff, A. Feldhoff; *Angew. Chemie Int. Ed.* **2023**.
DOI: <https://doi.org/10.1002/anie.202312473>.
- 7 **Multiplying oxygen permeability of a Ruddlesden-Popper oxide by orientation control via magnets.** Z. Zhao, G. Chen, G. Escobar Cano, P.A. Kißling, O. Stölting, B. Breidenstein, S. Polarz, N.C. Bigall, A. Weidenkaff, A. Feldhoff; *Angew. Chemie* **2023**.
DOI: <https://doi.org/10.1002/ange.202312473>.
- 8 **The influence of sample mass (scaling effect) on the synthesis and structure of non-graphitizing carbon (biochar) during the analytical pyrolysis of biomass.** R.R. Nair, P.A. Kißling, A. Schaate, A. Marchanka, M. Shamsuyeva, P. Behrens, D. Weichgrebe; *RSC Adv.* **2023**, *13*, 13526–13539.
DOI: <https://doi.org/10.1039/D3RA01911J>.
- 9 **Biochar synthesis from mineral and ash-rich waste biomass, part 2: characterization of biochar and co-pyrolysis mechanism for carbon sequestration.** R.R. Nair, P.A. Kißling, A. Marchanka, J. Lecinski, A.E. Turcios, M. Shamsuyeva, N. Rajendiran, S. Ganesan, S.V. Srinivasan, J. Papenbrock, D. Weichgrebe; *Sustain. Environ. Res.* **2023**, *33*, 14.
DOI: <https://doi.org/10.1186/s42834-023-00176-9>.

- 10 **Sol-Gel process based molten-flux synthesis of plate-like $\text{La}_2\text{NiO}_{4+\delta}$ particles.** G. Escobar Cano, Y. Brinkmann, Z. Zhao, P.A. Kißling, A. Feldhoff, *Crystals* **2022**, *12*, 1346.
DOI: <https://doi.org/10.3390/cryst12101346>.
- 11 **Controlled methylamine synthesis in a membrane reactor featuring a highly steam selective K^+ -LTA membrane.** F. Rieck genannt Best, A. Mundstock, H. Richter, P.A. Kißling, K. Hindricks, A. Huang, P. Behrens, J. Caro; *Microporous Mesoporous Mater.* **2022**, *337*, 111920.
DOI: <https://doi.org/10.1016/j.micromeso.2022.111920>.
- 12 **Boosting dimethylamine formation selectivity in a membrane reactor by in situ water removal.** F. Rieck genannt Best, A. Mundstock, P.A. Kißling, H. Richter, K.D.J. Hindricks, A. Huang, P. Behrens, J. Caro, *Ind. Eng. Chem. Res.* **2022**, *61*, 1, 307–316.
DOI: <https://doi.org/10.1021/acs.iecr.1c04149>.
- 13 **Reaction sintering of $\text{Ca}_3\text{Co}_4\text{O}_9$ with BiCuSeO nanosheets for high-temperature thermoelectric composites.** R. Hinterding, D. Rieks, P.A. Kißling, L. Steinbach, N.C. Bigall, A. Feldhoff; *J. Electron. Mater.* **2022**, *51*, 2, 532–542.
DOI: [10.1007/s11664-021-09336-2](https://doi.org/10.1007/s11664-021-09336-2).
- 14 **One-step formation of hybrid nanocrystal gels: deposition of metal domains on CdSe/CdS nanorod and nanoplatelet networks.** D. Zámbo, A. Schlosser, R.T. Graf, P. Rusch, P.A. Kißling, A. Feldhoff, N.C. Bigall; *Adv. Opt. Mater.* **2021**, *9*, 17, 2100291.
DOI: <https://doi.org/10.1002/adom.202100291>.
- 15 **Pd-doped cellulose carbon aerogels for energy storage applications.** N. Ramirez, D. Zámbo, F. Sardella, P.A. Kißling, A. Schlosser, R.T. Graf, D. Pluta, C. Deiana, N.C. Bigall, *Adv. Mater. Interfaces.* **2021**, *8*, 12, 2100310.
DOI: <https://doi.org/10.1002/admi.202100310>.
- 16 **Capacitive behaviour of activated carbons obtained from coffee husk.** N. Ramirez, F. Sardella, C. Deiana, A. Schlosser, D. Müller, P.A. Kißling, L.F. Klepzig, N.C. Bigall; *RSC Adv.* **2020**, *10*, 62, 38097–38106.
DOI: <https://doi.org/10.1039/D0RA06206E>.
- 17 **Characterization data of reference cement CEM III/A 42.5N used for priority program DFG SPP 2005 “Opus Fluidum Futurum – Rheology of reactive, multiscale, multiphase construction materials”.** Z.C. Lu, M. Haist, D. Ivanov, C. Jakob, D. Jansen, M. Schmid, P.A. Kißling, S. Leinitz, J. Link, V. Mechtcherine, J. Neubauer, J. Plank, W. Schmidt, C. Schilde, C. Schröfl, T. Sowoidnich, D. Stephan, *Data in Brief*, Volume 30, **2020**, 105524.
DOI: <https://doi.org/10.1016/j.dib.2020.105524>.
- 18 **Comparability of cementitious suspensions and paste of concrete.** T. von Bronk, D. Cotardo, P.A. Kißling, M. Haist, N.C. Bigall, L. Lohaus, 2nd International RILEM Conference: Rheology and Processing of Construction Materials (RheoCon2), 2019, Dresden.

Talks

- 1 **Analysis of time-variant nano- and microscopic mechanisms for modelling the meso- and macroscopic segregation stability of concrete subject to vibration.** P.A. Kißling, T. von Bronk, L. Lohaus, M. Haist, N.C. Bigall, 3rd Annual Meeting Priority Programme SPP2005 **2021**, Hannover online.
- 2 **Effect of low-pressure on the morphology and chemical composition of ettringite.** P.A. Kißling, D. Cotardo, T. von Bronk, L. Lohaus, N.C. Bigall, 1st Winter School Priority Programme SPP2005 **2020**, Grainau.
- 3 **Micro sedimentation behavior of cement suspensions.** T. von Bronk, P.A. Kißling, N.C. Bigall, M. Haist, L. Lohaus, 1st Winter School Priority Programme SPP2005 **2020**, Grainau.
- 4 **Comparability of cementitious suspensions and the paste of concrete.** T. von Bronk, D. Cotardo, P.A. Kißling, N.C. Bigall, M. Haist, L. Lohaus, RheoCon **2019**, SCC2019, Dresden.
- 5 **Analysis of time-variant nano- and microscopic mechanisms for modelling the meso- and macroscopic segregation stability of concrete subject to vibration.** P.A. Kißling, T. von Bronk, N.C. Bigall; 1st Annual Meeting Priority Programme SPP2005 **2018**, Dresden.

Posters

- 1 **Impact of ettringite on the rheological properties of quartz suspensions.** P.A. Kißling, J. Link, M. Heinemann, F. Lübke mann-Warwas-Warwas, F. Rieck genannt Best, T. Sowoidnich, A. Mundstock, H.-M. Ludwig, L. Lohaus, M. Hiast, N.C. Bigall, NanoDay **2022**, Laboratorium für Nano- und Quantenengineering Leibniz Universität Hannover.
- 2 **Hydration stop of cementitious suspensions.** P.A. Kißling, L. Lohaus, N.C. Bigall, Leibniz University Chemistry Symposium LUCS **2022**, GDCh Hannover.
- 3 **Hydration stop of cementitious suspensions by three techniques.** P.A. Kißling, D. Cotardo, T. von Bronk, L. Lohaus, N.C. Bigall, Bunsentagung **2021**, Universität Regensburg online.
- 4 **Hydration stop of cementitious suspensions.** P.A. Kißling, D. Cotardo, T. von Bronk, L. Lohaus, N.C. Bigall, NanoDay **2019**, Laboratorium für Nano- und Quantenengineering Leibniz Universität Hannover.
- 5 **Analysis of time-variant nano- and microscopic mechanisms for modelling the meso- and macroscopic segregation of concrete subject to vibration.** P.A. Kißling, D. Cotardo, N.C. Bigall; Particle Based Materials Symposium **2018**, Erlangen.